UNIVERSITY OF SOUTHAMPTON

FACULTY OF MEDICINE

Clinical and Experimental Sciences

An investigation of Amyloid Beta (Aβ) induced pathology in Age-related Macular Degeneration

.

by

SAVANNAH AMY LYNN, BSC

Thesis for the degree of Doctor of Philosophy

October 2018

UNIVERSITY OF SOUTHAMPTON

ABSTRACT

FACULTY OF MEDICINE

Clinical and Experimental Sciences

Thesis for the degree of Doctor of Philosophy

AN INVESTIGATION OF AMYLOID BETA (Aβ) INDUCED PATHOLOGY IN AGE-RELATED MACULAR DEGENERATION

Savannah Amy Lynn, BSc

Age-related Macular Degeneration (AMD) is the leading cause of irreversible vision loss in the western world, accounting for 8.7% of global blindness. However, current therapeutics are only applicable to 50% of patients and are ineffective in long-term treatment. This is due to an incomplete understanding of the aetiology underpinning Retinal Pigment Epithelium (RPE) and photoreceptor atrophy in AMD. Lysosomal malfunction within the RPE is believed to result in failed photoreceptor outer segment (POS) phagocytosis and the increased accumulation of protein/lipid aggregates in early AMD. Amyloid beta (Aβ), a highly toxic and penetrative peptide associated with Alzheimer's disease, has also been shown to deposit in the ageing retina and associated with key stages of AMD. The purpose of this work was to elucidate the association of Aβ with AMD pathology and test the hypothesis that Aβ accumulates within RPE lysosomes and perturbs normal organelle function.

An *in vitro* model of the outer retina was successfully established and exploited to investigate the subcellular localisation of $A\beta_{1-42}$, as well as its effects on lysosomal function. Colocalisation analysis showed that 40.7 ± 8.6% of Aβ resided within RPE lysosomes, whilst live cell imaging and QPCR determined temporal changes in Cathepsin B activity and expression. Elevated Cathepsin B activity was found at 0.5 ($p<0.0001$) and 3 hours ($p=0.0095$) post exposure but returned to baseline at 24 and 48 hours, however mRNA expression remained consistent. Increased Aβ colocalisation with lysosomal Cathepsin B continued up to 24 hours despite a decline in activity. A functional assay also assessed Aβ effects on RPE phagocytic function, which showed decreased POS colocalisation with LAMP-1 at 20 hours. Insights into the biological function of Aβ within the retina were gained through ELISA, which demonstrated increased secretion of Aβ from the basal RPE surface ($p=0.0004$). We also assessed the toxicity of Aβ *in vivo* using subretinal injections in C57BL6/J mice. Here, ERG and OCT revealed no significant effect on global retinal function or thickness of constituent layers, although Aβ appeared to induce retinal pathology akin to CNV. Finally, a case-control pilot study was initiated to determine the association of vitreous Aβ concentration with AMD.

The work presented within this thesis demonstrates the presence of Aβ within RPE lysosomes for the first time, where it potentially modulates the function of RPE clearance mechanisms. Similarly, we associate Aβ with CNV *in situ* through the novel use of non-invasive imaging techniques. These studies provide mechanistic insights into the cytotoxic effects of Aβ within the retina that could ultimately drive the RPE atrophy and inflammatory processes associated with AMD pathology. In particular, the functional consequences of Aβ on the RPE endolysosomal system may identify Aβ as a novel therapeutic target for early AMD.

Publications

Original research papers related to thesis

1. **Savannah A Lynn**, Gareth Ward, Eloise Keeling, Jennifer A Scott, Angela J Cree, David A Johnston, Anton Page, Enrique Cuan-Urquizo, Atul Bhaskar, Martin C Grossel, David A Tumbarello, Tracey A Newman, Andrew J Lotery, J Arjuna Ratnayaka (2017). Ex-vivo models of the Retinal Pigment Epithelium (RPE) in long-term culture faithfully recapitulate key structural and physiological features of native RPE. *Tissue and Cell*, 49(4):447-460.

2. George Taylor-Walker, **Savannah A Lynn**, Eloise Keeling, Rosie Munday, David A Johnston, Anton Page, Jennifer A Scott, Srini Goverdhan, Andrew J Lotery, J Arjuna Ratnayaka (2016). The Alzheimer's-related amyloid beta peptide is internalised by R28 neuroretinal cells and disrupts the microtubule associated protein 2. *Experimental Eye Research*, 153:110-121.

3. **Savannah A Lynn**, Eloise Keeling, Jennifer M Dewing, David A Johnston, Anton Page , Angela J Cree , David A Tumbarello, Tracey A Newman, Andrew J Lotery, J Arjuna Ratnayaka (2018). A convenient protocol for establishing a human cell culture model of the outer retina. F1000 Research, 7:1107.

Review papers related to thesis

1. **Savannah A Lynn**, Eloise Keeling, Rosie Munday, Gagandeep Gabha, Helen Griffiths, Andrew J Lotery, J Arjuna Ratnayaka (2017). The complexities underlying age-related macular degeneration: could amyloid beta play an important role? *Neural Regeneration Research*, 12(4):538-548.

Book chapters related to thesis

1. J. Arjuna Ratnayaka and **Savannah A Lynn** (2016). Alzheimer's-Related Amyloid Beta Peptide Aggregates in the Ageing Retina: Implications for Sight Loss and Dementia, Update on Dementia, Dr. Davide Moretti (Ed.), InTech, DOI: 10.5772/64790.

Original research papers unrelated to thesis

1. Kaitlyn Hair,Malcolm R Macleod, Emily S Sena, **The IICARus Collaboration** (2018) A randomised control trial of an Intervention to Improve Compliance with the ARRIVE guidelines (IICARus) [preprint].bioRxiv, DOI: https://doi.org/10.1101/370874

Table of Contents

Table of Contents

List of Tables

Table of Figures

List of Accompanying Materials

Electronic appendices are included on the disc or electronic folder provided. The materials on this disc include:

- Representative AVI compilation of sequential z-stacks through an RPE cell to demonstrate Alexa Fluor® 488 tagged $A\beta_{1-42}$ colocalisation with LysoSensor DND-160 (Appendix A).

- Example videos of sequential OCT scans for $A\beta_{1-42}$, vehicle/sham and BSA injected mice referenced in Chapter 4 (Appendix B)

Academic Thesis: Declaration of Authorship

I, Savannah Amy Lynn, declare that this thesis and the work presented in it are my own and has been generated by me as the result of my own original research.

An investigation of Amyloid Beta (Aβ) induced pathology in Age-related Macular Degeneration

I confirm that:

1. This work was done wholly or mainly while in candidature for a research degree at this University;
2. Where any part of this thesis has previously been submitted for a degree or any other qualification at this University or any other institution, this has been clearly stated;
3. Where I have consulted the published work of others, this is always clearly attributed;
4. Where I have quoted from the work of others, the source is always given. With the exception of such quotations, this thesis is entirely my own work;
5. I have acknowledged all main sources of help;
6. Where the thesis is based on work done by myself jointly with others, I have made clear exactly what was done by others and what I have contributed myself;
7. Parts of this work have been published as:

    a.) Lynn SA, Ward G, Keeling E, Scott JA, Cree AJ, Johnston DA, Page A, Cuan-Urquizo E, Bhaskar A, Grossel MC, Tumbarello DA, Newman TA, Lotery AJ, Ratnayaka JA (2017). Ex-vivo models of the Retinal Pigment Epithelium (RPE) in long-term culture faithfully recapitulate key structural and physiological features of native RPE. *Tissue and Cell*, 49(4):447-460.

    b.) Taylor-Walker G, Lynn SA, Keeling E, Munday R, Johnston DA, Page A, Scott JA, Goverdhan S, Lotery AJ, Ratnayaka JA (2016). The Alzheimer's-related amyloid beta peptide is internalised by R28 neuroretinal cells and disrupts the microtubule associated protein 2. *Experimental Eye Research*, 153:110-121.

    c.) Lynn SA, Keeling E, Dewing JM, Johnston DA, Page A, Cree AJ, Tumbarello DA, Newman TA, Lotery AJ, Ratnayaka JA (2018). A convenient protocol for establishing a human cell culture model of the outer retina. *F1000 Research*, 7:1107.

Signed: .....

Date: .....

Acknowledgements

This research project would not have been possible without the guidance and expertise of my four supervisors, Dr Arjuna Ratnayaka, Dr Tracey Newman, Mrs Angela Cree and Professor Andrew Lotery, all of whom have consistently provided invaluable and constructive feedback throughout the duration of this project. I could not have asked for a better supervisory team. They have ensured that this PhD was both productive and enjoyable. In particular, Arjuna has been extremely generous in giving up his time, and has not only taken an active interest in developing my scientific skills, including writing and experimental design, but also my career development. For this, I am eternally grateful.

I would also like to express my deepest gratitude to Dr David Johnston for his help with confocal imaging and experimental design and for being extremely supportive since day one. David has always been a friendly face to talk through experimental ideas with, and to work out solutions when things have not quite gone to plan. Many thanks must also go to Dr Anton Page for his help with transmission electron microscopy, Professor Louise Serpell and Dr Karen Marshal for teaching me the oligomeric $A\beta_{1\text{-}42}$ preparation technique, Dr David Chatelet for his advice regarding colocalisation analysis, and to Dr Emilie Simon for her guidance and support with qPCR design and procedure. A special mention must also go to Miss Jenny Scott and Dr Helena Lee who have helped tremendously with teaching the techniques needed for the *in vivo* chapter of this thesis. They have been brilliant fun to work with and have become great friends. I am also grateful for everyone else within the Vision group for their moral support and encouragement. It is a privilege to work within this group, whose commitment and dedication to their work has furthered my enthusiasm for science. I look forward to continuing to work with them over the next two years.

Similarly, I would like to acknowledge all the clinical staff that have helped to make analysis of human vitreous possible, primarily to Professor Lotery, Amanda Smith and Thea Sass for orchestrating this process, but also to Mr Steve Lash for allowing me to collect samples from his theatres and to see the clinical side of Ophthalmology. Additionally, to Mr Hussein Al Muhtaseb who voluntarily agreed to be a second inter-rater and provided me with example fundus and OCT images. I must also extend a vote of thanks to the rest of the clinical team whose jovial but professional attitudes made this an enjoyable experience.

Thanks are also due to the NC3Rs for their generous funding, without whom this exciting research project would not have been possible.

Most importantly, I cannot thank my Mum and Pops enough for their love and support. I would not be where I am today without their guidance, encouragement, and the sacrifices they made to ensure I received a good education. They have always taught me to give my best and have instilled in me their own work ethic. I would like them to know how grateful I am for the opportunities they have given me and for always believing in me. I hope to do them proud.

Finally, I would like to thank my fiancé, Alec Rodgers who has consistently provided kind words of encouragement throughout my PhD, and keeps me motivated on a daily basis. He has always taken an active interest in my project and has listened, and provided advice when I have needed it most. We have had many long discussions about my research over the past 3 years and I truly believe that he is now well equipped to defend this thesis! I could not ask for a more loving and supportive person to have shared this journey with, and would like to let him know how grateful I am for his support.

All data collected within this thesis was conducted by myself, with the exception of several instances. Here, help was given by colleagues, or project students supervised by myself and is formally acknowledged below.

- Dr Lizzie Angus cut the Transwell® membranes for transmission electron microscopy presented in Section 3.3.1, Chapter 3.
- Mr Dillon Davies aided with RNA extraction from experimental cultures in Section 3.3.4 and performed the quantification in Section 3.3.5, Chapter 3.
- Professor Andrew Lotery provided clinical advice with respect to the pathology observed in Figure 39, Chapter 4.
- Miss Rosie Munday performed all cryosectioning, H&E staining, and the analysis of histology in Section 4.3.3, Chapter 4.
- The Ophthalmology Research Team conducted the screening and recruitment of suitable patients for Chapter 5.

Nomenclature

A2E	N-retinylidene-Nretinylethanolamine
ACE	Acetylcholine Esterase
ACTB	Beta Actin
AD	Alzheimer's Disease
AICD	APP Intracellular Domain
AMD	Age-related Macular Degeneration
ApoE	Apolipoprotein E
APP	Amyloid Precursor Protein
AREDS	Age-related Eye Disease Study
Aβ	Amyloid Beta
BCA	Bicinchoninic Acid
BF	Brightfield
BRB	Blood-Retinal Barrier
BSA	Bovine Serum Albumin
C2	Complement Factor 2
C3	Complement Factor 3
CAA	Cerebral Amyloid Angiopathy
CFB	Complement Factor B
CFH	Complement Factor H
CFI	Complement Factor I
cGMP	cyclic Guanosine Monophosphate
CME	Cystoid Macula Edema
CNS	Central Nervous System
CNV	Choroidal Neovascularisation
CRALBP	Retinaldehyde-binding protein 1
CSF	Cerebrospinal Fluid
CTSB	Cathepsin B
CYC1	Cytochrome C1
DAPI	4’, 6’-diamino-2-phenylindole
ddH2O	Double distilled Water
DMEM	Dulbecco's Modified Eagle’s Medium
DMSO	Dimethylsulfoxide
DR	Diabetic Retinopathy
EIF4A2	Eukaryotic Initiation Factor 4A2
ELISA	Enzyme Linked Immunosorbant Assay
ELN	Endolysosomal Network
ERG	Electroretinogram
ERM	Epiretinal Membrane
ETPRS	Photoreceptor End Tips
FAK	Focal Adhesion Kinase
FDA	Food and Drug Administration
ffERG	full-field ERG
FITC	Fluorescein isothiocyanate
FITC-POS	Fluorescein isothiocyanate conjugated photoreceptor outer segments
GA	Geographic Atrophy
GAPDH	Glyceraldehyde-3-phosphate Dehydrogenase

GWAS	Genome Wide Association Study
H&E	Haematoxylin and Eosin
HRP	Horseradish Peroxidase
HSP	Heat Shock Protein
HUVECS	Human Umbillical Vein Endothelial Cells
Ig	Immunoglobulin
IL-1β	Interleukin-1β
IL-8	Interleukin-8
INL	Inner Nuclear Layer
IOP	Intraoccular Pressure
IP	Intraperitoneal
IPL	Inner Plexiform Layer
LAL	Limulus Amebocyte Lysate
LAMP-1	Lysosome Associated Membrane Protein 1
LAMP-2A	Lysosome Associated Membrane Protein 2A
LMP	Lysosomal Membrane Permeabilisation
LoD	Linearity of Dilution
M1	Manders' Coefficient 1
M2	Manders' Coefficient 2
mAb	monoclonal Antibody
MAP	Mean Arterial Pressure
MCP-1	chemokine monocyte chemotactic protein-1
MerTK	Tyrosine Kinase c-mer
MFG-8	Milk Fat Globule-EGF8
MH	Macular Hole
mRNA	messenger RNA
NC3Rs	National Centre for the Replacement, Reduction and Refinement of Animals in Research
NF-kB	Nuclear Factor kappa-light-chain-enhancer of activated B cells
NGS	Normal Goat Serum
NHS	National Health Service
NTC	No Template Control
OCT	Optical Coherence Tomography
OCT	Optimal Cutting Temperature medium
ONL	Outer Nuclear Layer
OPL	Outer Plexiform Layer
P	Passage number
pAb	polyclonal Antibody
PBS	Phosphate Buffered Saline
PCR	Polymerase Chain Reaction
PDE	Phosphodiesterase
PDMPO	LysoSensor Yellow/Blue DND-160
PEDF	Pigment Epithelium Derived Factor
PFA	Paraformaldehyde
PI3 Kinase	Phosphoinositide Kinase
PIS/IS	Photoreceptor Inner Segments
POS/OS	Photoreceptor Outer Segments
QPCR	Quantitative Real-Time Polymerase Chain Reaction
RGC	Retinal Ganglion Cells
RNFL	Retinal Nerve Fibre Layer

Nomenclature

ROI	Region Of Interest
ROS	Reactive Oxygen Species
RPE	Retinal Pigment Epithelium
RPE65	Retinal Pigment Epithelium Specific Protein 65
sAPPα	soluble APPα
SEM	Standard Error of the Mean
SHM	Subretinal Hyperreflective Material
SNP	Single Nucleotide Polymorphism
SQSTM1	Sequestosome 1
SR	Spike Recovery
T(A)	A-wave Implicit Time
T(B)	B-wave Implicit Time
TEER	Transepithelial Electrical Resistance
TEM	Transmission Electron Microscopy
TNF-α	Tumour Necrois Factor α
UP	Ubiquitin Proteasome
UT	Untreated
VEGF	Vascular Endothelial Growth Factor
VF	Vitreous Floaters
VH	Vehicle
VMT	Vitreomacular Traction Syndrome
VR	Vitreoretinal
WT	Wild Type
ZO	Zonula Occludens

Chapter 1 Introduction

1.1 General introduction

Vision is a remarkable evolutionary adaptation that is common to most animals. Indeed, ocular structures across distinct lineages of the phylogenetic tree are almost identical despite significant phenotypic, genetic, behavioural and phenological differences. Conservation of this complex sensory process highlights its obvious evolutionary advantage. This is evidenced by specialised species-specific differences that exist within the visual system that are refined to an animal's environmental needs. For example, herbivores exhibit a wider visual field to increase predatory awareness[1], rods dominate the mouse retina to facilitate nocturnal vision[2] and birds possess two fovea as well as a thicker lens to detect prey from high altitudes[3]. Even the blind mole rat, whose eyes are thought to be visually none functional, appears to rely on the detection of light for circadian rhythmicity[4]. Such diversity highlights the relative plasticity of the visual system and its importance for survival.

The human eye has adapted to accommodate high acuity visual processes that are essential for basic human behaviour and societal interaction. It is therefore not surprising that blindness and impaired vision are among the most feared medical conditions after cancer and cardiovascular disease[5]. This is of particular concern for individuals afflicted with Age-related Macular Degeneration (AMD). This chronic blinding condition is the leading cause of ocular morbidity in the developed world and is responsible for over 50% of registered blindness and partial sight in the UK alone[6]. Vision loss associated with AMD impairs performance of routine daily tasks and thus imposes a significant financial and emotional burden on both patients and their families. Hence, a number of additional complications accompany disease including a loss of independence, compromised life quality, and as a result depression[7].In spite of AMD's prevalence, no cure exists and only 50% of late stage cases are manageable with current therapeutic treatments[6]. This is largely due to an incomplete understanding of the fundamental molecular mechanisms that underpin disease. Nonetheless, the gradual degeneration and atrophy of the Retinal Pigment Epithelium (RPE) appears to be integral to the disease process. This occurs exclusively within the region of the retina critical for visual acuity, and results in secondary photosensory cell degeneration and visual loss. In order to devise

effective therapies, an increased understanding of disease aetiology is first required.

More recently, an increasing body of literature has implicated the Alzheimer's Disease (AD) associated Amyloid β (Aβ) peptide with key stages of AMD[8]. This cytotoxic peptide is known to accumulate within the ocular environment with age and be associated with several aspects of RPE dysfunction[8 9]. However, one major function in which the effects of Aβ have not yet been investigated is the phagocytic ability of the RPE, which is required for the daily internalisation and processing of shed photoreceptor outer segments (POS). This is surprising given the association of impaired RPE clearance mechanisms, including proteosomal[10], autophagic[11] and endo-lysosomal degradation[12], with an AMD phenotype. Similarly, there is a body of evidence that supports Aβ mediated lysosomal dysfunction in neurons[13-15], and its association with impaired autophagy in early AD pathogenesis[16]. By acquiring an increased understanding of the molecular mechanisms by which Aβ drives RPE dysfunction, novel targets may be identified for the development of therapeutic and preventative agents for early disease.

The main themes outlined in this thesis explore the association of Aβ with AMD pathology. Specifically, we study the effects of Aβ *in vivo* using a subretinal injection mouse model, as well as in human ocular fluids to evaluate the relationship between Aβ levels and AMD pathology. However, we mainly focus on the molecular effects of Aβ on the RPE lysosomal system, which is now increasingly regarded as impaired in the initial stages of AMD. In order to provide context for this work, a brief description of the eye's anatomy, retinal function and anatomical structures affected in AMD will first be discussed.

1.2 The eye

The eye may be regarded as a highly specialised extension of the Central Nervous System (CNS) that enables visual perception. This complex phenomenon requires the orchestrated function of several anatomical structures within both the eye and brain[17]. Damage at any one point within the visual pathway can have a devastating impact on this biological process and lead to ocular disease.

1.2.1 Anatomy of the eye

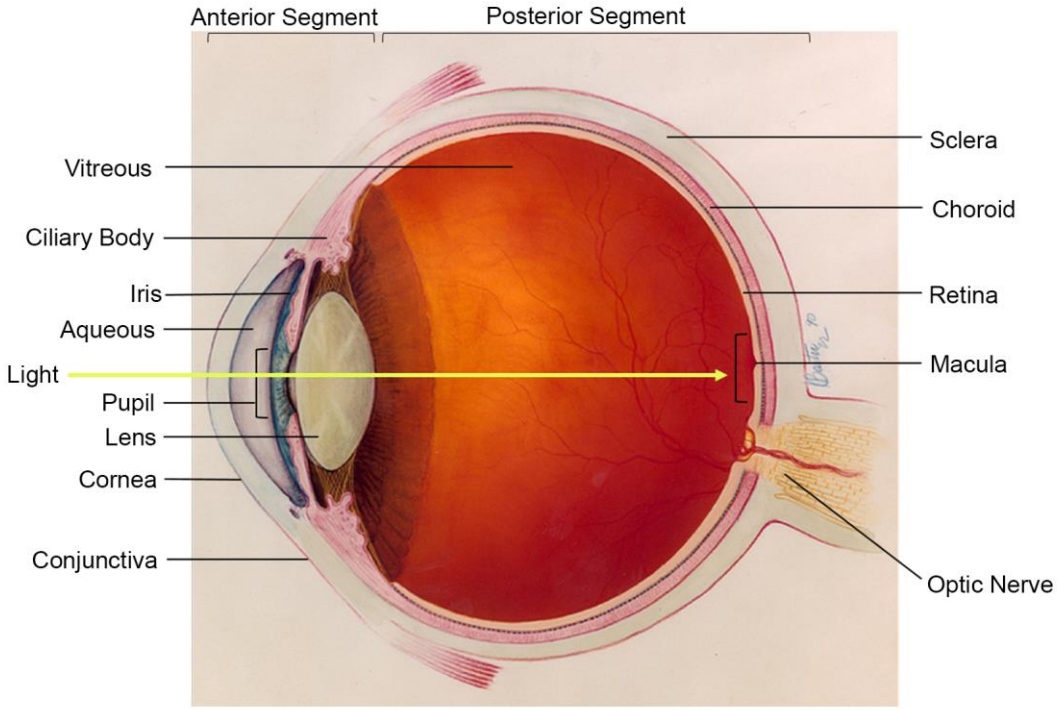

Figure 1: The anatomy of the human eye.

Diagram showing the anatomical structure of the human eye. The cornea and the sclera form the outer most layers of the human eye, which in conjunction with the aqueous and vitreous humours maintain spherical architecture. The choroid lies anterior to the sclera and provides a vascular supply that is essential for the proper function of the adjacent outer retinal complex. The focusing of light onto the retina involves the fine tuning of the pupil and lens by muscular components within the iris and ciliary body. These are responsible for controlling pupillary diameter as well as lens shape and refractive index. Visual input is transduced into neuronal signals within the retinal layers, which are subsequently relayed to the visual cortex via the optic nerve. The optic nerve maintains the anatomical connection of this sensory organ with the brain[17]. Image sourced from the National Eye Institute Photos and Images catalogue, National Institutes of Health. This may be accessed via the following link: https://nei.nih.gov/photo.

Structurally, the eye is enclosed by three layers of tissue (the retina, the uveal tract and the sclera)[17]. These, in combination with the aqueous and vitreous humours, confer structural support to this fluid filled sphere, as illustrated in Figure 1[17]. The vitreous comprises approximately 80% of the eyes volume and is a transparent,

viscous fluid that lies within the posterior chamber of the eye[17]. In addition to structural support, phagocytic hyalocytes reside within the vitreous and remove debris and blood to ensure optimal light transmission[18]. The proximity of the vitreous to the retinal environment results in its composition reflecting local physiological processes. This has led to its use in diagnostics, and has aided in the mechanistic understanding of several retinal diseases[19]. This property of the vitreous is of critical importance to this thesis and has been exploited in subsequent chapters. The aqueous humour is a clear watery substance that fills the eye's anterior chamber, produced at a high rate by the ciliary processes[17]. A specialised meshwork of cells, known as the limbus, functions together with the ciliary processes to facilitate the drainage of spent aqueous humour. Light enters the eye through the cornea, passes through the aqueous humour and is projected onto the retina by the focusing mechanisms of the pupil and the lens. Specialised muscular components within the ciliary body and iris help to achieve this function by adjusting the refractive power of the lens and the diameter of the eyes aperture, the pupil, respectively[17]. The retina itself is surrounded by the uveal tract, which collectively comprises the choroid. This is a rich capillary bed that provides nourishment to the neural retina, underlying Retinal Pigment Epithelium (RPE), the ciliary body and the pupil[20]. The sclera, a white fibrous tissue, constitutes the outermost surface of the eye. This functions to protect the eye from injury and facilitates the attachment of extraocular muscles involved in eye movement. The sclera is continuous with the cornea, which together form a fibrous tunic to help to maintain the eye's structural integrity[17].

1.2.2 The retina

1.2.2.1 Retinal morphology and circuitry

The retina comprises five neuronal layers, the photoreceptors, horizontal cells, bipolar cells, amacrine cells and Retinal Ganglion Cells (RGCs)[21]. In addition, the RPE constitutes the outermost layer of the retina and is of vital importance for correct retinal function[22]. An acellular layer below the RPE called Bruch's membrane separates the RPE from the choroid. This is not integral to the retina but is a critical element in the maintenance of visual function[17]. The basic circuitry of the retina and the arrangement of its constituent layers are shown in Figure 2.

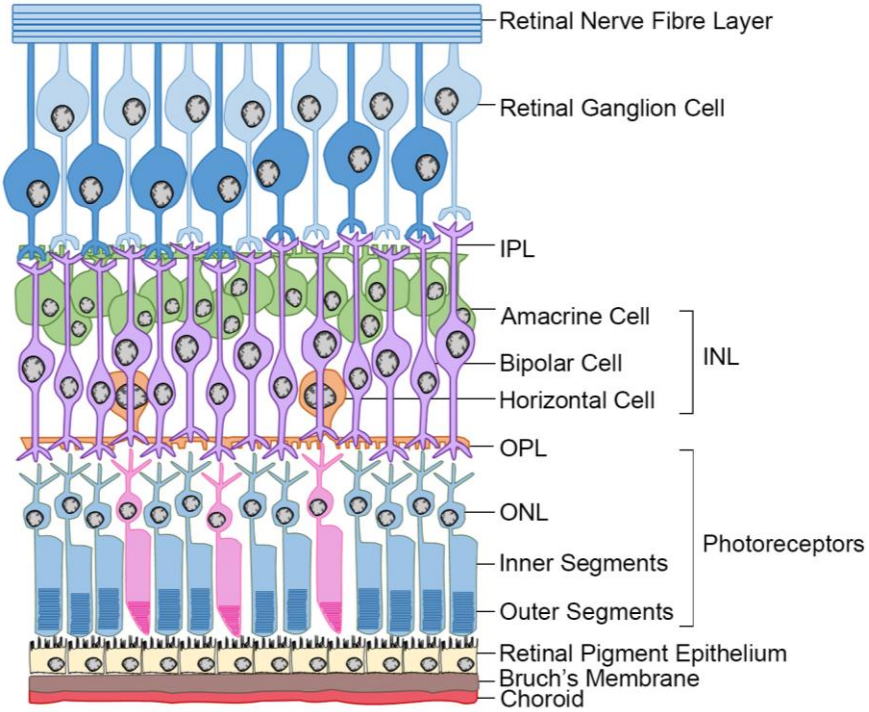

Figure 2: Structural organisation of the mammalian retina.

Diagram illustrating the basic neural circuitry within the mammalian neuroretina. Retinal cell bodies exist within the Inner Nuclear Layer (INL) and Outer Nuclear Layer (ONL), whereas their neuronal processes occupy the Outer Plexiform Layer (OPL) and Inner Plexiform Layer (IPL). The exception to this rule is the Retinal Ganglion Cells (RGC), where nuclei exist within the RGC layer and axonal processes extend from the nerve fibre layer through the optic nerve to the visual regions of the brain. The most direct route of visual transmission occurs via the three-neuron chain comprising photoreceptors, bipolar cells and RGCs[17].

The photoreceptors are the only photosensitive neuronal type in the retina and perform the first stage of visual processing, the conversion of light into graded electrical activity (see Section 1.2.2.2)[17]. Two disparate categories of photoreceptor exist, rods and cones. These are categorised by the photopigment molecule expressed within POS discs, as well as the shape and distribution of synaptic connections. Rods constitute the majority of photoreceptors (95%) in the human

retina, contain the photopigment rhodopsin, and are required for scotopic (low light) vision[23]. On the other hand, cones are specialised for photopic (normal/high light) visual processing, visual acuity and colour vision. The latter is achieved through expression of the photopigment opsin, which exhibits sensitivity to a particular wavelength of light depending upon its structural conformation[17]. Visual information passes from the photoreceptors inner segment to the bipolar cells and subsequently the RGCs, which extend their axonal processes through the optic nerve to the visual centres of the brain. For an in depth description of this process refer to Ratnayaka and Lynn (2016)[24]. This synaptic arrangement is known as the three-neuron chain and is the main route by which visual information is propagated[17 21]. The horizontal and amacrine cells are less abundant and form part of an indirect path to mediate lateral information transmitted from photoreceptors. It is hypothesised that this arrangement of horizontal cells confers sensitivity to luminance[17]. Amacrine cells display considerable heterogeneity in function highlighting the complexity of the retinal circuitry[25]. The arrangement of neuronal cell bodies within the Ganglion Cell Layer (GCL), Inner Nuclear Layer (INL) and Outer Nuclear Layer (ONL), as well as axons within the Inner Plexiform Layer (IPL) and Outer Plexiform Layer (OPL) result in the typical layered structural appearance of the retina[26].

1.2.2.2 Visual phototransduction

Once focused onto the retina, incident light passes through the entire structural thickness (0.5mm) before undergoing visual phototransduction within the POS discs[21]. This is the process by which light stimuli are converted into neuronal impulses, to be relayed along the three-neuron chain to the visual cortex. Despite differing morphologies, both rods and cones exhibit similar phototransductory chemical process[17]. The mechanistic specifics of phototransduction are beyond the scope of this thesis, but are summarised briefly in Figure 3. For an extensive explanation see Purves *et al.* (2008)[17].

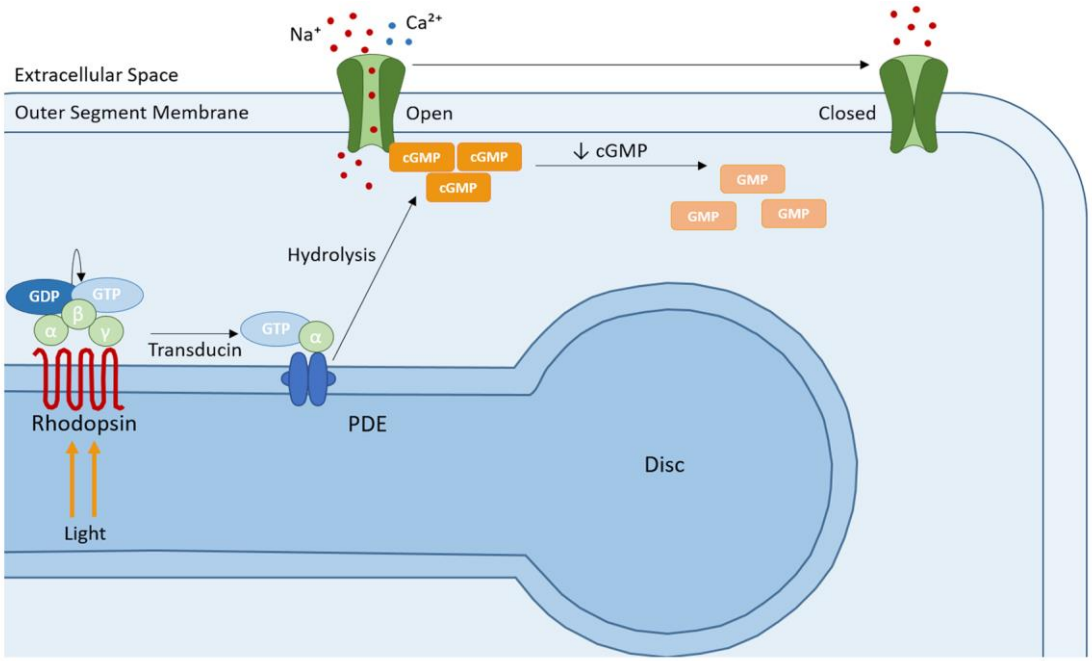

Figure 3: Basic principles of visual phototransduction.

A conformational change from 11-*cis*-retinal to all-*trans*-retinal occurs within the photopigment rhodopsin upon absorption of a photon of light. This induces activation of the intracellular messenger transducin, and consequently phosphodiesterase (PDE) mediated cyclic Guanosine Monophosphate (cGMP) hydrolysis. Hydrolysis of cGMP causes closure of Na^+ channels within the OS membrane and initiates a graded change in membrane potential (hyperpolarisation) along with altered neurotransmitter release from the axonal terminal of rod photoreceptors onto postsynaptic neurons. This in turn affects the activity of complementary bipolar cells that synapse with rods and cones, and subsequently the Retinal Ganglion Cells (RGCs). The axons of RGCs converge at the centre of the retina where they exit the eye through the optic disc, and synapse with several diencephalic and midbrain structures. Axonal termini include the lateral geniculate nucleus, the superior colliculi and the suprachiasmatic nucleus. Image adapted from Purves *et al.* (2008)[17].

The light-induced electrochemical changes characteristic of phototransduction and signal processing through the three-neuron chain form the basic principles of the Electroretinogram (ERG). ERG recordings are frequently used in both the clinic and laboratory to evaluate retinal function[27]. Typically, two measurements are obtained, termed the A-wave and the B-wave. The negative A-wave results from the closure of Na^+ channels following cyclic guanosine monophosphate (cGMP) hydrolysis, causing a reduction in dark current and hyperpolarisation[28]. Thus, light-induced functional activity and functional integrity of the photoreceptors is reflected in the A-wave amplitude. The positive B-wave reflects the summed function of distal retinal cells, mainly ON-centre bipolar cells, but also OFF-centre bipolar cells, amacrine cells and ganglion cells. However, the exact cellular origins and mechanisms of this wave remain to be fully elucidated[28]. In addition to the amplitude, the temporal properties of the A-wave and B-wave are used to interpret proper retinal function. These are measured as the time taken from the onset of the stimulus to the peak of each respective wave and are referred to as the implicit time. An additional component of the ERG termed the C-wave exists, which

originates from the RPE following light induced alterations to the extracellular K^+ concentration and thus its transepithelial potential difference. Due to the integral role of the photoreceptors in altering the extracellular K^+ concentration, the C-wave has also been said to reflect the photoreceptor/RPE relationship[28]. However, this has not exploited within this thesis. The key components of human ERG following dark adaptation are shown in Figure 4.

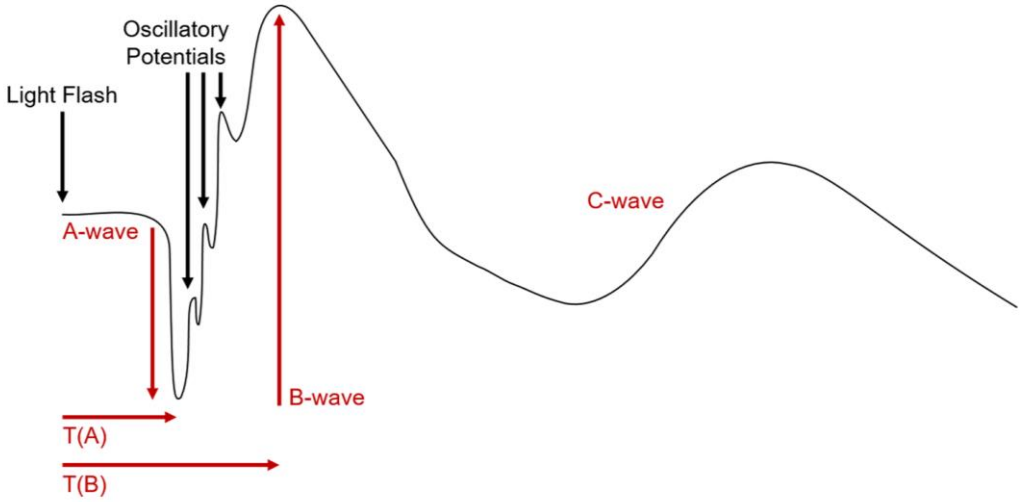

Figure 4: The main wave components of scotopic human Electroretinograms (ERGs).

Schematic to show the typical components of normal scotopic human ERGs. The time elapsed from flash onset to the negative peak of the A-wave is referred to as the A-wave implicit time (T(A)), and the time taken from the light flash to the positive B-wave peak is termed the B-wave implicit time (T(B)). These in addition to the A-wave and B-wave amplitudes are used to gain insights into the function of the photoreceptors and inner retinal cells respectively. An additional component termed the C-wave reflects the function of the Retinal Pigment Epithelium. Oscillatory potentials are also evident in scotopic human ERGs on the rising phase of the B-wave, which are thought to reflect the function of amacrine and inner retinal cells[27].

1.2.2.3 The macula

The majority of light from the central visual field is refracted on to the macula lutea. This is an area at the centre of the retina that is responsible for visual acuity and depth perception[20]. When observed clinically this region appears as a small, yellow area of approximately 5.5mm diameter to the nasal side of the optic disc[17].

The high visual acuity associated with the macula is the result of the spatial distribution of both rod and cone receptors within the retina[20]. In contrast to the peripheral retina, the macula comprises a high cone density, which increases 200-fold towards the midpoint of the macula termed the fovea centralis. The diameter of cones is also significantly reduced within this region to achieve a high density. In fact, the central 300μm of the fovea, the foveolar, is completely rod free[17]. The specialised morphology and function of cone photoreceptors here, in addition to

an equal ratio of constituent cells in the three-neuron chain, confers high visual acuity and detailed image perception. Displacement of the inner retinal layers within the fovea also ensures minimal obstruction to incident light in creating a clear foveal image[17]. Hence, upon examination via optical coherence tomography (OCT), the fovea appears as a depression in the retinal image of approximately 1.5mm in diameter. A direct path of light is further maintained by the absence of inner retinal blood vessels within this region[17]. Macula photoreceptors are therefore highly reliant on the underlying RPE for metabolic support. This essential relationship is highlighted by the relative density of RPE within the macula compared to the peripheral retina which must support approximately 45 and 30 photoreceptors per cell respectively[29]. The numerous functions and adaptations of the RPE that support global retinal homeostasis are discussed in the following section.

1.2.3 The Retinal Pigment Epithelium

The RPE is a monolayer of cuboidal, pigmented epithelial cells that forms a dynamic barrier between the light sensitive photoreceptors and vessels of the choriocapillaris. Here, it exerts highly specialised and unique functions that are essential to the homeostatic maintenance of the neural retina. This includes the phagocytosis of shed POS, secretion of growth factors and cytokines, transepithelial transport, visual pigment regeneration and the absorption of scattered light[30]. Additionally, the RPE forms an integral component of the blood-retinal barrier (BRB)[31]. The main roles of the RPE are summarised in Figure 5. RPE specialisation and morphology are therefore of critical importance for proper function. This is exemplified by structural variations in the appearance of RPE cells, which alter with ocular location and localised retinal requirement. For instance, peripheral RPE are shallow and elongated, in some cases spanning 60μm, whereas RPE within the macula are compact and measure approximately 14μm by 12μm[32]. Such localised morphological adaptations highlight the fundamental role of this monolayer in retinal function. This section summarises several important RPE properties and functions related to this thesis.

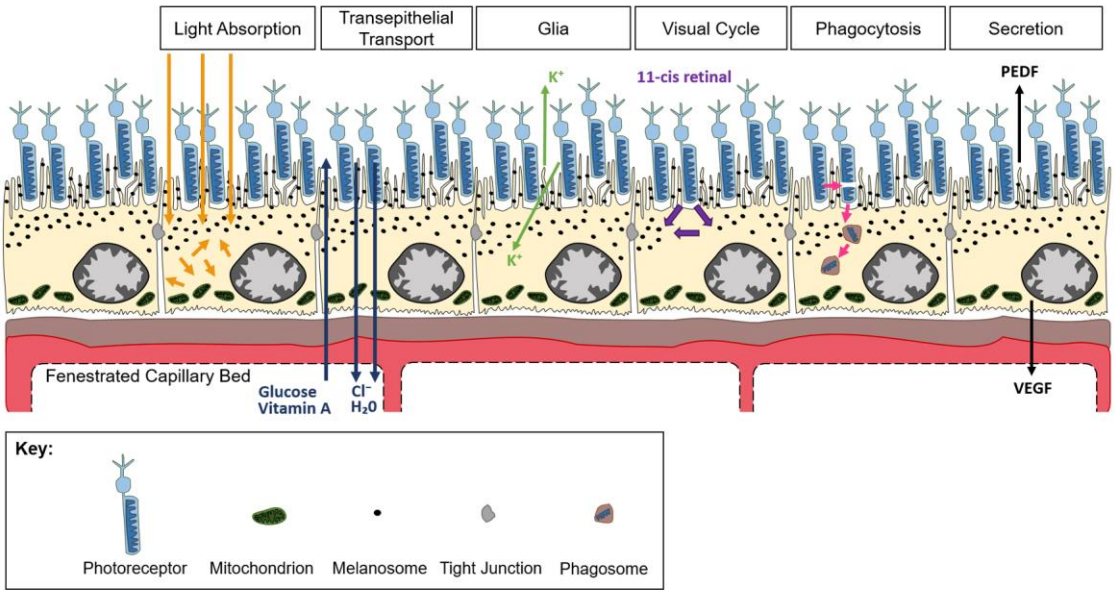

Figure 5: Major functions of the Retinal Pigment Epithelium.

The Retinal Pigment Epithelium (RPE) exhibits numerous physical, metabolic and transport functions that aid in the maintenance of retinal homeostasis and normal visual function. These include the absorption of scattered light, formation of a blood-retinal barrier, transepithelial transport to and from the choroid, the secretion of various cytokines/growth factors as well as playing an integral role in phototransduction via the recycling of 11-cis retinal. Of vital importance is the phagocytosis of shed photoreceptor outer segments by the RPE, which is essential for the maintenance and survival of this photosensitive cell layer. Abbreviations: PEDF, Pigment Epithelial Derived Factor; VEGF, Vascular Endothelial Growth Factor. Image adapted from Strauss (2005)[30].

1.2.3.1 Polarity

The apical-basolateral polarity axis of the RPE is required for several of its inherent functions. However, contrary to most epithelium, the RPE apical surface borders tissue as opposed to lumen. Here, long processes termed microvilli protrude from the apical membrane into the subretinal space. Two types of microvilli exist. Thin microvilli of approximately 5-7μm function to increase the surface area for transepithelial transport, whereas photoreceptor sheaths interdigitate with rod and cone photoreceptors enabling phagocytic activity and retinal attachment[22 30]. This interaction establishes itself during embryonic development where functional differentiation of the retina and RPE are inter-reliant[30]. Accordingly, destruction of this interaction is associated with pathogenesis[33], for example, the photoreceptor loss observed secondary to RPE atrophy in the majority of AMD cases.

Numerous invaginations also exist on the basolateral surface of the RPE to increase the surface area for metabolite and nutrient exchange between the retina and systemic circulation[30]. These basal infolds constitute the first layer of Bruch's membrane, a pentalaminar interaction matrix that essentially functions as a 'biological sieve'. The choroicapillaris endothelium basement membrane forms the

fifth layer of Bruch's membrane with the intermediate layers comprising the inner collagenous zone, elastin later and outer collagenous zone[34]. Several pumps, receptors, channels and transporters also show polarised distribution within both the RPE apical and basal membranes to achieve specific functions. For example, asymmetric positioning of Na^+/K^+ ATPase in conjunction with apical inward rectifier K^+ channels (Kir7.1) and apical/basal Cl^- channels drive transepithelial transport, and maintain an optimal intraocular pressure[30]. Additionally, the phagocytic function of the RPE necessitates the apical distribution of the receptors α5β5 integrin and tyrosine kinase c-mer (MerTK)[22 30]. An example of such specialisation can be observed in Figure 6.

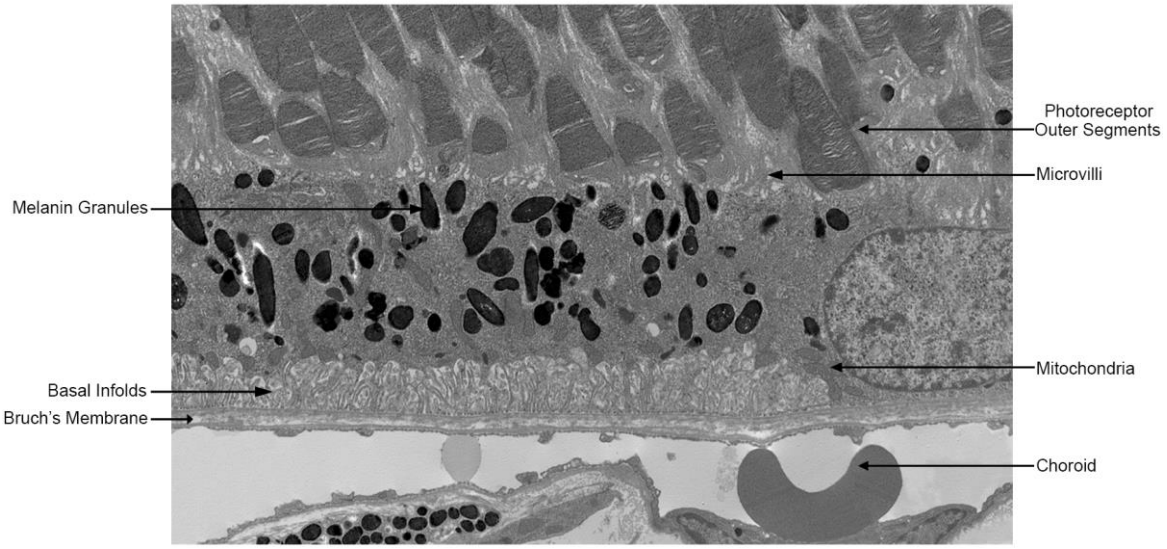

Figure 6: The polarised morphology of the Retinal Pigment Epithelium.

A transmission electron micrograph of the mouse retinal pigment epithelium (RPE) seen in the z-axis to demonstrate the polarised nature of this monolayer. Long, thin microvilli of cells can be seen to extend from the apical surface and form close associations with the distal part of photoreceptor outer segments. Melanin pigments typically localise towards the apical portion of RPE cells where they are responsible for the absorption of scattered light and protection against reactive oxygen species. The basal membrane of the RPE boasts numerous invaginations that increase the surface area for ion and metabolite exchange between the retina and choroidal vasculature. Abundant mitochondria can be seen adjacent to the basal membrane and are required for the high metabolic activity of the RPE. Image sourced from Cuenca N. (2008) Pigment Epithelium. Department of Physiology, Genetics and Microbiology, Faculty of Science, University of Alicante, Spain. Accessed from: http://www.retinalmicroscopy.com/pigment.html on 22nd October 2018.

The intracellular distribution of organelles is an additional example of RPE polarisation. Abundant mitochondria predominantly localise towards the RPE basal surface along the same axial plane as the nucleus[30]. Conversely, cigar shaped melanosomes (2-3μm) localise towards the RPE apical surface in the presence of light, where they are involved in the extensive absorption of photoxidative energy and protection against Reactive Oxygen Species (ROS)[33]. Typically, RPE reach their full complement of melanosomes close to the 14th week of gestation[35]. Two

additional types of RPE pigment granule exist, referred to as lipofuscin and melanolipofuscin, which are unpolarised in distribution. These pigment molecules are also more commonly associated with age, accumulating throughout life and have been associated with RPE impairment[29 35]. This is discussed further in Section 1.4.2.3.

1.2.3.2 Blood-retinal barrier function

The retina, akin to the brain, is separated from the systemic circulation via a blood-neural interface. This is essential in creating the specialised environment required for efficient retinal function. In addition to the immune modulatory function of the RPE, two blood-retinal barrier components exist which confer this property. The first is formed by the retinal vasculature endothelial cells in the inner retina. The second, by the RPE in collaboration with Bruch's membrane[36].

The lateral surfaces of RPE are joined by a circumferential belt of apical tight junctions, which function collectively to form a seal, isolating the retina from the systemic circulation[30 36]. Such tight junctions retard diffusion meaning that substances must be actively transported via the transcellular pathway. The active transport of substances across the RPE monolayer is essential for maintaining a concentration gradient, as well as regulating movement across the BRB[22 37 38]. This is achieved through the selective distribution of pumps, receptors, channels and transporters within the RPE (Section 1.2.3.1).

The permeability, selectivity and degree of tightness of this seal to the diffusion of solutes is determined by the composition of occludins, claudins and zonula occludens (ZO) that constitute RPE tight junctions[36 37]. ZO are early tight-junction proteins that form a scaffold by interacting with both the actin cytoskeleton, as well as occludin and claudin proteins[39]. Claudins are particularly important with regards to permeability and selectivity, which differ depending upon the claudin protein expressed out of a family of 24[36 40]. Claudin-19, claudin-3 and claudin-10 have all been reported in the tight-junction complex of human RPE[40]. Claudin-19 is the most abundantly expressed in RPE from human origin[40] and appears to be particularly important, as illustrated where mutations within its encoding gene (*CLDN19*) have been associated with severe visual impairment[41]. Expression of the 60kDa membrane protein occludin, allows further regulation of tight-junction permeability, and is often indicative of enhanced barrier function in *in vitro* RPE cultures where claudin expression is absent[42]. Adherens and gap junctions also exist between adjacent cells, which control the passage of solutes and allow the

metabolic coupling of the RPE respectively[33]. Among other changes to the RPE, attenuation/impairment of BRB function has been implicated in retinal diseases such as AMD.

1.2.3.3 Secretory activity

Communication of the RPE with neighbouring tissues is achieved through the secretion of various growth factors and signalling molecules, which modulate and maintain the structural integrity of both the choroidal vasculature and neural retina[22 30]. The secretion profile of the RPE has been shown to encompass a variety of important molecules implicated in retinal pathology, such as Pigment Epithelium Derived Growth Factor (PEDF) and Vascular Endothelial Growth Factor (VEGF)[22 43]. PEDF is secreted from the RPE apical surface where it provides neurotrophic support to the retina and helps maintain an antiangiogenic retinal environment[22]. Conversely, VEGF is preferentially secreted in low concentrations from the basal RPE membrane, and is essential in maintaining a healthy vasculature[30]. Secretion of these two opposing proteins is tightly regulated within the RPE, where perturbations in the relative amounts of VEGF and PEDF lead to proliferative phenotypes including Choroidal Neovascularisation (CNV)[44]. This is discussed further in Section 1.3.4.2.2. The RPE also secretes a cocktail of other factors including TNF-α, Interleukin-8 (IL-8), Complement Factor H (CFH), Ciliary Neurotrophic Factor , Platelet Derived Growth Factor and Tissue Inhibitor of Matrix Metalloprotease that are critical in the maintenance of retinal homeostasis in addition to immune and extracellular matrix modulation, but which are not directly studied here[22].

1.2.3.4 Phagocytic activity

The degree of light focused on to the back of the eye creates a highly oxidative retinal environment[33]. This is exacerbated by choroidal oxygen concentration, which exhibits approximately 90% saturation[45]. The RPE is equipped to compensate for high levels of photo-oxidative damage through the expression of pigment granules[35] (Section 1.2.3.1). However, constant photo-oxidative damage to the overlying photoreceptors destroys their function, and thus renewal of rod and cone OS is crucial for vision[46]. Normal photoreceptor renewal occurs from the base of POS upon shedding 7-10% of their volume, where the completion of POS renewal has been predicted to occur within 10 days[33]. The RPE possesses a high phagocytic capacity to accommodate this constant proteolytic burden, with each cell being responsible for the diurnal removal of up to 30-50 POS tips daily[29 47]. Shedding,

phagocytosis and renewal is controlled by circadian rhythm and light onset, and is facilitated by cellular machinery present within the RPE[48]. Three receptors are integral for the regulated internalisation and destruction of POS; the receptor tyrosine kinase c-mer (MerTK), αvβ5 integrin and the macrophage phagocytosis receptor CD36[30]. Various studies involving knock-out models have provided insight into the specific functions of each. It is now widely accepted that MerTK is involved in the activation of phagocytosis[49 50], CD36 is essential for POS internalisation[30] and αvβ5 integrin is required for the binding of POS to the RPE and the circadian regulation of phagocytosis[51]. In brief, the current accepted theory of internalisation involves exposure of phosphatidylserines, binding of POS to αvβ5 integrin, initiation of the focal adhesion kinase (FAK) signalling cascade, phosphorylation and activation of MerTK followed by internalisation and processing of shed POS[30 48]. More recently, MerTK has also been shown to undergo a negative feedback loop in which MerTK is cleaved into soluble MerTK in an attempt to downregulate the phagocytic ability of RPE cells[52]. Similarly, Gas6 and Protein S ligands are involved in the modulation of phagocytosis, which have opposing roles to decrease or increase POS phagocytosis. Hence, Gas6 expression is decreased at light onset and has been shown to increase thereafter[53]. Activation of αvβ5 integrin and MerTK by Milk Fat Globule-EGF8 (MFG-8) and tubby-like proteins respectively, are also thought to be key for photoreceptor phagocytosis rhythmicity[54]. Once internalised, POS are trafficked to the basal region of the RPE in phagosomes for processing in the endo-lysosomal pathway. Sustained POS phagocytosis exerts a high proteolytic burden on the RPE monolayer, particularly given its post mitotic status. In fact, the RPE has among the highest proteolytic burdens in the human body with a single macula RPE engulfing in excess of one billion OS discs over an individual's lifetime[55]. The RPE has therefore evolved to comprise several efficient clearance mechanisms to accommodate the high volume of phagocytic material, in addition to internal clearance of damaged organelles and misfolded proteins. These are discussed in turn in Section 1.2.3.5.

1.2.3.5 RPE clearance pathways

Several clearance mechanisms exist within the RPE, which collectively function to maintain cellular protein homeostasis, or 'proteostasis', under functional or environmental stress[56]. Three of these processes are interrelated and culminate in the proteolytic degradation of components within lysosomes. These include endocytosis, phagocytosis and autophagy. The fourth was originally regarded as a distinct network and occurs via the Ubiquitin Proteasome (UP)[57]. Components are

directed to a specific clearance pathway depending upon their substrate specificity. In general, damaged, misfolded or aggregated proteins are targeted to the UP, whereas membrane-bound or organelle associated proteins are targeted to lysosomes via endocytic or autophagy pathways[56]. The major RPE clearance mechanisms that are essential for cell viability are summarised in Figure 7.

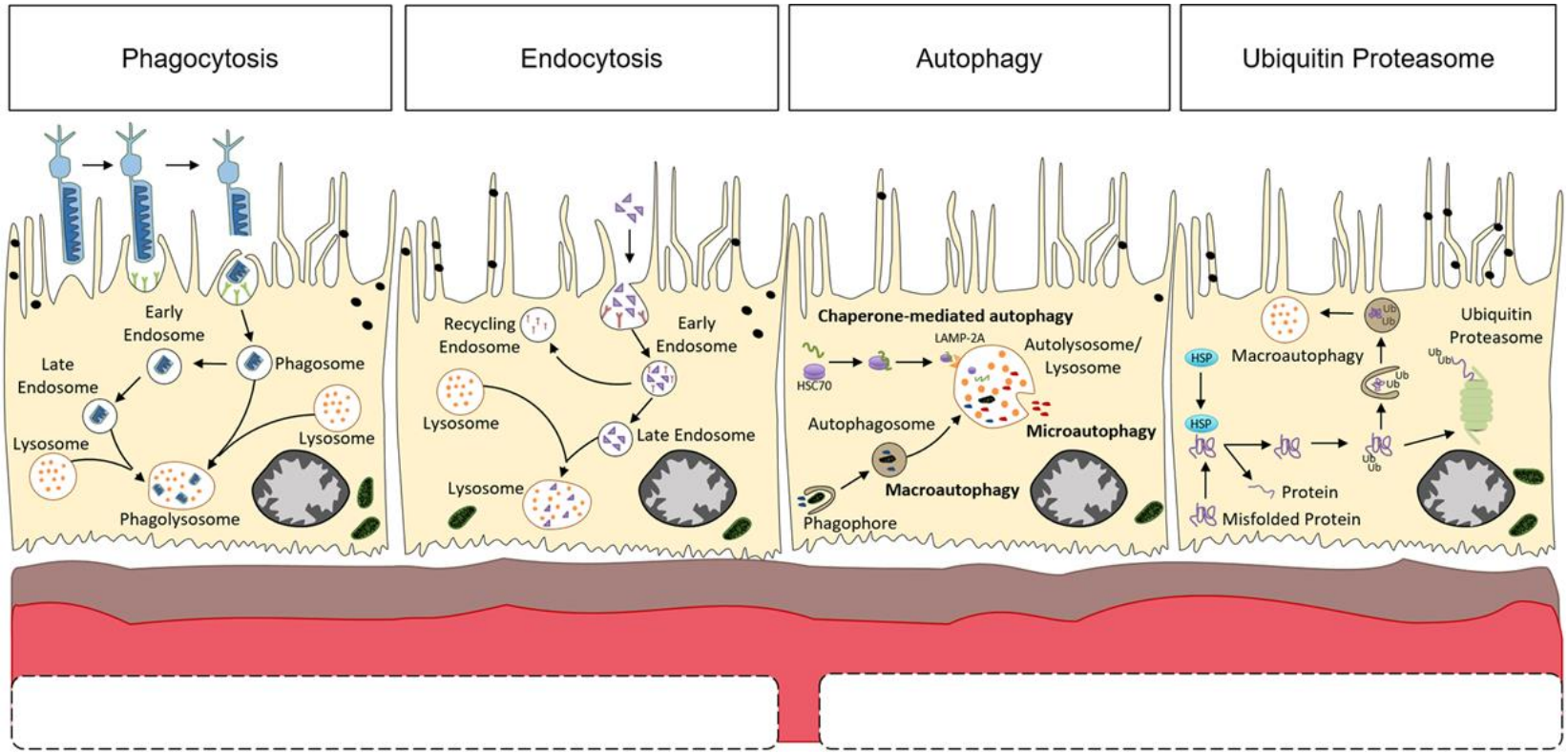

Figure 7: RPE clearance mechanisms and their inter-dependence on the lysosome.

Schematic summarising the major RPE clearance mechanisms and their reliance on the lysosome for efficient substrate degradation. Photoreceptor outer segments are internalised in phagosomes following receptor mediated recognition, and are trafficked to lysosomes via convergence with the endocytic pathway or by direct fusion to form a phagolysosome[12]. Similarly, extracellular cargo is internalised and trafficked to the lysosome through various endocytic intermediaries. The degradation of intracellular material generally occurs via autophagy or the Ubiquitin Proteasome (UP). Broadly, autophagy refers to the directing of cytosolic substrate to the lysosomal lumen via autophagosome fusion (macroautophagy), direct membrane invagination (microautophagy), or Lysosome-Associated Membrane Protein 2A (LAMP2A) and chaperone mediated translocation[56]. Misfolded proteins are targeted to the UP by polyubiquitination if Heat Shock Proteins (HSPs) fail to restore native protein conformation[56]. However, more recently it has been recognised that ubiquitinated proteins can also be trafficked to the lysosome via macroautophagy for degradation if the UP fails[56-58].

1.2.3.5.1 Phagocytosis/Endocytosis

Cargo originating from the RPE apical extracellular environment or plasma membrane is internalised and degraded through either the endosomal or phagocytic pathways[12]. Endocytosis refers to the engulfment of material via budding of the plasma membrane lipid bilayer, and may occur via several mechanisms[59]. In brief, material is trafficked along microtubules to the basal axis of the RPE through various endocytic intermediaries, which comprise a distinct internal milieu of membrane associated proteins and functionally active lytic enzymes[60]. This process initiates as early endosomes, where ingested material may be selectively retrieved for recycling to the plasma membrane[61 62]. Beyond this point vesicles progressively mature into late endosomes and lysosomes[63]. This is an extremely dynamic process mediated by specific Rab and effector proteins and has been reviewed extensively[12 62]**.** Nonetheless, a major characteristic of vesicle maturation is the progressive acidification of the vesicle lumen. Early endosomes are typically pH 5.9-6.8[12], whereas the lysosomal lumen exhibits a pH of 3.8-5.0[64]. Phagocytosis represents an additional method of cargo internalisation that is initially distinct from endocytosis, and which is integral to the processing of POS following their recognition by specific RPE surface receptors (Section 1.2.3.4). Indeed, this is of particular importance to the RPE, which has been coined a 'non-professional phagocyte'[65]. Here, cargo recognition and Rac1 activation induces remodelling of the actin cytoskeleton and protrusion of the membrane in the direction of POS[66], which appears to be a prerequisite for their internalisation[67]. Membrane protrusions then surround and encompass the target cargo creating a *de novo* vesicle, termed an early phagosome[68]. These may either fuse directly with a lysosome, or mature into late phagosomes via fusion and fission with various components of the endocytic pathway. In both instances, the final stage of phagocytosis is the formation of a phagolysosome upon fusion with a lysosome. This is where POS degradation occurs[12 68]. Not surprisingly, the RPE comprises an extremely active lysosomal system to accommodate this load, which constitutes a significant proportion of the cells cytoplasmic volume[29].

In both pathways, the multimeric membrane proton pump vacuolar-type H^+ ATPase (vATPase) plays an essential role in vesicle maturation. This selectively pumps H^+ generated through ATP hydrolysis into the vesicle lumen to maintain varying degrees of intraluminal acidity[12]. The regulation and maintenance of acidic pH within lysosomes is of critical importance for acid hydrolase function. These exhibit optimal function over a narrow pH range, whereby fluctuations of circa 0.5 can

diminish enzymatic activity by half[69 70]. Consequently, hydrolytic enzymes are only active in late endosomes and lysosomes, where activation is regulated further by compartment specific posttranslational modifications. For example, the major RPE cysteine proteases Cathepsin B and Cathepsin D undergo successive cleavage from the pro to the active form of the protein[71]. Once within the lysosomal lumen, internalised components are subject to over 60 lysosomal acid hydrolases[72], including proteases, nucleases, glycosidases, lipases, phospholipases and phosphatases[73], which are essential for efficient cargo degradation. The majority of RPE lysosomal acid hydrolases involved in the proteolysis of POS are members of the cathepsin family of cysteine proteases[35 74]. Specifically, Cathepsin B and D are thought to play a pivotal role in RPE function, and have been shown to exhibit increased expression within the RPE and under conditions of oxidative stress[75].

1.2.3.5.2 Autophagy

The process of autophagy, first coined by de Duve in 1963[76], largely refers to the process by which misfolded/aggregated protein and damaged organelle 'turnover' occurs in cells[77]. However, it may also be initiated as a homeostatic response under conditions of cell stress including nutrient restriction, oxidative stress and inflammation[77]. This housekeeping function is particularly important in postmitotic tissues such as the RPE, which incur sustained damage. Three types of autophagy exist including macro-autophagy, micro-autophagy and chaperone mediated autophagy[78]. Macroautophagy refers to the compartmentalisation of substrate within a double membrane bound phagosome, which then fuses with a late endosome or lysosome following complex maturation, to create an autolysosome where material is degraded and components are recycled[56]. In microautophagy, the lysosome directly engulfs cytoplasmic content via membrane invagination[56 78]. Alternatively, chaperone mediated autophagy involves the coordinated function of the Lysosomal Associated Membrane Protein 2A (LAMP-2A) and molecular chaperones termed Heat Shock Proteins (HSP), usually following recognition of a specific motif, which bind and transport the target substrate into the lysosomal lumen for degradation[78 79]. Similar to endocytosis and phagocytosis, autophagy terminates in the degradation of substrate within the lysosome[78], and is therefore reliant on normal RPE lysosomal function.

1.2.3.5.3 RPE Ubiquitin Proteasome

Chronic light exposure and oxidative stress within the RPE induces protein misfolding. This is further exacerbated by sustained POS phagocytosis in addition to the high oxygen consumption of the RPE[56]. Hence, healthy RPE comprise

intracellular protein quality control mechanisms to repair or remove misfolded proteins from the cytoplasm. HSPs constitute the first line of defence, which mediate the restoration of correct protein conformation and prevent the intracellular accumulation of toxic/misfolded proteins[56].However, failure of HSP mediated repair results in the targeting of molecules to the UP following conjugation to a polyubiquitin chain[10 56]. This is achieved via a three-step cascade mechanism involving three classes of enzymes, E1, E2 and E3, which function sequentially to attach this 'degradation signal'[10]. Polyubiquitin signals are recognised by the 26S UP complex where proteolysis occurs. The UP is a multicatalytic complex composed of a catalytic 20S core and a 19S regulatory domain[80], and represents the major-non lysosomal proteolytic pathway in the RPE. Approximately 80-90% of intracellular proteins are processed through this pathway[56], highlighting its requirement for normal cellular protein homeostasis and in coping with intracellular stresses. The UP was initially regarded as a distinct clearance mechanism with no point of intersection with autophagic and endocytic/phagocytic degradation[57]. However, coordination of the UP with lysosome dependent clearance mechanisms is now known to occur[57]. For example under cellular stress, where the UP is affected, p62 targets ubiquitinated proteins for autophagy and appears to be pivotal in enhancing cell viability when the UP is compromised[81 82]. This highlights the dynamic nature of RPE clearance mechanisms as well as the central role of the lysosome in cellular proteostasis and maintenance. In fact, increasing evidence suggests that these clearance pathways may represent divergence of a single proteolysis network.

1.2.3.6 RPE clearance and implications in human disease

Advancing age is thought to correlate with a reduction in the RPE's ability to effectively clear intracellular proteins[29 56]. However, an increasing body of evidence has also implicated impaired RPE 'proteostasis' with retinal diseases including Stargardt's disease, Best's vitelliform dystrophy, choroideremia and AMD[12 83]. The most prevalent of these is AMD, which constitutes a major public health problem. Here, defective degradative processing, as well as removal of waste by the RPE, are thought to result in the accumulation of material both inside and adjacent to this important monolayer. The notion that this constitutes an initiating factor for downstream AMD pathologies is gaining increased credibility[56 84]. The following section summarises the importance of research into this common blinding disease, in addition to AMD classifications and basic clinical hallmarks referred to in subsequent sections.

1.3 Age-related Macular Degeneration (AMD)

1.3.1 Epidemiology

AMD is the commonest cause of irreversible vision loss in the western world[5 85] accounting for 8.7% of global blindness[86], and 50% of registered blindness in developed countries. In fact, it is currently estimated that AMD affects 170 million individuals globally[87]. AMD prevalence increases exponentially with age posing a significant risk to individuals over the age of 55, with approximately one in three exhibiting some form of AMD by their 7th decade[85]. The incidence of advanced AMD also increases from less than 1% in those under 65 to over 25% in those over 90 years of age[85]. This puts a significant strain on health care expenditure with global costs being estimated at US $254.8 billion in 2010 alone[88], a figure that will inevitably rise as we confront an ageing demographic profile. A recent epidemiological study predicted that AMD costs the UK economy £1.6 billion annually[89]. However, with prevalence statistics suggesting a three-fold increase within the next 20 years[85], reaching 288 million by 2040[90], expenditure is expected to reach new heights. In the UK, AMD outpatient appointments have risen by 1/3 over a 4 year period, with approximately 200 new AMD cases presenting daily and 70,000 annually[91]. However, despite the inevitable AMD epidemic, research into this blinding disease remains underfunded. In 2014, only 0.6% of charity funding associated with sight loss was allocated to AMD research along with only 0.2% of medical government research funding[91]. AMD clearly constitutes a major public health problem with an urgent need to devise effective therapies, and tools for early clinical diagnosis.

1.3.2 Disease classification

Since AMD was first described by Nettleship in 1884[92], several classification schemes have been devised in an attempt to develop a common framework between studies including normalising phenotype, terminology and grading. Grading schemes employed in larger population based studies include the Wisconsin Age-related Maculopathy, Chesapeake Bay Watermen, and the Age-related Eye Disease Study (AREDS) grading systems[93]. The most widely utilised approach among clinicians is AREDS which combines both the simplicity of the Chesapeake Bay Watermen grading system with the reliability of the Wisconsin Age-related Maculopathy grading system[93]. The AREDS classification system categorises patients into one of 4 stages ranging from mild AMD, to neovascular AMD or central

geographic atrophy (GA) upon examination of colour fundus images with grid templates[92 93]. This approach has been adopted to determine AMD status in the work presented in this thesis. A more recent AREDS report has introduced an improved nine step severity scale[94], although this is yet to be implemented in the majority of AMD clinics.

1.3.3 Risk factors

The multifactorial nature of AMD suggests a complex combination of factors that confer disease susceptibility and which influence disease progression. To date, multiple risk factors have been attributed to the likelihood of developing AMD. These can be broadly categorised under demographic factors, environmental influence and genetic susceptibility, which are discussed in brief below.

1.3.3.1 Demographic risk factors

Advanced age is the largest risk factor for disease with 25% of the population showing some sign of early AMD by the age of 80[95]. However, several additional demographic factors have been associated with a higher disease prevalence. Studies investigating gender influence on disease have revealed that exudative AMD is more common in women[20 96]. Possible explanations for this include increased average female life expectancy as well as altered oestrogen levels and/or ratios[97], although this remains to be confirmed. Ethnicity also appears to play a role in the development of disease with AMD exhibiting a higher prevalence in Caucasian populations as opposed to individuals of African, Asian and Hispanic origin[98-100]. Geographical location is thought to further influence disease phenotype with Icelandic and Norwegian populations demonstrating a higher GA: CNV ratio than Europeans, Australians and Americans[101]. The reason for this geographic influence remains unclear, but may involve varied seasonal daylight hours in the far northern hemisphere.

1.3.3.2 Environmental risk factors

The risk of developing AMD has also been linked to several environmental and lifestyle factors. A causal relationship between cigarette smoking and AMD exists[102], with an observed three-fold increase in AMD diagnosis in smokers[103 104]. In fact, smoking ≥20 cigarettes per day has been shown to double the prevalence of early AMD[105]. Quitting smoking appears to reduce this risk, with 20 years being the bench mark for comparable risk rates to non-smokers[105]. Smoking has further been

associated with the coexistence of hypertension, which reduces choroidal blood flow and consequently alters retinal homeostasis. Hypertension is thought to be an important risk factor for wet AMD. However, it is not yet clear whether increased AMD prevalence occurs as a result of prescribed antihypertensive drugs, or clinical hypertension itself given the lack of non-prescription control cases in such studies, as well as inconsistencies in the literature regarding the association of hypertension with disease[106 107].

Finally, nutritional status is significantly related to the development and progression of AMD[108] with obesity, associated with poor dietary choices[109], and increased alcohol consumption[110] both associated with increased disease risk. Other dietary factors that can influence AMD development include a high fat[109], and β-carotene intake in the case of CNV[111]. However, evidence is confined to a small number of studies that exhibit a less consistent relationship than that characterised for smoking and AMD[112]. Nonetheless, this highlights several modifiable factors that may be promoted to reduce disease prevalence.

1.3.3.3 Genetic susceptibility

Over the past 13 years, our understanding of the genetic basis of AMD has advanced significantly. This has led to the use of family history as a useful clinical indicator of disease, where genetic background is associated with a higher disease risk. To date, mutations within genetic loci associated with complement pathway regulation, lipid metabolism, oxidative stress, angiogenesis and the remodelling of the extracellular matrix[5] have been associated with a predisposition to AMD. For example, sequence variations in Complement factor H (CFH)[113 114], Complement Factor I (CFI)[115] Complement Factor 2 (C2), Complement Factor 3 (C3) and Complement Factor B (CFB)[116] have all been shown to modulate disease risk, highlighting the importance of the complement pathway in disease pathology. Meta-analysis of AMD genome wide association studies (GWAS) has also identified risk mutations within VEGFA[117], which increase CNV susceptibility. Finally, Single Nucleotide Polymorphisms (SNPs) within mitochondrial ARMS2, matrix metalloproteinase inhibitor, TIMP3, the heat shock serine protease, HTRA1 and Apolipoprotein E (ApoE) have also been associated with AMD risk. In contrast to genetic associations in AD, the ApoE2 SNP is risk conferring in AMD, whereas the ApoE4 SNP is protective. The reason for this remains unknown but could involve the interaction of these proteins with the Bruch's membrane[24 118].

1.3.3.4 Ocular associations

Ocular characteristics including blue iris colour, nuclear sclerosis, cataract surgery and hyperopia are also thought to increase AMD risk. However, further evidence is required before these can be firmly correlated with AMD[119 120].

1.3.4 Clinical features of disease

AMD is well characterised clinically, with two distinct phenotypes; early and advanced AMD. In both cases, the key anatomical structure affected is the macula. Hence, disease advancement correlates with a profound and debilitating loss in central vision. The types of visual changes that occur with disease progression are shown in Figure 8. Clinical symptoms and pathology exhibited by patients are used by clinicians to categorise patients into a distinct AMD stages. These are discussed in brief below.

Figure 8: Visual Impairment in Age-related Macular Degeneration.

Diagram illustrating the characteristic appearance of the visual field in individuals with **A.** Normal vision **B.** Early AMD and **C.** Advanced Wet AMD. The blurred region, termed a central scotoma, in the centre of the image represents visual field defects typical of CNV. In advanced dry AMD patients usually present with impaired contrast adaptation and perception and/or blurred vision. Subtle visual changes including distorted vision in early AMD make disease onset difficult to detect.

1.3.4.1 Early AMD

The first clinical indicator of disease, and major pathological hallmark of early AMD, is the appearance of lipid rich extracellular aggregates within the macula, between the RPE and the inner collagenous layer of Bruch's membrane (Figure 6)[121]. These deposits are termed drusen and comprise approximately 60 proteins that have been identified to date[122]. Several distinct morphological forms of drusen exist, which are categorised based on their size and structure. Hard drusen (>50μm) with

distinct borders within the peripheral retina are considered a normal part of ageing[93]. However, larger soft drusen (≥125μM) exhibiting a 'cotton-ball' like appearance within the macula region, as well as pigmentary abnormalities within the RPE, are a sign of increased disease susceptibility[119]. These often coalesce to become more confluent larger drusen[9 93] and are associated with a 6-fold higher likelihood of developing advanced AMD[123]. Reticular drusen, which appear as a lattice like network on the apical surface of the RPE have been described more recently, and are also associated with AMD progression[20]. Immunohistochemical analysis and mass-spectrometry of post-mortem eyes has identified the molecular composition of drusen, which are now known to comprise lipids, proteins, cellular debris and extracellular matrix components. These include, but are not limited to vitronectin, serum amyloid P component (SAP), clusterin, ApoE, Aβ, complement components and inflammatory mediators[122 124]. Interestingly, 24 druse associated proteins are common to the senile plaques of Alzheimer's brains, suggestive of a common pathogenic pathway in AD and AMD[9]. Additionally, hyperpigmentary changes to the RPE, and RPE hypertrophy are among the earliest detectable signs of AMD. The typical pathological changes to the retina associated with early AMD are summarised in Figure 9.

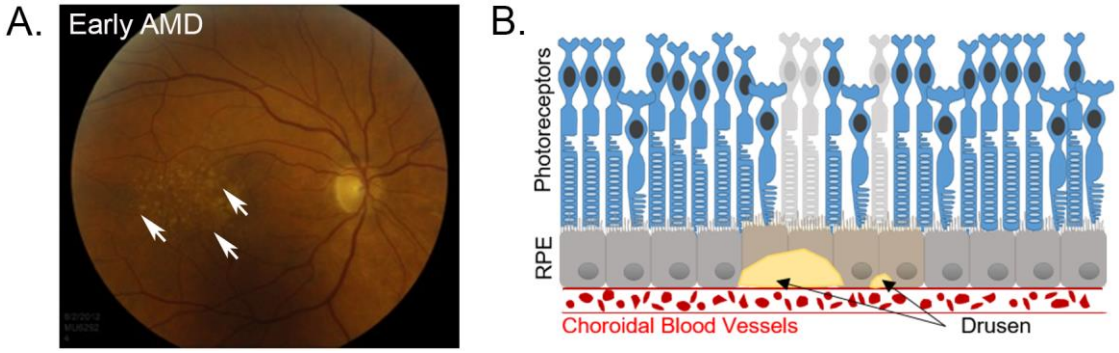

Figure 9: Clinical features of early Age-related Macular Degeneration.

Figure showing typical pathological changes associated with the early stages of Age-related Macular Degeneration (AMD). **A.** Fundus image from a patient afflicted with early AMD of the inner retinal surface. White arrows indicate confluent soft drusen within the macular region. **B.** Early AMD is characterised by the emergence of small focal drusen beneath the RPE associated with minor impairment of macula RPE and photoreceptors. Image sourced from Haugsdal et al. (2013)[125].

Early AMD is commonly described as asymptomatic and thus diagnosis in a clinical setting is challenging. Considerable damage to the RPE and Bruch's membrane within close proximity to drusen however suggests that this is not strictly true. Irreversible damage often occurs prior to the manifestation of clinical symptoms despite incipient pathology remaining undetected in most patients. In this respect, AMD exhibits further similarities with AD in which clinical diagnosis typically occurs years after disease onset.

1.3.4.2 Advanced AMD

Late AMD prevalence increases four-fold for every 10 years after the 6th decade of life[91]. This may be subcategorised into GA and CNV based upon disparate clinical features. Contrary to some reports, it is now thought that both advanced AMD forms exhibit a comparable prevalence[91].

1.3.4.2.1 Geographic Atrophy

GA or dry AMD is a non-exudative form of disease, which often develops gradually. Central to dry disease pathology is the progressive degeneration of the RPE and overlying photoreceptors, referred to as a GA lesion (Figure 10)[93]. This is often seen as hypopigmented regions upon fundus imaging[93]. Other clinical hallmarks of GA include RPE hypopigmentation, RPE hypertrophy and RPE hyperpigmentation, usually as a consequence of compensatory RPE cell proliferation in areas adjacent to RPE and photoreceptor atrophy[126].

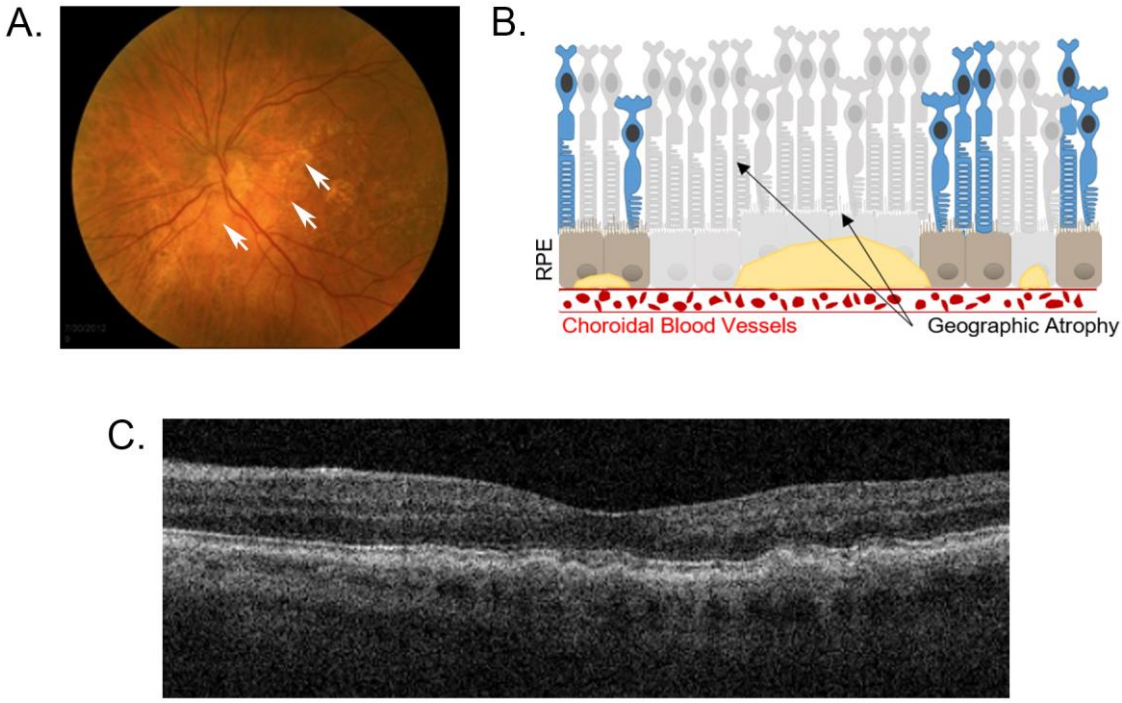

Figure 10: Clinical features of dry Age-related Macular Degeneration

Figure showing the pathological retinal changes associated with late stage, dry Age-related Macular Degeneration (AMD). **A.** Fundus image of the inner retinal surface acquired from a patient with dry AMD. White arrows indicate regions of geographic atrophy (GA) within the macula region. **B.** Dry AMD is characterised by the presence of larger, more confluent drusen associated with significant areas of photoreceptor and RPE atrophy. **C.** OCT image of a patient with dry AMD exhibiting multiple large drusen, RPE hypopigmentation and retinal thinning. OCT images are commonly used by clinicians in addition to fundus photographs when making an AMD diagnosis. Image A sourced from Haugsdal et al. (2013)[125].

Upon clinical examination, RPE atrophy appears as large, well demarcated areas that are pale in colour in which the underlying choroidal vessels may be more visible than surrounding regions[93] (Figure 10). A considerable increase in the size of these areas or contiguous mottled depigmentation is termed a GA lesion[93]. Some dry AMD patients may retain a normal level of vision, although severe cases can lead to registered blindness.

1.3.4.2.2 Choroidal Neovascularisation

Wet AMD, also termed CNV, features the growth of abnormal, leaky blood vessels from the choriocapillaris into the retinal space[20]. The endothelia of these nascent neovascular membranes are fragile and susceptible to rupture. This can result in subretinal fluid accumulation, swelling, exudation and haemorrhage, leading to RPE/neuroretinal detachment as well as scarring of the macula[93 125]. An example of wet AMD pathology is shown in Figure 11. Eventually fibrosis and collagen deposition occur resulting in advanced visual impairment[93].

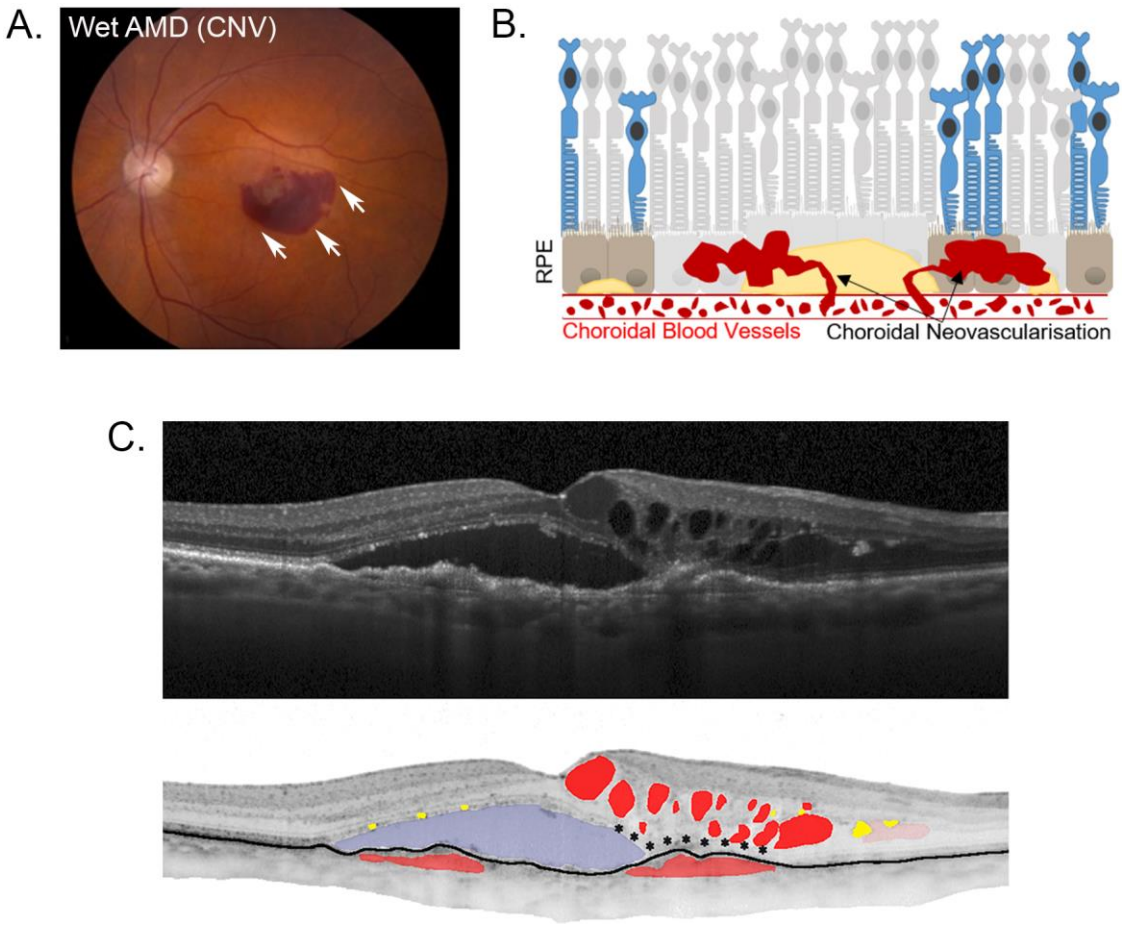

Figure 11: Clinical features of wet Age-related Macular Degeneration.

Figure showing the pathological changes associated with late stage, wet Age-related Macular Degeneration (AMD). **A.** Fundus image of the inner retinal surface from a patient with wet AMD. White arrows indicate subretinal haemorrhage resulting from Chroidal Neovascularisation (CNV) within the macula. **B.** Wet AMD is characterised by the growth of blood vessels from the choroidal vasculature into the subretinal space. These may rupture resulting in fluid leaks and swelling beneath the macula. **C.** OCT image of a patient with typical features of wet AMD including intraretinal cystoid fluid (bright red), subretinal fluid (blue), RPE detachment (dark red) and photoreceptor alterations (yellow). OCT images are commonly used by clinicians in addition to fundus photographs when making an AMD diagnosis. Image A sourced from Haugsdal et al. (2013)[125] and C from Schmidt-Erfurth et al. (2016)[127].

An alternative form of wet AMD also exists termed Retinal angiomatous proliferation (RAP). In RAP, neovascularisation originates in the intraretinal capillaries and extends into the subretinal space and RPE, eventually communicating with the choroid[20 93]. In both instances, penetration of the normally avascular outer retinal layers by new, leaky blood vessels compromises the immune privileged state of the retina, allowing access to inflammatory mediators from the peripheral vasculature[93]. Under normal conditions perfusion of the choroid is maintained by the actions of VEGF. This facilitates the passage of nutrients and oxygen from the choroid to the retina[30]. However, upregulation of the proangiogenic cytokine VEGFA is typical of CNV and is thought to promote angiogenesis and disease progression[5 93].

1.3.5 AMD diagnosis

Several techniques are employed by clinicians to inform AMD diagnosis or when categorising patients into a specific disease stage. These include but are not limited to fundus photography, slit lamp biomicroscopy, autofluorescence imaging, fluorescein angiography, indocyanine green staining and OCT. Typically, fundus photography, slit lamp biomicroscopy and autofluorescence imaging provide a broad indication as to the health of the 'eye grounds' as well as the degree of lipofuscin accumulation, and are used in the diagnosis of both dry and wet AMD. However, indocyanine green staining and fluorescein angiography are mainly used to provide prognostic information in wet AMD and are useful for detecting new choroidal vessels below blood layers, exudate and RPE detachment, and determining the extent and location of CNV respectively[128]. The use of OCT offers greater insight into the underlying pathological changes in both dry and wet AMD including visualisation of individual retinal layers and has thus displaced other diagnostic techniques in terms of its usefulness in early disease prognosis and diagnosis[128].

1.3.6 Current treatment strategies

At present AMD is incurable, with as many as 50% of cases regarded as untreatable[91]. This is highlighted by the clinical vacuum that exists for FDA approved therapies that manage dry AMD progression. AREDS investigated the effects of nutritional supplementation with antioxidants and demonstrated that vitamin E, beta-carotene, vitamin C and zinc may significantly retard disease progression to advanced stages in some patients with intermediate AMD[129]. However, this remained ineffective in approximately 75%-80% of patients[5 129]. A second AREDS study therefore sought to identify the potential benefits of the lutein, zeaxanthin and omega 3 fatty acid addition to the original AREDS formula, but these substances had no effect on preventing progression to late stage AMD[130].

In contrast to dry AMD, several clinical management strategies exist for the exudative form of the disease, including VEGF inhibitors, photodynamic/thermal laser therapy and anti-neovascular agents[5]. Anti-VEGF medications currently available on the NHS include Ranibizumab, a recombinant humanized monoclonal antibody fragment that targets the receptor binding site of active VEGFA[131], and Aflibercept, a human recombinant fusion protein that comprises VEGF receptor 1(VEFFR1) and VEGF receptor 2 (VEGFR2) extracellular binding domains[131]. These exhibit a high binding affinity for the VEGF receptor and VEGFA respectively, and

either preferentially outcompete, or sequester endogenous VEGF to alleviate VEGF-driven pathology[131]. However, treatment usually involves sequential intravitreal injections with a specific anti-VEGF agent, owing to the short effective duration of therapy. A number of unpleasant side effects are also associated with anti-VEGF treatments including increased intraocular pressure, minor bleeding and inflammation within the eye[132]. In fact, prolonged treatment with anti-VEGF inhibitors in wet AMD patients appears to damage the remaining RPE, with an incidence as high as 17% leading to the GA form of AMD[133]. This highlights the limitations of employing therapies based upon an incomplete understanding of the disease pathophysiology. In order to develop treatments that prevent/arrest AMD progression in its early stages, a better understanding of the fundamental aetiological mechanisms underpinning disease is required[134].

1.3.7 AMD aetiology: an incomplete picture

The aetiology of RPE dysfunction and atrophy that precedes advanced AMD remains unclear, despite years of basic and clinical research[135]. It is thought that multiple and cumulative alterations to cell function and metabolism within the macula underpin the molecular basis of disease. This includes age-associated alterations to the RPE, photoreceptors, choroid and Bruch's membrane[135]. Nonetheless, the RPE has consistently been identified as the fulcrum of AMD pathogenesis[136]. Heterogeneous RPE mechanisms have been associated with AMD pathology including altered inflammatory signalling[135 136], oxidative stress[56], dysfunctional clearance pathways[56 136] and lipofuscinogenesis[56 135]. However, the initial molecular changes that drive these events, as well as common links, remain unclear[135]. To date no definitive pathway has been identified by which disease progression occurs. Nonetheless, insights into the mechanisms that appear to be integral to disease progression may be gained through studying RPE changes seen with age and disease.

1.4 Age and disease associated RPE dysfunctions

The central role played by the RPE is supported by the pathologies observed in AMD, Sorsby's fundus dystrophy, Stargardt disease, Best disease, Leber congenital amaurosis, diabetic retinopathy (DR), pattern dystrophies and albinism patients[20 29 34] although the origin of RPE dysfunction is not always clear. Nonetheless, the RPE exhibits several morphological and functional changes with age that are thought to compromise its normal activity. A brief summary of such characteristics identified to date are presented below. In particular, we outline observations in RPE clearance pathways and their link with AMD, which constitutes the central theme of this thesis.

1.4.1 General alterations

With age, the RPE progressively exhibits several alterations to structure and function. For example, melanin loss and photobleaching have been shown to occur and are associated with a decreased anti-oxidant activity of the RPE[29 137]. In fact the RPE exhibits a 2.5-fold decrease in melanin content by the age of 90[137], with depletion occurring across the retina by the 4th decade of life[33]. Additionally, alterations in the RPE apical surface have been reported including microvilli atrophy and shortening, which are thought to influence the enzymes responsible for the antioxidant, transcellular transport, visual cycle and phagocytic processing activities of the RPE[29]. The thickening, as well as the altered chemical composition and decreased elasticity of the underlying Bruch's membrane also occurs[138] alongside other mechanisms, which are thought to result in improper clearance of secreted material from the RPE[29]. This may explain the formation of drusen between the RPE basal surface and Bruch's membrane with advancing age[9 29]. The aforementioned changes are indicative of altered RPE function with normal ageing. However, these appear to be exacerbated in AMD[29 33].

1.4.2 Alterations to RPE clearance pathways

1.4.2.1 Ubiquitin Proteasome impairment

It is well established that inherent changes occur within the UP with age, leading to a decline in its activity and in cellular proteostatis[80 139 140]. This is evidenced by impaired HSP chaperone induction[141], altered proteasome integrity and composition[80], as well as the accumulation of damaged or misfolded proteins[142]. In fact protein aggregates themselves have been shown to obstruct normal

proteasome function[143] thus potentially exacerbating their build-up through a detrimental positive feedback loop[80]. It is therefore not surprising that the UP has been implicated in several age-related neurodegenerative disorders in which protein inclusions are a major feature. These include Amyloid Lateral Sclerosis, Huntingdon's disease, AD[80], and more recently AMD[10]. A plethora of evidence suggests a role for the UP in AMD. For example sub-RPE drusen are permeated with ubiquitin protein-conjugates, indicative of an inability of the RPE proteasome to degrade substrate proteins[10 144]. Hence, impairment of the UP along with other RPE clearance pathways may be etiologically related to drusen deposition. Impairment of the RPE proteasome also appears to induce altered inflammatory and pro-angiogenic signalling that is analogous to changes seen in AMD. Specifically, treatment of RPE cells with proteasome inhibitors showed a 7 and 2-fold increase in VEGF expression and secretion respectively, along with diminished NF-κB signalling[145]. This also corresponded with a downregulation in monocyte chemoattractant protein-1[145] , which seems to play an important role in preventing AMD-like pathology, including photoreceptor atrophy, lipofuscin accumulation and CNV in an experimental AMD model[146]. Similarly, RPE cells have been shown to display increased expression of IL-8 following prolonged UP inhibition[147]. Collectively, this supports a role for impaired UP functionality in the pathogenesis of AMD although evidence for a direct correlation is still lacking[10].

As stated previously, coordinated collaboration of the UP with autophagy may occur under conditions of cellular stress[148]. Here, proteins may be processed through a parallel pathway in an attempt to compensate for impaired degradative function, and prevent the accumulation of cytotoxic protein inclusions. This likely occurs in the above instance of UP dysfunction, where studies have shown a corresponding increase in SQSTM1/p62 expression and redirection of proteins to the autophagy-mediated degradation pathway following UP impairment with MG-132[81 149]. This is further supported by upregulation of the PI3 kinase signalling pathway upon proteasomal inhibition[150], which plays an essential role in driving autophagosome maturation[151]. However, alterations to autophagy have also been implicated in AMD, suggesting a global dysfunction of cellular clearance mechanisms.

1.4.2.2 Autophagy dysregulation

A significant decline in the RPE's autophagic capacity has been associated with age, although an increasing body of literature now also suggests its role in AMD. This has been discussed in several reviews[11 152]. To date, isolated RPE from AMD tissues have been shown to exhibit an autophagosome count of over double along with

the intracellular accumulation of known autophagy substrates and an impaired autophagic flux[153]. This is supported by evidence from AMD mouse models as well as donor tissue samples[154]. Further, RPE exposure to chronic oxidative stress, a recognised AMD risk factor, appears to impair autophagy[154] and has been associated with mitochondrial damage, elevated ROS production and increased AMD susceptibility[153]. Indirect evidence also comes from the composition of drusen, which contain known autophagy substrates such as carbohydrates, lipids, proteins and other cellular debris[11]. In effect, impaired fusion with RPE lysosomes and autophagic clearance is thought to result in the release of autophagic material from exosomes into the sub RPE space as drusen, in an attempt to restore normal function[155]. However, this is speculation. Despite its apparent involvement in disease processes, no hard evidence exists to date that firmly implicates altered autophagy as a key driver of AMD pathology. Nor are the mechanisms known by which autophagic dysfunction occurs. It could be that dysfunctional autophagy may occur as a secondary feature of lysosomal dysfunction. The involvement of lysosomes in driving this phenotype is supported by the imbalance between the formation and elimination of autophagosomes seen in AMD[11 152]. Autophagosomes constitute the precursory terminal vesicle of the autophagic pathway, and are reliant upon fusion with lysosomes for the efficient clearance of internal constituents[12]. In fact, multiple changes to lysosomal function and morphology have also been associated with age and AMD, as discussed in Section 1.4.2.3.

1.4.2.3 Lysosomal impairment

Of specific interest to this project is the role of impaired RPE lysosomal function in AMD pathology. The lysosome is the main point of convergence for several disease associated RPE clearance mechanisms (Figure 7), and presents a prime target to investigate with respect to understanding the mechanisms that may drive RPE dysfunction in AMD.

Perhaps the most characteristic feature of aged RPE is an increased residual body count and increased lysosomal accumulation of the autofluorescent pigment lipofuscin[29]. This largely consists of protein-lipid by-products[74] and has been shown to account for approximately 19% of the cells cytoplasmic volume by an individual's 6th decade[35]. The exact origin of RPE lipofuscin remains under debate, although substantial evidence suggests that this represents modified indigestible material resulting from incomplete POS degradation[74]. Over time, and with increasing age, impaired lysosomal clearance of shed POS is thought to cause the build-up of incompletely degraded products including lipofuscin and its fluorescent

component, N-retinylidene-N-retinylethanolamine (A2E) [74] [29] [82]. Despite the exact role of lipofuscin/A2E in AMD aetiology being somewhat unclear, the increased accumulation of these materials has been associated with a disease-like state of the RPE[29]. Prolonged and significant A2E exposure perturbs lysosomal pH and disrupts vesicle membrane integrity, thereby affecting the intrinsic activity of lytic enzymes which exhibit a tight pH dependence[84] [156]. In fact, lipofuscin exposure has been shown to reduce acid hydrolase activity by up to 50%[157]. Furthermore, lipofuscin and A2E are phototoxic resulting in the generation of ROS. For example, lipofuscin induced oxidative stress in the RPE has been associated with impaired cellular renewal and an increase in the number of intracellular misfolded proteins[158]. In some instances, Lysosomal Membrane Permeabilisation (LMP) may also occur following lipofuscin/A2E accumulation[159], whereby lysosomal contents are released into the cytoplasm. By this mechanism, cytosolic components are subject to attack by the cells own digestive system. Insights into the role of lipofuscin and A2E in RPE cells have also been gleaned through studies in Stargardt's Abca4 knock out mice[160]. These animals exhibit enhanced complement activity as well as deposition of waste material in the RPE/Bruch's membrane interface following lysosomal lipofuscin accumulation. Further evidence to support a role for impaired lysosomal function in AMD comes from analysis of RPE isolated from diseased human tissues, which exhibit enlarged, annular lysosomes[153]. Similarly, aged RPE display an increased residual body count[29] and beta-galactosidase activity[153], which supports progressive lysosomal impairment. Owing to the convergence of several pathways/functions on this important organelle, impaired lysosome function likely has widespread effects on overall RPE clearance and function. However, the cause for lysosomal dysfunction in AMD and other retinopathies and what triggers the switch to a diseased state remains unknown. Alterations to the major RPE clearance pathways reported in the literature to date are briefly summarised in Figure 12.

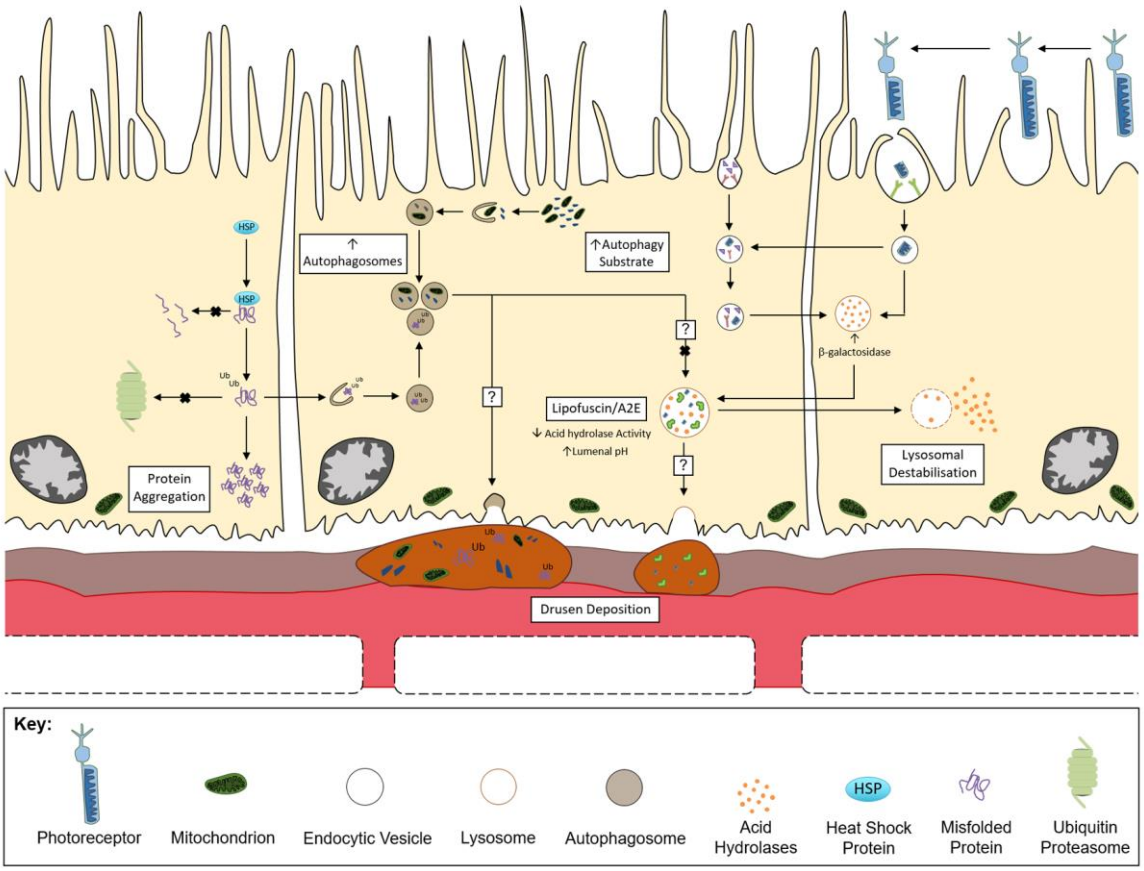

Figure 12: The hypothesized molecular mechanisms and potential link between impairment of the RPE clearance pathways and the deposition of sub-RPE drusen.

Schematic representation of the alterations to the ubiquitin proteasome, autophagy, phagocytic and endolysosomal pathways that have been associated with age and AMD pathology. Interestingly, all of these mechanisms converge at the level of the lysosome, which undergoes several changes indicative of a decreased functional ability with age. This includes the accumulation of lipofuscin/A2E, increased β-galactosidase activity and decreased lytic enzyme function. Hence, several hypotheses now posit that failure to clear intracellular material via this organelle may underlie drusen deposition, which represents a major risk factor for developing AMD.

1.4.3 Potential therapeutic avenues

An increasing body of literature is concerned with removing or preventing the accumulation of toxic material in the retinal environment. This identifies a novel therapeutic avenue for the treatment of dry AMD. However, before effective therapies can be devised an increased understanding of mechanisms that lead to the accumulation of various factors is first required. Recently, the observation that the AD-associated Aβ peptide accumulates within the aging retina and AMD eyes has shed new light on this complex disorder. In particular, it associates a known pathogenic agent that has the potential to impair several RPE clearance mechanisms with aspects of AMD pathology [8 9].

1.5 Amyloid Beta (Aβ)

1.5.1 APP processing and the generation of Aβ

Aβ denotes peptides of between 36-43 amino acids (~4KDa) that result from the sequential proteolysis of the amyloid precursor protein (APP)[161 162]. Several APP isoforms exist, of between 365 to 770 nucleotides, which arise from alternative splicing of the APP transcript[163]. The most prominent isoform in neurons is APP695[164], whereas endothelial cells typically express APP770 and APP751[165]. These type I integral transmembrane glycoproteins comprise a large N-terminal ectodomain and a shorter intracellular C-terminal domain that may be processed by one of two mutually exclusive pathways, the amyloidogenic or non-amyloidogenic pathway[166]. A simplified schematic of these processes can be seen in Figure 13.The non-amyloidogenic pathway precludes Aβ formation by cleavage of Lys^{16}-Leu^{17} within the C-terminal Aβ domain by the aspartyl proteases, α-secretase and γ-secretase to produce soluble APPα (sAPPα), APP Intracellular Domain (AICD) and p3[162 163]. This is the predominant pathway by which APP processing proceeds and is important for neurotrophic and neuroprotective function[167]. The amyloidogenic pathway, however results in the production of Aβ. In this pathway, APP is cleaved by β-secretase (BACE-1) mainly at N-terminal Asp^{1} to produce the membrane-associated fragment C99, or in some cases at Glu^{11} to produce C89[162 168] and β-secretase liberates sAPPβ, which is shed into the lumen or extracellular fluid[162]. Subsequent cleavage of C99 by γ-secretase generates the short intracellular fragment AICD, along with Aβ peptides of between 38-43 amino acids[161]. The length of the Aβ peptide generated is dependent on the exact cleavage point of γ-secretase[162]. The two most prevalent Aβ isoforms within both the brain and retina are $Aβ_{1-40}$ and $Aβ_{1-42}$, which are produced upon γ-secretase cleavage at residues 712 or 714 respectively[164]. The heterogeneous mixture of Aβ isoforms produced vary in structure, solubility and stability and thus differ in both biological properties and function[169]. In the healthy nervous system Aβ likely performs an important physiological role, as it is present in the brain and cerebrospinal fluid (CSF) of healthy individuals and is a normal by-product of neuronal metabolism[162 169]. This is supported by the deleterious effects observed upon APP knock-out as well as the presence of Aβ in the absence of neurodegeneration. In fact, several studies have implicated Aβ in modulating synaptic plasticity, memory formation and neuronal survival. However, certain Aβ isoforms and conformational states have been

associated with neuronal injury and AD pathology in the ageing brain[162 169 170], as well as several retinal disorders[8 171].

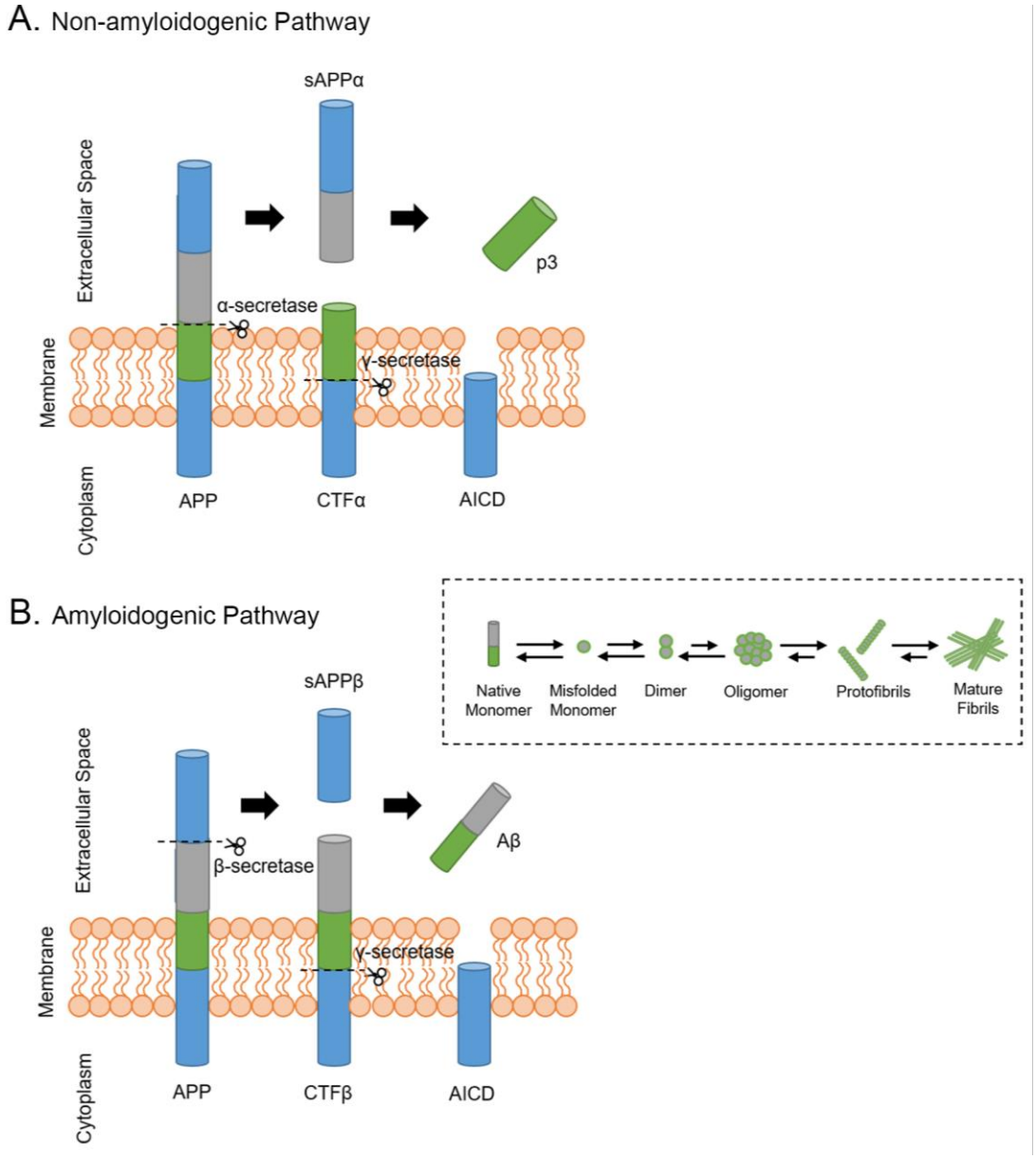

Figure 13: Routes of Amyloid Precursor Protein (APP) processing and their associated cleavage products.

The amyloid precursor protein (APP) is a type I transmembrane protein that may be processed by one of two routes, the non-amyloidogenic pathway or the amyloidogenic pathway. **A.** In the non-amyloidogenic pathway, α-secretase cleaves APP within the extracellular space to produce the N-terminal secreted ectodomain, soluble APPα (SAPPα), and the 83 amino acid residue C-terminal transmembrane fragment, CTFα. Subsequent cleavage of CTFα by γ-secretase occurs to produce non-amyloidogenic p3 and APP intracellular domain (AICD). **B.** In the amyloidogenic pathway, APP cleavage by β-secretase yields the soluble N-terminal ectodomain APPβ (sAPPβ), and the 99 residue membrane associated C-terminal fragment (CTFβ). Similar to the amyloidogenic pathway, subsequent proteolysis by γ-secretase cleaves CTFβ to produce the C-terminal membrane bound fragment AICD. However, prior cleavage by β-secretase results in the generation of the soluble beta amyloid (Aβ) protein as opposed to p3. Progressive accumulation, misfolding and aggregation of Aβ into amyloid fibrils occurs under certain conditions, and has been implicated in the neurodegeneration observed in Alzheimer's disease. Adapted from Chow et al. 2010[172] and Kumar et al. 2011[173].

These conformational states are by-products of an ordered Aβ self-association process that appears to be essential in conferring Aβ toxicity.

1.5.2 Amyloid aggregation and toxicity

Under physiological conditions, the majority of Aβ within the brain is soluble[162]. However, due to unknown factors, Aβ may undergo ordered aggregation into insoluble fibrils. Several structural intermediates within this process exhibit a strong correlation with AD severity and are currently thought to drive disease advancement. Initially, it was thought that amyloid fibrils present within senile plaques of AD brains were the main mediators of cytotoxicity[162 166]. However, a revised amyloid cascade hypothesis has since been proposed, owing to observations that showed poor correlation between plaque load and cognitive impairment[162]. The revised hypothesis postulates that small soluble aggregates of the Aβ peptide exert potent neurotoxicity in the brain, and are the primary impetus of disease progression[166]. These include oligomers, Aβ-derived diffusible ligands and protofibrils[162 166]. In fact, studies have shown that Aβ oligomer exposure inhibits hippocampal long-term potentiation[174], impairs learned memory function in rodents[175], and induces synaptic alterations, including decreased dendritic spine density and synaptic loss, within glutamatergic hippocampal neurons[174], the latter of which shows a strong correlation with AD[162].The implication of Aβ oligomers in AD is further supported by evidence of a 10-fold higher inherent toxicity than Aβ fibrils[171] in addition to an increased penetrative ability[9]. In spite of this, the precise molecular identity of the causative oligomeric species remains to be ellucidated, and has been the subject of much debate. Currently, the soluble Aβ species deemed responsible for neurotoxicity in the AD brain[162] refers to a large range of Aβ structures. Nonetheless, the process of Aβ self-aggregation appears to be essential for toxicity[162]. Knowledge of the biophysical parameters that affect Aβ self-association is far from complete. However, studies investigating the aggregation and structural properties of Aβ *in vitro* have provided insights into the kinetics of this process, as well as its various structural intermediates[176 177 178]. This has proven particularly useful in informing Aβ isolation for cell culture studies, where the effects of a specific conformer are often tested. It is now widely accepted that Aβ fibril assembly occurs according to the nucleation dependent polymerisation model, as explained in Figure 14.

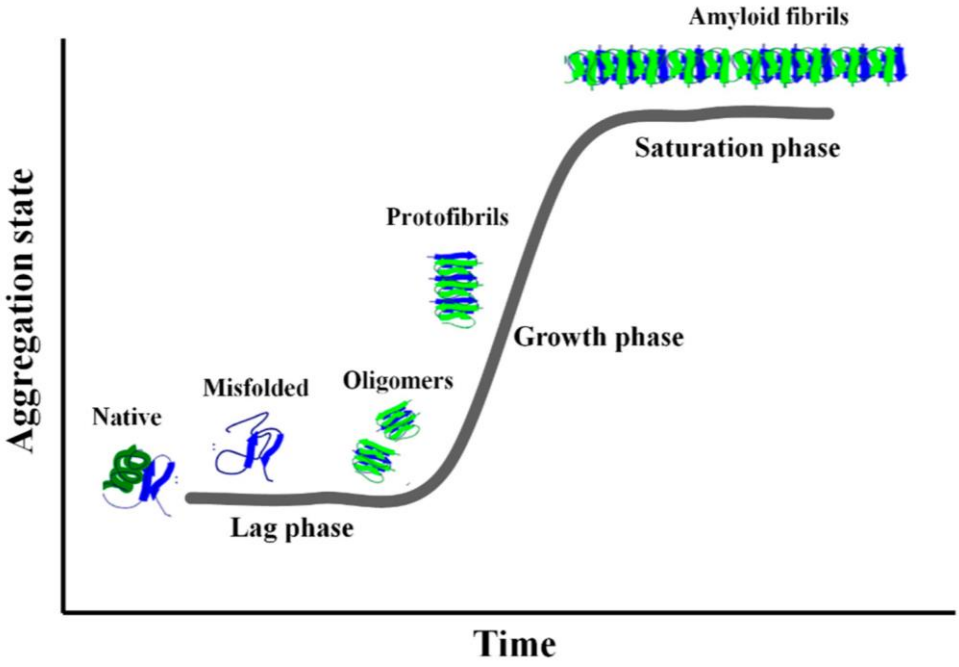

Figure 14: The nucleation dependent polymerisation model of Aβ assembly.

The most widely accepted method of Aβ self-assembly is the nucleation dependent polymerisation model of fibril formation. This constitutes two major phases; the lag phase and an elongation/growth phase. The lag phase involves the misfolding of α-helical native Aβ monomers and subsequent dimerization and aggregation into small intermediate Aβ oligomers with a β-sheet, termed 'nuclei'. This phase is thermodynamically unfavourable and thus proceeds slowly. Once formed, nuclei rapidly elongate with increased availability into more mature Aβ species including protofibrils and mature fibrils with a cross-β sheet in the growth phase. Amyloid fibrils constitute the final species in the aggregation process and thus Aβ cannot further assemble, as represented by saturation. Reprinted from Iannuzzi et al. 2014[179].

Here, protein aggregation follows a complex process initiating with an anomalous conformational change from soluble Aβ to insoluble monomers, followed by reversible self-assembly of insoluble α-helical monomeric Aβ species into low molecular weight dimers and trimers[9 180]. This step is proceeded by a thermodynamically unfavourable lag phase in which a rate limiting conformational change occurs to β-sheets[9 181 182]. This refers to the time taken to form Aβ oligomeric 'nuclei', which have been proposed to form metastable intermediaries via nucleated conformational conversion. This increase in cross β-sheet structure promotes the formation of amyloid fibrils and consequently higher ordered structures emerge including protofibrils and mature amyloid fibrils with a cross-β structure[9 179 180]. This is defined as the growth phase. The kinetics of the Aβ aggregation phase are of paramount importance in determining the rate of synthesis of structural intermediates within this pathway, where the relative concentration, temperature, pH and incubation time have all been shown to influence the dynamics of Aβ assembly[177 179 182]. This must be taken into account during experimental design to ensure consistency of desired aggregation intermediates.

1.5.3 $A\beta_{1-40}$ and $A\beta_{1-42}$ in disease

$A\beta_{1-42}$ is more susceptible to conformational changes and amyloid fibrillogenesis than the more commonly produced $A\beta_{1-40}$ isoform[183], and ultimately increases oligomer content in the brain. Hence, the relative abundance of the $A\beta_{1-42}$ isoform appears to be of critical importance in AD pathogenesis. The exact reason for this increased aggregation propensity remains unknown, although it has been suggested that two additional hydrophobic amino acids (Ile & Ala) confer this property[183 184]. Several lines of evidence have demonstrated that perturbations in the ratio of $A\beta_{1-40}$ and $A\beta_{1-42,}$ in favour of $A\beta_{1-42}$ are associated with an AD phenotype. For example, mutations within presenilin and APP are known genetic risk factors for early and aggressive AD onset[185], along with mutations near the γ-site of APP, which grant increased $A\beta_{1-42}$ synthesis[162]. Further, increased $A\beta$ within the brain in general has also been linked with AD onset[162]. Duplication of the APP locus on chromosome 21, and mutations within the $A\beta$ encoding region proximate to β, γ and α sites that grant increased $A\beta$ production, are sufficient to induce an AD phenotype[162 186]. Similarly, transgenic mice expressing mutant human APP exhibit pathological changes simultaneously with elevated extracellular $A\beta$[187]. However, it is not yet clear whether this phenotype is attributable to elevated $A\beta_{1-42}$, total $A\beta$, or an altered $A\beta_{1-40}$:$A\beta_{1-42}$ ratio. Further evidence of $A\beta$-mediated brain toxicity derives from studies of Down's syndrome patients. Trisomy on chromosome 21 is known to elevate APP expression in sufferers thereby increasing $A\beta$ levels and resulting in comparable pathological changes to that observed in AD patients upon autopsy[162 186]. Genetic associations for AD are rare with familial cases constituting a mere 1-5% of disease incidence[188]. In sporadic AD cases, increased $A\beta$ load in brain tissue and cerebral blood vessel walls as Cerebral Amyloid Angiopathy (CAA) mainly arises from the deficient clearance of soluble $A\beta$[189 190]. Specifically, impaired neprilysin, insulin degrading enzyme, lipoprotein receptor-1 and perivascular drainage mediated mechanisms of $A\beta$ disposal have all been associated with both age and disease[189 191]. Nonetheless, a major observation in both familial and sporadic AD is an elevated presence of $A\beta$.

$A\beta$ evidently plays a fundamental role in the degenerative brain where therapeutic research is largely focused towards targeting $A\beta$ oligomer production[162 186 192 193]. In light of recent studies that have connected ocular $A\beta$ deposition with visual dysfunction in AD as well as glaucoma and AMD, it has been proposed that similar mechanisms of $A\beta$ pathogenesis may also be applicable to retinal disease.

1.6 Aβ in the retina

1.6.1 Retinal sources of Aβ

The healthy retina is constitutively exposed to Aβ. In fact, recent findings have demonstrated that Aβ synthesis occurs at local sites within the retinal environment including the RPE and RGCs[8 194-196]. Currently, it is thought that the RPE is the principal source of Aβ production and secretion, which has the capacity to both synthesise APP and generate Aβ through enzymatic processing. This is supported by the observation that Aβ synthesis occurs in both murine and human RPE cell cultures isolated from healthy tissue[196]. The RPE also expresses transcripts for the three major APP isoforms, APP^{770}, APP^{751} and APP^{695}, along with the necessary factors for regulated Aβ synthesis[165 197 198]. These include β-secretase, γ-secretase and the Aβ degrading peptidase neprilysin. Evidence of sustained retinal Aβ exposure also comes from studies investigating bovine and mouse ocular fluids that report the presence of $Aβ_{1-40}$ and $Aβ_{1-42}$ in pM to nM quantities in both aqueous and vitreous humours[199]. Under normal physiological conditions it appears that $Aβ_{1-40}$ is the most predominant species[199]. This is supported by Aβ concentrations within human vitreous, which exhibits a 10-fold higher $Aβ_{1-40}$ concentration than $Aβ_{1-42}$[200]. Here, Aβ was also reported within the pM range, although a more rigorous quantification study is required to validate this finding. Finally, studies involving APP knockouts have demonstrated the relative importance of the APP precursor and its products in retinogenesis and retinal function[201]. APP expression appears to coincide with specific stages of retinal differentiation associated with second-order retinal cell development, and may be involved in synaptogenesis. These mice also exhibit impaired retinal and amacrine cell development, as well as amacrine modulation of inner retinal function, highlighting an important role for APP and its products in visual processing[201]. However, as yet the physiological role of APP and Aβ in the retina remains incompletely understood. The phototoxic environment within the human retina provides optimal conditions for Aβ accumulation. Consequently, Aβ deposition is a normal process in the ageing retina, and exhibits an increased prevalence in ageing humans and experimental models[165 202 203].

1.6.2 Age-associated retinal Aβ deposition

The decreased ability to clear Aβ is well documented in the aged brain, and is thought to result from a perturbed Aβ synthesis and clearance equilibrium[204 205]. The use of transgenic mice has identified that alterations to several key proteins involved in these processes are also sufficient to increase retinal Aβ deposition. For example, neprilysin-deficient mice exhibit Aβ accumulation between the RPE/Bruch's membrane interface[197], whilst increased APP expression and Aβ immunoreactivity has been reported in the RGCs and INL of aged AD mice expressing mutant presenilin (PS1) and APP[195 206]. Similarly, RPE isolated from aged wild-type mice exhibit increased $A\beta_{1-40}$ and $A\beta_{1-42}$ production, increased BACE-1 activity, and a reduction in neprilysin mRNA expression compared to RPE cells isolated from younger controls[207]. These age-dependent alterations together with aberrant Aβ processing in the retina, most likely result in the increased accumulation of Aβ in areas adjacent to sites of retinal synthesis. Of particular focus to this research is the deposition of Aβ in and adjacent to the RPE.

1.6.2.1 Outer retinal Aβ accumulation

Aβ deposits have been reported in multiple retinal locations including the photoreceptors[203], the RPE/Bruch's membrane interface[165 202 208 209] and within the vasculature of both the inner and outer retina[203]. This pattern of Aβ accumulation occurs in both rodent models and human post-mortem tissue and, unsurprisingly, exhibits an age-dependent increase. Firstly, evidence demonstrates an age-dependent accumulation of Aβ within ocular blood vessels within Wild Type (WT) rodents exhibiting Aβ within the retinal and choroidal vasculature at just 3 months of age[203]. Interestingly, Aβ deposited along the entirety of the retinal vasculature, but appeared to concentrate at focal regions. This is concordant with observations in some mouse models of AD[206] and may in part explain the reduction in blood flow and thinning of retinal blood vessels observed in AD patients, many of whom report visual complications[9 210-212]. In contrast, choroidal Aβ was observed in distinct vessels, where others showed no evidence of Aβ accumulation[203]. Secondly, in the normal mouse retina encapsulation of the POS by Aβ-containing material was seen by scanning electron microscopy at just 12 months[203]. This pattern of Aβ deposition appeared to initiate at the POS apical portion and progressively accumulated along the anterior length with age. Interestingly, a distinct boundary was maintained between the IS and POS, with Aβ accumulation confined to the latter. By 24 months, POS were morphologically altered with bulbous tips, perhaps indicative of age-

associated alterations to the RPE phagocytic system. Inspection of post-mortem ocular tissues from donors aged 31-90 also revealed increased Aβ deposits on the POS with age[203]. The accumulation of Aβ in and around the POS is further supported by intravitreal $A\beta_{1-40}$ injections in wild-type rats, which show preferential Aβ accumulation adjacent to the RPE apical surface[213].

This age-dependent accumulation likely takes its toll on the RPE with regards to its phagocytic function and role in POS renewal. In fact, the use of antibodies that detect Aβ as well as APP, have shown immunoreactivity within the cytoplasm of RPE cells adjacent to drusen[165]. This may indicate a failure in RPE clearance mechanisms in the presence of Aβ, and is corroborated by the deposition of photoreceptor derivatives and Aβ within the RPE/Bruch's membrane interface as drusen[202 208 209]. Hence, Aβ has been associated with key stages of AMD pathology. Given its association with AMD, it is perhaps also not surprising to learn that Aβ has been implicated in several other retinal pathologies (Section 1.6.3).

1.6.3 Aβ associations with ocular disease

An increasing number of ocular disease phenotypes have been associated with the Aβ peptide. These include retinal abnormalities in AD patients[210-212], in addition to chronic ocular conditions such as glaucoma[171] and AMD[8 9].

1.6.3.1 Retinal Aβ in Alzheimer's disease

AD is commonly referred to as a complex neurodegenerative disorder associated with a progressive decline in cognition, memory, and social function that ultimately results in death[214]. However, a variety of visual symptoms have been documented in addition to brain pathology[24]. These include object agnosia, prosopagnosia, visual hallucinations and visuo-constructional/visuo-perceptual dysfunctions, which have been attributed to defects in both cortical and retinal visual processing[215 210 211]. Nonetheless, local retinal damage appears to play a central role in retinal pathology, with patients exhibiting similar alterations to that reported in glaucoma[216]. Extensive RGC loss, optic neuropathy and visual functional impairment have all been associated with visual dysfunction in AD[216-218 214], and occur alongside retinal Aβ deposition in experimental AD models[206 216 219]. Additionally, funduscopic investigations of AD retinae have identified a co-occurrence of peripheral drusen with AD[220], highlighting the presence of geographically distinct but comparable hallmarks to AMD. Interestingly, systemic injection of curcumin correlated the extent of retinal Aβ deposition with plaque deposition and disease severity in

transgenic AD mice[24 221] and showed that retinal Aβ deposition may occur up to 2.5 months prior to Aβ deposition in the brain[221]. As such, the eye is under scrutiny as a non-invasive *ante mortem* biomarker of AD[24 216 222].

1.6.3.2 Aβ in Glaucoma

Glaucoma is a neurodegenerative disease of the retina that affects approximately 60 million individuals globally, in which patients experience a gradual loss of vision terminating in blindness[223]. The main pathological hallmarks of glaucoma include RGC apoptosis, gliosis, optic nerve atrophy and in some instances increased intra-ocular pressure (IOP)[223]. This is remarkably similar to retinal pathology reported in patients with AD. In fact, several clinical studies have shown a high-rate of co-morbidity between AD and glaucoma[224 225]. Data derived from animal models of AD and glaucoma, as well as post-mortem tissue provides evidence for common retinal pathology including damage to the NFL and RGC[171 221 226]. This is not surprising as glaucoma, similar to AD-linked neuropathology, is associated with drainage pathway failure in aged tissues. Here, elevated IOP is thought to result in increased retinal Aβ deposition, suggesting an imbalance between Aβ synthesis and clearance that ultimately leads to neurodegeneration[171 227 228]. The role of Aβ in the cellular processes underlying a glaucomatous phenotype is supported by increased RGC Aβ expression in rodent models of glaucoma[227], in addition to the dose-dependent induction of RGC apoptosis observed upon exogenous $A\beta_{1-42}$ application[171]. Combination therapy of several drugs targeting Aβ production, clearance and aggregation appeared to rescue this phenotype and was associated with a decline in RGC atrophy[171]. One study also suggested a reduction in vitreal $A\beta_{1-42}$ concentration in glaucoma patients[229], mimicking changes in $A\beta_{1-42}$ CSF content seen in AD patients[230]. In summary, Aβ appears to be involved in the visual pathology associated with both glaucoma and AD and supports the convergence of disease mechanisms in a common driver of disease pathology.

1.6.3.3 Aβ in Age-related Macular Degeneration

AMD represents the primary focus of this research and is a distinct retinal degeneration to that observed in glaucoma and AD. However, Aβ also appears to be central to AMD pathology. As mentioned in Section 1.3.4.1, the increased deposition of drusen is a major clinical indicator of early AMD[121]. Aβ is a major constituent of drusen where it accumulates as highly organised spherical structures, termed amyloid vesicles, of approximately 2-10μm in diameter[165]. These

constitute the majority of the space within a druse but vary in both size and number[165]. Immunogold labelling in combination with transmission electron microscopy revealed that these vesicular Aβ assemblies comprise a concentric ring-like interior with varying electron densities[202]. The use of various antibodies, including 4G8 (amino acids 17-24 of Aβ), WO1 (mature amyloid fibrils), 6E10 (amino acids 1-17 of Aβ and APP) and OC (amyloid fibrils of various molecular weights), has confirmed that mature Aβ fibrils typically concentrate within the outer shell of these structures[202 208]. The presence of protofibrils and non-fibrillar oligomers have also been reported within drusen[8 208], although toxic soluble non-fibrillar oligomers constitute the most abundant Aβ conformer[208]. Specifically, one study reported that 22-36KDa and 50-64 kDa oligomers are the most abundant types of Aβ within the retinal and choroidal tissues[203]. These dominate the space adjacent to the inner collagenous layer of Bruch's membrane where they concentrate in 'amyloid oligomer cores' with a relatively consistent diameter of approximately 10-15μm[8 209]. Over time, amyloid oligomer cores are thought to interact with complement proteins and lipids within drusen to form mature fibrils ultimately resulting in the typical 'amyloid vesicle' structure[8]. This is supported by the observation that amyloid oligomer cores do not appear to colocalise with the vesicular structures reported in previous studies[209]. However, the mechanisms underpinning amyloid vesicle formation are yet to be established. Further evidence of the involvement of Aβ in AMD pathology comes from a study of 152 post mortem eyes, in which elevated drusen numbers correlated with an increased prevalence of Aβ assemblies implicating Aβ in the advancement of AMD[202]. Interestingly, a small study of 9 post-mortem human retinae postulated that Aβ is exclusive to the drusen of AMD patients[231]. However, it is indisputable that this investigation exhibited a low statistical power, and that further examination of post-mortem eyes must be conducted to increase the reliability of such findings, especially as other investigations have reported the presence of amyloid vesicles in drusen of control and AMD retinas[165].

The case for the involvement of Aβ in AMD pathogenesis is further enhanced by its apparent role in disease inflammatory processes. AMD is considered a chronic inflammatory disease in which the complement system plays a significant role[232]. Genetic variations within complement-associated genes are sufficient to either increase or decrease the risk of disease development (Section 1.3.3.3). Aβ has been shown to colocalise with both CFH and iC3b within drusen[8 165] where it is predicted to induce activation of the alternative compliment cascade by binding and blocking

the action of CF1, thereby preventing cleavage of C3b, and resulting in iC3b activation[233]. This Aβ constituent is also sufficient to induce increased RPE expression of CFB, the principal activator of the alternative compliment pathway[8 233 234]. It is thought that this occurs via an Aβ-mediated increase in RPE secretion of MCP-1, which in turn upregulates macrophage/microglial IL-1β and TNF-α secretion and enhances RPE expression of CFB[8 233 234]. This is supported by the observation that migration of microglia from the inner retina to the subretinal space has been observed in AMD retinae as well as AMD and AD mouse models[8 206 235].

Finally, Aβ has been shown to induce TNF-α, caspase-1, NLRP3, IL-18, IL-1β and IL-6 upregulation in RPE cells[213], suggesting a potential involvement in NLRP3 inflammasome activation and innate immunity. NLRP3 and its effector cytokines have increasingly been implicated in AMD pathogenesis[236]. For example, NLRP3 activation and cleaved caspase-1 were apparent in a dry AMD mouse model[237], drusen isolated from AMD tissues activated NLRP3 in LPS-primed macrophages causing IL-18 and IL-1β release[238], and RPE at sites of dry and wet AMD pathology exhibit elevated NLRP3 expression[239]. Similarly, NLRP3 activation and IL-18 upregulation were demonstrated in the RPE of AMD donor tissues, which were also sufficient to drive RPE atrophy in vitro[239]. Here, inflammasome activation and subsequent IL-18 and IL-1β release were shown to proceed via lysosomal destabilization and Cathepsin B release. This could potentially be initiated by a number of AMD-associated insults[82 239], and is the predicted mechanism by which Aβ assembles/activates NLRP3 in AD[240 241]. These findings suggest that Aβ may also be in part, if not exclusively, responsible for inflammatory events associated with RPE and photoreceptor impairment.

It remains unclear whether increased Aβ within the retinal environment directly contributes to RPE and photoreceptor atrophy in AMD. Nonetheless, the main point to draw from this section is the consistent association of Aβ with retinal disease. Evidently, Aβ associated pathology extends to the retina and exerts detrimental effects on components of the visual system. The RPE is at the hub of sites of Aβ accumulation and so not surprisingly it is thought that Aβ may exacerbate aberrant RPE cell function leading to cell atrophy typical of AMD. An increasing body of literature supports this notion, which has implicated Aβ with various aspects of RPE dysfunction.

1.7 Aβ: evidence as an orchestrator of RPE dysfunction

To date Aβ has been implicated in both RPE alterations and dysfunctions typical of AMD. For example, Aβ accumulation correlates with features indicative of outer BRB impairment. This is demonstrated by the attenuation of tight-junction proteins (ZO-1 and occludin), as well as actin cytoskeletal disorganisation observed after subretinal injection with oligomeric $A\beta_{1-42}$ in wild-type C57BL/6 mice[242 243]. Similar results have been reported in oligomer exposed RPE cell cultures and 5XFAD mice, which correlate the presence of Aβ with compromised RPE BRB integrity[242 244].

Aβ exposure has also been associated with an altered RPE secretory profile. Studies investigating the effects in neprilysin knockouts and human RPE cultures consistently exhibit increased levels of pro-angiogenic VEGF, and decreased secretion of the anti-angiogenic factor PEDF upon exposure to $A\beta_{1-42}$[197]. VEGF is known to be upregulated in CNV patients[92] and perhaps suggests a role for Aβ in the progression from dry to wet AMD. Concordantly, conditioned media isolated from Aβ treated ARPE-19 cultures was sufficient to induce tubule formation in a Human Umbilical Endothelial Cells (HUVECs)[197], whilst $A\beta_{1-42}$ injections in Zebrafish significantly increased retinal capillary bed density[245]. It is likely that such phenotypes occur as a consequence of VEGF upregulation. The reason for this imbalance remains unclear and the effects of Aβ alone may not be sufficient to induce CNV, as it has been suggested that the integrity of Bruch's membrane must first be compromised[197]. However, taken together these findings implicate Aβ in the later pathological stages of AMD.

Functional changes within the RPE that are associated with Aβ include markedly lower levels of RPE65 and Retinaldehyde-binding protein 1 (CRALBP)[242], suggestive of an altered role for the RPE in the visual cycle, in addition to a reduced mitochondrial redox potential and increased generation of ROS[242]. Further, Aβ induces morphological changes *in vivo* corresponding to key pathological hallmarks of AMD. These include RPE hypertrophy, hyperpigmentation and hypopigmentation[242]. At physiologically relevant concentrations neither $A\beta_{1-40}$ nor $A\beta_{1-42}$ appear to be directly cytotoxic to RPE cells[243], although observations in neprilysin gene-disrupted mice that display RPE atrophy indicate that prolonged Aβ exposure may be necessary to induce cell death[197]. The age-dependent accumulation of Aβ within drusen almost certainly meets this condition.

The literature presented regarding Aβ induced RPE alterations is by no means exhaustive. A substantial body of literature exists regarding Aβ's effects on various RPE functions that is constantly expanding. In spite of this, little, if any, investigation has been conducted into the effects of Aβ on RPE clearance mechanisms, in particular the effects of Aβ on the RPE lysosomal system. For example, a search conducted in NCBI PubMed (http://www.ncbi.nlm.nih.gov/pubmed), using the terms 'Lysosome', 'Retinal Pigment Epithelium' and 'Amyloid' yields 0 returns. This is surprising given the proposed involvement of impaired RPE clearance in the initial stages of disease, as well as the known toxic effect of $A\beta_{1-42}$ on neuronal lysosomes. Evidently, research into the effects of Aβ on this specific aspect of RPE function is required.

1.8 Summary

The literature reviewed thus far implicates Aβ in key stages of AMD, where age-dependent amyloid deposition has been demonstrated at several locations in the retinal environment. Significant increases in Aβ exposure in the form of multiple 'reservoirs' are likely to exert local toxic effects on the RPE and photoreceptors both intracellularly and extracellularly[9]. Thus, it is logical that there is a correlation between such Aβ deposits and RPE dysfunction in AMD. Further, the information presented highlights the substantial involvement of RPE clearance with AMD progression, with the UP, autophagy and lysosomal degradation all demonstrating disease associated alterations. By investigating how Aβ targets RPE clearance mechanisms, in particular RPE lysosomes, novel insights may be gained to further our understanding of the fundamental molecular mechanisms driving RPE atrophy and the progression of this complex disorder.

1.9 Aims, hypotheses and objectives

The overarching aim of this PhD was to explore the interrelation of Aβ with AMD pathology. The prior literature review rationalises the need for its investigation. This was achieved via three research avenues, each investigating a particular research hypothesis, as outlined below.

1. Aβ accumulates within RPE lysosomes, disrupts lysosomal acid hydrolase activity and impairs normal organelle function. In turn this results in a failure of clearance through RPE lysosomal dependent clearance pathways, giving rise to morphological alterations typically associated with AMD

2. Aβ is a key driver of retinal disease and induces pathological features of AMD *in vivo*

3. Vitreous Aβ concentration is higher in AMD patients than 'normal' controls and may therefore be used as an ocular biomarker for disease progression.

In order to test the above research hypotheses, objectives were devised as follows:

- Establish and characterise an *in vitro* model of the outer retina
- Characterise Aβ aggregation to obtain oligomer enriched fractions
- Assess whether Aβ localises to RPE lysosomes
- Determine Aβ effects on lysosomal acid hydrolase activity
- Measure Aβ effects on normal lysosome function

- Analyse Aβ induced retinal pathology *in vivo* using qualitative methods
- Quantify Aβ's effects on component retinal layers
- Measure Aβ's effects on retinal function *in vivo*

- Quantify the concentration of Aβ in the vitreous of AMD patients and 'normal' controls to investigate its association with disease status/stage.

Chapter 2 Materials and Methods

This chapter contains the standardised methodology of techniques employed in this research project. Specific details of experimental protocols can be found in the corresponding methods section of each results chapter.

2.1 ARPE-19 cell culture

2.1.1 ARPE-19 cell line

ARPE-19 cells[246] were obtained from the American Tissue Culture Collection (ATCC, USA) and were maintained in a 37°C humidified incubator with an atmosphere of 5% CO_2 and 95% air. Cells were cultured in complete medium in either 25cm^2 flasks, 8-well Ibidi μ–slides (Thistle Scientific Ltd, UK) or Transwell® Permeable Supports with a 0.4μm polyester membrane (Corning, UK). Complete medium comprised Dulbecco's modified Eagle's Medium (DMEM) with 4.5g/l L-D glucose (high glucose), L-glutamine and pyruvate (Life Technologies, UK), supplemented with 1% heat inactivated foetal calf serum (Sigma-Aldrich, UK) and 1% penicillin streptomycin stock solution (10,000 units/ml penicillin, 10mg/ml streptomycin in 0.85% saline; Sigma-Aldrich, UK). Growth volumes for each culture vessel are detailed in Table 1. In all cases cells were used between passages 23-26 and media change was performed every 2-3 days according to Table 1. Transwell® inserts were maintained in culture for a minimum two months prior to experimentation to ensure structural/functional specialisation of ARPE-19 monolayers.

Table 1: ARPE-19 cell culture conditions

Details of cell culture vessels and corresponding volumes used for ARPE-19 culture. Media change was conducted every 2-3 days to the percentages detailed.

Culture Vessel	Growth Volume (ml)	Media Change (%)
25cm2 Flask	5	100
Corning® 24mm Transwell® Permeable Support	Insert: 2 Well: 3	Insert: 100 Well: 20
Corning® 12mm Transwell® Permeable Support	Insert: 0.5 Well: 1.5	Insert: 100 Well: 20
8-well Ibidi glass bottom μ-slide	0.3	100
6-well Plate	2.6	100

2.1.2 Cell passage

Culture medium was aspirated from 25cm^2 flasks and cells were washed thrice with pre-warmed Ca^{2+} and Mg^{2+} free 1x Hank's Balanced Salt Solution (HBSS; Life Technologies, UK). Incubation at 37^{o}C with 1.5ml of 0.25% Trypsin/EDTA (Life Technologies, UK) for 6 minutes facilitated cell detachment. Following incubation, 7ml of complete medium was added to detached cells to inhibit the dissociation reagent, and the cell suspension was centrifuged at 1000RPM for 5 minutes. The resultant cell pellet was resuspended in 2ml of fresh medium. An aliquot of cell suspension was then stained 1:1 with Trypan Blue (Sigma-Aldrich, UK) and transferred to a haemocytometer to calculate the number of cells per ml in solution. Continued culture was achieved by splitting ARPE-19 cells 1:3 into sterile 25cm^2 flasks containing 5ml growth medium.

2.1.3 Plate coating

Extracellular matrix proteins are used to coat culture vessels to provide an attachment framework and to facilitate cell attachment. Lyophilised fibronectin (Sigma Aldrich, UK) was prepared to a final working concentration of 50µg/ml in double distilled water (ddH_2O), and was applied to the apical surface of Transwell® inserts and Ibidi µ-slides according to the volumes detailed in Table 2. Plates were partially covered and allowed to dry overnight in laminar flow hoods. The following day, the remaining fibronectin was aspirated from plates, which were subsequently washed thrice with 1xPBS prior to cell seeding. Reconstituted fibronectin was thawed at 4^{o}C overnight prior to plate coating to prevent irreversible precipitation.

Table 2: Cell culture coating and washing volumes

Recommended coating volumes and wash volumes for the coating of cell culture surfaces. Volumes and growth surface area were taken directly from the manufacturer's protocol.

Culture surface	Growth Surface Area (cm^2)	Coating Volume (ml)	Wash Volume (ml)
24mm Corning® Transwell® Permeable Support	4.67	0.6	1
12mm Corning® Transwell® Permeable Support	1.12	0.25	0.4
8-well Ibidi glass bottom µ-slide	1.0	0.3	0.3
6-well plate	9.5	1	2

2.1.4 Cell seeding

Following cell passage, P23-26 ARPE-19 cells were seeded on to fibronectin coated culture surfaces at the seeding densities listed in Table 3. For Transwell® inserts and 6-well plates, cells were left undisturbed for 4 days to facilitate adhesion prior to media change. For colocalisation studies, ARPE-19 cells were allowed to adhere for at least 2 days prior to use in experiments.

Table 3: Cell seeding densities

Details of the specific culture vessels used in the culture of ARPE-19 cells along with their corresponding recommended seeding densities. Abbreviations: PET, Polyethylene terephthalate.

Culture Vessel	Seeding Density (Cells/Well)
Corning® 24mm, 0.4mm pore, PET Transwell® Permeable Support	$5x10^4$
Corning® 12mm Transwell® Permeable Support	$1.25x10^4$
8-well Ibidi glass bottom μ-slide	$1x10^4$
6-well plate	$1x10^5$

2.1.5 Freezing and thawing of ARPE-19 cells

ARPE-19 cells were periodically expanded and frozen throughout the duration of the project to maintain stocks. Cells were detached from culture flasks (Section 2.1.4) and were resuspended in freezing medium comprising 75% complete culture medium and 25% dimethylsulfoxide (DMSO, Sigma-Aldrich, UK), to a density of $1x10^6$ cells/ml. A 1ml volume of the resultant cell suspension was transferred to a cryo-vial and frozen in a Mr. Frosty™ freezing container (ThermoFisher Scientific, UK) containing 100% isopropanol at -80°C overnight. The following day cells were transferred to liquid nitrogen for long term storage at -195.8°C.

Thawing of ARPE-19 cell stocks was achieved by rapid warming of cryo-vials in a 37°C water bath, drop wise addition of pre-equilibrated culture medium to prevent osmotic shock, and transfer to a $25cm^2$ flask containing 5ml complete culture medium.

2.2 Trans-epithelial Electrical Resistance Measurements

Trans-Epithelial Electrical Resistance (TEER) of ARPE-19 cultures was measured as an indicator of barrier integrity/polarisation using an EVOM2 epithelial voltohmmeter and 4mm STX2 chopstick electrode (EVOM2; World Precision Instruments Inc., Sarasota, FL, USA) according to the manufacturer's instructions. The electrode was sterilised in 70% ethanol, rinsed in ddH_2O and equilibrated in pre-warmed culture medium before being simultaneously introduced into both chambers. Five measurements were recorded for each well, from which an average experimental value was calculated. TEER measurements were taken from at least three inserts containing plated cells every week for the duration of the experiment. The reference value from a fibronectin-coated Transwell® insert without cells was subtracted from the average experimental value to give net TEER measurements. Net TEER measurements were subsequently corrected for the effective growth area of the Transwell® insert using Equation 1.

$$Final\ TEER\ (\Omega.cm^2) = Net\ TEER\ (\Omega) \times\ Area\ of\ Transwell\ Filter\ (cm^2) \quad \text{Equation 1}$$

All measurements were performed at ambient temperature within 6 minutes after removal from the incubator and were conducted over a period of 11 weeks. A full media change was also performed after each measurement to minimise potential contamination.

2.3 Enzyme Linked Immunosorbent Assay (ELISA)

2.3.1 Vascular Endothelial Growth Factor ELISA

Secreted levels of human VEGF were quantified using the Novex® human VEGF solid-phase sandwich Enzyme Linked Immunosorbant Assay (ELISA) (Life technologies, UK) according to the manufacturer's instructions. Conditioned media harvested from apical and basal compartments of 2 month ARPE-19 cultures (n=3) was diluted 1:1 in the standard diluent buffer prior to use. In brief, 100μl of known VEGF standards were applied to appropriate wells of a microtitre plate, precoated with capture antibody, and containing 50μl of incubation buffer. 50μl volumes of sample and control were also loaded in triplicate into allocated wells, to which 50μl incubation buffer and 50μl standard diluent buffer had been added, and plates were incubated for 2 hours. Plates were subsequently washed four times with 1X Wash Buffer and 100μl detector antibody was applied to wells for 1 hour, before plates were washed as previously and 100μl of detection enzyme was added to wells for 30 minutes. The final four washes were followed by the addition of 100μl of Stabilised Chromogen to each well, and incubation in the dark for 1 hour. Finally, 100μl of Stop Solution was added to each well. In the case of the chromagen blank, the detector antibody and detection enzyme was excluded from wells. Unless otherwise stated all incubation was performed at room temperature and three technical replicates were performed for each sample.

A microtitre plate reader (FLUOstar Optima; BMG LABTECH,UK) was used within 1-2 hrs after addition of substrate to obtain optical densities at 405nm, taking into account the wavelength correction at 570nm. Data was analysed in Microsoft Excel. Details regarding detection components employed can be seen in Table 4.

Table 4: Detection components of Novex® Human VEGF ELISA

Detection components included within the Novex® Human VEGF ELISA used to quantify VEGF levels within conditioned cell culture medium. Abbreviations: HRP, Horseradish Peroxidase; VEGF, Vascular Endothelial Growth Factor.

Detection Component	Details
Capture Antibody	Polyclonal anti-human VEGF 165
Detector Antibody	Monoclonal anti-human VEGF Biotin Conjugate
Detection Enzyme	Streptavidin-HRP
Stabilized Chromagen	Tetramethylbenzidine (TMB)
Stop Solution	Sulphuric Acid

2.3.2 Pigment Epithelial Derived Growth Factor ELISA

Secreted levels of human PEDF were quantified using a human PEDF solid-phase sandwich ELISA (BioVendor, Germany). Conditioned apical and basal media collected from 2 month ARPE-19 cell cultures grown on Transwell® inserts (n=3) was diluted 1:9 in dilution buffer prior to use in the assay. 100µl of known PEDF standards, quality controls, samples and dilution buffer (blank) were applied to allocated wells of a microtitre plate precoated with capture antibody and were incubated for 1 hour on an orbital shaker (ca. 300rpm). Following incubation wells were washed five times with Wash Solution, before 100µl of detector antibody was applied to wells and incubated as previously. Washing was repeated and 100µl detection enzyme was added to wells and incubated as before. A final five washes with Wash Solution was conducted before addition of 100µl Substrate Solution to each well for 5 minutes proceeded by the addition of 100µl Stop Solution. All incubations were performed at room temperature and three technical replicates were performed for each sample. Optical densities were determined by measuring the absorbance at 450nm with a microtitre plate reader (FLUOstar Optima; BMG LABTECH, UK), taking into account the 570nm wavelength correction. Absorbance was measured within 5 minutes of Stop Solution addition and data was analysed in Microsoft Excel. Details regarding detection components employed can be seen in Table 5.

Table 5: Detection components of the BioVendor Human PEDF ELISA.

Detection components included within the BioVendor PEDF ELISA used to quantify PEDF levels within conditioned cell culture medium. Abbreviations: PEDF, Pigment Epithelium Derived Factor; HRP, Horseradish Peroxidase.

Detection Component	Details
Capture Antibody	Polyclonal anti-human PEDF
Detector Antibody	Biotinylated polyclonal anti-human PEDF
Detection Enzyme	Streptavidin-HRP
Stabilized Chromagen	Tetramethylbenzidine (TMB)
Substrate Solution	Sulphuric Acid

2.3.3 $A\beta_{1-x}$ ELISA

The level of total Aβ ($A\beta_{1-28}$, $A\beta_{1-40}$, $A\beta_{1-42}$) secreted by ARPE-19 cells was quantified using a Human $A\beta_{1-x}$ solid-phase sandwich ELISA (IBL, Japan) according to the manufacturer's protocol. Conditioned apical and basal media collected from 2 month ARPE-19 cell cultures grown on Transwell® inserts (n=3) was diluted 1:3 in EIA buffer (1%BSA, 0.05% Tween 20 in PBS) prior to use in the assay. 100µl of

sample, controls and known $A\beta_{1-40}$ standards were applied to appropriate wells of a microtitre plate precoated with capture antibody and were incubated at 4°C overnight. Following incubation, plates were washed eight times in Wash Buffer, before 100µl of labelled antibody solution was added to wells for 1 hour at 4°C. Wells were washed an additional nine times and 100µl of Chromogen was added to wells for 30 minutes in the dark at room temperature. A total of three technical replicates were performed for each sample. Finally 100µl of stop solution was added to wells and the optical density at 450nm was determined with a microtitre plate reader (FLUOstar Optima;BMG LABTECH, UK) taking into account the 570nm wavelength correction. Data was analysed in Microsoft Excel. Details regarding detection components employed can be seen in Table 6.

Table 6: Detection components of the IBL Human Aβ1-x ELISA

Details of the specific detection components included within the IBL Human Aβ1-x ELISA used to quantify total Aβ levels within conditioned cell culture medium and human vitreous samples. Abbreviations: HRP, Horseradish Peroxidase.

Detection Component	Details
Capture Antibody	Mouse IgG monoclonal anti-human Aβ (N)(82E1)
Labelled Antibody	HRP conjugated mouse IgG monoclonal anti-human Aβ (11-28)
Stabilized Chromagen	Tetramethylbenzidine (TMB)
Substrate Solution	Sulphuric Acid

2.3.3.1.1 Linearity of Dilution and Spike Recovery of vitreous samples

Vitreous samples were diluted 1:7 for Spike Recovery (SR), to ensure spiked samples fell within the range of the standard curve. Known concentrations of $A\beta_{1-40}$ corresponding to low spike (30pg/ml), medium spike (62.5pg/ml) and high spike (125pg/ml) were added to samples and were directly compared to Standard Diluent (SD) spiked in parallel. Linearity of Dilution (LoD) was performed by diluting vitreous biopsies 1:2, 1:4, 1:6, 1:8, 1:25 and 1:50 in standard diluent. Samples prepared for SR and LoD were run simultaneously on an $A\beta_{1-x}$ ELISA as per the previously stated manufacturer's instructions, and were performed on three independent samples to assess matrix effects and kit accuracy respectively. All quantification was performed in Microsoft Excel from standard curves run in parallel.

2.4 Preparation of $A\beta_{1-42}$

This method has been described previously[176 247] and was established at the University of Southampton during the duration of this project as a result of a

collaboration with Professor Louise Serpell, an Aβ structural expert from the University of Sussex.

Oligomeric $A\beta_{1-42}$ was prepared by solubilizing lyophilised $A\beta_{1-42}$ 1,1,1,3,3,3-hexafluoro-2-propanol (HFIP) purchased from rPeptide (Bogust, GA, USA) at 1mg/ml in HFIP (Sigma-Aldrich, UK). The mixture was vortexed vigorously for 60 seconds and sonicated in a 50Hz FS100 Frequency Sweep bath sonicator (Decon, UK) for 5 minutes. Dry nitrogen was then passed over the vial and the resultant peptidic film was vacuum desiccated for 30 minutes to remove residual resuspension solvent. Dimethyl sulfoxide (DMSO; ACROS Organics, US) was subsequently used to resuspend the $A\beta_{1-42}$ peptide to a concentration of 1mg/ml. The Aβ peptide in DMSO was vortexed and allowed to stand for 1 minute before being added to a 2ml, 7K Zeba buffer exchange spin column (Thermo Scientific, UK) equilibrated with Aβ buffer, followed by 40μl of Aβ buffer stacker. Constituents of the Aβ buffer are detailed in Table 7. Columns were then centrifuged at 1000g for 2 minutes in a 4°C controlled centrifuge. Finally, the eluted peptide in Aβ buffer was collected and centrifuged at 16,000g for 30 minutes in a 4°C controlled Eppendorf 5415R micro-centrifuge (Eppendorf, UK) to remove pre-formed fibrillar aggregates and the supernatant was transferred to a LoBind Eppendorf microcentrifuge tube (Sigma Aldrich, UK) and kept at 4°C until further use to minimise the formation of fibrils. Concentrations of soluble Aβ were determined by measuring the absorbance at 280nm using a ND-1000 Nanodrop spectrophotometer (Nanodrop Technologies, Wilmington, DE, USA) and using the molar extinction co-efficient of Aβ of 1490 $M^{-1}.cm^{-1}$. Alexa Fluor®-tagged $A\beta_{1-42}$ was prepared as previously described. However prior to loading of $A\beta_{1-42}$ in DMSO to Zeba Columns, 20μl of 1M sodium bicarbonate and 10μl of 11.3nm/μl dye dissolved in ddH_2O were added to $A\beta_{1-42}$ in DMSO, pipette mixed and incubated for 15 mins at room temperature. The resultant tagged peptide was then added to the column and the protocol was followed as detailed above. Concentrations of Alexa Fluor® 488-tagged $A\beta_{1-42}$ and Alexa Fluor® 647-tagged $A\beta_{1-42}$ were determined as above taking into account the respective Alexa Flour® contributions to 280nm absorbance as stated in the manufacturer's protocol. Preparations were incubated on ice for 1.5 hours prior to application to ensure the highest concentration of $A\beta_{1-42}$ oligomers. $A\beta_{1-42}$ samples exhibit variability in measured concentration, which may affect the kinetics of oligomerisation. To exercise control over this parameter an inclusion criterion of Aβ sample concentrations of 50-130μM was adopted. Working concentrations were achieved by diluting peptide stocks directly into ARPE-19 cell culture media.

Table 7: Composition of Aβ Buffer

Displays the constituents along with their respective concentrations added to prepare the Aβ buffer (vehicle). Buffer was typically prepared in 50ml volumes with MilliQ H_2O, adjusted to pH 7.4 and passed through a 22µm filter to maintain sterility prior to use. Aβ buffer was applied to control wells in all experiments as vehicle/sham.

Constituent	Concentration (mM)
HEPES	10
NaCl	50
KCl	1.6
$MgCl_2.6H_2O$	2
$CaCl_2.6H_2O$	3.5

2.5 Limulus Amebocyte Lysate (LAL) endotoxin test

Levels of bacterial endotoxin within Aβ preparations were measured using a Limulus Amebocyte Lysate (LAL) Endosafe® PTS cartridge (Charles River Laboratories Inc., US) capable of detecting endotoxin levels of 0.05–5 endotoxin units/ml. Prior to use, it was first checked that the lot of LAL test cartridges employed met quality control testing requirements for an archived standard curve, negative controls and positive product control results. Cartridges were allowed to warm to room temperature before being placed into an Endosafe® PTS unit (Charles River Laboratories Inc., US) precalibrated to 37°C. Using pyrogen free sterile pipette tips, 25µl of $A\beta_{1-42}$ preparation or vehicle/sham was loaded into each of the four lanes of the cartridge. Machine readings for endotoxin units per ml and percentage recovery were recorded where a percentage recovery of 50-200 was considered a valid test.

2.6 Fluorescence microscopy

2.6.1 Immunofluorescence staining of ARPE-19 cells.

ARPE-19 cultures were washed in 1X HBSS (Life Technologies, UK) and fixed in ice-cold PBS containing 4% paraformaldehyde (Sigma Aldrich, UK) for 30 minutes at 4°C. Following fixation, cells were washed thrice in 1X PBS and blocked in 5% Normal Goat Serum (NGS) in 0.1% PBST for 1 hour to prevent non-specific binding.

Addition of primary antibody solution, as shown in Table 9, at 4°C overnight allowed detection of the target protein where secondary antibody controls were incubated with blocking solution alone. Cells were then washed thrice in 0.05% PBST and incubated with the appropriate Alexa Fluor® labelled secondary antibody prepared in 0.05% PBST for 1 hour, as detailed in Table 10. Three washes in 1X PBS and one wash in ddH_2O proceeded secondary antibody incubation. 1μg/ml 4', 6'-diamino-2-phenylindole (DAPI) was then applied for 10 minutes to stain nuclei and finally cells were washed thrice in ddH_2O before Transwells® were mounted between two glass coverslips with Mowiol® mounting medium containing Citifluor antifadant, and stored at 4°C. The recipe for the Mowiol® mounting medium employed is detailed in Table 8. Unless otherwise stated, all incubations were performed at room temperature. Images were obtained using either a Leica SP5 or Leica SP8 laser-scanning confocal microscope (Leica Microsystems, UK). Minor amendments to the above protocol were made in the case of specific primary antibodies. These are detailed where appropriate in the methods section of the corresponding results chapter.

Table 8: Preparation of Mowiol® mounting medium

Details regarding the preparation of Mowiol® mounting medium employed in immunofluorescence studies. In brief, PBS and Mowiol® 4-88 were heated to 60°C and glycerol was added and stirred. This mixture was then cooled to room temperature before the addition of Citifluor antifade and centrifugation at 3,500RPM for 30 minutes to pellet undissolved Mowiol®. Weights and volumes of each constituent added are listed along with the supplier from which products were purchased. Mowiol® stock solutions were prepared by Dr David Johnston (Biomedical Imaging Unit, University of Southampton) and were collected as 1.5ml frozen aliquots.

Constituent	Weight/Volume	Supplier
Mowiol 4-88®	20g	Harlow Chemical Company Ltd., UK
1x PBS (pH 7.4)	80ml	Sigma Aldrich, UK
Glycerol	40ml	British Drug House, UK
AF3 Citifluor antifade, PBS base	2.4ml	Agar Scientific, Stanstead, UK

Table 9: Primary antibodies used in immunofluorescence studies.

Details of the primary antibodies used for fluorescence microscopy. Antibodies were diluted in 5% Normal Goat Serum in 0.1% PBST to the ratios detailed in the right hand column. Ig: Immunoglobulins, mAb: Monoclonal antibody, pAb: Polyclonal antibody.

Product Name	Target	Company	Catalogue Number	Clone/Isotype	Species	Reactivity	Dilution
ZO-1 antibody	Mid-region of early junctional complex ZO-1	Invitrogen	40-2200	IgG, pAb	Rabbit	Human, Mouse, Rat, Dog	1:100
Occludin antibody	1-150 C-terminal residues of mid-late tight junction protein occludin	Invitrogen	71-1500	IgG, pAb	Rabbit	Dog, Rat, Human	1:100
Anti-RPE65 antibody	RPE microsomal membrane fraction RPE-65	abcam	ab78036	IgG1, mAb	Mouse	Mouse, Rat, Chicken, Cow, Human, Xenopis laevis, Monkey	1:100
Anti-alpha 1 Sodium Potassium ATPase antibody	α1-subunit of Na^+/K^+ ATPase	abcam	ab7671	IgG1 Kappa, mAb	Mouse	Mouse, Rat, Sheep, Rabbit, Dog, Human, Pig, Xenopus laevis, Monkey	1:100
Anti-human Amyloid β (N) (82E1) antibody	N-terminal residues 1-16 (DAEFRHDSGYEVHHQK) of human Aβ	IBL	10323	82E1, IgG1, mAb	Mouse	Human	1:100
Anti-LAMP-1antibody	Lysosomal-associated membrane protein 1 (LAMP-1)	abcam	ab24170	IgG, pAb	Rabbit	Mouse, Rat, Chicken, Hamster, Cat, Dog, Human, Xenopus laevis, Zebrafish, African green monkey	1:1000
Anti-Rhodopsin [RET-P1] antibody	Rod photoreceptor specific light sensitive receptor protein, Rhodopsin	abcam	ab3267	IgG1,mAb	Mouse	Mouse, Rat, Cow, Human	1:100

Table 10: Secondary antibodies used in immunofluorescence studies.

Details of the secondary antibodies used for fluorescence microscopy. Antibodies were diluted in 0.05% PBST to the ratios detailed in the right hand column. Ig: Immunoglobulins, pAb: Polyclonal antibody.

Product Name	Company	Catalogue Number	Antibody Form	Clone/Isotype	Species	Reactivity	Dilution
Alexa Fluor® 546	Life Technologies	A11071	F(ab')2 Fragment	IgG, pAb	Goat	Rabbit	1:200
Alexa Fluor®546	Life Technologies	A11018	F(ab')2 Fragment	IgG, pAb	Goat	Mouse	1:200
Alexa Fluor®594	Life Technologies	A11072	F(ab')2 Fragment	IgG, pAb	Goat	Rabbit	1:200
Alexa Fluor®594	Life Technologies	A11020	F(ab')2 Fragment	IgG, pAb	Goat	Mouse	1:200
Alexa Fluor®488	Life Technologies	A11070	F(ab')2 Fragment	IgG, pAb	Goat	Rabbit	1:200
Alexa Fluor®488	Life Technologies	A10684	F(ab')2 Fragment	IgG, pAb	Goat	Mouse	1:200

Table 11: Staining reagents used in immunofluorescence studies

Details of the staining reagents used during immunofluorescence experiments. DAPI was reconstituted to 1mg/ml in 1x PBS to form stock solutions. Abbreviations: DAPI: 4', 6'-diamino-2-phenylindole

Product Name	Catalogue Number	Company	Dilution
DAPI	D9542	Sigma Aldrich, UK	1:1000

2.6.2 Lysosomal imaging for colocalisation assessment

2.6.2.1 Endo-lysosomal indicator: LysoSensor Yellow/Blue DND-160

The lysosomal probe LysoSensor Yellow/Blue DND-160 (PDMPO; ThermoFisher Scientific, UK) was used for colocalisation assessment with late endosomes/lysosomes in this study. PDMPO comprises a fluorophore that is quenched at neutral pH as a result of photoinduced electron transfer by a weak-base side chain[248]. It exhibits high selectivity for acidic organelles as a result of partial protonation[248]. Accumulation within lysosomes and subsequent protonation results in a conformational change in the previously occluding basic side chain, which leads to unquenched fluorescence that may be detected by fluorescence microscopy[248]. Unlike the LysoTracker probes, PDMPO demonstrates dual emission fluorescing yellow in acidic environments and blue in more alkaline environments[248], thus facilitating the ratiometric imaging of pH within lysosomes. This property of PDMPO was not exploited for the purpose of this project due to laser constraints and thus only late-endosomes and lysosomes with pH 3.0 were detected. The excitation and emission spectra for PDMPO is shown in Figure 15.

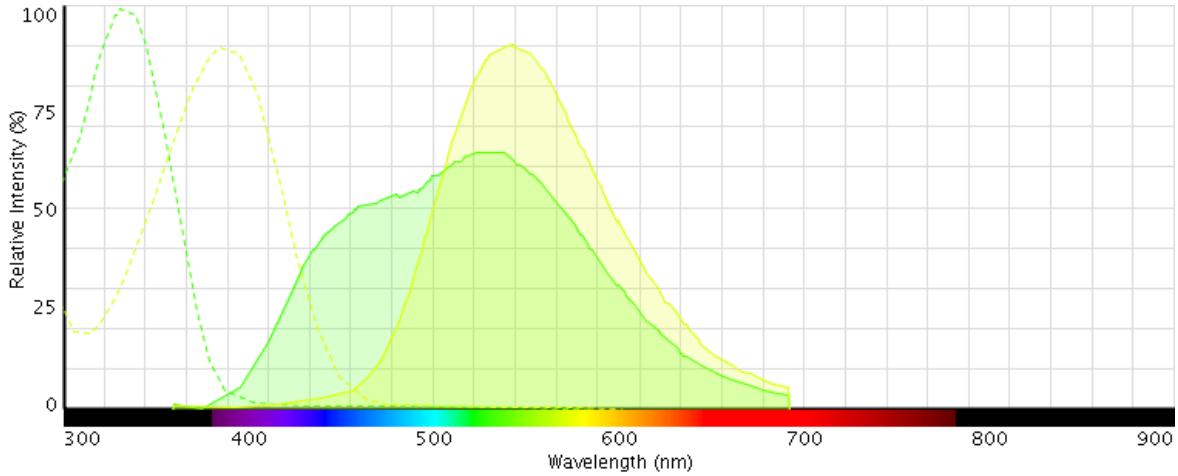

Figure 15: Fluorescence excitation and emission spectra of LysoSensor DND-160.

Green shows the spectral characteristics of less acidic compartments (pH 9.0) whereas yellow shows that of acidic lysosomes (pH 3.0). Excitation and emission spectra are indicated as dotted lines and solid lines respectively.

2.6.2.2 Optimisation of LysoSensor Yellow/Blue DND-160 for colocalisation studies

Guidelines for the working concentrations of PDMPO are provided in the manufacturer's instructions. However, staining conditions vary considerably with the specific cell type employed, where overloading causes non-specific labelling of additional structural components and PDMPO induces lysosomal alkalinisation following prolonged exposure[248]. Thus, careful optimisation is required prior to use. As such, fresh culture medium containing 1μM, 5μM or 10μM PDMPO was applied to ARPE-19 cultures grown on Ibidi glass bottom μ-slides to determine the optimal working concentration. In all instances cultures were incubated with PDMPO for 5 minutes. The results of the optimisation procedure can be seen in Figure 16.

2.6.2.3 LysoSensor Yellow/Blue DND-160 loading

Where possible PDMPO concentration should be kept to a minimum to avoid potential artefacts[248]. Therefore a 5μM working concentration was employed in experiments. PDMPO stock concentration was diluted ARPE-19 culture medium to 5μM and 300μl was incubated with cells for 5 minutes at 37°C in the dark. Following incubation, cells were washed briefly in prewarmed culture medium and were imaged immediately as described in Section 2.6.2.4.

2.6.2.4 Data acquisition

Z-stacks were obtained from duplicate random fields of view at x63 magnification across three wells using a Leica SP5 laser-scanning confocal microscope. Lasers and wavelengths used to excite and detect fluorophores are detailed in Table 12**.** Images were acquired in quick succession to minimise potential lysosomal alkalinisation following prolonged exposure. Typical acquisition times were 12 minutes per image. Sequential imaging of probes was performed to prevent potential bleed through interfering with colocalisation analysis and images were subsequently analysed in the Volocity software suite (PerkinElmer, UK) according to Section 2.12.1.

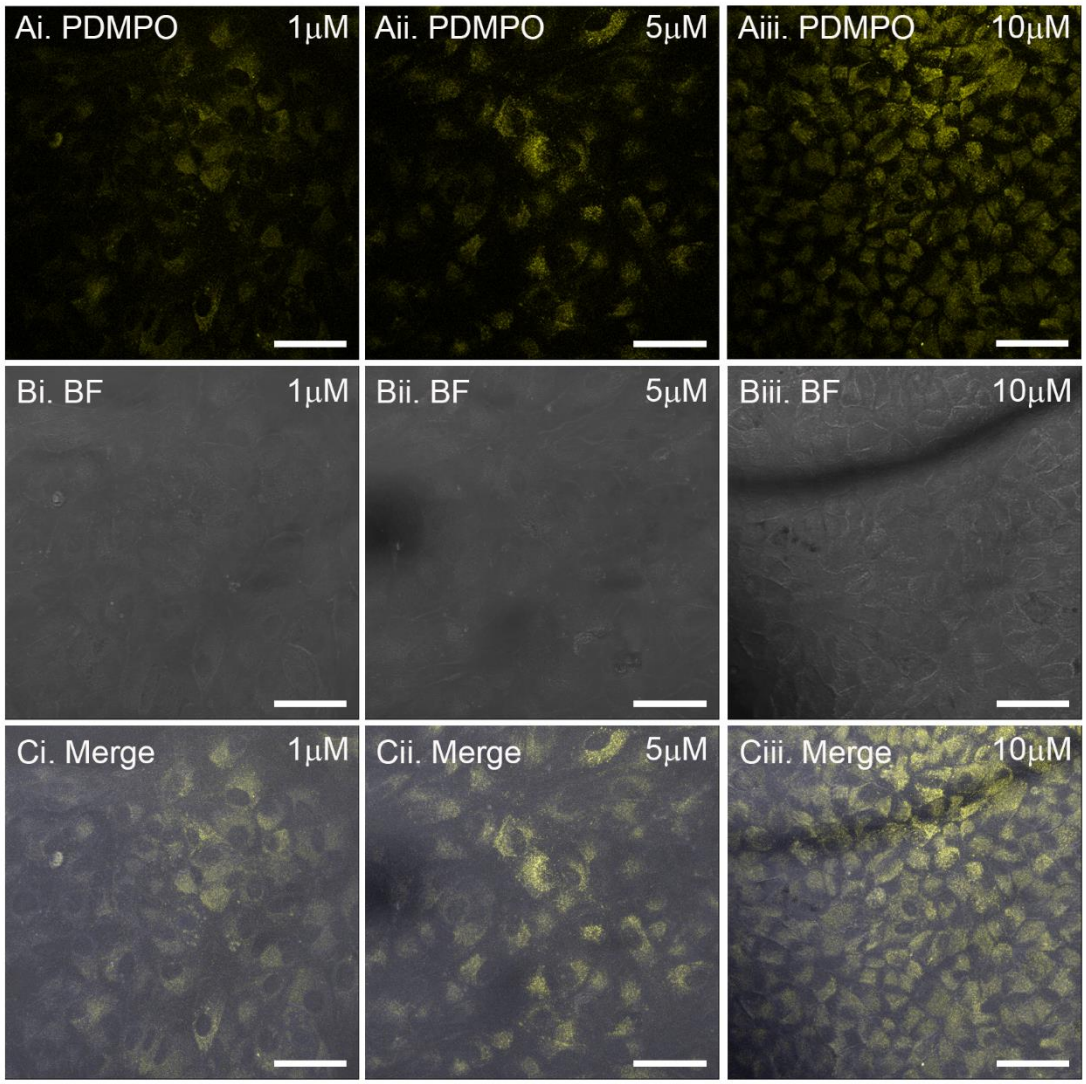

Figure 16: Optimisation of LysoSensor Yellow/Blue DND-160 in ARPE-19 cells.

Ai-Aiii. Fluorescence images showing the concentrations of LysoSensor Yellow/Blue DND-160 (PDMPO) tested within the ARPE-19 cell line. Identification of an optimal working concentration was required prior to the use of the probe in experiments to eliminate artefacts and prevent lysosomal alkalinisation. **Bi-iii.** ARPE-19 cells visualised under bright field (BF) settings to assess cell health upon application of the corresponding concentration of PDMPO in panel A, and therefore eliminate concentrations that exhibit cellular toxicity. **Ci-iii.** Merged fluorescence images showing the distribution pattern of PDMPO within the ARPE-19 cell line. At 5μM and 10μM, the probe efficiently and reliably stains endocytic compartments of ARPE-19 cells, but at 1μM yields a relatively weak fluorescence signal. Of note, the concentrations tested do not appear to affect ARPE-19 cell health. Images were acquired with a x63 objective where scale bars correspond to 50μM.

Table 12: Confocal laser configurations used for imaging LysoSensor Yellow/Blue DND-160 and the $A\beta_{1-42}$ Alexa Fluor® 488 conjugate.

Details of the laser configuration, excitation wavelength and emission bandwidth used during confocal fluorescence microscopy to assess colocalisation, along with the corresponding fluorophore each was used to visualise. Each fluorophore was imaged sequentially to avoid bleed through. The excitation wavelength reflected by the dichroic mirror ensures that the fluorophore is excited by only light of the correct wavelength whereas the emission bandwidth ensures that only emitted light of the specified wavelengths passes through the pinhole of the detector.

Fluorophore	Laser	Excitation Wavelength (λ)	Emission bandwidth (nm)
$A\beta_{1-42}$ Alexa Fluor® 488 conjugate	UV	405	469-671
LysoSensor Yellow/Blue DND-160 (PDMPO)	Argon	488	502-576

2.6.3 Functional assessment of lysosomal acid hydrolases

2.6.3.1 Cathepsin B activity indicator: Magic Red™

The Cathepsin B activity indicator Magic Red® (ImmunocytoChemistry Technologies, USA) was employed to assess responses in lysosomal acid hydrolase activity following $A\beta_{1-42}$ insult. This indicator employs Cresyl violet chemistry. Upon addition, Cresyl violet is bi-substituted to two Cathepsin B target sequences, specifically arginine-arginine (RR) , which quenches the fluorescence signal emitted at 550-590nm[249]. Cleavage of either one or both dipeptide Cathepsin B target sites results in a fluorescence signal, the intensity of which correlates with the cellular activity of Cathepsin B. A schematic of the mechanism of action of Magic Red® is shown in Figure 17.

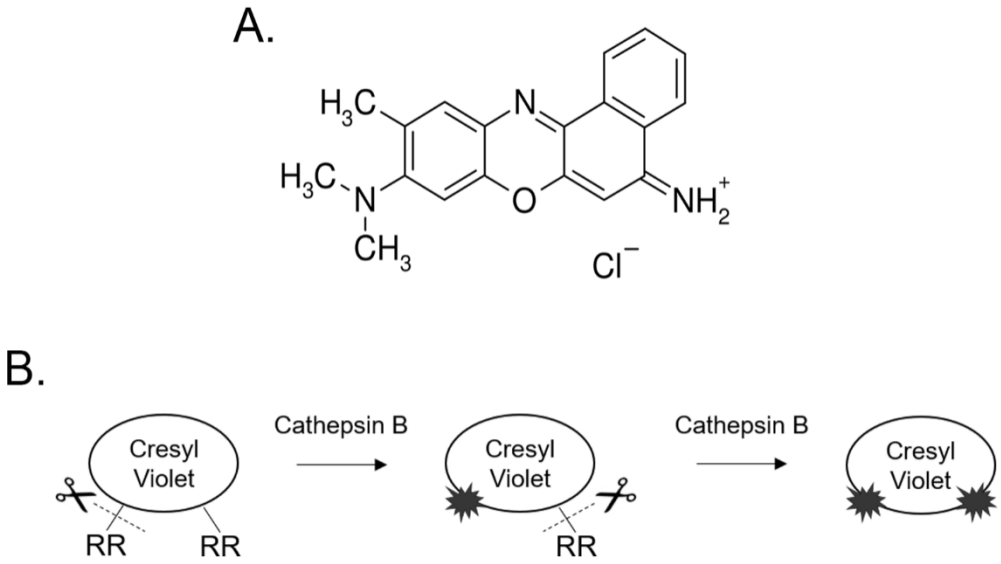

Figure 17: Characteristics and mechanism of Magic Red®.

A. Chemical structure of unsubstituted Cresyl Violet employed in the Magic Red® kit to measure the level of cellular Cathepsin B activity when excited at 550-590nm. **B.** Schematic of the principle underpinning the Magic Red® probe. Bi-substituted Cresyl Violet fluorescence is unquenched upon cleavage at one or both arginine-arginine (RR) amide linkage sites by the lysosomal cysteine protease, Cathepsin B. The mono-substituted and unsubstituted Cresyl Violet fluorophores exhibit fluorescence when excited at 550-590nm providing an indication of the level of Cathepsin B activity, where increased fluorescence intensity corresponds to increased Cathepsin B activity[249]. Image adapted from PubChem Compound record for Cresyl Violet. PubChem identifier: CID 29092, URL: https://pubchem.ncbi.nlm.nih.gov/compound/Cresyl_violet#section=Top.

2.6.3.2 Optimisation of Magic Red™ labelling for acid hydrolase activity studies

A general guideline advising 30-60 minute incubation with Magic Red® is detailed in the manufacturer's protocol[249] but incubation durations should be optimised for specific cell types. Therefore, ARPE-19 cells were cultured on Ibidi glass bottom μ-slides for three days (~80% confluence) prior to application of Magic Red® staining solution for 30, 45 and 60 minutes to determine an optimal incubation time (Figure 18). Preparation and loading of Magic Red® staining solution is described in Section 2.6.3.3.

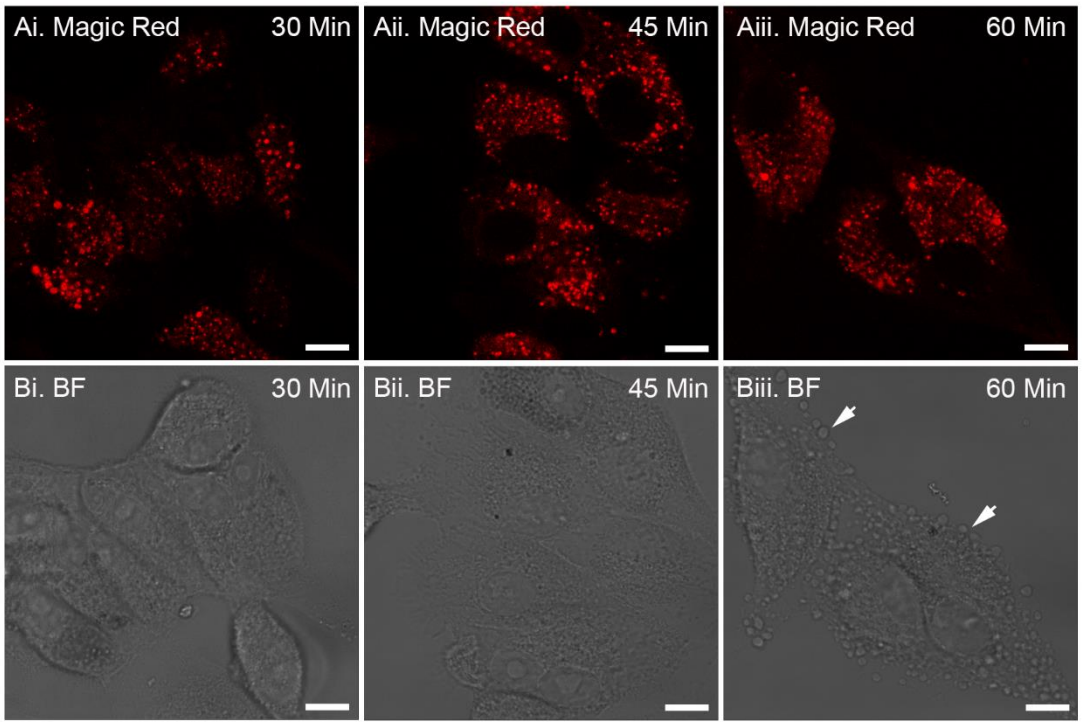

Figure 18: Optimisation of Magic Red® within the ARPE-19 cell line.

Ai-iii. Confocal fluorescence images showing the incubation periods tested with the Magic Red® Cathepsin B substrate in the ARPE-19 cell line. Identification of an optimal concentration was required prior to use of the substrate so that Cathepsin levels could be reliably detected without exerting toxicity. **Bi-iii.** Bright field images of ARPE-19 cells acquired to assess Magic Red® effects on cell health. The fluorescence signal generated upon excitation at 550nm appeared sufficiently bright at all time points tested. However, bright field images revealed that after 60 minutes of incubation, cells appeared unhealthy, where blebbing (white arrows) and in some instances cell detachment was observed. Images were acquired with at x63 where the scale bar corresponds to 10μM.

2.6.3.3 Magic Red™ loading

Magic Red® stock was reconstituted with DMSO to a 260x stock solution and stored at -20°C. Stock solution was diluted 1:10 in diH_2O to yield a 26x staining solution immediately prior to application to prevent substrate hydrolysis. Sufficient staining solution for all wells was prepared by dilution of staining solution in culture medium at 1:24 and solutions were mixed. Finally, 300μl of working solution was applied to wells for 30 minutes at 37°C, working solution was removed, cells were washed thrice in prewarmed culture medium and imaging was performed immediately as described in Section 2.6.3.4. An identical concentration of DMSO diluted initially in diH2O, and subsequently in prewarmed culture medium was applied to control wells.

2.6.3.4 Data acquisition

Images were acquired from 10 random fields of view at x63 magnification across a single optical plane, and over 3 independent experiments using a Leica SP8 laser-

scanning confocal microscope. Lasers and wavelengths used to excite and detect fluorophores are detailed in Table 13**.** As with PDMPO, images were acquired in quick succession to minimise predicted aggregation of the fluorescence product within lysosomes. Images were acquired every 30 seconds. A single z-stack series was also acquired following imaging of experimental conditions to demonstrate internalisation of Alexa Fluor® 488 conjugated $A\beta_{1-42}$. As before, sequential imaging of probes was performed to prevent potential bleed through that interferes with colocalisation analysis. Data pertaining to Magic Red® Cathepsin B activity is presented as mean fluorescence intensity above a threshold value determined as described in Section 2.12.2. In the case of colocalisation analysis, images were analysed in Volocity (PerkinElmer, UK) using the Costes *et al.* algorithm.

Table 13: Confocal fluorescence microscopy laser configurations used for the imaging of Magic Red® Cathepsin B activity indicator and the $A\beta_{1-42}$ Alexa Fluor® 488 conjugate.

Details of the laser configurations and excitation/emission wavelengths used during confocal fluorescence microscopy along with the corresponding fluorophore each was used to visualise. The excitation wavelength reflected by the dichroic mirror ensures that the fluorophore is excited by only light of the correct wavelength whereas the emission wavelength ensures that only emitted light of the correct wavelength passes through the pinhole of the detector.

Fluorophore	Laser	Excitation Wavelength (λ)	Emission Wavelength (λ)
$A\beta_{1-42}$ Alexa Fluor® 488 conjugate	Argon	488	500-550
Magic Red® Cathepsin B Substrate	DPSS	561	600-700

2.7 Transmission Electron Microscopy (TEM)

2.7.1 Processing of Transwell® Inserts for TEM

Conditioned culture medium was removed from Transwell® inserts and cells were washed in 1X HBSS before being fixed for 1 hour in primary fixative containing 3% glutaraldehyde and 4% formaldehyde in 0.1M PIPES (pH 7.2). Inserts were then rinsed twice in 0.1M PIPES for 10 minutes and were post fixed in 1% osmium tetroxide in 0.1M PIPES for 1 hour. Following osmification, an additional two 10 minute rinses in 0.1M PIPES were performed, cells were briefly washed in ddH_2O and inserts were stained in 2% uranyl acetate for 20 minutes. Inserts were then dehydrated by passing samples through a battery of ethanol (30%, 50%, 70% and 95%) for 10 minutes each followed by two 20 minute incubations with absolute ethanol (100%). Finally, a 10 minute incubation in acetonitrile followed by overnight incubation in 1:1 acetonitrile:Spurr resin was performed. The following day inserts were transferred to Spurr resin (Agar Scientific, Stansted, UK) for 6 hours and were subsequently embedded in fresh resin and polymerised at 60°C for 24 hours. Semi-thin microtome sections were cut using a Reichert Ultracut E (Leica Microsystems, UK) and stained with 1% toluidine blue in 1% borax (Electron Technology, Stanstead, UK) for examination prior to cutting gold ultrathin sections. Ultrathin sections were collected on 200 mesh carbon and formvar coated copper grids and were stained with uranyl acetate. Examination of grids was performed with a Hitachi 7000 transmission electron microscope (Hitachi, Germany) fitted with a SIS Megaview III plate camera (EMSIS camera). All procedures were carried out at room temperature unless otherwise stated.

2.7.2 Immunogold labelling

20µl aliquots of $A\beta_{1-42}$ (Section 2.4) were prepared in LoBind Eppendorf microcentrifuge tubes, corresponding to 0, 1.5, 3, 24, 48 and 72 hours. At the appropriate time point 5µl of 4% formaldehyde in 0.1M PIPES buffer was applied to tubes and pipette mixed to prevent further aggregation of samples. After all time points had been collected, 5µl of sample was adsorbed onto 200 mesh formvar and coated carbon coated copper grids for 5 minutes and blotted dry. Grids were then washed in 0.1M phosphate buffer with 1% bovine serum albumin (BSA) for 5 minutes before being labelled with primary antibody. Following incubation with primary antibody, grids were washed three times for 1 minute each, and were incubated with gold-conjugated secondary antibody for 1 hour. Washing of grids

was repeated thrice for 1 minute each proceeded by one wash in distilled water and grids were again blotted dry. 5µl of negative stain consisting of 3% ammonium molybdate in 0.1M ammonium acetate buffer pH 7.0 and 1 grain of sucrose/ml were then applied for 10 seconds and grids were gently blotted dry. Finally, grids were allowed to air-dry prior to examination on a Hitachi H7000 microscope (Hitachi, Germany) fitted with a SIS Megaview III plate camera (EMSIS camera) to assess the aggregation state of $A\beta_{1-42}$ at each time point. All incubations were performed at room temperature. Details of antibodies used are detailed in Table 14.

Table 14: Antibodies employed in immunogold labelling for TEM.

Details of the primary (1^0) and secondary (2^0) antibodies used during immunogold labelling experiments of Aβ preparations. Primary and secondary antibody solutions were prepared in 0.1M phosphate buffer containing 1% bovine serum albumin. Abbreviations: Ig; Immunoglobulin, pAb; Polyclonal antibody, mAb; Monoclonal antibody, EM; electron microscopy, TEM; Transmission Electron Microscopy.

Product Name	Company	Catalogue Number	Clone/Isotype	Species	Reactivity	Dilution
Anti-human Amyloid β (N) (82E1) antibody	IBL, Japan	10323	IgG1, mAb	Mouse	Human	1:10
Immunogold conjugated EM goat anti-mouse (5nm)	Elektron Technology	R14009-1	IgG (H)	Goat	-	1:50

2.8 Quantitative Real-time Polymerase Chain Reaction (PCR)

2.8.1 Cell preparation

ARPE-19 cells seeded onto fibronectin coated 6-well plates (Section 2.1) were allowed to reach confluence prior to use in experiments. Cells were harvested from two independent wells per condition across three experiments.

2.8.2 RNA extraction

To determine the effect of $A\beta_{1-42}$ on Cathepsin B mRNA expression, total RNA was isolated from ARPE-19 cells at 0.5, 3, 24 and 48 hours following acute exposure as follows. Cells were rinsed briefly in 1x HBSS, homogenised in 500µl Trizol® reagent (ThermoFisher Scientific, UK), and transferred to 1.5ml RNAse/DNAse free Eppendorf's. Next, phase separation was achieved by the addition of 200µl of 1-bromo-3-chloropropane (Sigma Aldrich, UK) to cell homogenates, inversion (~10 times), incubation at room temperature for 2 minutes and centrifugation at 12,000g for 15 minutes. The resultant aqueous supernatants containing RNA were then transferred to Eppendorf's containing 2µl RNase-free glycogen (ThermoFisher Scientific, UK) following which 250µl of isopropanol (Sigma Aldrich, UK) was added to samples for 20 minutes, and samples were centrifuged at 12,000g for 10 minutes to facilitate the precipitation of RNA. Isolated RNA pellets were resuspended in 500µl 75% ethanol (Sigma Aldrich, UK) to remove contaminants and were pelleted at 12,000g for 10 minutes. Ethanol supernatants were aspirated and RNA pellets were left to air dry until clear to remove residual ethanol. Finally, RNA pellets were solubilized in 20µl RNAse free water and RNA yields were determined using a NanoDrop ND-1000. Unless otherwise stated all procedures were performed on ice and incubation and centrifugation were performed at 4°C to prevent RNA degradation. Extracted RNA was stored at -80°C awaiting cDNA synthesis. In all cases, benchtops and pipettes were cleaned with RNAse-Away (ThermoFisher Scientific, UK) prior to protocol commencement to prevent RNAse contamination of labware as well as DNA contamination.

2.8.3 Quantitation and quality assessment of RNA

Isolated RNA was quantified by measuring the nucleic acid absorbance of samples at 260nm and 280nm relative to the blank with a Nanodrop ND-1000

spectrophotometer. The 260nm/280nm and 260nm/230nm ratios were consulted as a measure of sample purity and to assess contamination with residual phenol, chaotropic salts, alcohol or protein. Typically, isolated RNA with a 260/280nm ratio of 1.8-2.2 and a 260nm/230nm ratio greater than 1.7 indicated high sample purity and was deemed suitable for use.

2.8.4 cDNA synthesis

Isolated RNA was transcribed into cDNA using the iScript cDNA synthesis kit (BioRad, UK). In brief, 1000ng RNA in RNAse-free water (Fisher Scientific, UK) was added to the iScript MasterMix (4μL 5x iScript reaction mix: 1μL iScript reverse transcriptase solution) at a ratio of 3:1. Typically 20μl reaction volumes were set up and samples were mixed and spun briefly prior to being transferred to a MJ Research Tetrad 2 thermal cycler (Bio-Rad, UK). cDNA synthesis was performed using the reaction conditions detailed in Table 15. Samples were stored at -20°C and were used within 1 month.

Table 15: cDNA synthesis Thermocycling Conditions.

Thermocycling conditions used during the reverse transcription of RNA to cDNA using the iScript cDNA synthesis kit (Biorad, UK).

Step	Temperature (°C)	Duration (Minutes)
Primer Annealing	25	5
DNA polymerization	42	30
Enzyme Deactivation	85	5
Hold	4	Indefinitely; until use

2.8.5 Primer design and specificity

All primers employed in QPCR experiments were designed using the Primer-BLAST web based software supplied by the National Centre for Biotechnology Information (NCBI). Primers were specifically designed to span exon-exon junctions to eliminate contaminating genomic DNA. Accession numbers for reference sequence details of specific target genes were inserted into the algorithm and returned primer pairs were assessed against design criteria. Typically candidate primers with an amplicon size of 70-300, a GC content of 45-50%, a self-complementarity score of <5, a 3' self-complementarity score of <5 and a melting temperature of ~60°C that is within <1°C of the complementary primer were deemed appropriate for use in the study. Primers were purchased at desalted purity with 0.025μM scale from Sigma Aldrich. The details of primers used here can be found in Table 16.

Table 16: Quantitative Real-Time PCR Primers

The sequences of both the forward (F) and reverse (R) primers used to amplify cDNA fragments in quantitative real-time PCR analysis. The corresponding gene is detailed along with primer guanidine and cytosine (GC) content, and expected amplicon length in base pairs (bp). Primers were designed using PrimerBlast (NCBI) against the listed accession number for each gene and to span exon-exon junctions. Abbreviations: CTSB; Homo sapiens cathepsin B ACTB; Homo sapiens actin beta, GAPDH; Homo sapiens glyceraldehyde-3-phosphate dehydrogenase, CYC1; Homo sapiens cytochrome c1, EIF4A2; Homo sapiens eukaryotic translation initiation factor 4A2.

Gene	Accession Number	Sequence (5'-3')	Tm (°C)	GC Content (%)	Amplicon Length (bp)
CTSB	NM_001908.4	F: GGGCCGGGAGGGTACTTA	60.0	66.7	145
		R: GATCCTAGATCCACCCAGCG	59.4	60.0	
ACTB	NM_001101.3	F: ACAGAGCCTCGCCTTTGCC	62.9	63.2	70
		R: GATATCATCATCCATGGTGAGCTGG	61.2	48.0	
GAPDH	NM_001289745.1	F:GAAGACGGGCGGAGAGAAAC	60.7	60.0	151
		R:CGACCAAATCCGTTGACTCC	58.9	55.0	
CYC1	NM_001916.4	F: TACGGACACCTCAGGCAGT	60.2	57.9	183
		R: CACGGTGAGACCACGGATAG	59.9	60.0	
EIF4A2	NM_001967.3	F: GGTCAGGGTCAAGTCGTGTT	59.9	55.0	136
		R: CCCCCTCTGCCAATTCTGTG	60.7	60.0	

2.8.6 Quantitative Real-Time PCR (QPCR)

Quantitative real-time PCR was performed on a CFX96 Real-Time PCR detection system (Bio-Rad, UK) using the SYBR Green method. PCR reactions were prepared as 20μl volumes on ice comprising; 0.6μl of 10μM forward primer, 0.6μl of 10μM reverse primer, 6.8μl UltraPure™ DNase/RNase-Free distilled water (Invitrogen, UK), 10μl iTaq Universal SYBR Green Supermix (Bio-Rad, UK) and 2μl of sample cDNA. PCR reactions were prepared on 96 well PCR plates, secured with PCR caps and spun briefly at 3,000rpm for 30 seconds before QPCR was run using the conditions detailed in Table 17.

Table 17: QPCR cycling conditions

The QPCR cycling parameters consisted of an initial denaturation step at 95°C for 10 minutes, followed by 49 cycles of denaturation at 95°C for 15 seconds and annealing at 60°C for 1 minute. Extension was subsequently performed at 72°C for 10 minutes followed by post-amplification melt curve analysis to assess reaction specificity and to check for primer-dimer artefacts. Upon completion samples were held at 4°C.

Step		Temperature (°C)	Duration	Cycles	Melt-Curve Analysis
Polymerase Activation & DNA Denaturation		95	10 Minutes	1	60-95°C, 0.5°C increment, 5 seconds/step
Annealing	Denaturation	95	15 Seconds	49	
	Annealing & Plate read	60	1 Minute		
Extension		72	10 Minutes	1	

Three technical replicates were run for each sample, for both Cathepsin B (CTSB) and the reference gene, and triplicate PCR reactions were performed for each experimental condition and time point from three independent experiments. Data was normalised to the mean of eukaryotic initiation factor 4A2 (EIF4A2) for each sample. Once complete, PCR products were resolved on a 1.2% agarose gel alongside a 100bp DNA ladder at 120V, 400mA for 40 minutes to confirm primer specificity according to Section 2.8.7. Relative quantification of samples was calculated in Excel along with fold change in expression of both $A\beta_{1-42}$ and vehicle treated cultures in relation to untreated samples.

2.8.7 Agarose gel electrophoresis

1.2% agarose gels were prepared by addition of 4μl GelRed (Cambridge Bioscience, UK) to 0.72g genetic analysis grade agarose (Fisher Scientific**,** UK), dissolved in 60ml 1x Tris/Borate/EDTA (TBE) buffer (Fisher Scientific, UK). These were then set in casting trays for approximately 20 minutes prior to use. Gel cassettes were inserted into a tank containing 1xTBE, and 10μl of PCR product combined with 1/6 volume 6x DNA loading dye (ThermoFisher, UK) was loaded into wells alongside 6μl 100bp DNA ladder (New England BioLabs Inc., UK). Products were resolved using a Basic PowerPac™ (Biorad, UK). Running conditions for each gel are detailed in the corresponding figure legend, however in most instances gels were resolved at 120v, 400mA for 45 minutes. Upon completion gels were imaged in a High Performance UV Transilluminator fitted with a Canon S2 IS PC1130 digital camera.

2.9 Photoreceptor Outer Segment preparation

2.9.1 Rod Photoreceptor Outer Segment isolation

Fresh porcine eyes were obtained from Upton's of Basset butchers (Southampton, UK) and POS were isolated immediately according to published procedures[250 251]. Upon receipt an incision was made proximate to the ora serata, the anterior segment of the eyeball was removed, and retinae were carefully extracted and pooled in KCl buffer (0.3M KCl, 10mM HEPES, 0.5mM $CaCl_2$, 1mM $MgCl_2$; pH 7.0) with 48% w/v sucrose. Isolated retinae were then subject to agitation for 2 minutes and centrifugation at 5000g for 5 minutes. The POS containing supernatant was subsequently aspirated and filtered through a sterile gauze into Eppendorf's containing KCl buffer (0.3M KCl, 10mM HEPES, 0.5mM $CaCl_2$, 1mM $MgCl_2$; pH 7.0) at a dilution of 1:1. The resultant solution was centrifuged at 4000g for 7 minutes to pellet isolated POS. Finally, POS pellets were washed thrice in 1xPBS, resuspended in DMEM with 2.5% sucrose w/v and stored at -80°C for a maximum of 6 months. Total protein content of POS preparations was quantified by bicinchoninic acid (BCA) assay (Thermo Fisher, UK) as described in 2.9.2

2.9.2 BCA protein assay

The concentration of FITC-OS samples prepared according to Section 2.9.1 was quantified using the Pierce BCA Protein Assay (ThermoFisher Scientific, UK). Standard curves were generated from 2000 μg/ml, 1500 μg/ml, 1000 μg/ml, 750 μg/ml, 500 μg/ml, 250 μg/ml, 125 μg/ml, 25 μg/ml, and 0 μg/ml BSA protein standards prepared in DMEM with 2.5% sucrose. A 25μl volume of known standards and unknown samples were pipetted into allocated wells of a microplate along with 200μl of working reagent (50:1, Reagent A:Reagent B) and plates were agitated on an orbital shaker for 30 seconds. Finally, plates were incubated at 37°C for 30 minutes, cooled to room temperature and the absorbance was measured immediately at 562nm using a microtitre plate reader (FLUOstar Optima; BMG LABTECH, UK). Samples were protected from light throughout the quantitation procedure.

2.9.3 Labelling of photoreceptor OS for light microscopy

Isolated rod POS were covalently labelled with the fluorescent dye Fluorescein isothiocyanate (FITC)[252] to enable visualisation in subsequent assays. POS were resuspended in 5ml labelling buffer (20mM phosphate buffer pH 7.2, 5mM taurine with 10% w/v sucrose) and 1.5ml FITC stock solution (2mg/mL FITC isomer I in 0.1M Na_2CO_3 buffer; pH 9.5) following which suspensions were rotated on a Stuart SB2 Rotator (Camlab Ltd, Cambridge, UK) for 1 hour in the dark. Suspensions were subsequently spun at 3,000g for 5 minutes, the supernatant containing unbound FITC was aspirated and FITC-OS pellets were resuspended in DMEM with 2.5% sucrose w/v. Aliquots were stored at -80°C prior to use in experiments for a maximum of 6 months.

2.10 Pathological assessment of Aβ *in vivo*

This section details procedures performed *in vivo*. The research presented within this thesis was funded by the National Centre for the Replacement, Reduction and Refinement of Animals in Research (NC3Rs) and thus methods have been written to conform with the ARRIVE guidelines[253].

2.10.1 Housing and husbandry

All animal studies were carried out in accordance with the UK Animal [Scientific Procedures] Act 1986, conformed to the ARVO statement for the Use of Animals in Ophthalmic and Vision Research and were overseen by the institution's ethical research committee.

For non-invasive retinal imaging procedures, 18 female C57BL/6, test naïve mice aged 117 ± 4 days, typically weighing 22.8g ± 0.23 at experimental onset were sourced from the Biomedical Research Facility (University of Southampton, UK). Mice were maintained in a 12 h: 12 h light-dark cycle at 19-24°C and were allowed access to standard laboratory chow and water ad libitum. Mice were housed in conventional cages containing Lignocel 2/2 (IPS Ltd, UK) bedding and environmental enrichment with no more than 10 mice per cage. All experiments were performed between the hours of 9:00 and 18:00 in the light stage of the light-dark cycle. Body weight loss was monitored throughout all experiments as a surrogate measure of animal welfare, where studies were terminated if a change greater than 10% occurred over a period of 3 days.

The experimental sample size was determined using the resource equation method given in Equation 2.

$$E = A_t - A_g \qquad \text{Equation 2}$$

E = Degree of freedom of Analysis of Variance (ANOVA)
A_t =Total number of animals
A_g =Total number of groups

This method was adopted as opposed to calculation by power analysis as effect size calculation was not possible. Here, five mice were allocated to each experimental condition. However, surplus mice were ordered to account for attrition rates associated with subretinal injection success, as discussed in Chapter 4, and were injected with Aβ and vehicle/sham. Therefore n=7 for $A\beta_{1\text{-}42}$, n=6 for vehicle/sham and n=5 for BSA.

Histological analysis of eyes subject to subretinal injection was also performed on tissue obtained from prior pilot experiments. In this instance 11 female C57BL/6 test naïve mice of 131 ± 2 days, typically 24.91g ± 1.16 in weight at the time of experimental onset, were obtained from the Biomedical Research Facility (University of Southampton, UK).

2.10.2 Animal preparation

Mice were anaesthetised with 1mg ketamine (Bayer PLC, UK) and 0.005mg dexmedetomine hydrochloride (Centaur Services, UK) per 10g weight via intraperitoneal (IP) injection. The use of ketamine facilitates pupillary dilation and is thus an optimal anaesthetic for ocular imaging and functional assessment. Animals were then placed in the dark following IP injection until cessation of motor function to minimise stress. Pupils were subsequently further dilated by application of 1 drop 2.5% w/v phenylephrine hydrochloride (Chauvin Pharmaceuticals Ltd, UK) for 2 minutes followed by 1 drop of 1% w/v Tropicamide (Chauvin Pharmaceuticals Ltd, UK) for 2 minutes, and dilated eyes were kept hydrated throughout anaesthesia via repeated application of Viscotears (Alcon, UK) to prevent the formation of cataracts. During anaesthesia mice were maintained on a heat pad and breathing rate was monitored. Upon experimental completion mice were revived via subcutaneous injection with 200μl 0.5mg/ml antipamezole hydrochloride (Centaur Services, UK), recovered on a heat pad and only once righting reflexes had returned were mice returned to the home cage. All procedures described herein were carried out in the laboratory.

2.10.3 Transcleral subretinal injection surgery

Animals were prepared according to Section 2.10.2 and Transcleral subretinal injections were performed under a Stativ Opmi CS/S4 surgical microscope (Carl Zeiss Ltd, UK). Needles were first sterilised prior to use in 70% ethanol and sterile water. A 6mm glass coverslip (VWR, UK) was then placed onto the cornea to prevent light diffraction before a bevelled 34-gauge Hamilton syringe (Hamilton Company, Reno, NV) was inserted under the retina and either 1.5μl of 625nM recombinant human $A\beta_{1\text{-}42}$ (n=7), 625nM BSA (n=5) or vehicle/sham (n=6) was slowly expelled by controlled depression of the plunger. BSA is known to induce ocular inflammation[254] [255] and thus served as a positive control for the experiment. The needle was left in place for 5-10 seconds following fluid delivery to prevent back flow of treatment as a result of pressure differentials. Subretinal injection was subsequently

confirmed by visualisation of a retinal bleb through the operating microscope. All mice in which retinal bleeds were induced, or intra-vitreal injection was performed following perforation of the retina (indicated by a bolus in the vitreous), were excluded from subsequent experiments and analyses. The order of treatment was $A\beta_{1-42}$ injection followed by BSA and vehicle so as to ensure subretinal delivery of predominantly Aβ oligomers. Here, treatment groups were assigned via randomisation, where the statistical unit was the individual mouse. Subretinal injection was chosen over intravitreal injection as this approach not only delivers treatment in close proximity to the photoreceptors and RPE, the main cell types compromised in AMD, but also circumvents post-operative inflammatory complications such as vitritis and endophthalmitis.

2.10.4 Fundoscopy

Fundoscopic imaging of mouse retinae was performed using the Micron IV Retinal Imaging System (Pheonix Research Labs, Pleasanton, CA, USA). Mice were prepared as described in Section 2.10.2 and were placed on the imaging platform with corneas aligned with the lens. Images were acquired with the bright field imaging modality (450-650nm) and were visualised in the Pheonix Micron IV Retinal Imaging Microscope Software (Pheonix Research Labs, Pleasanton, CA, USA). As before, eyes were maintained with Viscotears throughout the procedure to prevent the formation of cataracts.

2.10.5 Full-field electroretinogram (ffERG) recordings

Mice were dark adapted for a minimum of 12hrs prior to ERG recordings and were prepared as described in Section 2.10.2, where the room temperature was maintained at 27°C throughout the entire duration of the procedure. ERG traces were recorded using the Generation II Image-Guided ERG modality attachment to the Micron IV Retinal Imaging System (Pheonix Research Labs, Pleasanton, CA, USA) inside a 6-panel aluminium, copper mesh Faraday cage (Micro Control Instruments Ltd, UK) to minimise signal interference from external electrostatic fields and electromagnetic waves. Test subjects were placed on a heated platform and were connected to three electrodes. A ground electrode was inserted into the tail, a reference electrode into the head, and corneal contact was achieved by positioning of the cornea onto the gold-plate objective lens. ERGs were recorded by stimulation with white LED light (6.8 cd-s/m^2) of 1.5mm diameter for 1 ms. Stimulation was performed in two sweeps with a two minute interval from which an average

recording was determined. In all cases, *oculus dexter* measurements were conducted first for consistency and the order of animal assessment was random. ERGs were visualised in the V3 Pheonix LabScribe ERG software suite (Pheonix Research Labs, Pleasanton, CA, USA), where the a-wave and b-wave amplitudes were calculated as the measurement from baseline to the a-wave trough and the a-wave trough to the b-wave peak respectively. All subsequent generation of graphs were produced using GraphPad Prism Version 7 (GraphPad, Manufacturer). The implicit time (the time interval between stimulus onset and the wave peak) for both the A and B waves was also recorded and analysed in GraphPad Prism Version 7 (GraphPad, Manufacturer).

2.10.6 Optical Coherence Tomography

OCT imaging was performed at baseline as well as day 8 and 15 following subretinal injection in the same session as ERGs using the Envisu R2200 VHR SDOIS Mouse Imaging system (Bioptigen Inc., Durham, NC), where mice remained under anaesthesia and were subject to identical preparatory steps. As before, Viscotears ocular lubrication ointment was applied as needed during anaesthesia. Briefly, mice were wrapped in a surgical swab and were loaded into the imaging platform where the head was secured on a bite bar. The eye of interest was positioned in line with the mouse retina lens using the multi-axial rodent alignment stage apparatus, following which the cornea was cleaned with surgical spears and Systane lubricant eye drops (Alcon, Camberley, UK). Cross-sectional previews as well as real-time en face fundus images were used for final alignment with the OCT probe in the InVivoVue Clinic software (Bioptigen Inc., Durham, NC). Images were centred round the optic nerve head before 1.4mm volumetric scans were acquired through a 50-degree field of view comprising 100 B-scans, each of which consisted of 1000 A-scans. Finally, OCT images were segmented for the Retinal nerve fibre layer (RNFL), GCL, INL, OPL, ONL, IS, OS, Photoreceptor end tips (ETPRS) and the RPE using the InVivoVue 2.4 Diver automated analysis software (Leica Microsystems, UK). Segmentation was performed up to a distance of 476μm from the ONH at 24 retinal locations, where in all cases at least one point of the segmentation grid was positioned on the optic nerve. Measurements were subsequently averaged to acquire a representative thickness for individual retinal sublayers and total retinal thickness was also recorded as the thickness from the RNFL to the RPE.

2.10.7 Globe preparation, fixation and sectioning

Experimental mice were euthanized on day 15 post transcleral subretinal injection by cervical dislocation and cutting of the carotid artery. Mice were enucleated immediately and globes were rinsed briefly in 1X PBS and fixed by immersion in 4% PFA for 30 minutes at 4°C. Following fixation, eyes were washed thrice in 1X PBS and were dehydrated through a series of sucrose gradients according to Table 18.

Table 18: Cryoprotection of mouse eye tissue

Details of the sucrose gradients mouse eyes were processed through to cryoprotect/partially dehydrate tissue, along with the corresponding immersion time and temperature at which each stage was performed. Sucrose solutions were prepared by dissolving sucrose (Sigma Aldrich, UK) in 1x PBS to the % of total solution volume stated.

Sucrose solution (% of total volume)	Time (Minutes)	Temperature (°C)
5	60	20
10	30	20
12.5	30	20
15	30	20
20	960	4

Dissection of eyes was subsequently performed using a Leica DM100 LED dissection microscope (Leica Microsystems, UK). In brief, connective tissue and optic nerve remnants were cut from the eye, an incision was made proximate to the ora serrata with a 30G needle (Esslab**,** Essex, UK) and the anterior segment was removed with micro scissors and micro forceps (John Weiss & Son Ltd., Milton Keynes, UK) along with the lens. Posterior eye cups comprising the sclera, choroid, RPE and retina were then transferred to moulds filled with Optimal Cutting Temperature medium (OCT) and were frozen on dry ice. Afterwards, 16μm sections were cut using a Leica CM1850 Cryostat (Leica Microsystems, UK) and were collected consecutively on 15 Superfrost Plus microscope slides (Fisher Scientific, UK) with approximately 12 sections per slide. Adjacent sections corresponded to a distance of ~192μm. Slides were stored long-term at 4°C.

2.10.8 Haematoxylin and Eosin (H&E) staining

Slides were dried in a SI60 37°C incubator (Stuart**,** UK) for 1 hour to remove moisture and were processed through the series of solutions detailed in Table 19. Upon completion DPX Mountant (Sigma Aldrich, UK) was applied and slides were mounted with a glass coverslip. Imaging of slides was performed using an Olympus dotSlide

virtual microscopy system (Olympus, UK) and were visualised using the OlyVIA software suite (Olympus, UK).

Table 19: Haematoxylin and Eosin (H&E) staining of mouse eye sections.

Sequence of solutions and corresponding immersion times slides containing mouse eye sections were processed through during Haematoxylin and Eosin (H&E) staining. Haematoxylin was filtered prior to use. Sections were immersed in tap water following staining with Haematoxylin until blue, then in 0.03% acid alcohol until the background was pale and again in tap water until blue. All stages in which slides were incubated for 0.5 minutes consisted of 5 dips in the corresponding solution.

Solution	Duration (Minutes)
Haematoxylin (Sigma Aldrich, UK)	10
Tap water/ Scott's water	8
0.03% Acid alcohol	8
Tap water/ Scott's water	8
0.5% Eosin (Sigma Aldrich, UK)	1
Distilled water	0.5
50% Ethanol	0.5
70% Ethanol	0.5
90% Ethanol	0.5
100% Ethanol	0.5
100% Ethanol	0.5
Xylene	5

2.11 Human sample acquisition

2.11.1 Study cohort selection

The study cohort was identified from vitreo-retinal pre-operative lists of patients scheduled for vitrectomy, or vitrectomy following Phacoemulsification and intraocular lens implant (Phaco & IOL) at Southampton University Hospital Eye Unit. Eligibility of patients to participate in the study was determined by thorough screening against the inclusion/exclusion criteria detailed in Table 20**.** Participants were recruited onto the study if all criteria were satisfied subject to patient autonomy.

Vitreoretinal (VR) surgery requires underlying ocular pathology, and thus healthy donors without ocular complication could not be included in the study[256]. Ocular conditions, detailed in the study inclusion criteria in Table 20, represent a "normal" state control, where associated pathology is unlikely to affect the vitreous proteome. Patients in which the vitreous protein composition may be subject to systemic influence were excluded from the study cohort. Similarly, retinal vein occlusion and DR were excluded from study cohorts to prevent misdiagnosis of AMD[257]. Additionally, fundoscopy and OCT images from preoperative assessments were examined by two independent ophthalmologists regarding AMD status to reduce researcher bias. If the two diagnoses were conflicting, a third consultant was recruited to assess AMD status. Efforts were also made to ensure a representative sample in the case of age associated analyses, where suitable patients over the age of 18 were approached, as well as both genders, to consider study participation.

Table 20: Study inclusion and exclusion criteria

Details of the inclusion and exclusion criteria used to identify suitable candidates. Patients were recruited on the study if all criteria were satisfied. Abbreviations: AMD, Age-related Macular Degeneration; CNV, Choroidal Neovascularisation; GA, Geographic Atrophy.

Inclusion Criteria	Exclusion Criteria
Age ≥ 18 **Caucasian Origin** Control group: **Diagnosis confirmed by Consultant Ophthalmologist for at least one of the following pathological states:** • **Cataract** • **Epiretinal membrane** • **Macular hole** • **Vitreous floaters** • **Vitreomacular Traction Syndrome** Experimental group: **Diagnosis confirmed by Consultant Ophthalmologist for AMD:** • **Dry AMD** • **Wet AMD** • **Previous Wet AMD/Scar** • **AMD classification according to AREDS categories 2-4:** **Category 2: Multiple small drusen/single intermediate drusen (63-124μm) or RPE abnormalities** **Category 3: Extensive intermediate drusen, at least one large druse (≥125μm) or GA not involving centre of fovea** **Category 4: GA involving fovea and/or CNV**	Any ocular condition in which the vitreous proteome may be subject to systemic influence. Diagnosis confirmed by Consultant Ophthalmologist for any of the following pathological states: • Diabetic Retinopathy • Retinal Haemorrhage • Retinal Detachment • Vitreous Haemorrhage • Retinal Vein Occlusion • Wet AMD with vitreous haemorrhage Age < 18 Participants lacking capacity to consent

2.11.2 Sample size

The study presented forms a pilot study to investigate the relationship of Aβ with AMD. As such the sample size employed adhered to that stated in the existing ethics under which the study was conducted. A total of 30 controls and 30 cases were specified in the recruitment notes for patients over the age of 55. Younger control patients, being restricted to those over the age of 18, were recruited in addition to investigate the effects of age on vitreous Aβ concentrations.

2.11.3 Vitreous sample acquisition

Undiluted core vitreous biopsy (~0.4ml) was obtained at the onset of surgical *pars planar* vitrectomy. Prior to irrigation, the vitreous humour was manually aspirated from the centre of the vitreous cavity through a vitrectomy cutter into a 1ml syringe, with infusion off. Upon receipt, vitreous samples were immediately placed on ice, divided into 100μl aliquots and stored at -80°C to prevent proteolytic degradation until sufficient sample numbers were achieved. Sample size aspirated was kept consistent to limit the influence of additional vitreous substructures on proteome composition[258]. All vitreous samples were collected between 20.08.15 – 22.09.17.

2.11.4 Additional sample information

Prior to surgery, participants were consulted regarding smoking status, including average cigarette number per day and the number of years the participant had smoked, as well as medical and drug history. Blood pressure measurements were also obtained and recorded on sample information sheets. All other relevant information including demographics (age and gender) and coexistant medical conditions were obtained from medical records/archives by a member of the patient's clinical team (to ensure patient anonymity). The acquisition of such was performed to investigate additional associations with vitreous Aβ concentration and AMD.

2.11.5 Ethical considerations

The study in question was executed under study title 'A study of the Molecular and Cellular Pathophysiology of Retinal Disease', Rec Ref: 09/H0504/67, Local Ref: RHM OPH 0142, and was performed in accordance with the Research Governance Framework for Health and Social Care (2005) and the Declaration of Helsinki (2008). The study commenced only after approval by the local Research Ethics Committee review board and Research and Development for University Hospital Southampton. In the majority of cases, participants received a patient information leaflet at least 24 hours prior to surgery. However, if deemed appropriate, e.g. in emergency cases, patients were recruited onto the study up to 1 hour prior to surgery. Informed consent was obtained from all participants and sample storage adhered to the guidelines specified in the Human Tissue Act (HTA).

2.12 Statistical Analyses

2.12.1 Quantitative colocalisation analysis

Colocalisation mentioned in this study refers to the assessment of subcellular fluorochrome co-occurence to determine the spatial localisation of two proteins. Specifically, two molecules of interest are labelled with fluorochromes, each assigned primary pseudocolours. The presence of the associated primary subtractive colour within merged confocal micrographs is then assessed as a measure of the degree of overlap. Most commonly, owing to the mechanisms underlying human visual perception, the pseudocolours red and green are assigned with yellow indicative of fluorochrome overlap. Qualitative analysis of colocalisation involves the presentation of single alongside merged channels but is subject to visual bias. Moreover, the degree of yellow observed may be manipulated in image processing software by modification of image intensity histograms. Quantitation is therefore required for the valid, objective interpretation and statistical analysis of fluorochrome colocalisation. For the purpose of this thesis quantitative colocalisation analysis was employed to compare the colocalisation of proteins of interest across several treatment groups.

2.12.1.1 Considerations

Quantitative colocalisation analysis necessitates up-stream consideration of several factors prior to image acquisition. First is the employed fluorochromes which must be precisely selected to avoid bleed-through/cross-talk and spherochromatism[259] [260]. Where possible Alexa Flour® 488 or FITC was partnered with fluorochromes exhibiting red shifted excitation spectra e.g. Cresyl Violet (Magic Red®) or Alexa Fluor® 594 or 647.However, in the case of initial assessment of $A\beta_{1\text{-}42}$ localisation within lysosomes, Alexa Flour® 488 was partnered with PDMPO. In all cases of image acquisition, confocal hardware was configured by an expert (Dr David Johnston, Biomedical Imaging Unit, University of Southampton) to minimise user error, and sequential acquisition was performed to minimise detection of alternate fluorochromes. Single labelled specimens were also assessed prior to acquisition to confirm detection specificity and unlabelled specimens facilitated autofluorescence thresholding. Pixel saturation is also known to prevent proper quantification of colocalisation[259] and thus efforts was made to avoid saturation during image acquisition. Efforts were also made to minimise noise by employing a line average of 4 and acquisition rate of 600Hz.

Lastly, quantitative colocalisation analysis must be conducted on numerous consecutive optical sections. As such, colocalisation was quantified across the entire volumetric area of the cell or monolayer. The only exception to this rule was with regards to Cathepsin B colocalisation with $A\beta_{1-42}$ (Section 3.3.4.3) in which multiple z-stacks could not be obtained per field of view due to probe constraints. In order to combat this limitation, 10 single plane images were assessed per treatment, across three biological replicates to improve accuracy.

2.12.1.2 Costes *et al.* method of colocalisation quantification

Several methods to quantify colocalisation have been developed in which the degree of colocalisation is measured by specified coefficients. The most accepted method is currently that described by Costes *et al*[260]*.* This is included in the Volocity software package (PerkinElmer, UK) and was used in the quantification of colocalisation in this study. The Costes *et al.* threshold-based automatic algorithm negates the requirement for user defined thresholds thereby eliminating subject bias and improving the reliability of returned results. A detailed explanation of the statistical methods underpinning the algorithm can be found in Costes *et al.* [260], however the underpinning principles can be summarised as follows.

The algorithm calculates the linear least square fit line for the pixel intensity scatterplot, where x and y axes represent the two flourochrome intensities. A threshold is then set for one axis and its intersect with the least square fit line set as the corresponding threshold for the other axis. The Pearson correlation coefficient (*r*) is calculated for the remaining data below the thresholds. Thresholds are then reduced using an iterative approach until *r* approaches zero. Subsequently, data points where both fluorochrome intensities are above the Costes thresholds, are plotted on 2D scatterplots for each analysed image. Here, the Costes thresholds are signified by black regions along axes providing a qualitative indication of colocalisation[260]. The Pearson correlation and Manders split coefficients provide quantitative outcomes from this kind of analysis, defining the degree of association, and co-occurence between the two fluorochromes respectively[260 261]. These are calculated using only the intensities above the Costes thresholds.

For the purpose of colocalisation quantitation in this study the Manders coefficients were employed to quantify the degree of colocalisation between fluorochromes. Coefficient values presented provide an indication of the fraction of red coincident with green and vice versa. Here, the Manders colocalisation metrics were selected

in preference over the PCC due to independence of signal proportionality, and the intuitive nature of result interpretation[261].

2.12.1.3 Limitations of colocalisation analysis

Due to the optical resolution limit of confocal light microscopy, the interaction of two fluorochromes could not be determined beyond 200nm in the present study. However, lysosomal volumes range between 100-1200nm[262]. Thus, positive colocalisation of two proteins within lysosomal compartments refers to the majority (90.9%) of the lysosomal volumetric range (200-1200nm).

2.12.2 Measurement of Cathepsin B activity

To quantify the level of Cathepsin B activity within cells, the mean fluorescence intensity of Magic red® above a defined threshold was measured across entire images using FIJI. Here, the threshold was determined by measuring the intensity within 10 nuclei per image, across all samples and time points. Measurements were acquired from 10 random fields of view per experimental condition. This was repeated across three independent experiments.

2.12.3 ERG wave enumeration for functional analysis

Quantification of ERG recording wave components was performed by obtaining an average measurement from both injected eyes per experimental unit (mouse). Wave components included the A wave, B wave, A wave implicit time (T (A)) and B wave implicit time (T (B)). A total of 7, 6 and 5 average measurements were plotted for mice subject to subretinal injection with $A\beta_{1\text{-}42}$, BSA and vehicle/sham respectively. In the case of average ERG graphs, the average amplitude in μV across all recordings was obtained per time point (ms), and was plotted per experimental condition.

2.12.4 Segmentation for retinal thickness analysis

For quantification of the thickness of component retinal layers, thickness measurements were determined from OCT images for 24 retinal locations per eye. An average thickness measurement was calculated per mouse to acquire the representative thickness of the RNFL, GCL, INL, OPL, ONL, IS, OS, ETPRS and the RPE. Total retinal thickness was also recorded as the thickness from the RNFL to the RPE. Measurements were repeated for all experimental time points.

2.12.5 Quantification of H&E stained tissue sections

Pathological observations in tissue sections were quantified as follows. Out of the 15 slides obtained for each eye, 5 were analysed at 240μm intervals for morphological changes in the outer retina. A region of interest (ROI) corresponding to 100μm by 300μm was analysed at 200μm intervals across entire retinal sections and a score of 1 or 0 was assigned to the Photoreceptor Inner Segments (PIS), the POS, and the RPE/Choroid per ROI corresponding to normal or abnormal morphology within cell layers respectively. A total of 15 retinal sections were assessed per eye (3 equivalent sections per slide) and scores were collated to produce a % abnormality score. Exclusion criteria included a 200μm radius from the injection site to omit areas of mechanical trauma. In this instance the unit of statistical analysis was the individual eye. All analysis was performed blind using OlyVIA and ImageJ. This specific method of analysis was chosen as it eliminates misinterpretation of results introduced by potential cutting artefact or user bias, and facilitates quantification of localised pathology in relation to the whole retina, indicating the extent of retinal damage.

2.12.6 Statistical methods

Statistical analyses were performed using the GraphPad Prism Software (GraphPad; San Diego, US). In the case of normally distributed data, results were analysed using either the unpaired student's t-test or one way ANOVA with Tukey's multiple comparisons depending on the number of experimental groups. Data in which the assumption of Gaussian distribution could not be met were analysed using the Mann Whitney test or Kruskal-Wallis test with Dunn's multiple comparisons. For correlation analyses, normality of residuals was assessed with the Shapiro-Wilk test using IBM SPSS Statistics, Version 24.0 (IBM Corporation, Armonk, New York) and statistical comparisons were made using Pearson's correlation coefficient (PCC). Finally, inter-rater reliability for the determination of AMD status in Section 5.2.2 was assessed using Cohen's kappa statistic. All data are expressed as means ± standard error of the mean (SEM). The only exception being in Section 4.3.1.2 and Section 5.3.4, where box and whisker plots are employed to provide additional information regarding data collected. In all instances n represents the number of replicates with statistical significance indicated as * $p \leq 0.05$, ** $p \leq 0.01$, *** $p \leq 0.001$, **** $p \leq 0.0001$.

Chapter 3 Aβ effects on RPE lysosomes

3.1 Background

Similar to AMD, a number of cytopathological studies have implicated the dysfunction of cellular clearance pathways in the pathogenesis of AD. Such pathways include the UP, autophagy, and endocytic pathways. In many respects, the understanding of proteolytic compromise in AD is advanced relative to AMD, with over 20 years of investigation. Hence, advancements in the AD field may be employed to better understand this new paradigm in AMD research.

There is compelling evidence that endosomal and lysosomal dysfunction are early events in AD[16 263]. Specifically, an elevated neuronal endosome mass, with a 2.5-fold increase in cytoplasmic endosome volume, and 32-fold increase in endosome size has been shown to correlate with disease progression[264]. Similarly, evidence for the involvement of the UP in AD pathogenesis has come from studies demonstrating a significant reduction in the UP activity of post mortem tissue[265], along with an increased presence of ubiquitin-protein conjugates at sites of AD lesions[266]. Given the interrelationship of the UP with the autophagy pathway (Section 1.2.3.5.3), it may also not come as a surprise that altered autophagy has also been implicated in AD pathogenesis. This research has been largely driven by Nixon and colleagues, who have associated the accumulation of autophagic intermediates, including autophagosomes, amphisomes, multilamellar bodies and autolysosomes, with disease pathogenesis[267]. These constitute a significant proportion of cytoplasmic volume in dystrophic neurites, and potentially highlight a role for impaired autophagic vacuole maturation in AD. In fact, it has been suggested that the burden of undigested or partially digested waste products is comparable to that observed in several primary lysosomal storage disorders[16]. Collectively, this suggests an increased endosomal activity, but an impaired autophagic flux, endocytic progression and UP clearance ability in diseased brains. The involvement of the UP and autophagy in AD pathogenesis is further bolstered by the cells reliance on these mechanisms for the clearance of misfolded/aggregated proteins, including Aβ, the accumulation of which is also typical of disease[161 162 268]. Interestingly, all of these pathways rely on lysosome-mediated degradative mechanisms, albeit to differing extents. The question therefore arises are these early disease hallmarks a consequence of disrupted substrate proteolysis, and/or vesicle maturation following lysosomal impairment?

The notion for impaired lysosomal function in AD is supported by several lines of evidence. For example, pre-lysosomal autophagic vacuoles and autolysosomes have been shown to accumulate in neurons[16 263 269], as well as post-lysosomal dense bodies in the dystrophic neuronal processes of AD brains[263 270]. This may indicate an inability of the lysosome to cope with its degradative burden. In fact, this is further supported by reported perturbations to lysosomal acid hydrolase biosynthesis[271], distribution[272] and activity[273] in diseased brains. One mechanism by which this may occur is LMP, which induces the release of lytic enzymes into the cytosol, and may indirectly induce cell death[274]. Hence, LMP may highlight an early mechanism of neuronal compromise in AD[275 276]. Despite the proposed involvement of Aβ in AD pathogenesis, it is currently unknown whether lysosomal alterations occur exclusively upstream or downstream of Aβ generation in endocytic compartments. It therefore remains unknown whether a direct link between $A\beta_{1-42}$ accumulation and lysosomal dysfunction in AD exists. However, $A\beta_{1-42}$ is a known lysomotropic agent which has been shown to aggregate within late endosomes and secondary lysosomes, where it forms degradation resistant aggregates, exhibits pH dependent irreversible insertion into the lysosomal membrane, and induces LMP mediated leakage of lysosomal constituents [13 277]. Studies of post-mortem AD and transgenic mouse brains have also highlighted the potential pathogenic role of endo-lysosomal Aβ accumulation in the pathogenesis of AD, which demonstrate a preponderance of lysosomal $A\beta_{1-42}$ upon examination of intraneuronal Aβ[278 279]. This is largely suggestive of a causal role for Aβ in this facet of AD pathology.

Highly localised and significant damage to clearance mechanisms are also reported in AMD[152 280] (Section 1.4.2). In fact, one hypothesis for AMD associated RPE degeneration is an age-related decline in RPE proteostasis and metabolism[56]. This is evidenced by an increase in autophagosome number and enlarged/swollen lysosomes in RPE cultures isolated from post-mortem AMD tissues[153], as well as the aforementioned increase in RPE lysosomal lipofuscin and A2E content with age (Section 1.5.3)[29]. The autophagy, endocytic and phagocytic pathways of the RPE are all inter-dependent on the lysosome, and necessitate correct lysosomal function, integrity and mechanistic balance for the complete degradation of substrate. Hence the gradual accumulation of partially degraded inclusions within RPE lysosomes with age, and in disease, results in impeded phagolysosome formation, increased intracellular residual bodies, and ultimately disrupted RPE metabolism and cell senescence[82 152]. It is currently hypothesised that altered RPE metabolism and exosome release from the RPE associated with the improper degradation of protein cargo ,may in fact precede drusen formation in AMD[155 281]. It remains unknown

whether RPE clearance perturbations are antecedent to, or a consequence of disease. However, given the implications of Aβ on lysosomal function in AD as well as commonalities between AMD and AD pathology, it is possible that Aβ may exert comparable effects on RPE lysosomes resulting in a reduced lysosomal capacity and impaired fusion with associated clearance pathways. In turn, this would accelerate the lipofuscinogenesis and protein deposition characteristic of age and disease. Collectively, such changes may exert a cumulative effect on RPE cell function, including impaired POS degradation[56 82] , ultimately resulting in the RPE atrophy and chronic inflammation associated with AMD.

In this chapter we have employed a well-established cell culture model to study the effects of Aβ on RPE lysosomes. We tested the ability of Aβ to localise to RPE lysosomes, and subsequently investigated its impact on lysosomal function. This included assays to assess alterations to acid hydrolase expression and activity, as well as the RPE phagocytic capability, the primary aim being to determine the involvement of $A\beta_{1-42}$ in driving clearance alterations typical of early AMD pathology. Prior to commencing this work, *in vitro* models were characterised in respect of protein expression, ultra-structural morphological adaptations, BRB formation and polarised functional ability. Similarly, as this study constituted the first use of the $A\beta_{1-42}$ preparation technique in our laboratory, the dynamics of its aggregation were also assessed.

3.2 Methods

This section describes specific experimental details of methods employed in Chapter 3. For in depth technical protocols please refer to Chapter 2.

3.2.1 Cell culture

ARPE-19 cells were cultured as described in Section 2.1. Colocalisation studies within this chapter were conducted on Ibidi glass bottomed μ-slides in order to minimise autofluorescence, whereas all other functional investigations utilised fully differentiated RPE cultured within Transwell® inserts, as shown in Figure 19. All cells used in experiments were between P23-26.

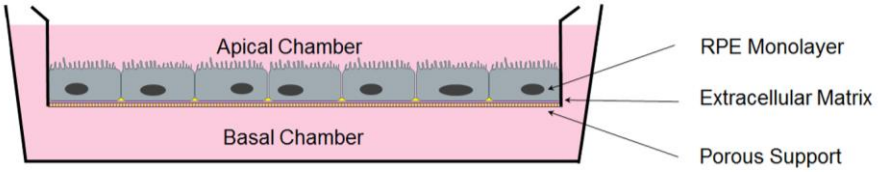

Figure 19: Schematic of the Transwell® cell-culture system employed.

Diagram illustrating the *in vitro* biosynthetic RPE-Bruch's membrane complex. RPE cells were seeded onto porous Transwell® inserts that had been precoated with 50μg/ml fibronectin. Cultures maintained over long periods differentiate into mature, confluent and cuboidal RPE monolayers with comparable function and morphology to native RPE. This *in vitro* culture model presents a powerful tool to study functional RPE monolayers, which can be exploited for investigation of polarised function and is amenable to microscopy based assays as well as genetic manipulation[282]. Please note this image is purely for illustrative purposes and is not to scale. Image sourced from Ratnayaka (2015)[180].

3.2.2 Immunofluorescence

Immunofluorescence was conducted on 2 month old cultures to confirm the expression of key proteins and to evaluate the differentiation status and maturity of RPE cells cultured on inserts. Transwells® were stained for the early tight junction protein ZO-1, mid-late tight junction protein occludin, Na^+/K^+ ATPase and the retinoid isomerohydrolase, RPE-specific 65 KDa protein (RPE-65) as described in Section 2.6.1. For studies investigating $A\beta_{1-42}$ colocalisation with specific cell components, oligomeric $A\beta_{1-42}$ was applied to Transwells® containing ARPE-19 cells at a concentration of 1μM for 48 hours. Immunostaining for 82E1 was subsequently performed to validate sustained conjugation of the 488 Alexa Fluor® to $A\beta_{1-42}$.

To investigate the degree of FITC tagged POS lysosomal localisation, cells cultured in Ibidi glass bottom μ-slides were immunostained for LAMP-1. Here, minor amendments were made to the staining protocol detailed in Section 2.6.1 as

follows. Cells were fixed in 4% PFA for 30 minutes at 4°C, and blocked in blocking buffer comprising 1% BSA prepared in 3% PBS-Tween for 30 minutes at room temperature. Incubation with the primary antibody was then performed in blocking buffer overnight at 4°C. Following incubation, cells were washed thrice in 1x PBS and incubated in secondary antibody solution prepared in blocking buffer. All subsequent steps in the procedure conformed to the protocol detailed in Section 2.6.1. Details of primary antibodies are listed in Table 9. In the case of labelling controls, cells were co-stained with Rhodopsin to assess FITC-POS specificity. Specific details regarding imaging parameters for colocalisation analysis not specified in Chapter 2, are detailed in Table 21. All antibodies were optimised prior to commencement of the project.

Table 21: Confocal fluorescence microscopy laser configurations used to assess colocalisation between LAMP-1 and the Photoreceptor Outer Segment FITC conjugates.

Details of the laser configurations, excitation wavelengths and emission bandwidths used during confocal fluorescence microscopy to assess colocalisation between LAMP-1 and Photoreceptor Outer Segment (POS) FITC conjugates, along with the fluorophore each was used to visualise. Fluorophores were sequentially imaged to avoid bleed through. The excitation wavelength reflected by the dichroic mirror ensures that the fluorophore is excited by only light of the correct wavelength whereas the emission bandwidth ensures that only emitted light of the specified wavelengths passes through the pinhole of the detector. Abbreviations: FITC, Fluorescein isothiocyanate; POS, Photoreceptor Outer Segments.

Target	Fluorophore	Laser	Excitation Wavelength (λ)	Emission bandwidth (nm)
POS	FITC	Argon	488	495-550
LAMP-1	Alexa Fluor® 594	Argon	561	570-620

3.2.3 Transepithelial Electrical Resistance (TEER)

The integrity and permeability of ARPE-19 monolayers was assessed through TEER measurements according to Section 2.2. Measurements were taken from three independent wells, where an average of five technical replicates were recorded per well at each experimental time point. Raw TEER measurements were then corrected for the reference well and the effective growth area of the Transwell® insert. Data is presented as $\Omega.cm^2 \pm$ SEM.

3.2.4 ELISA quantification of secreted proteins

Solid-phase sandwich ELISA was employed here to assess the ability of RPE cells grown on Transwell® inserts to directionally secrete specific cytokines. ARPE-19 cells were cultured for 7 weeks in 24mm diameter Transwell® inserts that had been precoated with 50μg/ml fibronectin according to Section 2.1. A complete apical

and basal media change was performed 72 hours prior to commencement of the experiment to enable accurate protein quantification within each compartment. Proteins measured included VEGF, PEDF and total Aβ using the Novex® human VEGF ELISA (Life technologies, UK), human PEDF ELISA (BioVendor, Germany) and Human $Aβ_{1-x}$ ELISA (IBL, Japan) kits respectively. Methods were carried out according to the manufacturer's instructions which are detailed in Section 2.3. Protein secretion was assessed over 3 independent wells for which 3 technical replicates were performed. Following ELISA quantification, measurements were corrected for the effective volume of growth medium within each compartment as well as the dilution factor.

3.2.5 Preparation of oligomeric $Aβ_{1-42}$

$Aβ_{1-42}$ or Alexa Fluor® tagged $Aβ_{1-42}$ was prepared according to the published method described in Section 2.4. Preparations were aggregated on ice for 1.5 hours post preparation in order to obtain high concentrations of $Aβ_{1-42}$ oligomers prior to use. Working $Aβ_{1-42}$ concentrations were achieved by direct dilution into cell culture medium. In all experiments 1μM $Aβ_{1-42}$ was employed to maintain physiological relevance and to induce a membrane inserted state of Aβ within lysosomes similar to previous lysosomal investigations of $Aβ^{13}$.

3.2.6 Limulus Amebocyte Lysate endotoxin test

To validate sample sterility and eliminate the possibility of bacterial pyrogen confounding experimental results, the levels of bacterial endotoxin within $Aβ_{1-42}$ preparations and vehicle/sham were assessed using the Limulus Amebocyte Lysate (LAL) Endosafe® PTS cartridge based assay according to Section 2.5. Here, a percentage recovery of approximately 50-200 was considered a valid test.

3.2.7 Transmission Electron Microscopy

3.2.7.1 Ultrastructural studies of RPE cultures

To investigate the presence of specific ultrastructural adaptations within ARPE-19 monolayers, culture medium was aspirated from 12mm Transwell® inserts and cells were fixed in primary fixative comprising 3% glutaraldehyde and 4% formaldehyde in 0.1M PIPES (pH 7.2) for 1 hour at room temperature. Transwells® were subsequently prepared for TEM according to the protocol detailed in Section 2.7.1 and sections were imaged using a Hitachi H7000 microscope fitted with a SIS Megaview III plate camera.

3.2.7.2 Immunogold labelling with 82E1

$A\beta_{1-42}$, prepared according to Section 2.4, was incubated on ice for 0, 1.5, 3, 24, 48 and 72 hours and 20μl aliquots were fixed in 5μl of 4% formaldehyde and 0.1M PIPES buffer to assess the conformational state of $A\beta_{1-42}$ at various intervals post sample preparation. Upon acquisition of all time points, 5μl of fixed sample was subject to immunogold labelling with 82E1, as detailed in Section 2.7.2. Again, samples were imaged using a Hitachi H7000 microscope fitted with a SIS Megaview III plate camera.

3.2.7.3 Magic Red™ Cathepsin B activity assay

To investigate the effects of $A\beta_{1-42}$ on Cathepsin B activity, ARPE-19 cells (P24) were seeded onto 50μg/ml fibronectin coated 8-well Ibidi glass bottomed μ-slides at $1x10^4$ cells per well according to Section 2.1. Cells were cultured for 3 days in complete medium prior to use. On the day of experimentation, 1μM Alexa Fluor® 488 tagged oligomeric $A\beta_{1-42}$ or an identical volume of vehicle/sham was applied to cultures and cells were incubated in a 37°C humidified incubator with 5% CO_2 for 3 hours. A negative experimental control was also included in which cells remained untreated as a direct comparator for vehicle/sham effects. Both $A\beta_{1-42}$ containing and mock treated medium were aspirated following incubation and cells were washed thrice in fresh culture medium, before being returned to the incubator for 0.5, 3, 24 and 48 hours. At each experimental time point 300μl of Magic Red® working solution (Section 2.6.3) was applied to wells for 30 minutes at 37°C. DMSO diluted in diH2O and subsequently culture medium to a comparable concentration was also applied to the control well of each treatment to assess its effects. The Magic Red® working solution was subsequently removed and cells were washed in prewarmed culture medium before being imaged on a Leica SP8 confocal microscope using the settings detailed in Section 2.6.3.4. To account for changes across samples, 10 random fields of view were acquired at x63 magnification across a single optical plane per experimental condition. Identical timings, including both the time of day and duration of incubation, were adhered to across the three experimental replicates. Magic Red® Cathepsin B activity was analysed using ImageJ software (Section 2.12.1) and is presented as average fluorescence intensity ± SEM. In the case of colocalisation analysis of Alexa Fluor® 488 tagged $A\beta_{1-42}$ and Magic Red®, images were analysed in the Volocity software suite (PerkinElmer, UK), see section 2.12.1, and are presented as average Costes colocalisation coefficient M1 ± SEM (section 2.12.1.2). Images presented are

average measurements of replicates and are thus representative of the entire sample cohort. An experimental timeline of the Magic Red Cathepsin B activity assay can be seen in Figure 20.

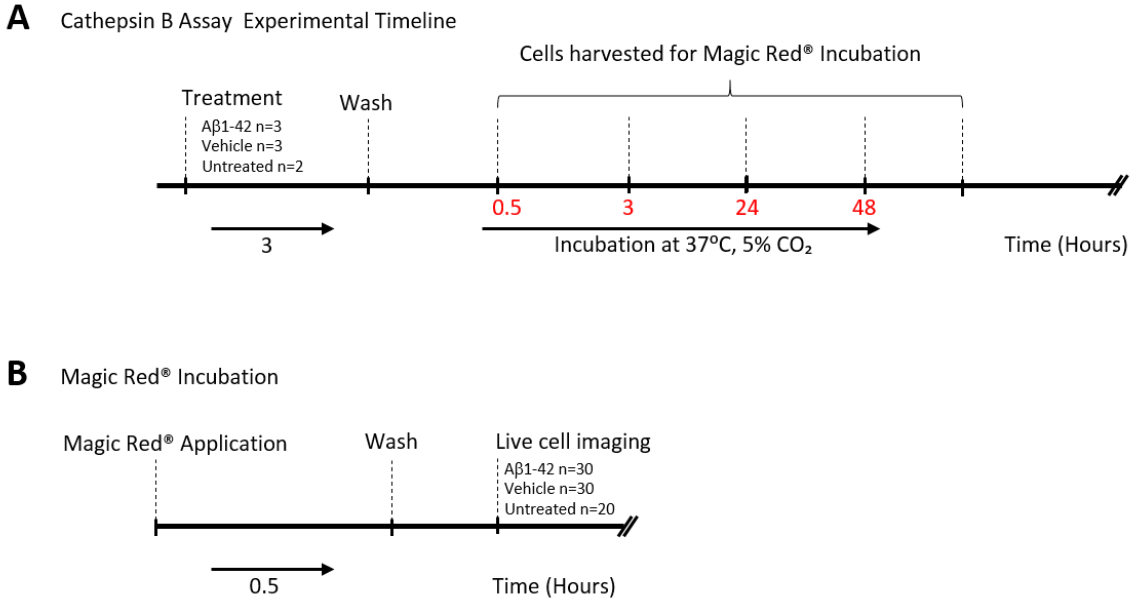

Figure 20: Magic Red® Cathepsin B activity assay experimental timeline.

Time course of events executed during the Magic Red® Cathepsin B activity assay. **A.** $A\beta_{1-42}$ or vehicle sham was applied to cultures for 3 hours, where untreated cells served as a negative control. Following treatment exposure, cells were washed and returned to a 37°c, 5% CO_2 for the timeframes indicated in red; 0.5,3, 24 and 48 hours. **B.** Magic Red® working solution was incubated with cells at elapsed time points for 30 minutes prior to washing thrice and imaging with a Leica SP8 confocal microscope. 10 fields of view were acquired per experimental replicate yielding n=30 fields of view for $A\beta_{1-42}$ and vehicle/sham and n=20 for untreated cultures.

3.2.7.4 LysoSensor Yellow/Blue DND-160 (PDMPO)

ARPE-19 cells (P27) were seeded onto 50μg/ml fibronectin coated, 8-well, glass bottomed Ibidi μ-slides at a density of $1x10^4$ cells per well (Section 2.12.1). Cells were then cultured in complete ARPE-19 medium for 2 days prior to use. To assess $A\beta_{1-42}$ colocalisation with lysosomes, 1μM Alexa Fluor® 488 tagged $A\beta_{1-42}$ was prepared as described in Section 2.4, and incubated with cells for 2.5 hours in a 37°C humidified incubator with 5% CO_2. Following incubation, $A\beta_{1-42}$ working solution was removed, cells were washed thrice and returned to the incubator overnight. The following day 5μM PDMPO working solution was applied to cells for 5 minutes, before the cells were washed in fresh medium. Z-stacks of 3 random fields of view across 3 wells were obtained using a Leica SP5 laser scanning confocal microscope (Leica Microsystems, UK) using the parameters detailed in Section 2.6.2.4. Vehicle/sham and Alexa Fluor® $A\beta_{1-42}$ controls facilitated the setting up of imaging parameters with respect to autofluorescence and potential bleed-through

respectively. Here, Alexa Fluor® 488 tagged $A\beta_{1-42}$ and PDMPO colocalisation was quantified using Volocity software (PerkinElmer, UK) according to Section 2.12.1.

3.2.8 Quantitative Real-Time PCR

ARPE-19 cells (P23-26) were seeded at a density of $1x10^5$ cells per well onto 6-well culture plates that had been precoated with 50μg/ml of fibronectin (Section 2.1). Cells were subsequently cultured for 2 weeks in complete ARPE-19 culture medium prior to use in experiments to ensure confluency. On the day of the experiment, 1μM $A\beta_{1-42}$ working solution or an equal volume of vehicle/sham in working solution was applied to wells for 3 hours at 37°C, 5% CO_2. As described in Section 3.2.7.3, a negative control comprising untreated cells was also included in experiments to assess the effects of vehicle/sham. Following incubation, the culture medium was aspirated, cells were washed in prewarmed culture medium thrice and incubated for 0.5, 3, 24 or 48 hours in a 37°C humidified incubator with 5% CO_2. At each experimental time point RNA extraction was then performed (Section 2.8.2). In total, three experimental replicates were performed with two technical replicates per treatment within each experiment. Next, RNA quality was assessed (Section 2.8.3), cDNA synthesis performed (Section 2.8.4), and QPCR conducted (Section 2.8.6) to determine Cathepsin B mRNA expression in response to $A\beta_{1-42}$ treatment. Specific primer pairs used for QPCR are detailed in Section 2.8.5. Here, the experimental plan with respect to incubation and harvest times was comparable to the cathepsin B assay detailed in Figure 20.

3.2.9 Phagocytosis assay

For the purpose of the POS phagocytosis assay, ARPE-19 cells were seeded onto 50μg/ml fibronectin coated Ibidi glass bottom μ-slides at a density of $1x10^4$ cells/well and cultured for 2 weeks prior to use to ensure a degree of differentiation. 1μM Alexa Fluor® 647 conjugated $A\beta_{1-42}$ or an equal volume of vehicle/sham (Section 2.4) was then applied to post-confluent RPE monolayers for 3 hours to keep in line with previous experiments, before washing thrice in complete culture medium. Untreated wells served as an additional control. Typically, a 23 hour window was left between successive feeding experiments to account for potential inhibitory mechanisms within native RPE that could prevent cargo internalisation[283]. FITC-POS (Section 2.9) were subsequently applied at a concentration of $4\mu g/cm^2$ [284] for 2 hours in a 37°C, 5% CO_2 humidified incubator to facilitate maximum binding of FITC-OS with minimal internalisation[285]. Cells were

then washed thrice in complete culture medium and were incubated at 37°C, 5% CO_2 until experimental time points had elapsed i.e. 4 hours, 8 hours and 20 hours after the initial POS challenge. Cells were then fixed at 4°C in 4% PFA for 30 minutes, washed in 1XPBS, and stored at 4°C awaiting immunofluorescence. Here, the time points employed corresponded to the time taken for POS internalisation, and lysosomal degradation reported previously within the ARPE-19 cell line[48]. As before, all images presented represent the average measurements of the sample cohort. A detailed workflow of the experiment can be seen in Figure 21. Here, confocal micrographs were acquired across 6 separate fields of view per treatment group, over 2 wells, and overlap coefficients were recorded.

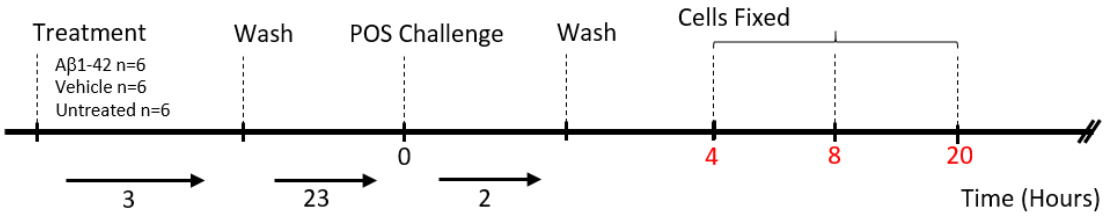

Figure 21: Phagocytosis assay experimental timeline

Timeline showing the sequence of steps performed during the Phagocytosis assay. Cultures were treated with oligomeric $A\beta_{1-42}$ (n=3) or vehicle/sham for 3 hours before cells were washed and incubated at 37°C, 5% CO_2 for 23 hours. The following day, FITC tagged Photoreceptor Outer Segments (POS) were applied to cultures for 2 hours, cells were washed to remove unbound POS and were turned to the incubator for the time points shown in red i.e. 4, 8 and 20 hours. At each time point cells were fixed in 4% PFA for immunofluorescence studies. Untreated cells (n=2) served as a negative control.

3.3 Results

3.3.1 Cell culture model characterisation

3.3.1.1 Expression of RPE cell specific markers

The initial aim of the study was to validate the model through examining the replication of vital RPE morphological/functional features *in vitro.* First, the expression pattern of RPE specific markers was assessed by confocal immunofluorescence microscopy following 2 months in culture to verify structural adaptation and maturation of RPE monolayers. ARPE-19 cultures were probed for the early epithelial tight junction protein ZO-1 and the mid-late integral tight junction protein occludin to assess the formation of BRB complexes. The expression pattern of ZO-1 was consistent with native RPE, exhibiting typical epithelial expression as a continuous band at the point of cell to cell contact[286] (Figure 22, Ai-Aiv). However, a low level of cytoplasmic and nuclear staining was also evident. In contrast, occludin staining revealed a less defined expression at the cell periphery compared to ZO-1 (Figure 22, Bi-Biv) with a non-uniform pattern of tight-junction complex formation, and significant cytoplasmic staining.

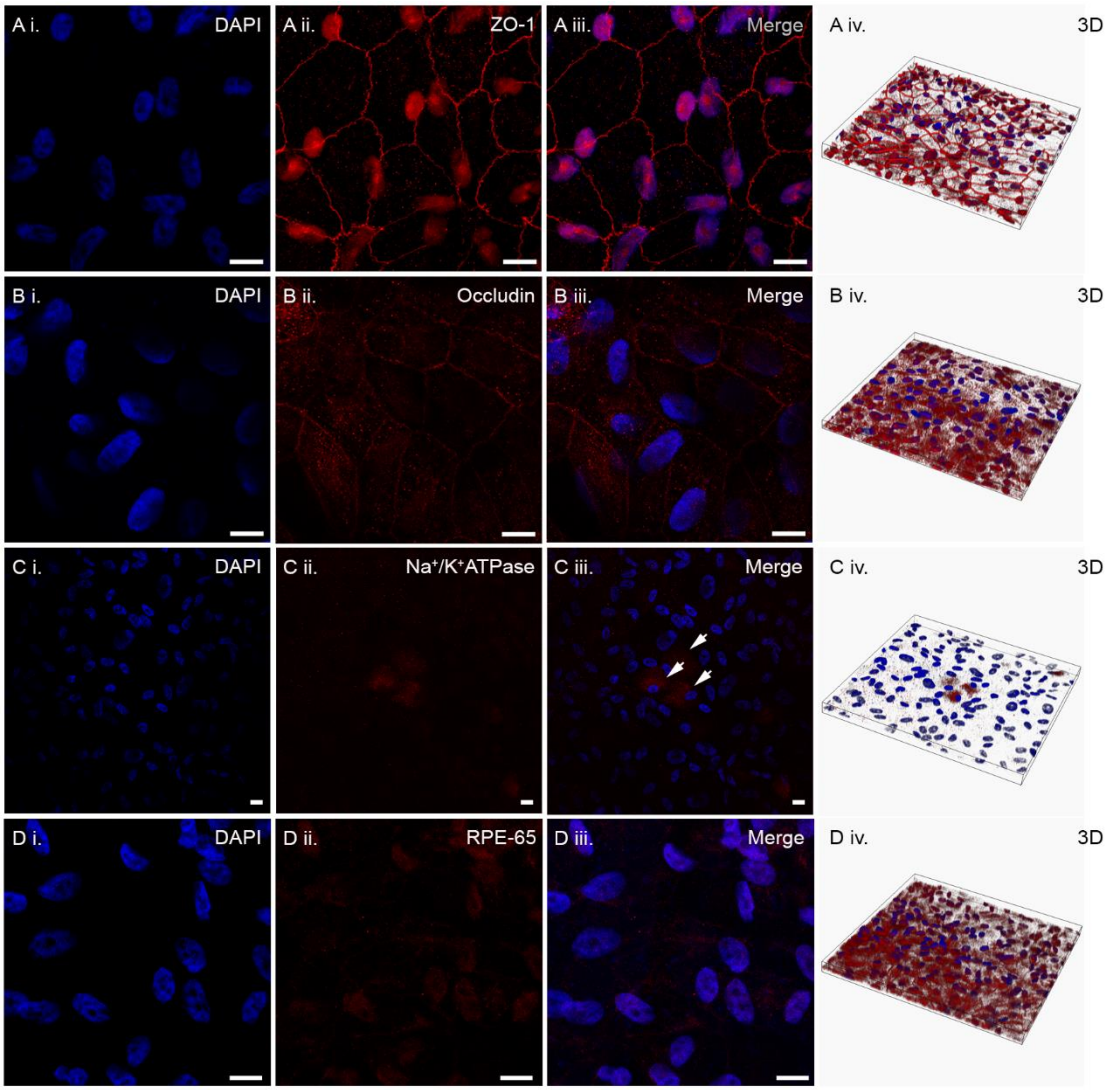

Figure 22: Expression of RPE specific markers within the ARPE-19 cell line.

Immunofluorescence confocal micrographs illustrating the expression pattern of tested antibodies (red) in the ARPE-19 cell line after 2 months in culture. Nuclei are counterstained with DAPI (blue). **Ai-Aiv.** ARPE-19 cells express the early tight junction protein ZO-1 (red) in the typical pattern expected with continuous labelling at the point of cell-cell contact. **Bi-Biv.** The distribution of mid-late tight-junction protein Occludin was discontinuous along intercellular junctions indicating limited expression at junctional complexes. **Ci-Civ.** Na^+/K^+ ATPase was expressed by a select population of cells at the apical surface within confluent monolayers. **Di-Div.** RPE-65 immunostaining (red) was employed to assess RPE cell specificity and revealed a punctate, cytoplasmic expression pattern across entire fields of view. **Aiv-Div.** 3D representations of expression patterns to demonstrate antibody distribution through the z-axis. Immunostaining patterns presented are representative of all fields of view acquired. En face images show a single z position through the cell. Scale bar represents 10μm. Abbreviations: DAPI; 4',6-diamidino-2-phenylindole. Republished from Lynn *et al.* (2018)[287] under the terms of the Creative Commons Licence.

The polarised phenotype of the RPE (Section 1.2.3.1) is essential in carrying out RPE functions including the absorption of stray light, the directional secretion of proteins, phagocytosis of shed POS and its integral role in the visual cycle[22 30]. This is facilitated by a repertoire of apical and basal associated membrane proteins. Therefore, apicobasolateral specialisation of cultured RPE cells was assessed. In the first instance by expression of the polarity protein Na^+/K^+ ATPase, which is implicated in the regulation of a well-differentiated, polarised epithelial phenotype[288]. Interestingly, Na^+/K^+ ATPase was limited to sub-populations of cells (Figure 22, Ci-Cii) with the majority of RPE showing weak or no Na^+/K^+ ATPase staining. To gain further insight into the expression of Na^+/K^+ ATPase within sub-populations, distribution though the z-axis was also examined (Figure 23). Here, Na^+/K^+ ATPase exhibited polarised expression towards the RPE apical surface. 3D reconstructions provide limited information as to apical distribution due to the step-size between consecutive z-stacks, but do highlight the sparsity of Na^+/K^+ ATPase expressing cells within ARPE-19 monolayers.

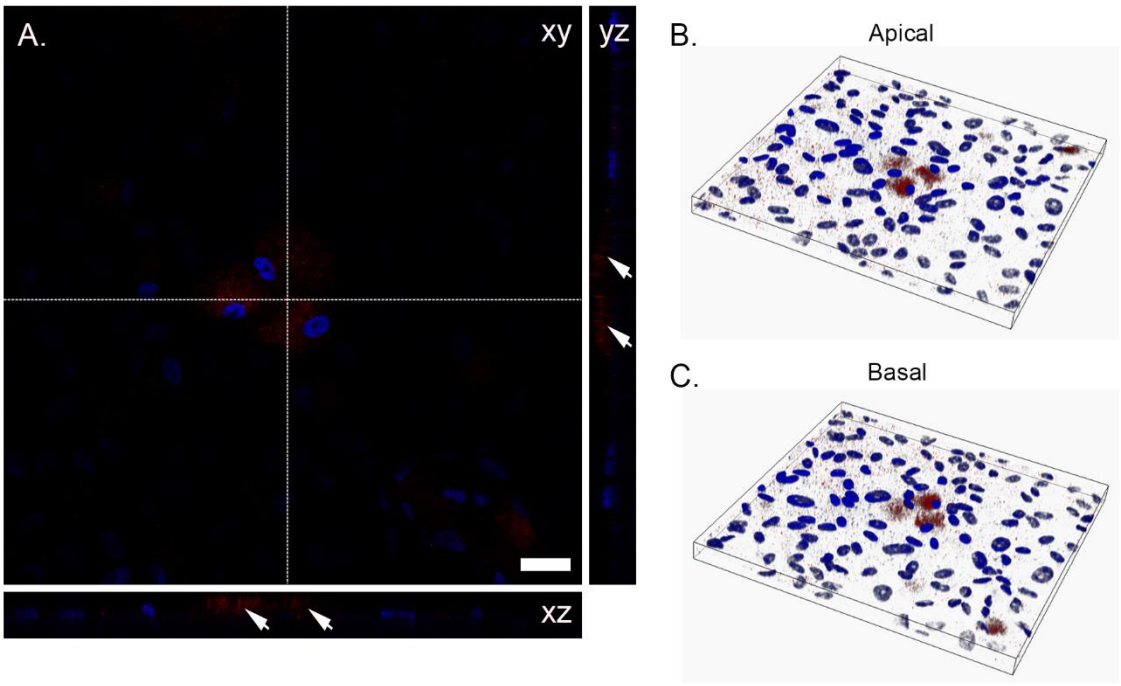

Figure 23: Expression of Na^+/K^+ ATPase in ARPE-19 cells

A. Confocal immunofluorescence micrograph showing the distribution pattern of Na^+/K^+ ATPase (red) in 2 month old ARPE-19 cultures. Nuclei are counterstained with DAPI (blue). The en face image shows a single z-plane through the apical surface of the monolayer. Panels below and to the right of the en face image correspond to the xz-axis and yz-axis of the cross sectional area shown (white dotted line) respectively. Note the apical expression of Na^+/K^+ ATPase in z-sectional views (white arrows). **B-C.** 3D representations of Na^+/K^+ ATPase immunostaining from the apical and basal perspective highlighting the apical distribution. Scale bar corresponds to 20μm. Abbreviations: DAPI; 4',6-diamidino-2-phenylindole. Republished from Lynn *et al.* (2018) under the terms of the Creative Commons License.

Finally, the expression pattern of the retinoid isomerohydrolase, RPE-65, was assessed to confirm RPE specificity. This exhibited a punctate expression pattern within the cell cytoplasm across all cells within the field of view (Figure 22, Di-Div) confirming monolayers were genuinely of RPE origin. Secondary antibody controls for antibodies can be seen in Figure 56, 0.

3.3.1.2 Ultrastructural adaptations of RPE monolayers

To further investigate the morphology and apicobasolateral specialisation of ARPE-19 monolayers, ultrastructural adaptions of cells grown on Transwell® inserts were analysed by TEM. Despite their limited barrier integrity, after 2 months in culture ARPE-19 cells displayed polarised membrane domains, with well-defined apical microvilli (Figure 24, B & D) and basal infolds (Figure 24, A & D). Apically localised pigment granules (Figure 24, B & D) were also evident which are often lost in culture[35]. Cell polarisation was also apparent in the distribution of intracellular organelles with putative lysosomes, identified as membrane bound vesicles of varying electron densities, along the apical-basal polarity axis (Figure 24, E), and abundant basal mitochondria (Figure 24, C). Evidence of putative lysosomal compartments at an ultrastructural level was particularly relevant in validating the use of this system for investigating the effects of Aβ on the endo/lysosomal system. Cellular junctions including tight junctions (Figure 24, F & G) and adherence junctions (Figure 24, F) were also seen in micrographs, typically found co-distributed along adjacent cell membranes and in some instances associated with the presence of desmosomes. Tight junctions were localised to the apical axis of the RPE at the point of cell to cell contact and were visualised as darker points of contact between cells in high magnification TEM sections.

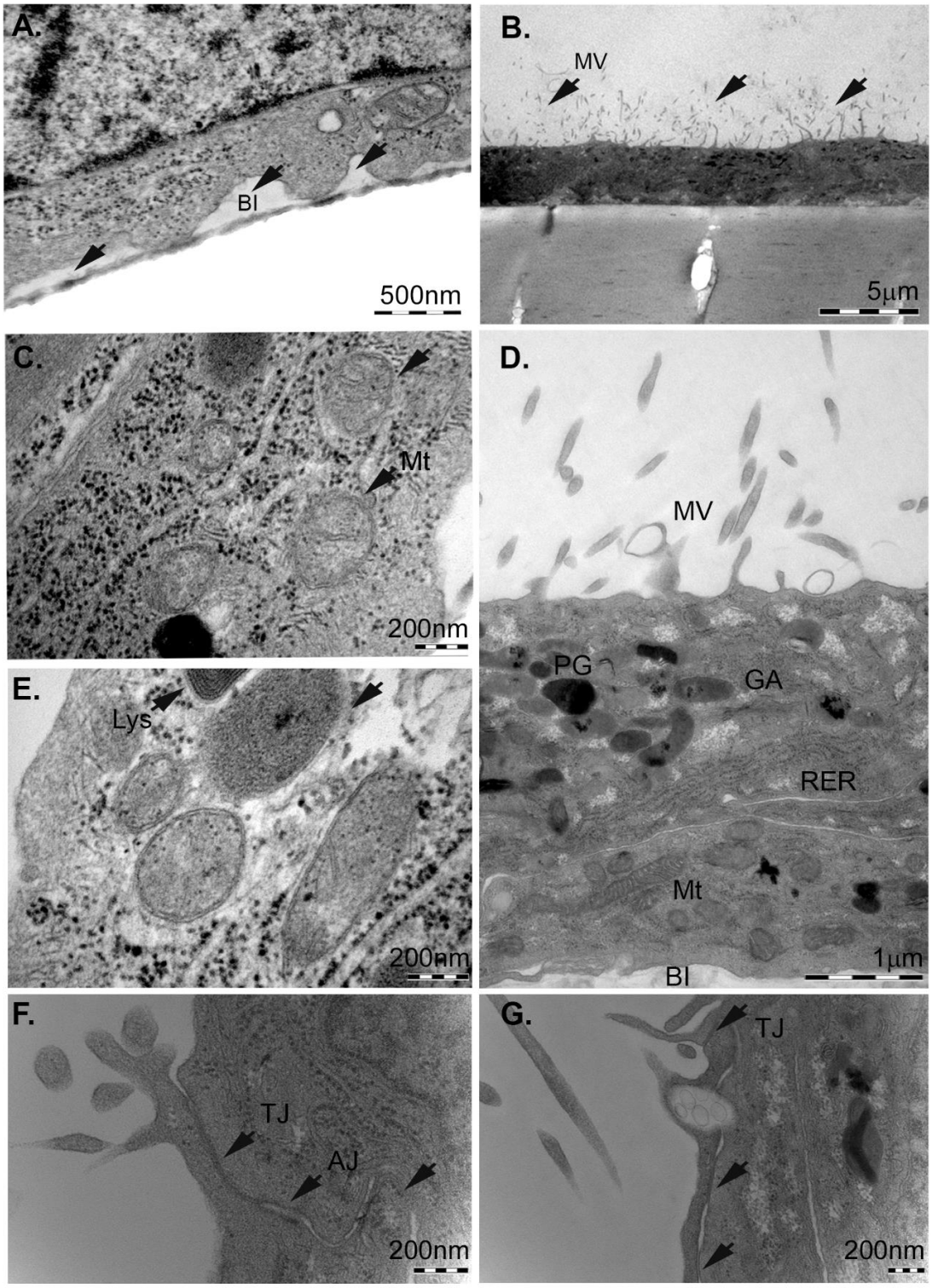

Figure 24: Ultrastructural adaptations of ARPE-19 monolayers.

Transmission electron microscopy (TEM) was employed to assess the ability of ARPE-19 monolayers to form structural adaptations akin to native RPE. **A.** Basal Infolds (Bl) on the basal surface of the epithelium in close proximity to the Tranwell® PET membrane. **B.** Apical Microvilli (MV). **C.** Abundant Mitochondria (Mt) localised to the basal membrane, identified as double membrane bound structures with cristae. **D.** Micrograph showing the polarised arrangement of structures/organelles in monolayers with apical Microvilli (MV) and Pigment Granules (PG), Golgi Apparatus (GA) and Rough Endoplasmic Reticulum (RER) distributed along the apical-basal polarity axis, and basal mitochondria (Mt) and infolds (Bl). **E.** Putative lysosomes identified as membrane bound vesicles of different electron densities. **F-G.** Tight Junction (TJ) complexes were evident at the apical surface of the epithelium, anterior to an Adherens Junction (AJ). Structures of interest are indicated by black arrows. Republished from Lynn *et al*. (2018)[287] under the terms of the Creative Commons Licence.

3.3.1.3 Blood-retinal barrier formation

In order to evaluate the functional ability of tight-junction complexes observed in earlier studies (Section 3.3.1.1 and Section 3.3.1.2), TEER measurements were performed over an 11 week period. Over the experimental time course, RPE monolayers showed a gradual increase in TEER despite an unexplained yet consistent decline between weeks 3 and 5. After 6 weeks in culture, ARPE-19 monolayers appeared to establish a stable barrier with an average TEER of 40.72Ω.cm^2, in line with previous reports[289]. By week 7, it is evident that there is a significant decline in the variation of subsequent recordings, indicating a peak/plateau in the BRB maturation of cultures. This is further demonstrated by Figure 25B, which shows absolute % change of recordings from the previous week to quantify barrier stability.

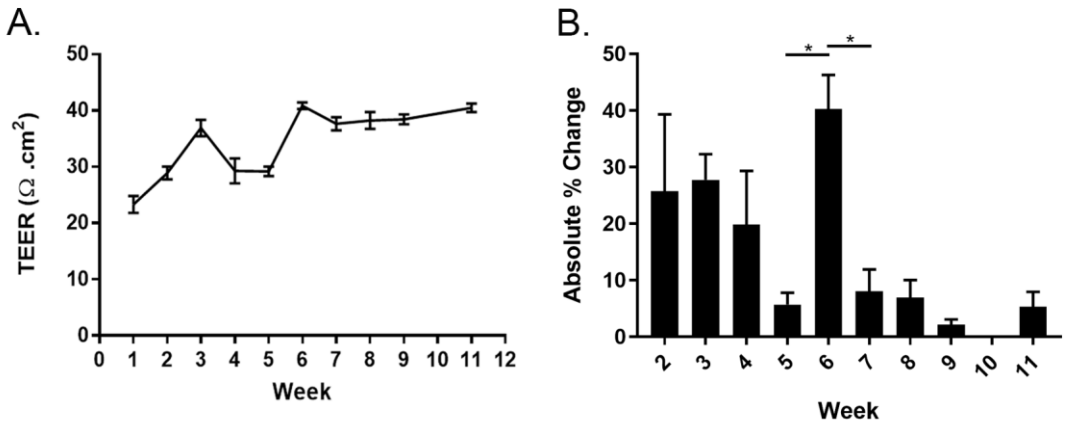

Figure 25: Transepithelial electrical resistance properties of ARPE-19 monolayers

Transepithelial electrical resistance (TEER) measurements of ARPE-19 monolayers were measured at 1-week intervals post seeding for a period of 11 weeks to assess barrier formation. **A.** Graph to show the TEER (n=3) across the 11 week time course. Results are plotted as mean ± SEM. **B.** Graph showing absolute % change from the previous measurement. Statistical comparisons were made using one-way ANOVA with Tukey's multiple comparisons to assess variation over the experimental time course. No measurement was taken at week 10. ARPE-19 cells appear to establish a relatively stable barrier after 6 weeks in culture. Panel A republished from Lynn *et al.* (2018)[287] under the terms of the Creative Commons Licence.

3.3.1.4 Directional protein secretion by RPE cultures

The artificial BRB created by the porous membrane in combination with ARPE-19 cells results in a system in which inter-compartmental communication must occur via the RPE monolayer. Evidence of polarisation was observed via confocal microscopy and TEM in Sections 3.3.1.1 and 3.3.1.2 respectively. Thus, our experiments next sought to ascertain whether this translated to polarised RPE function by evaluating the secretion profile of *in vitro* RPE. ELISA quantification was performed on conditioned apical and basal media harvested from 7 week old RPE

cultures to determine the level and directional secretion of several cytokines from the RPE (Figure 26). PEDF and VEGF are typically used to assess polarised function in *in vitro* RPE cultures[290 291] and were therefore used as outcome measures of functional polarity in this study. PEDF concentrations were comparable in apical (16.95 ± 0.72ng/ml) and basal (25.05 ± 3.92ng/ml) compartments (p= 0.1119). However, VEGF was significantly higher (p<0.0002) in basal conditioned media (2.852 ± 0.145ng/ml) as compared to apical conditioned media (0.942 ± 0.035ng/ml).

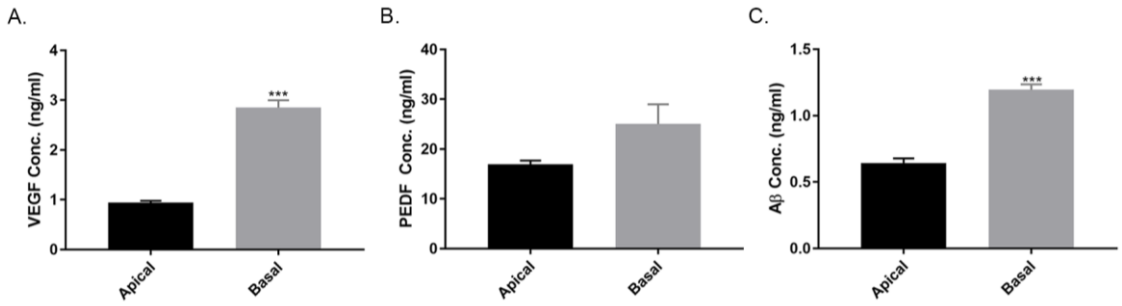

Figure 26: ELISA quantification of proteins produced by ARPE-19 cultures.

Quantification of specific proteins was performed on conditioned media harvested from apical and basal compartments of 2 month old ARPE-19 monolayers (n=3) to assess polarised secretion, 72 hours after a complete media change. **A.** Vascular endothelial growth factor (VEGF) was significantly lower in apical conditioned media (0.942 ± 0.035ng/ml), p<0.0002 compared to basal conditioned media (2.852 ± 0.145ng/ml). **B.** Pigment epithelium-derived factor (PEDF) concentrations were comparable in apical (16.95 ± 0.72ng/ml) and basal (25.05 ± 3.92ng/ml) compartments, p= 0.1119. **C.** Total Aβ was significantly higher in basal compartments (1.196 ± 0.0397ng/ml) compared to the apical chamber (0.645 ± 0.033ng/ml), p=0.0004. Results are expressed as mean ± SEM. Statistical comparisons were made using the unpaired student's t-test. A and B republished from Lynn *et al.* (2018)[287] under the terms of the Creative Commons Licence.

Thus far, reports of Aβ secretion from the RPE have been limited to uni-compartmental *in vitro* studies which lack information regarding directional secretion and which may provide insights into the ocular function of Aβ. As such, an ELISA detection kit for total Aβ ($A\beta_{1\text{-}28}$, $A\beta_{1\text{-}40}$, and $A\beta_{1\text{-}42}$) was employed to quantify total levels of Aβ within both apical and basal RPE conditioned media. Results showed that a total of 0.645 ± 0.033ng/ml Aβ was present within apical compartments and 1.196±0.0397ng/ml within basal compartments. Statistical tests confirmed this difference to be significant (p=0.0004) indicating predominantly basolateral secretion of Aβ by the RPE.

3.3.2 Preparation and validation of oligomeric $A\beta_{1\text{-}42}$

Section 3.3.1 validates the use of Transwell® systems for studies relating to RPE function and morphology, which demonstrate essential features of RPE *in situ*. An

Aβ source was next required to investigate Aβ effects on the RPE. As discussed in Section 1.6, the RPE is exposed to multiple Aβ species within the retinal environment including soluble oligomers, protofibrils, and mature amyloid fibrils[202 208 209], with soluble Aβ oligomers thought to constitute the majority of Aβ present within drusen[208]. The primary aim of this experiment was therefore to isolate oligomer enriched Aβ fractions for use in subsequent experiments to recapitulate RPE Aβ exposure with age and in early-AMD. This was achieved using a validated and well-established method of Aβ preparation that is widely utilised in the field of Aβ structural biology and AD research[176 247 292].

3.3.2.1 TEM to characterise the dynamics of Aβ aggregation

TEM was conducted on $A\beta_{1-42}$ samples at intervals following preparation to identify primary Aβ conformers present and to characterise aggregation dynamics. Previous reports indicate a predominance of oligomeric $A\beta_{1-42}$ up to 3 hours[293] post preparation with oligomer enriched fractions at 1.5 to 2 hours[176], and fibril formation within less than one week[293]. Distinct morphological Aβ conformations were observed over the 72 hour time course. TEM micrographs demonstrate small amorphous 15-75nm aggregates with a granular appearance at 1 hour, and small oligomers by 1, 1.5 and 2.5 hours. The appearance of protofibrils was not observed until 2.5 hours (Figure 27, C). Beyond this, proteins aggregate with a more filamentous nature associated with heavier negative staining (Figure 27, D, E & F). It is worth noting that fibrils formed at 48 hours exhibited greater structural organisation compared to those formed at 24 hours suggesting a change in structural organisation as fibres mature. This time course is concordant with previous reports which also conducted extensive characterisation with a variety of structural techniques[176 293]. Therefore, experiments undertaken in this thesis have utilised $A\beta_{1-42}$ harvested at 1.5 hours to obtain oligomer enriched preparations. Structures observed in Aβ TEM samples were absent in vehicle/sham (Figure 27, G).

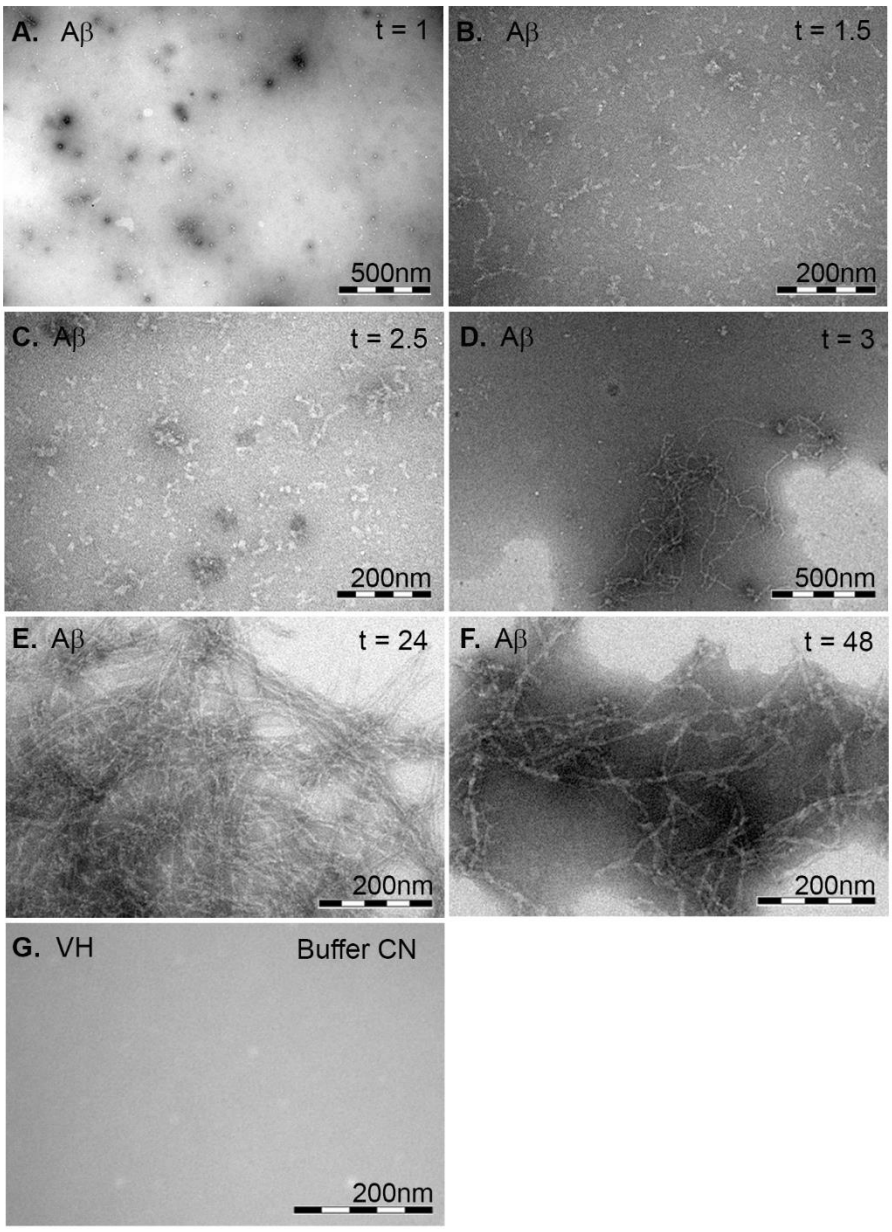

Figure 27: Aggregation dynamics of human recombinant $A\beta_{1-42}$ preparations.

Experimental time course showing transmission electron micrographs of 107.4μM $A\beta_{1-42}$ assembled *in vitro* after incubation on ice for **A.** 1 hour **B.** 1.5 hours **C.** 2.5 hours **D.** 3 hours **E.** 24 hours and **F.** 48 hours. Images are representative of structures seen in preparations at each time point. The highest concentration of Aβ oligomers was present between 1.5 and 3 hours post preparation. Protofibrils were apparent at 3 hours post preparation which progressively aggregated to produce mature fibrils by 24 and 48 hours. **G.** Note the absence of any negatively stained structures in the vehicle/sham control.

3.3.2.2 Immunogold labelling of Aβ with 82E1

To validate the identity of Aβ structures observed in Section 3.3.2.1 negative staining in combination with immunogold labelling for the Aβ specific antibody, 82E1, was performed on samples at various time points post preparation. A degree of labelling was observed at all tested time points, visible as black spots owing to the electron density of the 5nm gold particles conjugated to the detector antibody

(Figure 28). The local concentration of gold particles varied significantly with increased labelling being associated with more complex structural conformers such as fibrils (Figure 28, F). At 1 hour post preparation, isolated gold particles were evident (Figure 28, A), but as the time course progressed these accumulated along the length of protofibrils (Figure 28, C & D), and appeared to saturate mature fibrils at 72 hours (Figure 28, F). No immunogold labelling was observed in secondary antibody, isotype or vehicle controls thus confirming labelling and structural specificity.

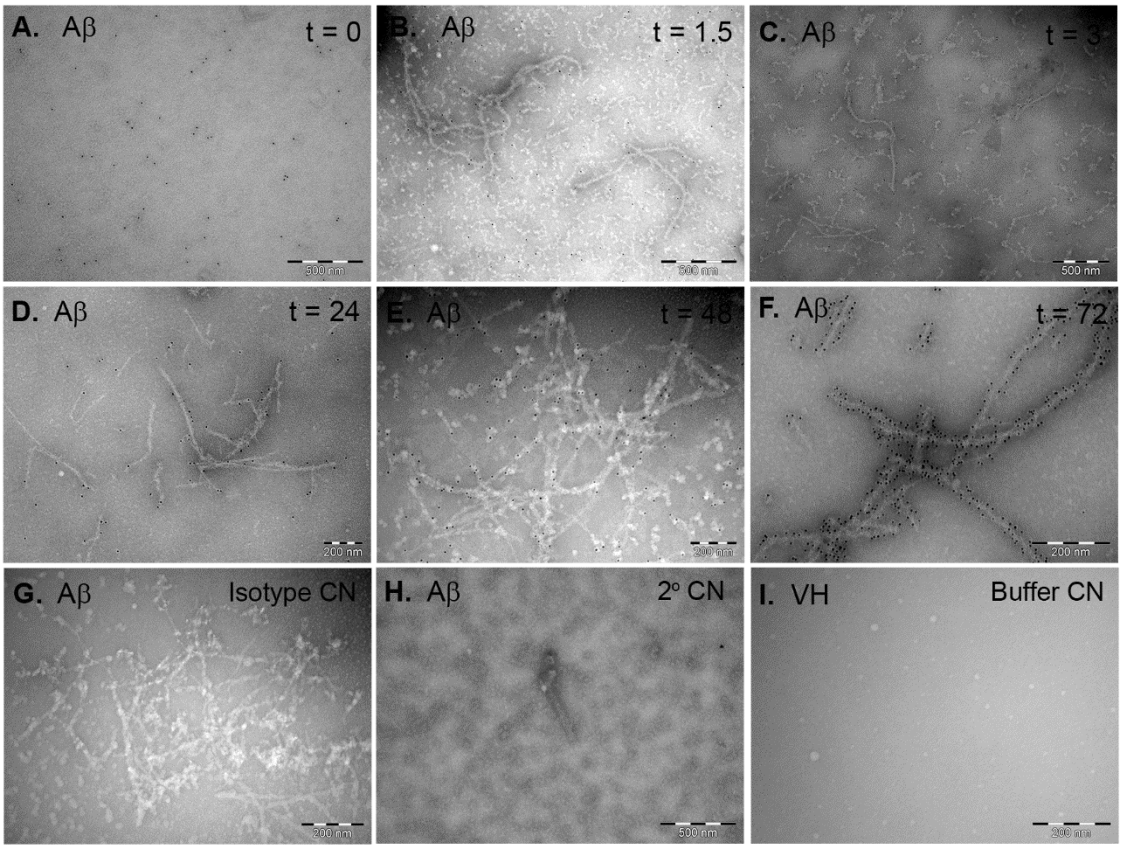

Figure 28: Immunogold labelling of human recombinant $A\beta_{1-42}$ preparations.

Transmission electron microscopy (TEM) immunogold labelling showing $A\beta_{1-42}$ assembled *in vitro* after incubation on ice for **A.** 0 hours **B.** 1.5 hours **C.** 3 hours **D.** 24 hours **E.** 48 hours and **F.** 72 hours. At each experimental time point samples were fixed in 4% formaldehyde in 0.1M PIPES and subjected to immunogold staining with anti-human Aβ specific antibody, 82E1(black dots). Images are representative of structures seen in preparations during the experimental time course. At all time points visible structures labelled with 82E1 (black dots), validating the presence of Aβ within samples. **G-H.** Note that no labelling was observed upon immunogold staining with the ZO-1 isotype control or in the secondary 5nm gold anti-mouse antibody control **I.** Similarly no structures or immunogold staining were observed in the vehicle/sham control.

3.3.2.3 Endotoxin testing of Aβ preparations

The ability of bacterial endotoxin to exert detrimental effects on cell physiology and function is well documented[294]. Hence, pyrogen free reagents/treatments are of paramount importance with regards to the reliability and repeatability of cell culture experiments. $A\beta_{1-42}$ samples and vehicle/sham were therefore subject to LAL endotoxin testing to quantify endotoxin units (EU/ml) in preparations at random and thus eliminate the possibility of pyrogen confounding experimental results. Test results can be seen in Table 22. All tests performed were considered valid as the positive product control recovery value was approximately 200%.

Table 22: Evaluation of bacterial endotoxin in $A\beta_{1-42}$ preparations

Endotoxin levels in $A\beta_{1-42}$ and buffer (vehicle/sham) preparations evaluated by *Limulus* amebocyte lysate tests. A % recovery of 50-200% was considered a valid test. The $A\beta_{1-42}$ preparation measured was 106.4μM. Abbreviations: EU; Endotoxin Units.

Test Sample	EU/ml	EU/mg	% Recovery
$A\beta_{1-42}$ Preparation	<0.5	<3	200
$A\beta_{1-42}$ Buffer	0.38	2.41	205

3.3.3 Endolysosomal localisation of $A\beta_{1-42}$

3.3.3.1 Assessment of Aβ and LysoSensor Yellow/Blue DND-160 colocalisation

The ability of oligomeric $A\beta_{1-42}$ to localise within lysosomes was investigated using confocal microscopy following staining of endocytic compartments with PDMPO. Assessment was conducted after incubation with oligomeric $A\beta_{1-42}$ for 2.5 hours and further incubation at 37°C with 5% CO_2 overnight to allow sufficient time for Aβ to reach lysosomes. Fluorescently tagged Aβ colocalised with PDMPO labelled vesicles, suggesting distribution within late endocytic and/or lysosomal compartments (Figure 29). Areas of colocalisation are indicated as areas of yellow in Figure 29A, where white arrows demonstrate a similar pattern of staining when both channels were viewed in isolation. Of note, lysosomal $A\beta_{1-42}$ appeared to associate with an enlarged/swollen lysosomal phenotype. A compiled AVI file of the multiple z-stacks acquired is shown in electronic Appendix A allowing better visualisation of colocalisation.

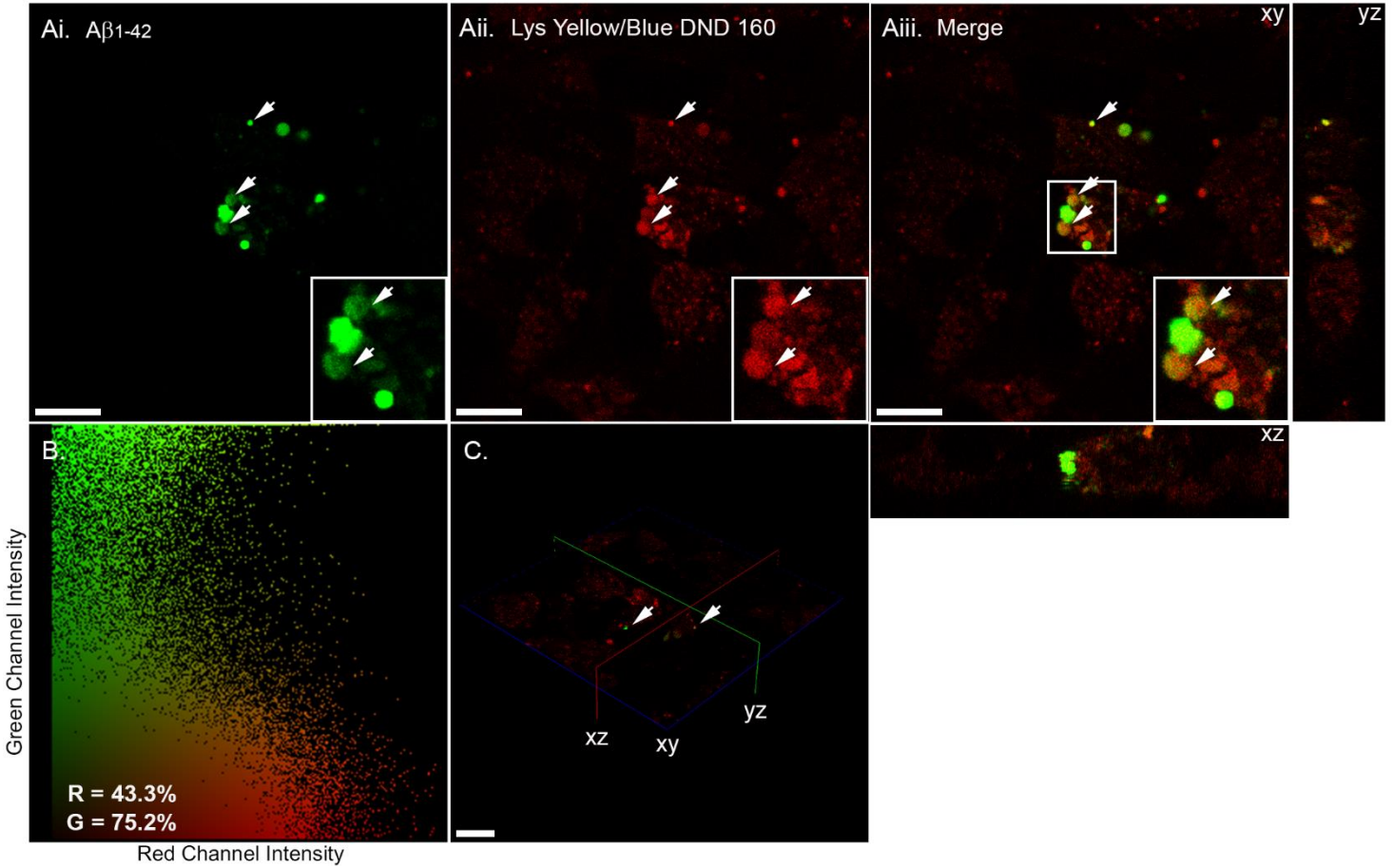

Figure 29: Assessment of LysoSensor Yellow/Blue DND-160 and Alexa Fluor 488 tagged $A\beta_{1-42}$ colocalisation in the ARPE-19 cell line.

Ai-Aiii. Confocal micrographs to assess colocalisation of Alexa Fluor 488 tagged $A\beta_{1-42}$ (green) with LysoSensor Yellow/Blue DND-160 (PDMPO; red) in ARPE-19s. Areas of colocalisation (white arrows) are seen as yellow in the merged en face image. Panels below and to the right correspond to the xz-axis and yz-axis of the cross sectional area shown respectively. Note the intracellular location of $A\beta_{1-42}$. **B.** Scatterplot of green ($A\beta_{1-42}$) and red (PDMPO) pixel intensities for panel A. The results indicate 43.3% or red (PDMPO) is colocalised with green ($A\beta_{1-42}$) and 75.2% of green ($A\beta_{1-42}$) is colocalised with red (PDMPO). Intensities below the threshold determined by the Costes *et al.* algorithm for the x and y axis are not shown (black). **C.** 3D view of colocalisation within ARPE-19 cells to highlight the intracellular distribution of $A\beta_{1-42}$. Scale bars correspond to 40μm.

It is clear from Figure 29 that a significant proportion of the Alexa Fluor® tagged Aβ and PDMPO signals were disperate. An automated and thus unbiased algorithm was therefore used to quantify the extent of Aβ colocalisation with PDMPO-positive vesicles. Scatterplots for red vs. green channel intensities were generated for 6 individual cells over three wells, and were subject to the Costes *et al.* statistical algorithm to determine maximum threshold intensities and quantify the extent of fluorophore overlap. For the image displayed in panel A, 43.3% of red and 75.2% of green were calculated as colocalised with green ($A\beta_{1-42}$) and red (PDMPO) respectively (Figure 29,B). Costes overlap coefficients, M1 and M2, for the 6 cells analysed are shown in Table 23. On average, 40.7 ± 8.6% of $A\beta_{1-42}$ was reported to colocalise with PDMPO, supporting the presence of Aβ within RPE lysosomes. Standard deviation of statistical data indicated a degree of spread within overlap coefficients, demonstrating variation in the amount of Aβ/PDMPO colocalisation within cells. However, all data points, except those from cells 2 and 3, fell within one standard deviation of the mean. This, in addition to the calculated SEM for both M1 and M2 coefficients, which is close to 0, validates a sample cohort representative of the whole lysosome population.

Table 23: Quantification of LysoSensor Yellow/Blue DND-160 and Alexa Fluor 488 tagged $A\beta_{1-42}$ colocalisation in the ARPE-19 cell line

Costes overlap coefficients M1 and M2 indicate the percentage of red (LysoSensor Yellow/Blue DND-160 (PDMPO) colocalised with green ($A\beta_{1-42}$) and green colocalised with red respectively. The results show 40.7 ± 8.6% of $A\beta_{1-42}$ was colocalised with PDMPO following acute exposure to $A\beta_{1-42}$ for 2.5 hours, and overnight incubation at 37°C with 5% CO_2. Measurements are presented for 6 cells across three fields of view. Quantification was performed in the Volocity software suite (PerkinElmer, UK).

	Colocalisation Coefficient	
Cell	M1	M2
1	0.177	0.543
2	0.433	0.752
3	0.2	0.175
4	0.189	0.256
5	0.381	0.406
6	0.175	0.309
Average	**0.259**	**0.407**
STDEV	0.116	0.212
SEM	0.047	0.086

As Alexa Fluor® tagged $A\beta_{1-42}$ was employed in the above and subsequent colocalisation studies, an experiment was required to verify sustained conjugation of the Alexa Fluor® tag following extended incubation. The time point we tested corresponded to the longest Aβ exposure of RPE cells employed in our experiments. Cultures were exposed to $A\beta_{1-42}$ for 48 hours and immunostained with 82E1 to assess the extent of Aβ colocalisation with the 488 signal (Figure 30). As shown in Figure 30, all Alexa Fluor® 488 appeared to colocalise with 82E1 upon visual inspection, thus confirming sustained conjugation. Occasional red regions (82E1) were observed upon merging of channels, which presumably correspond to endogenous human (and therefore untagged) Aβ within ARPE-19 cells.

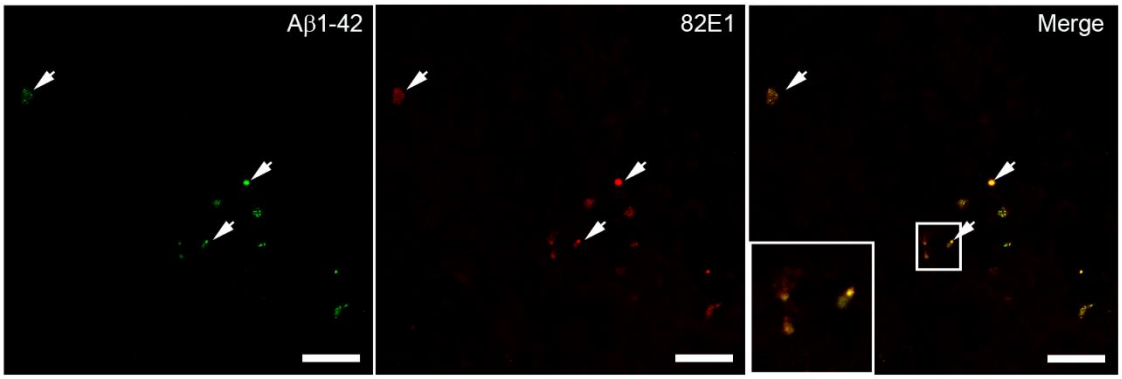

Figure 30: $A\beta_{1-42}$ and Alexa Fluor tag conjugation following extended incubation.

Confocal immunofluorescence micrographs to demonstrate continued conjugation of $A\beta_{1-42}$ preparations with the Alexa Fluor tag. At 48 hours post initial $A\beta_{1-42}$ application, the Alexa Fluor 488 tag (green) was seen to colocalise (white arrows) with Aβ (red). The merged view (right) demonstrates areas of colocalisation (yellow). Areas of red in isolation are likely to be attributable to endogenous Aβ within the ARPE-19 cell line. Scale bars correspond to 40μm.

3.3.4 $A\beta_{1-42}$ effects on RPE lysosomal acid hydrolases

3.3.4.1 Effect of $A\beta_{1-42}$ on Cathepsin B activity

Following our previous studies that showed $A\beta_{1-42}$ colocalising with RPE endocyctic/lysosomal compartments (Figure 29), we next sought to investigate how major lysosomal proteolytic enzymes respond to $A\beta_{1-42}$ exposure. Cathepsin B represents a major RPE cysteine protease that is involved in proteolytic degradation of cargo through the endolysosomal pathway and therefore presented a prime candidate to investigate Aβ's impact on the lysosome. As illustrated in Figure 31, increased Cathepsin B activity was observed at 0.5 ($p<0.0001$, $p<0.0001$) and 3 hours ($p=0.0095$, $p<0.0001$) after acute Aβ exposure relative to vehicle/sham and untreated baseline controls respectively. However, by 24 hours, the activity in Aβ cultures was statistically insignificant compared to vehicle/sham treated cultures

(p>0.9999), suggesting that following Aβ internalisation Cathepsin B levels return towards baseline activity. This is supported by the data obtained at 48 hours, which reported no change in activity between Aβ and vehicle/sham (p>0.9999), or untreated cultures (p=0.1490). To further assess the effects of Aβ on Cathepsin B activity over time, Magic Red® intensity was also plotted as a fold-change from vehicle/sham cultures for each time point over the three biological replicates (Figure 32). Here, Cathepsin B exhibited a comparable increase in activity at 0.5 hours, but was statistically insignificant relative to later time points. Similarly, reported pixel intensities representing Cathepsin B activity in $A\beta_{1-42}$ treated cultures were comparable at 3, 24 and 48 hours. This suggests an initial increase in Cathepsin B activity after $A\beta_{1-42}$ exposure, followed by a decline in enzyme activity between 0.5 and 3 hours.

The data presented provides novel insights into how RPE lysosomal hydrolases respond to the internalisation of Aβ, and supports a role for late endosomes and lysosomes in the processing of this highly toxic and aggregate-prone protein. In particular, the rapid response in enzyme activity at 0.5 hours is indicative of an important role for Cathepsin B in this process. Thus, we next sought to determine whether the observed up-regulation in lysosomal Cathepsin B activity was attributable to increased enzymatic activity, or the result of a transcriptional response following $A\beta_{1-42}$ internalisation.

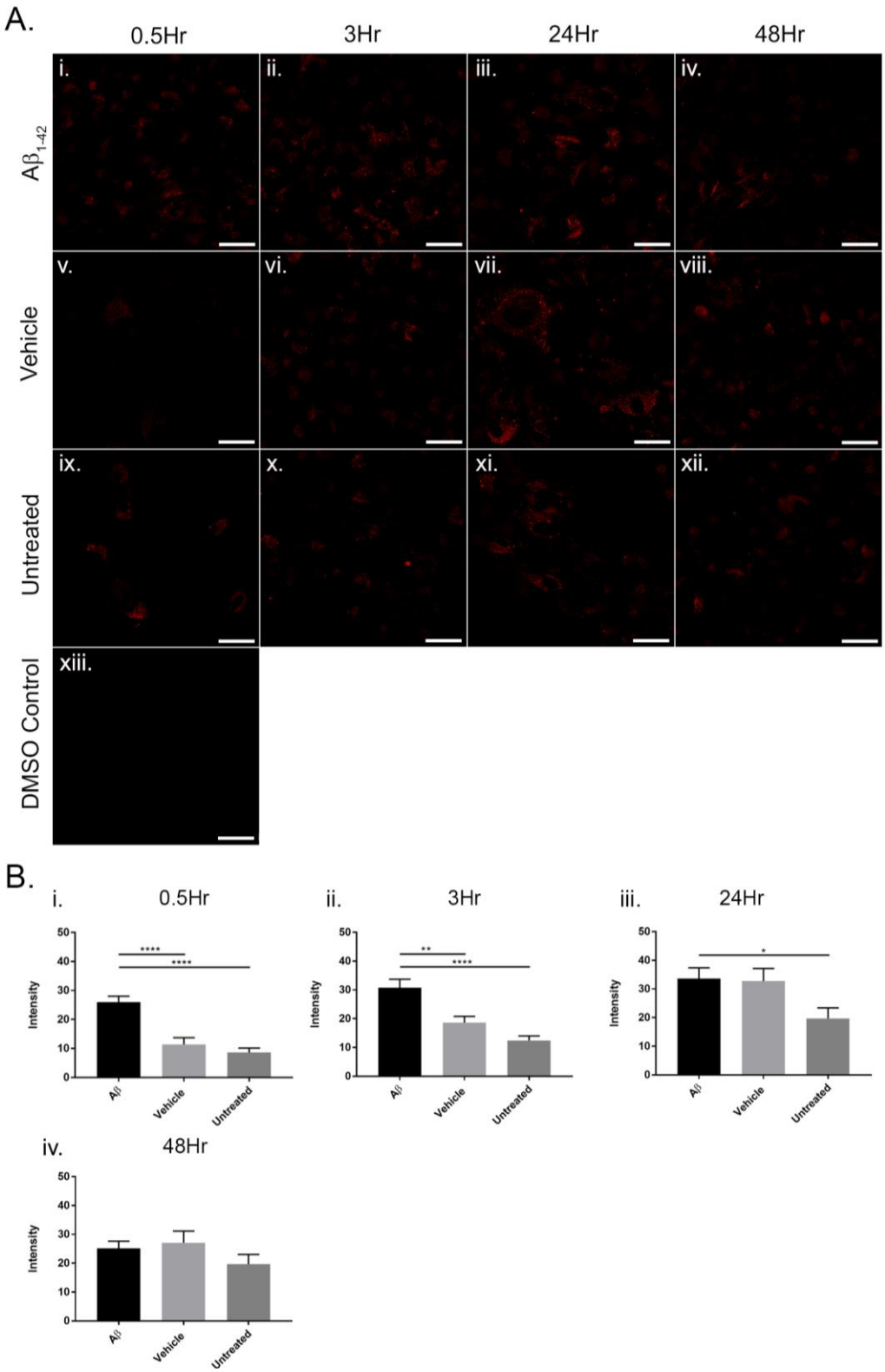

Figure 31: Oligomeric Aβ$_{1-42}$ increased Cathepsin B activity in ARPE-19 cells.

Magic Red® assay measuring Cathepsin B activity following acute oligomeric Aβ$_{1-42}$ exposure (3 hours). **Ai-xiii.** Representative confocal micrographs taken across single z-planes showing Magic Red® fluorescence (red) in response to treatment. No fluorescence signal was detected in DMSO controls. Scale bar represents 40μm. **B.** Quantification of Magic Red® fluorescence intensity from Aβ$_{1-42}$ (n=30), vehicle/sham (n=30) and untreated (n=20) images obtained across 3 independent experiments. Data is presented as mean pixel intensity ± SEM. Kruskal-Wallis with Dunn's multiple comparisons assessed statistical significance which is denoted as **** P<0.0001 and *P<0.05. Aβ$_{1-42}$ induced increased levels of Cathepsin B activity at 0.5 and 3 hours following initial exposure relative to controls.

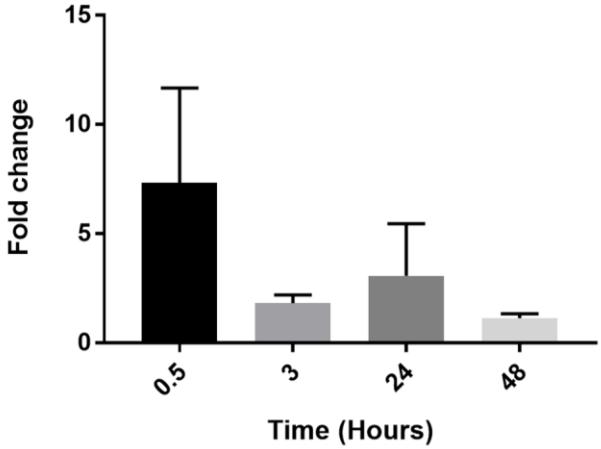

Figure 32: Temporal effects of lysosomal $A\beta_{1-42}$ on Cathepsin B activity.

Alternative representation of Figure 30, B showing Magic Red® fluorescence intensity in response to $A\beta_{1-42}$ as a function of time. Data is presented as mean fold change from vehicle for each of the biological replicates ± SEM (n=3). Changes in Cathepsin B activity between experimental time points were assessed using Kruskal-Wallis with Dunn's multiple comparisons, but found to be statistical insignificant.

3.3.4.2 Effect of $A\beta_{1-42}$ on Cathepsin B gene expression

The ability of an $A\beta_{1-42}$ induced transcriptional response to increase Cathepsin B activity within RPE cells was evaluated by QPCR at identical time points to the Magic Red® assay, in an attempt to assess the correlation between Cathepsin B mRNA expression and activity measured. However, this first required the identification of an appropriate reference gene.

Reference genes are internal reaction controls required for QPCR normalisation to account for intra and inter-kinetic variations that result from sample preparation procedures[295]. To produce valid results, reference genes must meet several important criteria. Transcription must exhibit minimal variability and remain unaffected by experimental factors, as well as specificity to a sequence different from that of the target gene[295 296]. To adhere to such criteria, housekeeping genes with roles in basic cellular metabolism are commonly employed including Beta Actin (ACTB) and glyceraldehyde-3-phosphate dehydrogenase (GAPDH). However, increasing literature suggests variation in housekeeping gene expression under different experimental conditions bringing their validity into question[296]. Accurate QPCR analysis necessitates careful reference validation prior to quantification, which is largely deficient in the literature.

A panel of reference genes was therefore evaluated for their potential use as internal normalisation controls (Figure 33). Primers were tested on experimental samples spanning all time points, treatments and experimental replicates to

identify a reference gene that exhibited minimal variability. Candidate genes exhibiting a variety of roles were tested to minimise the possibility of regulatory co-variation including genes involved in translation control (eukaryotic translation initiation factor 4A, EIF4A2) and mitochondrial energy metabolism (Cytochrome C1, CYC1). These were specifically selected due to their suggested use in the expression analysis of AD tissue samples[297]. GAPDH and ACTB were also tested to assess variance of these two commonly used genes under our employed experimental conditions. Panel A shows the amplification curves for the 4 primer sets. Typically, smooth sigmoidal amplification plots with a sudden exponential phase and plateau are desired with sample replicates showing tight co-distribution around the cycle threshold (Ct) value. In this respect, EIF4A2 and CYC1 demonstrated optimal amplification curve characteristics. Panels B and C demonstrate graphs generated from melt curve analysis following amplification. DNA dissociates into single-stranded DNA rapidly upon melting, with no intermediate state, and is thus seen as sigmoidal function (panel B). Similarly, corresponding melt peaks should display a single tall, sharp narrow peak indicative of single, specific target amplicon production. EIF4A2 and CYC1 both demonstrated optimal melt curve characteristics, whilst lack of target specificity was evident in the case of ACTB and GAPDH. This was confirmed upon agarose gel electrophoresis of QPCR products which displayed several bands (Figure 33, D). Multiple bands were also observed for CYC1 in the form of a ghost band directly below the desired product. This was less intense than the true positive and was not apparent in the negative control (Figure 33, D, lane 13). A band was also present in the negative control below the ladder suggesting the presence of primer dimers, despite this not being detected upon prior melt curve analysis. Nonetheless, one specific band was present at 136 base pairs upon EIF4A2 gel electrophoresis indicative of the desired product. The suitability of EIF4A2 as a reference gene is further supported by of Ct box plots (Figure 33, E) and standard deviation (Table 24). Here, EIF4A2 exhibited the least variability, as well as the lowest SEM and standard deviation relative to the other candidate genes. Further, minimal data spread was also observed where 83% of samples were within less than 1 standard deviation of the mean (Table 24). Thus, EIF4A2 was selected as a suitable QCPR reference control to investigate Aβ's effects on Cathepsin B mRNA expression over the experimental time course (Figure 34).

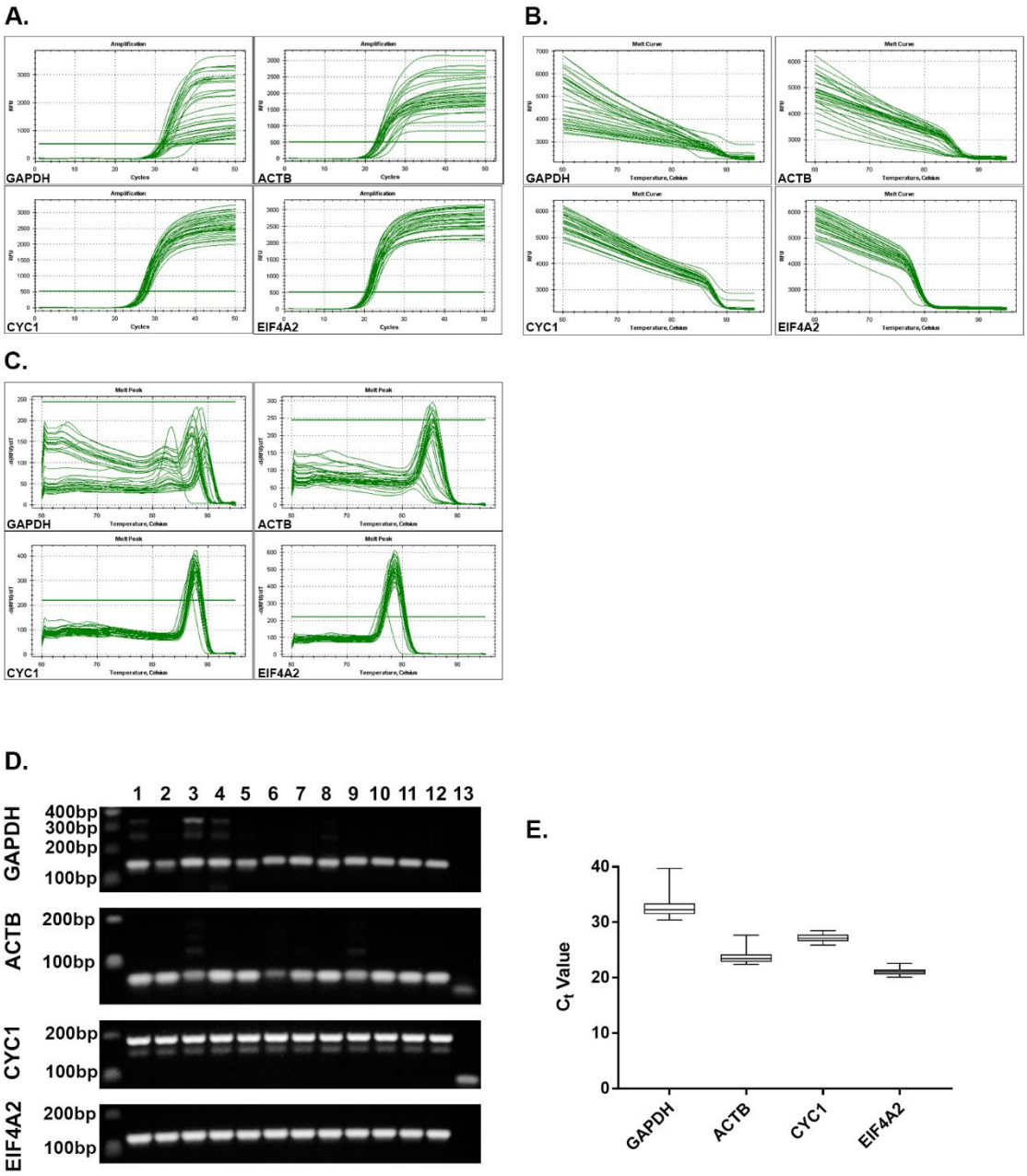

Figure 33: Stability analysis of reference genes for gene expression analyses.

Candidate primer pairs were tested on experimental samples to identify a suitable reference gene to be used for normalisation in gene expression analyses. **A.** Amplification curves for experimental samples subject to QPCR with GAPDH, ACTB, CYC1 and EIF4A2 candidate primers. Here, experimental samples across all wells, time points and treatment groups were tested. **B.** Melt curve analysis of samples with candidate primer pairs. **C.** Melt peaks determined from melt curve analysis indicating the size of amplicons produced during QPCR as well as corresponding melting temperatures. One distinct peak indicates one amplicon and thus primer specificity. **D.** Agarose gel electrophoresis of PCR products to assess primer specificity. Products were resolved on a 1.2% gel at 120v, 400mA for 45 minutes. The expected amplicon length of EIF4A2 is 136bp. Samples correspond to: 1, Aβ 0.5Hrs; 2, VH 0.5Hrs; 3, UT 0.5Hrs; 4, Aβ 3Hrs; 5, VH 3Hrs; 6, UT 3Hrs ;7, Aβ 24Hrs; 8, VH 24Hrs; 9, UT 24Hrs; 10, Aβ 48Hrs; 11, VH 48Hrs; 12, UT 48Hrs; 13, NTC. **E.** Box-plot graph indicating cycle threshold values of the four reference genes testes. Graphs are represented as medians (line), 25th percentile to the 75th percentile (boxes) and ranges (whiskers) for all samples to be tested in subsequent experiments. Abbreviations: ACTB, Actin Beta; bp, base pairs; CTSB, Cathepsin B CYC1, cytochrome C1; EIF4A2, Eukaryotic Translation Initiation Factor 4A2; GAPDH, Glyceraldehyde-3-Phosphate Dehydrogenase; NTC, no template control; UT, untreated; VH, vehicle.

Table 24: Column statistics of mRNA levels in candidate reference genes.

Column statistics of Ct values presented in Figure 33E to assess variability in candidate reference genes. These results identify EIF4A2 as the most stable reference gene across experimental samples.

	Candidate Reference Gene			
Column Statistics	GAPDH	ACTB	CYC1	EIF4A2
Minimum	30.41	22.37	25.89	20.12
25% Percentile	31.46	22.85	26.59	20.62
Median	32.29	23.46	27.1	21.08
75% Percentile	33.41	24.19	27.78	21.47
Maximum	39.72	27.67	28.49	22.59
Mean	32.91	23.77	27.14	21.12
Standard Deviation	2.131	1.265	0.683	0.6126
Standard Error of Mean	0.3551	0.2108	0.1138	0.1021

Relative quantification of sample Ct values was performed using the ΔCt method to assess Aβ's effects on Cathepsin B gene expression at each time point (Figure 34, C). Cathepsin B Ct values were first normalised to EIF4A2, and statistical comparisons were made across treatment groups within each experimental time point**.** No significant difference in Cathepsin B mRNA expression was detected using this method, and thus the ΔΔCt method was also employed to assess fold change in expression (Figure 34, D). This method of analysis is capable of detecting more subtle differences in gene expression. Again, statistical comparisons were performed across treatment groups within each experimental time point, which revealed no statistical significance in expression fold change of Cathepsin B mRNA across treatments. Nonetheless, a noticeable decrease in Cathepsin mRNA was observed at 0.5 hours relative to the vehicle/sham.

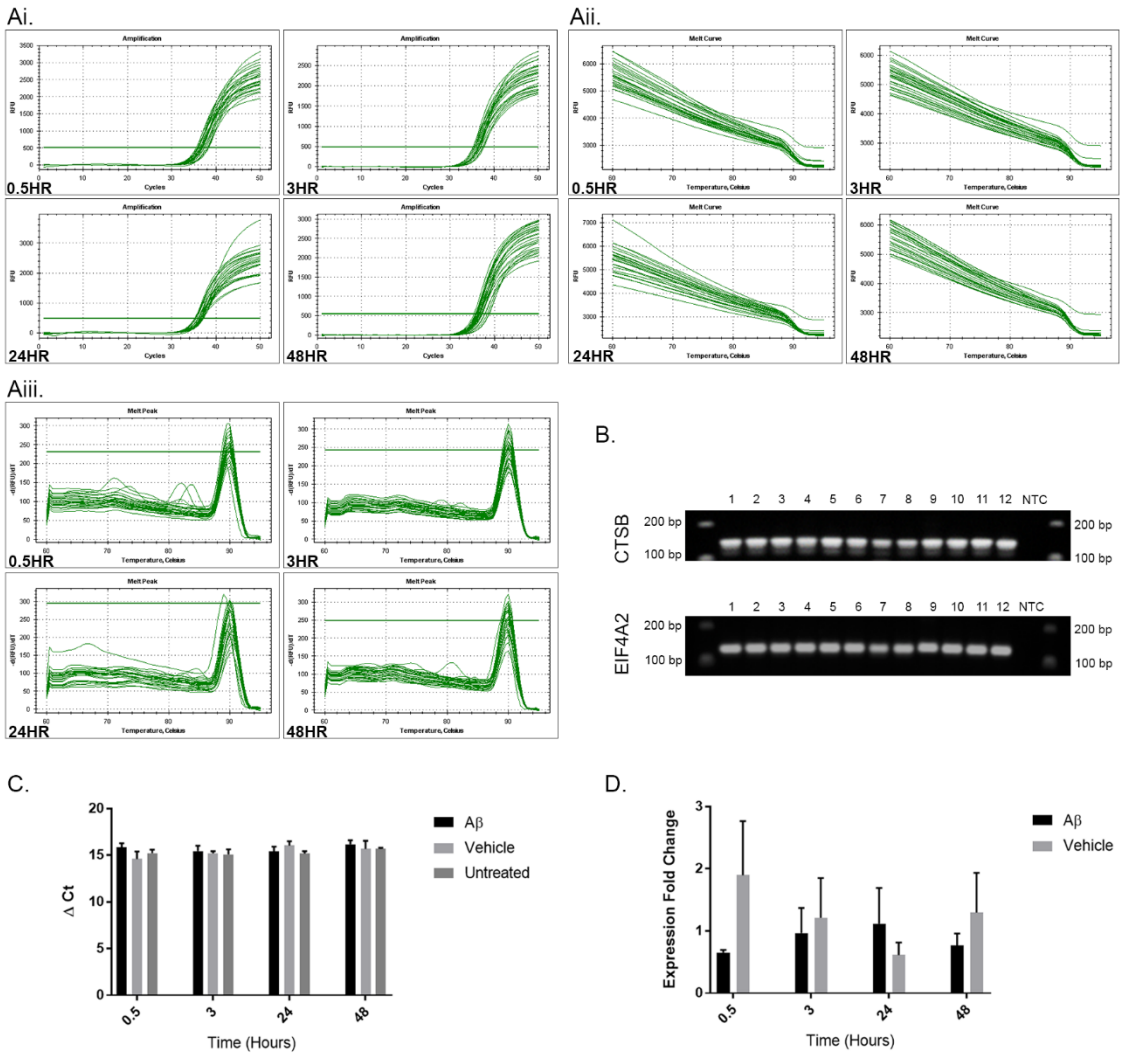

Figure 34: Cathepsin B gene expression analysis following $A\beta_{1-42}$ exposure.

Expression levels were calculated by quantitative real-time QPCR analysis. **Ai.** QPCR amplification curves of experimental samples at 0.5, 3, 24 and 48 hours post Aβ removal **Aii-iii.** Melt curve analysis and corresponding melt peaks determined from melt curve analysis indicating the size of amplicons produced from CTSB primers. **B.** Agarose gel electrophoresis of PCR products to assess primer specificity. Products were resolved on a 1.2% gel at 120v, 400mA for 45 minutes. The expected amplicon length of CTSB and EIF4A2 are 136bp and 145bp respectively. **C.** Relative quantification of samples in comparison to EIF4A2 using the ΔCt method. **D.** Expression fold change of Aβ and vehicle/sham treated cultures relative to the controls using the ΔΔCt method. Data is presented as mean ± SEM. One-way ANOVA with Tukey's multiple comparisons was adopted to compare expression levels between treatment groups. Samples correspond to: 1, Aβ 0.5Hrs; 2, VH 0.5Hrs; 3, UT 0.5Hrs; 4, Aβ 3Hrs; 5, VH 3Hrs; 6, UT 3Hrs ;7, Aβ 24Hrs; 8, VH 24Hrs; 9, UT 24Hrs; 10, Aβ 48Hrs; 11, VH 48Hrs; 12, UT 48Hrs. Abbreviations: bp, base pairs; CTSB, Cathepsin B; EIF4A2, Eukaryotic Translation Initiation Factor 4A2 NTC, no template control; UT, untreated; VH, vehicle.

3.3.4.3 $A\beta_{1-42}$ and Cathepsin B colocalisation

The colocalisation of Magic Red® with $A\beta_{1-42}$ was also assessed as a secondary outcome to determine the proportion of $A\beta$ present within lysosomes at experimental time points, as well as to establish the correlation between $A\beta$'s effects on Cathepsin B activity with its lysosomal presence. Again, the Costes *et al.* algorithm was employed here to determine the degree of overlap between Magic Red® (red) and $A\beta_{1-42}$ (green) for all acquired images. However, it must be understood that, due to probe constraints, this analysis was limited to the single z-plane acquired per field of view. Representative images for conditions and time points are presented in Figure 35A, along with overlap percentages and scatter plots.

Despite the inclusion of single labelled and autofluorescence controls, a degree of green signal was detected in vehicle and untreated cultures. This resulted in a low level of colocalisation being reported for controls (Figure 35, A). However, in all instances this was significantly lower than the Manders' coefficient recorded for $A\beta_{1-42}$ (Figure 35, A). As acquisition parameters were kept constant across experiments, comparisons between the degree of Magic Red® and $A\beta_{1-42}$ colocalisation in treated cultures relative to the vehicle/sham were made at all experimental time points. This assumes that background green levels affected the analysis proportionally (Figure 36). Note that all treatment groups followed a similar pattern across the experimental time course. $A\beta_{1-42}$ results were therefore corrected by subtracting the vehicle/sham control, to account for potential background (Figure 36, B). This revealed the amount of Magic Red® and $A\beta_{1-42}$ colocalisation to progressively increase up to 24 hours post exposure, after which a decline in Magic Red® and $A\beta_{1-42}$ colocalisation was observed.

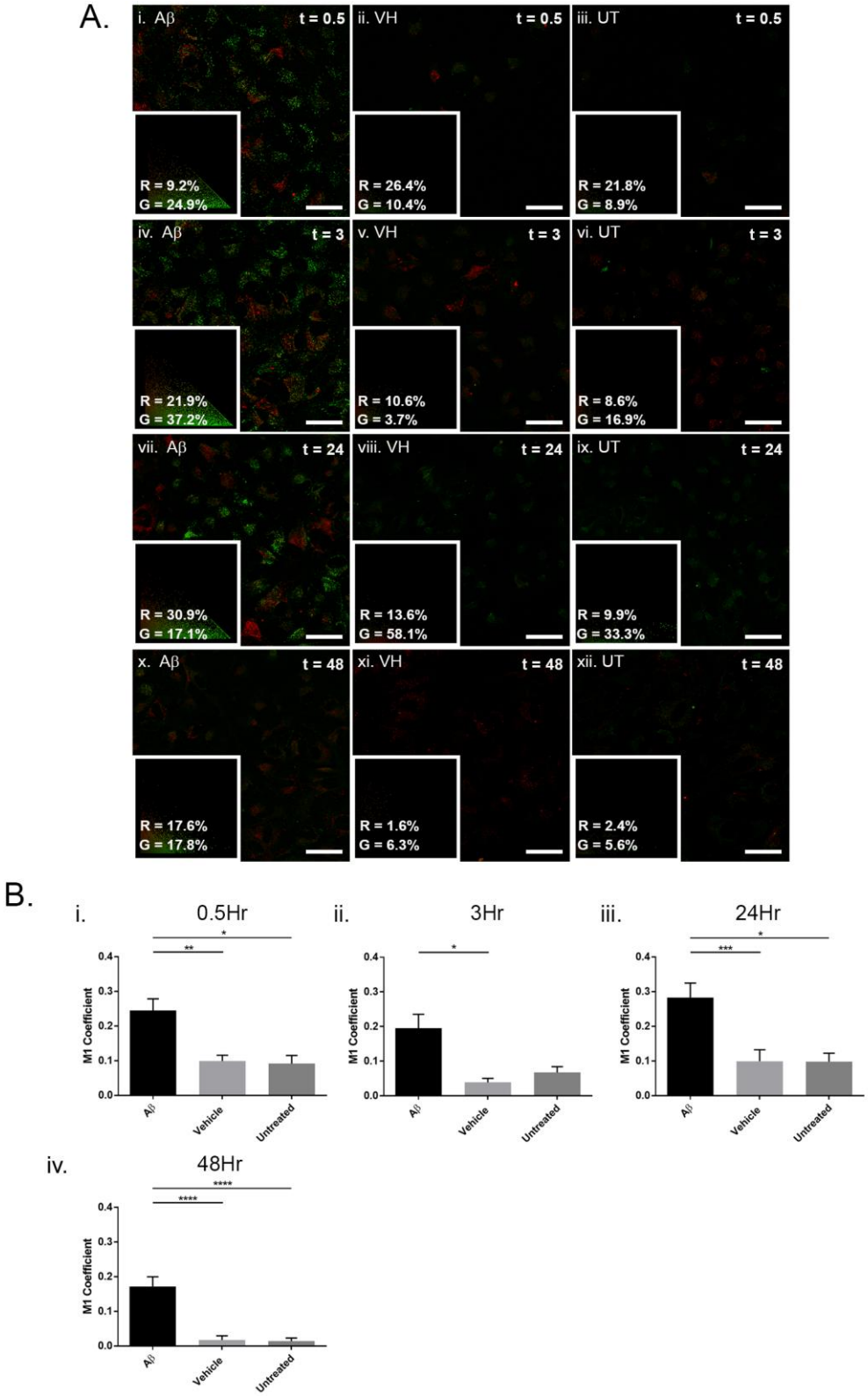

Figure 35: $A\beta_{1-42}$ and Cathepsin B colocalisation B in ARPE-19 cultures.

Alexa Fluor® 488 tagged $A\beta_{1-42}$ (green) and Magic Red® (red) colocalisation was assessed at **Ai-iii.** 0.5 hours **Aiv-vi.** 3 hours **Avii-ix.** 24 hours and **Ax-xii.** 48 hours following $A\beta_{1-42}$ incubation to determine the time course of lysosomal Aβ accumulation. Scatterplots presented in the bottom right indicate the percentage of red colocalised with green (R), and green colocalised with red (G). **B.** Statistical comparisons of colocalisation in $A\beta_{1-42}$ (n=30), VH (n=30) and UT (n=20) images were assessed using the Kruskal-Wallis test with Dunn's multiple comparisons. Data is presented as the mean M1 coefficient ± SEM with statistical significance denoted as **** P<0.0001, *** P<0.001, P** P<0.01 and *P<0.05. Scale bars correspond to 40μm.

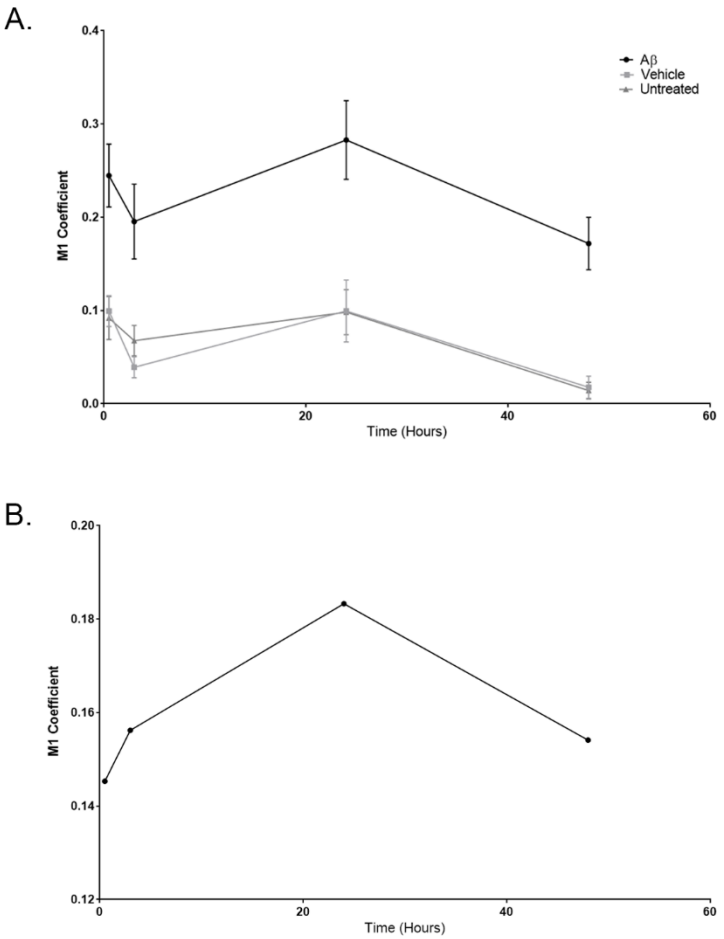

Figure 36: Magic Red® colocalisation with $A\beta_{1-42}$ as a function of time.

A. Graph showing M1 coefficients of Magic Red® colocalisation with $A\beta_{1-42}$ across experimental time points for $A\beta_{1-42}$, vehicle/sham and untreated cultures. Data is presented as mean ± SEM. **B.** Graph showing average corrected $A\beta_{1-42}$ M1 coefficients across experimental time points calculated as the average $A\beta_{1-42}$ M1 coefficient minus the average recorded M1 coefficient for vehicle/sham treated cultures at corresponding time points.

3.3.5 Functional effects of $A\beta_{1-42}$ on RPE lysosomes

3.3.5.1 $A\beta_{1-42}$ effects on photoreceptor OS internalisation and degradation within the RPE

Our studies previously demonstrated that exposure of RPE monolayers to physiological $A\beta_{1-42}$ levels resulted in their internalisation into late endosomes/lysosomes, in addition to causing an increase in lysosomal Cathepsin B activity up to 0.5 hours. Therefore, we conducted a functional experiment to assess whether the processing of Aβ within lysosomes translated to an impairment of RPE mechanisms reliant on efficient organelle function. To test this, we exploited the phagocytic function of the RPE (Section 1.2.3.4). Fluorescently-labelled POS were fed to $A\beta_{1-42}$ exposed and control cultures, and the effects of treatment on lysosomal function were evaluated across the duration of the experiment by

quantifying FITC-POS colocalisation with the lysosomal membrane-associated protein, LAMP-1 (Figure 37 and Figure 38, A). Time points assessed corresponded to those previously reported for POS internalisation and degradation within the ARPE-19 cell line[48].

Statistical comparisons between treatment groups showed that at 4 and 8 hours post POS incubation, the degree of FITC-POS and LAMP-1 colocalisation was comparable between treatment groups (Figure 37, B). However, at 20 hours, when lysosomal degradation of POS is expected [48], a significant decline in the degree of FITC-POS and LAMP-1 colocalisation in $A\beta_{1-42}$ treated cultures was observed compared to vehicle/sham. A similar, although statistically insignificant, decrease was also seen when compared to untreated cultures. Immunostaining with Rhodopsin validated sustained conjugation of FITC to POS (Figure 37, Axi). This data is also presented as a function of time (Figure 38) and suggests $A\beta_{1-42}$'s on POS processing at the level of the lysosome, which warrants further investigation.

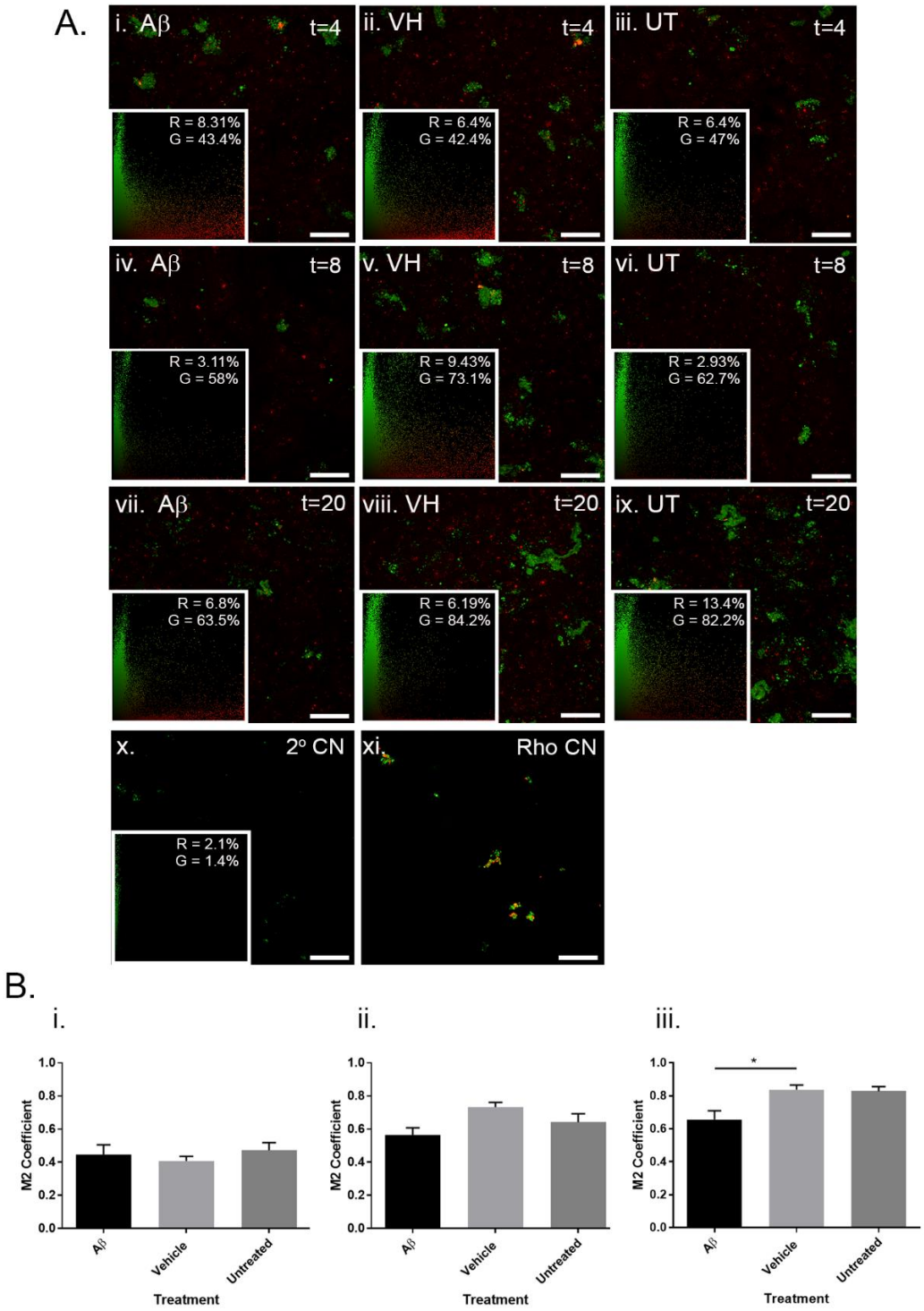

Figure 37: Functional assessment of Photoreceptor Outer Segments phagocytosis in ARPE-19 cells following acute $A\beta_{1-42}$ treatment.

Colocalisation assessment of FITC Photoreceptor Outer Segments (POS; green) with LAMP-1 (red) at **Ai-Aiii.** 4 hours **Aiv-Avi.** 8 hours and **Avii-Aix.** 20 hours following incubation for 3 hours with $A\beta_{1-42}$ or control, 23 hours at 37°C, and 2 hours with POS (Figure 21). Scatterplots presented in the bottom right of representative images indicate the percentage of red colocalised with green (R), and green colocalised with red (G). **Axi.** A Rhodopsin (Rho) labelling control was included to assess sustained FITC/OS conjugation (yellow). **Ax.** No LAMP-1 staining was observed in the secondary antibody control. **B.** Quantification of colocalisation at **Bi.** 4 hours **Bii.** 8 hours and **Biii.** 20 hours following OS removal in $A\beta_{1-42}$ (n=6), vehicle (n=6) and untreated (n=6 cultures). Data is presented as the mean M2 coefficient ± SEM. Statistical significance was assessed using the Kruskal-Wallis test with Dunn's multiple comparisons, where significance is denoted as *P<0.05. Scale bars correspond to 40μm.

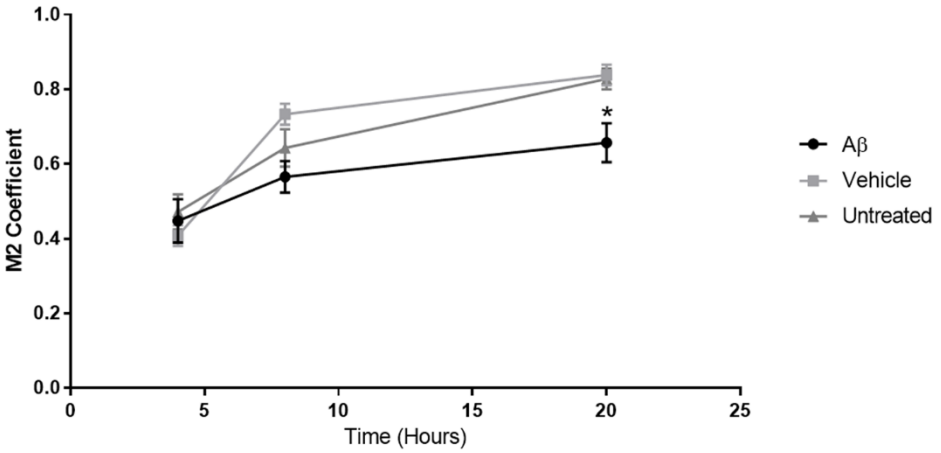

Figure 38: Photoreceptor Outer Segment (OS) colocalisation with LAMP-1 as a function of time following acute treatment with $A\beta_{1-42}$ and overnight incubation.

Colocalisation of FITC tagged photoreceptor outer segments with LAMP-1 at 4, 8 and 20 hours following incubation of ARPE-19 cells with $A\beta_{1-42}$ for 3 hours, incubation at 37°C for 23 hours and incubation with FITC-POS for 2 hours to assess effects of $A\beta_{1-42}$ on POS phagocytosis. Colocalisation is presented as M2 coefficients indicating the degree of overlap between FITC-POS and LAMP-1. Note that at 20 hours following FITC-POS incubation significantly less FITC-POS was colocalised with LAMP-1 in $A\beta_{1-42}$ treated cultures relative to vehicle/sham controls.

3.4 Discussion

3.4.1 Overview

Perturbations to cellular clearance pathways in AD are well documented with a growing evidence base that implicates the UP pathway, impaired autophagy and altered endocytic function with disease pathogenesis. Of particular interest is the convergence of these pathways on the lysosome, where $A\beta_{1-42}$ has been shown to accumulate and exert deleterious effects on several aspects of organelle function. Lysosomal $A\beta_{1-42}$ accumulation may therefore present an underlying cause for autophagy and endocytic alterations observed in AD, yet this remains largely speculative and is the subject of ongoing investigation. Both AMD and AD exhibit striking similarities in terms of damage to clearance pathways (Section 3.1). However, the involvement of Aβ in AMD pathology, particularly with regard to lysosomal clearance, remains to be established. Discerning the involvement of $A\beta_{1-42}$ in driving AMD associated lysosomal changes could potentially identify a target candidate for early AMD treatments, which at present has no effective therapy.

The work described in this chapter investigated the involvement of $A\beta_{1-42}$ on RPE lysosomal function. We exploited an *in vitro* model of the outer retina to test the hypothesis that Aβ accumulates in lysosomes, alters acid hydrolase activity and perturbs normal organelle function. Additionally, the secretion of $A\beta_{1-42}$ from the RPE was assessed during model characterisation to gain insights into the potential biological function of Aβ. Here we describe the novel data obtained over the duration of this project.

3.4.2 Cell culture model characterisation

An *in vitro* culture model replicative of the RPE/Bruch's membrane complex (Figure 19) is widely utilised in the literature to investigate aspects of RPE function and morphology. This system enables the study of mature, cuboidal RPE monolayers that display key features of native RPE and has been shown to support the extended culture of primary porcine RPE[282], primary murine RPE[298], human foetal RPE (hfRPE)[289 291 299 300], adult human RPE[301] and ARPE-19 cells[302 303]. In all cases, cultures display pigmentation, BRB function, apicobasolateral specialisation and transepithelial transport capability as well as the polarised secretion of cytokines, albeit to differing degrees[289 291 300 301]. This is largely suggestive of an RPE phenotype but constantly remains under refinement in the literature to better resemble native

RPE[287]. Additionally, this system is capable of recapitulating features of early AMD including drusen biogenesis and complement deposition. ApoE, clusterin, vitronectin and serum amyloid P component have all been demonstrated in Transwell® pores, highlighting its validity in studying the factors underpinning AMD pathogenesis[304]. The commonality between all these methods is the use of Transwell® inserts, which allows cells to be grown in a polarised state under more natural conditions. The power of this approach is highlighted by its use in the differentiation of epithelia from other sources including the lung[305], intestine[306] and kidney[307]. The research presented herein exploits this model to facilitate the experimental analysis of early structural and physiological changes to the RPE lysosomes in response to Aβ exposure.

Several RPE cell types were considered as an appropriate cell source prior to experimentation. The current 'gold-standard' for RPE cell culture is those derived from human induced pluripotent stem cells (hiPSC RPE), closely followed by foetal or adult human RPE, which closely mimic functional/morphological characteristics of RPE *in situ*. The incorporation of hiPSC RPE in *in vitro* cultures lends itself to the study of inherited retinal conditions, which facilitate the study of patient-specific RPE carrying the same disease-associated variant *ex situ*[308]. This unequivocally rivals alternate cell sources in terms of RPE phenotype and clinical applicability, although requires clinical collaboration and a labour-intensive iPSC programme, or alternatively collaboration with an equipped laboratory. Similarly, sourcing viable RPE from primary tissue is variable as tissue is scarce, and in most instances is not obtained until 24-48 hours after death. Even when successfully isolated, cells of primary origin are limited by the number of successive passages that may be incorporated into the model, and typically exhibit genetic alterations[309] as well as phenotypic drift and/or replicative failure by passage 15[310]. In this respect, the incorporation of RPE cell lines provides a dependable and widely used alternative to native RPE[311]. Two RPE cell lines have been trialled within this culture model including the rat SV-40T immortalised RPE-J cell line[309] and the spontaneously arising human ARPE-19 cell line[291 302]. ARPE-19s exhibit several advantages over RPE-J cells as they are derived from human origin and exhibit structural similarities akin to native RPE which are lost in the RPE-J cell line[309]. ARPE-19 cells have been shown to express/display desirable RPE characteristics up to and including passage 27 and have been used in retinal research for over 20 years. Additionally, their use facilitates a more standardised approach across laboratories as they offer both homogeneity and exhibit minimal variation between labs when cultured in a similar manner. This is in stark contrast to tissue of primary origin, which display donor-

donor genetic variability[311]. Given their ease of culture and relative accessibility, a large amount of work has been conducted to improve the phenotype of ARPE-19 cells within the Transwell® system and to increase the retention of properties essential to their native counterpart. This has largely been driven by the Coffey laboratory, and has vastly improved the applicability of this cell line to RPE research[302]. When cultured using the optimised technique, ARPE-19 cultures exhibit a normal karyotype[309], express key RPE proteins and display pigmentation[302 303], apicobasolateral specialisation[303], phagocytic capability[51 246 302], a degree of polarised secretion[291 302 303] and BRB formation[36 37 302 303]. In fact, recent evidence has shown that when cultured for 4 months in optimised medium, ARPE-19s within the model display a comparable transcriptome to native RPE in addition to the phenotypic characteristics reported previously[311]. Most importantly, this was comparable to RPE of primary fetal origin or hiPSC RPE, which are commonly reported as the 'gold standard' sources. Provided this cell line is used in an appropriately differentiated state, ARPE-19 Transwell® cultures present a powerful and easily obtainable tool in which to model RPE functions. As such, the ARPE-19 cell line was selected for use in this project. Section 3.3.1 details the experiments undertaken in validating this culture model prior to use in downstream experiments.

First, the expression of key RPE proteins was examined by confocal microscopy to assess the correct maturation and polarisation of cultured cells. The expression of the tight-junction proteins ZO-1 and occludin confirmed the presence of barrier properties within RPE monolayers. However, in addition to the typical peripheral staining pattern expected, a degree of ZO-1 staining was also apparent in the cytoplasm. This has been shown previously, and is most likely attributable to the proposed function of ZO-1 in growth and proliferation[312]. ZO-1 mRNA harbours nuclear localisation signals, which come into effect depending on the extent and maturity of cell-cell contacts[312 313]. This observation reflects the limited barrier function of the ARPE-19 cell line, which exhibits relatively leaky tight-junctions in comparison to native RPE. However, the presence of occludin indicated at least a certain degree of maturity within tight junctions. Taken together these observations indicate that ARPE-19 barrier function cannot be directly extrapolated from native tissue. The electrical resistance measurement of $40.72\Omega.cm^2$ across monolayers further highlights the relative immaturity of ARPE-19 tight-junctions in comparison to RPE from rodent, porcine and human origin, which exhibit TEER values of 150-200, 1400 and 200-1500 respectively[36]. This function was not used to investigate the effects of Aβ on RPE function, and therefore this limitation of ARPE-19 cells does not compromise the validity of conclusions drawn.

Na^+/K^+ ATPase expression was also assessed to determine the presence of functional plasma membrane polarity within cultures, which is required for the anti-photoxidative, vectorial transport, directional protein secretion and phagocytic functions of the RPE[314] (Section 3.3.1.1). In contrast to epithelia from both the kidney and gall bladder, Na^+/K^+ ATPase is mainly expressed on the RPE apical surface where it is thought to facilitate the process of phototransduction and has been implicated in the regulation of a well-differentiated, polarised epithelial phenotype[314]. This has led to its frequent use in the characterisation of RPE from different sources including cell lines, hfRPE, adult human RPE and hiPSC. It was evident here that Na^+/K^+ ATPase expression within monolayers was confined to select subpopulations of cells. When analysed for distribution in the z-axis, Na^+/K^+ ATPase was localised towards the apical surface of subpopulations in the manner expected, although neighbouring cells appeared to weakly express, or did not express this protein. The reason for this limited expression profile remains unknown but may indicate differing rates of maturation within monolayers. Apical expression has been shown to correlate with the degree of culture pigmentation[302], which often only occurs extensively after 3-4 months in culture. TEM confirmed RPE polarisation at an ultrastructural level, with RPE monolayers exhibiting apical microvilli and pigment granules, as well as basal mitochondria and infolds (Figure 24). The presence of such features, in addition to tight junction properties demonstrated, highlights the benefits of utilising ARPE-19 cells, where alternative cell lines (e.g. D407 cells) lack apical microvilli and fail to reproduce correct apico-basalateral localisation of key membrane proteins. This has been reviewed previously[314].

Finally, we investigated the directional secretion ability of RPE monolayers. This is a desirable feature of *in vitro* cultures and is critical for the correct maintenance of outer ocular tissues *in situ.* Growth factors and cytokines are preferentially secreted from the RPE basal or apical membrane to achieve different and directional functions. The compartmentalised nature of the Transwell® system facilitates the analysis and retention of this function, where protein concentrations may be measured in both the apical and basal compartments. Owing to their well-characterised native secretion profile (Section 1.2.3.3), PEDF and VEGF media concentrations are commonly used as functional outcome measures of polarity and were employed here in the validation of ARPE-19 cultures.

We observed that VEGF secretion in cultures was analogous to native RPE, favouring directional secretion from the basal surface. VEGF concentrations in both

comparable to that reported in hfRPE cultures[289].However, despite PEDF secretion being more comparable to hfRPE than reported previously using suboptimal culture medium[289], apical PEDF secretion appeared to be reduced. Taken together, Section 3.3.1 validates the identity of ARPE-19 cells within this system and supports its use in downstream experiments.

3.4.3 $A\beta_{1-42}$ oligomer isolation

The oligomeric $A\beta_{1-42}$ preparation technique employed within the research was established in the Ratnayaka laboratory by myself during the course of this research, after learning the technique by Professor Louise Serpell's laboratory at the University of Sussex. Thus, method validation was required prior to use in experiments. Collectively, the data presented in Section 3.3.2.1 and Section 3.3.2.2 validates both the identity and predominant structural conformer of $A\beta_{1-42}$ at 1.5 hours. Here, similar to previous reports[176 293], $A\beta_{1-42}$ oligomers and soluble $A\beta$ species appeared to dominate sample preparations with minimal protofibril formation. Fibrilar $A\beta$ assemblies were not evident until 24 and 48 hours post preparation. Such complex $A\beta$ assemblies have been suggested to accumulate within the outer concentric ring of amyloid vesicles, at distinct sites from amyloid oligomer cores[208], and may represent the eventual fate of soluble oligomers within drusen.

Additionally, we performed experiments to confirm the absence of bacterial endotoxin within $A\beta_{1-42}$ preparations to negate their potential influence on RPE function. This was particularly important given the recombinant lineage of the lyophilised $A\beta_{1-42}$ employed, and the fact that no literature reports exist to suggest that this has been done previously. Our results indicated that levels of endotoxin within both $A\beta$ and vehicle/sham were <0.5EU/ml and <3EU/mg. This is within the US Food and Drug Administration (FDA) limits for medical devices and parenteral drugs (<0.5EU/ml). As the recorded value for $A\beta_{1-42}$ fell within this guideline and did not deviate from recombinant-null vehicle/sham preparations, samples were deemed suitable for use.

3.4.4 $A\beta$ is secreted from the RPE basal surface

The RPE has been demonstrated to secrete both $A\beta_{1-40}$ and $A\beta_{1-42}$ *in vivo* and *in vitro*, and is thought to be the principle source of $A\beta$ in the posterior eye[9 196]. However, evidence of secreted $A\beta$ to date has been confined to studies assessing unilateral secretion. Glotin *et al.* showed that ARPE-19 cells secrete approximately 60 pg/ml

of $A\beta_{1-42}$[315], whereas Wang *et al.* demonstrated secretion of 65 pmol/ml of $A\beta_{1-40}$ and 8.5 pmol/ml of $A\beta_{1-42}$ from RPE isolated from aged mice[196]. This has limited the understanding of Aβ secretion by the RPE and as a consequence, its biological role in the retina. For the first time, our results indicate that Aβ is predominantly secreted from the basolateral RPE surface, where the Aβ concentration within Transwell® cultures was approximately 1.8-fold higher in the basal compartment over a 48 hour period. The RPE is also known to secrete several VEGF isoforms from its basal surface towards its biological target[30]. In this respect, our findings support previous observations postulating a role for Aβ, either alone or in combination with VEGF, in choroidal perfusion/maintenance. Particularly as *in vivo* studies concerned with elevated photoreceptor and VEGF expression found no evidence of a CNV phenotype[316 317]. For example, application of $A\beta_{1-40}$ to human RPE cultures induced a dramatic increase in VEGF at both the protein and mRNA level, concomitant with a decrease in PEDF expression[8 197]. Similarly, comparable observations in these proteins were replicated in neprilysin-deficient mice, a major Aβ degrading enzyme[197]. Studies investigating the application of conditioned media from $A\beta_{1-40}$ treated RPE to Human Umbilical Vein Endothelial Cells (HUVECS) also demonstrated a 2-fold increase in total tube length compared to controls, implicating a potential downstream target of Aβ and subsequent elevated VEGF secretion in spontaneous tube formation[197]. This effect on vasculature was confirmed *in vivo* where intra-ocular injection of $A\beta_{1-42}$ into the eyes of zebra fish induced aberrant blood vessel branching associated with increased capillary bed density[245]. Collectively this may suggest a potential role for Aβ metabolic dysregulation in the pathogenesis of CNV.

As previously stated, current AMD treatments are largely focused towards targeting excessive VEGF over-expression associated with a disease phenotype, which otherwise triggers both endothelial proliferation and increased vascular permeability. The association between Aβ and increased RPE VEGF expression proximate to the choroid, as well as the basolateral directional secretion of Aβ demonstrated herein, suggests the presence of a previously undiscovered regulatory pathway in choroidal homeostasis. Dysregulation of this pathway may reveal a potential mechanism by which CNV initiates/is driven and perhaps identifies Aβ as a novel molecular target for the treatment of wet AMD.

3.4.5 Endolysosomal processing of $A\beta_{1-42}$

A main objective of this chapter was to establish whether $A\beta_{1-42}$ is trafficked to RPE lysosomes following physiological exposure. This was achieved through

application of Alexa Fluor® tagged $A\beta_{1-42}$ and incubation with PDMPO, which indicates the location of late endosomes and lysosomes within live RPE cultures. Colocalisation was observed in all cultures, where quantification revealed that on average 40.7 ± 8.6% of $A\beta_{1-42}$ localised to late endosomes/lysosomes. This is supported by prior studies investigating Aβ internalisation in neurons and the RPE, which suggest a role for clathrin-mediated endocytosis and RAGE/p38-mediated Aβ internalisation respectively[318-320]. PDMPO labelling does not however label early endocytic compartments, which may also contain internalised Aβ and contribute to the 60% of signal that remained uncolocalised. Similarly, as the mechanisms of Aβ uptake and processing by the RPE remain largely unexplored, the possibility also exists that internalised Aβ may be directed to alternative degradative pathways. For example the UP has been frequently associated with Aβ in AD. Such Aβ induced UP impairment could increase the cells autophagic load, and ultimately its reliance on efficient lysosomal function. This scenario is unlikely in this instance given the acute exposure and near physiological concentration of $A\beta_{1-42}$ employed. However, it may bear relevance to AMD pathology as it identifies an additional mechanism by which Aβ may be 'shunted' into lysosomes following sustained and cumulative insult[10 281 321]. Additionally, the increased accumulation of lysosomal Aβ is anticipated as a result of sustained POS phagocytosis, which exhibits an age-dependent increase in Aβ staining (Section 1.6.2.1[203].

Interestingly, $A\beta_{1-42}$/PDMPO colocalisation was also associated with considerably larger lysosomes. This finding was largely observational and was not tested further. However, it may suggest alterations to late endosome and/or lysosome morphology following Aβ exposure. Further experimental investigations with endosomal/lysosomal specific markers are required to confirm in which endo-lysosomal compartment this phenotype resides. Similarly, quantitative comparative studies are required to evaluate the proportion of swollen compartments in $A\beta_{1-42}$ treated cultures relative to controls. Nonetheless, this finding is consistent with morphometric analyses of AD neurons, which report a significant increase in endosome size[264].In summary, the data presented demonstrates the presence of Aβ within RPE lysosomes for the first time, and may indicate a common mechanism of early cellular compromise in chronic neurodegenerative diseases such as AD and AMD.

3.4.6 $A\beta_{1-42}$ effects on lysosomal Cathepsin B activity

Studies in neurons have shown that $A\beta_{1-42}$ irreversibly inserts into the lysosomal membrane and has been associated with lysosomal alkalinisation, altered acid hydrolase function, and leakage of contents into the cytosol[13]. Experiments were therefore conducted to establish Aβ's effects on RPE lysosome acid hydrolase activity, given its endo-lysosomal localisation (Section 3.3.3.1). Cathepsin B is widely expressed by the RPE and has been exploited previously to investigate dose-dependent effects on RPE lysosomal protease function[322]. It was therefore employed herein to investigate the effects of Aβ on the degradative function of the RPE lysosomes. Our results indicated a significant increase in Cathepsin B activity at 0.5 and 3 hours following physiological Aβ exposure, after which levels gradually reduced back to baseline (Figure 31 and Figure 32). This initial increase in activity further supports the presence of $A\beta_{1-42}$ within late endosomes/lysosomes (Figure 29). At 24 and 48 hours, Aβ treated RPE exhibited comparable Cathepsin B activity to that observed in control cultures. However, it could not be inferred whether this reduction in activity was attributable to the efficient processing of $A\beta_{1-42}$, or whether this ensued following an Aβ-mediated effect on lysosomal lytic function. Therefore, we next evaluated colocalisation of the lysosomal Cathepsin B substrate with $A\beta_{1-42}$ at experimental time points, in an attempt to elucidate the factors underpinning decreased enzyme activity.

Colocalisation analysis of Magic Red® with $A\beta_{1-42}$ demonstrated that the degree of overlap continued to increase up to 24 hours (Figure 35), despite a decrease in Cathepsin B activity after 3 hours (Figure 31). This may occur as a consequence of increased lysosomal $A\beta_{1-42}$ accumulation rather than efficient clearance, and is supported by $A\beta_{1-42}$ fluorescence intensity measurements which did not differ appreciably between 0.5 to 24 hours. However, further experiments are required before conclusions can be drawn, particularly given the low level of signal observed in vehicle and untreated cultures. A decrease in colocalisation was not observed until 48 hours post $A\beta_{1-42}$ exposure (Figure 35). The reason for this observation remains unknown, although several possible explanations exist. The first is the accumulation of $A\beta_{1-42}$ within residual bodies as indigestible material, akin to reports by Nixon and colleagues in AD neurons[323]. Residual bodies have one of two fates; they are either discharged from the cell via exocytosis in an attempt to relieve the elevated lysosomal burden, or they remain within cells as intracellular lipofuscin[324]. In both cases, the associated outcome can be linked to AMD pathology. Exocytosis of undigested material by the RPE is thought to underpin

drusen formation[155 281]. In fact, studies have shown that inhibiting lysosomal degradation causes the secretion of material into the RPE/Bruch's membrane interface[325]. The retention of residual bodies as lipofuscin is also a key characteristic of compromised RPE and could explain the enlarged phenotype of $A\beta_{1-42}$ containing compartments (Figure 29). Similarly, the baseline Cathepsin B activity reported at 24 and 48 hours (Figure 31) could explain this phenotype, as undigested $A\beta_{1-42}$ is shuttled to compartments lacking hydrolytic enzymes for indefinite storage[324].

Alternatively, the reduction in colocalisation observed at 48 hours (Figure 35) could result from $A\beta_{1-42}$ induced alterations to lysosomal membrane integrity. The associated luminal change to alkaline pH would likely retard Cathepsin B activity, and either exacerbate the accumulation of $A\beta_{1-42}$ within residual bodies, or induce leakage and dispersal of lysosomal constituents into the cytosol. Cytosolic acid hydrolases are rapidly inactivated by endogenous protein inhibitors[326], e.g. cystatin C, which could also explain the decrease in Cathepsin B activity noted after 3 hours (Figure 31). It may be that prolonged or repeated exposure, as in disease, results in the second more severe phenotype that has been observed upon $A\beta_{1-42}$ application to cell cultures[13 327]. In such instances, cell lines were transfected to overexpress human Aβ, or concentrations in excess of 10μM were employed for periods up to 24 hours, and likely represent severe rather than subtle, incipient cellular damage[13 327]. It is more tenable that following impaired enzyme function, residual $A\beta_{1-42}$ is shuttled to residual bodies, particularly given the acute exposure and low concentration of $A\beta_{1-42}$ employed here.

Further experiments are required to determine the effects of $A\beta_{1-42}$ on RPE lysosomes. However, $A\beta_{1-42}$ induced lysosomal rupture fits the LMP model of NLRP3 inflammasome activation, whereby Cathepsin B functions as a cytoplasmic secondary messenger of cellular stress[328]. Interestingly, this has been implicated in AMD pathology and more recently following RPE treatment with Aβ (Section 1.6.3.3). If Aβ induced lysosomal destabilisation and Cathepsin B release is confirmed in the RPE, this could highlight a potential upstream mechanism for the chronic inflammation associated with disease, as well as the caspase-1, TNF-α NLRP3, IL-1β and IL-18 upregulation associated with retinal Aβ exposure[213]. This is largely speculative but places our findings in the wider context of Aβ's reported effects in AMD research

3.4.7 Transcriptional effects of $A\beta_{1-42}$ on Cathepsin B

In Section 3.3.4.1, we found both an increase and decrease in Cathepsin B activity at specific time points post $A\beta_{1-42}$ application. However, from the techniques employed it was not clear whether this occurred at a post translational or transcriptional level. Therefore, QPCR was employed to assess whether changes in Cathepsin B mRNA expression corresponded to fluctuations in enzyme activity (Figure 34). Here, relative quantification and expression fold-change analysis revealed no significant difference in Cathepsin B mRNA expression between all treatment groups and time points tested. A decreased trend in Cathepsin B mRNA expression was observed at 0.5 hours, although this appeared to resolve by 3 hours (Figure 34). Cathepsin B has a half-life of 14 hours[329] and thus maximal biological effects of Cathepsin B down-regulation would be expected to occur within this period. However, the reduction in Cathepsin B activity observed persisted at 24 and 48 hours (Figure 31) despite comparable gene expression between treatment groups at time points prior to each interval (Figure 34), as well as increased and sustained lysosomal $A\beta_{1-42}$ at 24 and 48 hours respectively (Figure 35, B). From these results we can infer that mechanisms downstream of transcription are implicated in the effect of $A\beta_{1-42}$ on Cathepsin B activity. However, additional experiments are required to determine whether such changes occur at the translational or protein level.

3.4.8 Phagocytic activity of $A\beta_{1-42}$ treated RPE cells

The lysosome is integral to the RPE's phagocytic capacity and is essential for retinal proteostasis. This is of particular importance to POS phagocytosis (Section 1.2.3.4), which is reliant on an operational endo-lysosomal system to accommodate the high proteolytic burden exerted on the RPE. With the decrease in Cathepsin B activity (Figure 31) and enlarged/swollen phenotype of vesicles (Figure 29) observed following prolonged $A\beta_{1-42}$ exposure, we postulated that such alterations could translate to a compromised phagocytic ability of the RPE. Our next experiments therefore sought to investigate the effects of $A\beta_{1-42}$ on this major RPE function.

A functional assay was devised, using LAMP-1 and FITC-POS colocalisation as the outcome measure, to indirectly quantify the percentage of functional lysosomes available to participate in POS phagocytosis following acute $A\beta_{1-42}$ exposure. $A\beta_{1-42}$ treatment exhibited no effect on the amount of POS present within lysosomes until 20 hours post application, corresponding to the time point at which maximal

lysosomal digestion of POS is anticipated in the ARPE-19 cell line[48]. This suggests that exposure to $A\beta_{1-42}$ may result in a reduced lysosomal capacity and/or function. However, additional investigations are required to confirm this effect as the reduction in lysosomal POS was insignificant between untreated cultures (18.31%), despite being comparable to vehicle/sham (18.55%). Nonetheless, this initial data may associate lysosomal $A\beta_{1-42}$ with the improper processing of POS which may exacerbate or cause lipofuscin and A2E accumulation over time within the RPE.

3.5 Conclusions

In conclusion, the results presented within this chapter report the accumulation of $A\beta_{1-42}$ within RPE lysosomes for the first time. We demonstrated that sustained and increased lysosomal $A\beta_{1-42}$ exposure appears to correlate with a decline in the enzymatic activity of the lysosomal acid hydrolase, Cathepsin B that is downstream of transcription. Further, our studies associated $A\beta_{1-42}$ with a reduced percentage of POS within lysosomes suggestive of a reduced RPE lysosomal capacity. Taken collectively, these findings implicate $A\beta_{1-42}$ with several RPE lysosomal changes reported in compromised RPE. If $A\beta_{1-42}$ reduces the lysosomal capacity of the RPE, efforts to rescue function and lipofuscinogenesis could be envisaged as a potential treatment for AMD. This would not only aid in preventing visual deterioration in susceptible individuals but would also significantly reduce the economic burden exerted on global health care systems, especially considering the impending ‘ageing epidemic’.

Chapter 4 Pathological effects of Aβ *in vivo.*

4.1 Background

In Chapter 3, we investigated the effects of oligomeric $A\beta_{1-42}$ on the RPE, where we demonstrated $A\beta_{1-42}$ induced changes to RPE lysosomal biology. Similarly, numerous reports have implicated oligomeric Aβ with other aspects of AMD-associated RPE alterations (Section 1.7)[197 213 242 318] . A significant proportion of this work has been conducted *in vitro*, and has provided significant insights into the effects of Aβ at the molecular and cellular level. However, these systems are limited by their relative simplicity, and do not model the intricate relationships between adjacent retinal cell layers. In particular, it is not possible to ascertain the summed effects of Aβ on total retinal morphology and function. This is required to support a *bone fide* role for Aβ in AMD pathology, and presents an appropriate application of *in vivo* modelling.

Currently, the most employed animal model in AMD research is rodents, which present a readily available source with several advantages over non-human primate, porcine and rabbit AMD models. These include low maintenance costs, ease of genetic manipulation, less ethics, and the relatively fast onset of disease features[330 331]. Despite lacking an anatomical macula, the mouse retina also mirrors the human retina in several structural characteristics that are thought to predispose the macula to disease. For example, the central mouse retina exhibits a higher photoreceptor density and thinner Bruch's membrane, and the photoreceptor to RPE ratio in the peripheral mouse retina is at least comparable to that observed in the human macula[332]. In this respect, mice present a suitable model to study the factors influencing disease progression. Interestingly, the photoreceptor to RPE ratio in the central mouse retina is also seven-fold higher than the human macula[332]. This increased phagocytic load on murine RPE may be exploited to exacerbate the consequences of impaired RPE clearance and/or phagocytic capacity in response to various insults, as well as assess its role in disease progression. In fact, this is of particular interest here, given the reported effects of Aβ on RPE lysosomal capacity (Chapter 3). Nonetheless, *in vivo* models should only be incorporated into experimental design following proof of concept *in vitro* studies, or where simplified culture models are deemed inadequate.

The presence of comparable pathological abnormalities are commonly used to validate rodent models of AMD, and support a role for specific agents and pathways in driving disease pathology. For example, CFH knockout and CFH transgenic mice develop features reminiscent of AMD including, subretinal autofluorescence, complement deposition, Bruch's membrane alterations, POS disorganisation and an increased resident immune cell count[333 334 331], thus, implicating impaired or downregulated CFH function with disease onset. Similarly, histopathological features such as RPE hypertrophy, RPE hypopigmentation, subretinal deposit accumulation, photoreceptor atrophy and CNV, are all observed in ceruloplasmin and hephaestin knockout mice, supporting a role for iron accumulation in AMD[331 335]. These are but a few examples, highlighting the use of AMD-like pathology as an outcome measure for unpicking the factors associated with this multifactorial disease.

This chapter investigates the effects of oligomeric $A\beta_{1-42}$, on the retinal morphology and function of the central mouse retina *in vivo*. The primary aim being to assess whether $A\beta$ induces pathological features similar AMD and determine its association with disease pathogenesis. Similar $A\beta_{1-42}$ concentrations to those employed in Chapter 3 were employed here to ensure that only physiological $A\beta$ concentrations reported in the literature for ocular fluids were used in *in vivo* modelling. Additionally, this study provides insights into the consequences of $A\beta$ induced RPE changes *in vitro* and on overall retinal homeostasis.

4.2 Methods

This section describes the specific experimental details of methods employed in Chapter 4. In depth technical protocols for techniques can be found in Chapter 2. Similar to Section 2.10, the results presented here are in respect of the NC3Rs objectives for the replacement, refinement and reduction of animals in research.

4.2.1 Experimental design

A longitudinal study was performed to assess the morphological and functional changes to the outer retina *in situ* following $A\beta_{1-42}$ exposure. This type of experimental design is advantageous as it both eliminates processing artefacts commonly observed in ocular histology, and accounts for intra-animal differences in retinal layer thickness and function. All measurements from non-invasive retinal imaging techniques were therefore compared to baseline in respect of this, following which comparisons between cohorts at experimental intervals were made. The experiment was conducted over a three week period, with subretinal injections performed at week 1, and OCT and ERGs performed at baseline, week 2 and week 3. A timeline of experimental procedures is shown in Figure 39. Mice were culled via schedule 1 upon completion of experiments at week 4.

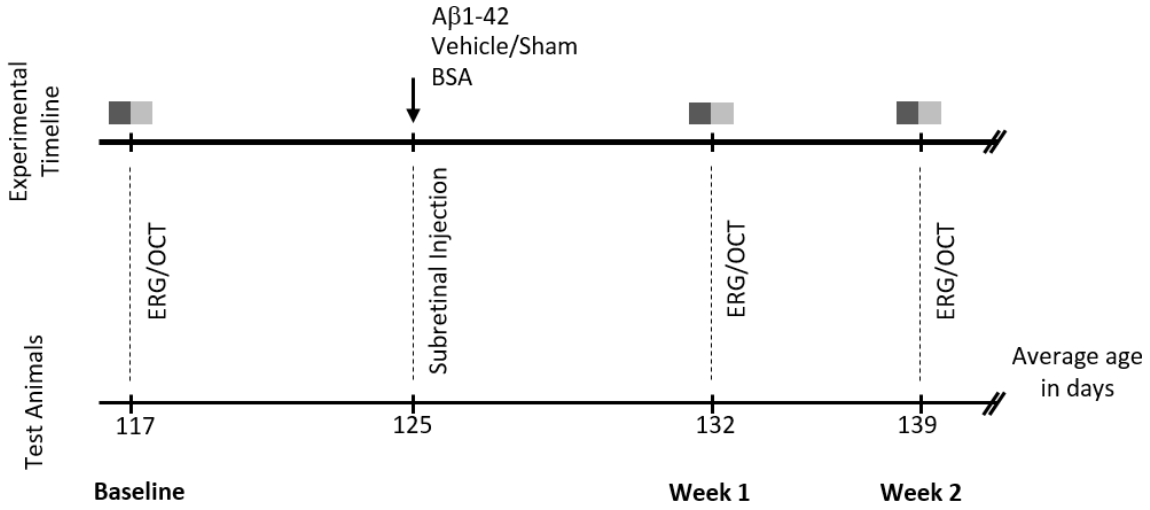

Figure 39: Experimental timeline of *in vivo* work.

Timeline showing the sequence of procedures mice underwent during the experiment. Boxes represent use of non-invasive imaging techniques (ERG/OCT) and arrows represent surgical intervention with either $A\beta_{1-42}$, vehicle/sham or Bovine Serum Albumin (BSA). The average age of mice (n=18) at each time point. Mice were culled at Week 2 (3 weeks after experimental onset) via schedule 1. Mice were left for 1 week after treatment to allow for retinal reattachment which has been predicted to occur within 18-24 hours after subretinal injection[242].

The experimental unit in all *in vivo* studies was the individual animal. This statistical parameter was chosen as opposed to randomised block design due to the potential for treatment to enter the systemic circulation and affect the contralateral eye.

4.2.2 Animal preparation and recovery

A total of 18 female C57BL/6 mice were sourced from the Biomedical Research Facility (University of Southampton) for experimentation, where numbers were determined using the resource equation method (Section 2.10.1). Mice used in this work were 117 ± 4 days old and weighed 22.8 ± 0.23g at experimental onset. In brief, animals were prepared for experimentation via anaesthesia (Section 2.10.2), phenylephrine hydrochloride and tropicamide were applied to eyes for 2 minutes respectively to achieve mydriasis and Viscotears was subsequently applied to prevent the formation of cataracts during experimental procedures. A suitable anaesthetic depth was indicated by loss of withdrawal reflex and was tested by both paw pinch and hind leg extension. Animals were maintained on a heat pad (27-29°C) during anaesthesia to maintain core body temperature at 37°C, whilst their and breathing rate was also monitored. Upon completion, animals received an IP injection with 200μl 0.5mg/ml antipamezole hydrochloride and were recovered on a heat pad until righting reflexes had returned. Body weight loss was also monitored throughout experiments as a surrogate measure of animal welfare, where experiments were terminated if a weight loss of greater than 10% occurred over a one week period. All information regarding animal housing and husbandry is detailed in Section 2.10.1.

4.2.3 Transcleral subretinal injection with $A\beta_{1-42}$

Transcleral subretinal injections (Section 2.10.3) were performed at week one. Mice were prepared (Section 2.10.2) and were randomly assigned to receive subretinal injection with 1.5μl of either 625nM oligomeric $A\beta_{1-42}$ (n=7), 625nM BSA (n=5) or vehicle/sham (n=6), where BSA served as a positive control for ocular inflammation[254 255]. $A\beta_{1-42}$ and vehicle/sham employed in this experiment were prepared as described in Section 2.4. A skilled ophthalmologist performed all subretinal injections, where the appearance of a retinal bleb through the operating microscope indicated a successful subretinal injection (Figure 40). Exclusion criteria included mice in which an intravitreal injection was performed or a retinal bleed was induced.

4.2.4 Fundoscopy of mouse retinae

Fundoscopic imaging of mouse retinae (Section 2.10.4) was performed on several pilot study mice to obtain examples of successful subretinal injection and to indicate the extent of retinal pathology induced by treatment groups. Fundoscopy was also attempted in the longitudinal experimental study design. However ocular clarity and anaesthetic depth following both ERG and OCT meant that the addition of this technique to the experimental design was unfeasible. Here, prolonged anaesthesia was associated with the formation of acute reversible cataract which precludes fundus examination.

4.2.5 Full-field Electroretinogram recordings

ERG recordings were conducted on experimental mice at baseline, week 1(day 8) and week 2 (day 15) post subretinal injection to assess treatment effects on retinal function. Mice were prepared (Section 2.10.2) and scotopic ffERGs were obtained following dark adaptation for 12 hours with a Pheonix Micron IV Retinal Imaging System and Generation II Image-Guided modality attachment (Section 2.10.5). ffERGs were conducted by stimulation with 1.5mm diameter, 6.8 cd-s/m2 white LED light for 1ms in 2 sweeps with a 120s interval, from which average A-wave and B-wave amplitudes, and T(A) and T(B) implicit times were calculated. These were subsequently calculated as a % change from baseline to account for inherent differences in retinal function. One-way ANOVA with Tukey's post hoc test assessed statistical comparisons with individual mice as the statistical unit. Data are presented as mean ± SEM. The statistical analysis of ffERGs is described further in Section 2.12.4.

4.2.6 Optical Coherence Tomography

OCT was performed immediately following ffERG at baseline, and week 1 (day 8) and week 2 (day 15) post subretinal injection, to assess treatment effects on the thickness of component retinal layers. OCT images were acquired as 1.4mm volumetric scans (100 B-scans comprising 1000 A-scans) after manual scanning of the retina for regions of pathology. If no pathology was evident, OCT scans were centred on the optic nerve. Further procedural and technical information regarding OCT is detailed in Section 2.10.6. Scans were segmented at 24 locations using the InVivoVue 2.4 Diver software for the RNFL, GCL, INL, OPL, ONL, IS, OS, ETPRS and the RPE. Thickness measurements were averaged to acquire a representative thickness for each layer and calculated as a percentage of baseline to account for

individual mouse differences. One-way ANOVA with Tukey's post hoc test assessed statistical comparisons, with individual mice as the statistical unit. Data are presented as mean ± SEM. As above, further information regarding the statistical analysis of OCT data is described in Section 2.12.4

4.2.7 Histological analysis of mouse eyes following subretinal injection

Histological analysis was performed on tissues obtained from a previous $A\beta_{1-42}$ subretinal injection pilot experiment involving 11 female C57BL/6 test naïve mice, to assess ocular pathology following $A\beta_{1-42}$ insult. These mice were aged 131 ± 2 days and 24.91 ± 1.16g at the time of experimental onset and had been randomly assigned to receive subretinal injection with either 625nM $A\beta_{1-42}$, or vehicle/sham. Experimental mice were culled via schedule 1 at week 2 (day 15) post subretinal injection, and eyes were processed for histology (Section 2.10.7). H&E staining was subsequently performed on retinal sections (Section 2.10.8), and pathological observations between treatment groups were quantified according to Section 2.12.5.

4.3 Results

4.3.1 Technical considerations of transcleral subretinal injection

4.3.1.1 Technique reproducibility

Subretinal injection success rates were calculated to determine technique reliability. Here, a technical expert (Dr Helena Lee) performed all subretinal injections to provide an accurate representation of technique success (Table 25). Of the 35 subretinal injections performed over the course of this project, 77.14% were successful. A failure rate of 22.86% existed, with intravitreal injection being the most common cause for technique failure closely followed by retinal bleed.

Table 25: Table to show the reliability of transcleral subretinal injections.

Details of success and failure rates for the 35 transcleral subretinal injections attempted across the experiment. In the case of failed subretinal injections, the failure criterion is detailed on the left along with the number of injections for which this occurred. It can be seen that, approximately 1 in 5 subretinal injections were unsuccessful with intravitreal injection being the most common cause for technique failure. This highlights the relative inconsistency of performing subretinal injections by hand.

	Transcleral Subretinal Injection			
Failure Criterion	**Success Rate**		**Failure Rate**	
	No.	**%**	**No.**	**%**
Intravitreal injection	30	-	5	-
Retinal bleed	32	-	3	-
Overall	27	77.14	8	22.86

4.3.1.2 Technique validation

Successful subretinal injection was confirmed by visualisation of a retinal bleb (Figure 40). This occurs when injected fluid detaches the retina and raises it in relation to the focal plane of the microscope. Thus, causing it to appear hyperreflective. The images presented in Figure 40 pertain to fundus images acquired in the initial pilot experiment. However, visualisation through the operating microscope was sufficient to confirm successful subretinal injection in the longitudinal experimental design. Interestingly, large areas of retinal pathology were evident in fundus images of BSA and oligomeric $A\beta_{1\text{-}42}$ injected eyes at one week post injection, corresponding to treatment-exposed regions. This occupied approximately a third of the field of view demonstrating the extent of treatment induced changes. However, retinas appeared normal upon inspection of vehicle/sham injected mice with no obvious areas of retinal pathology.

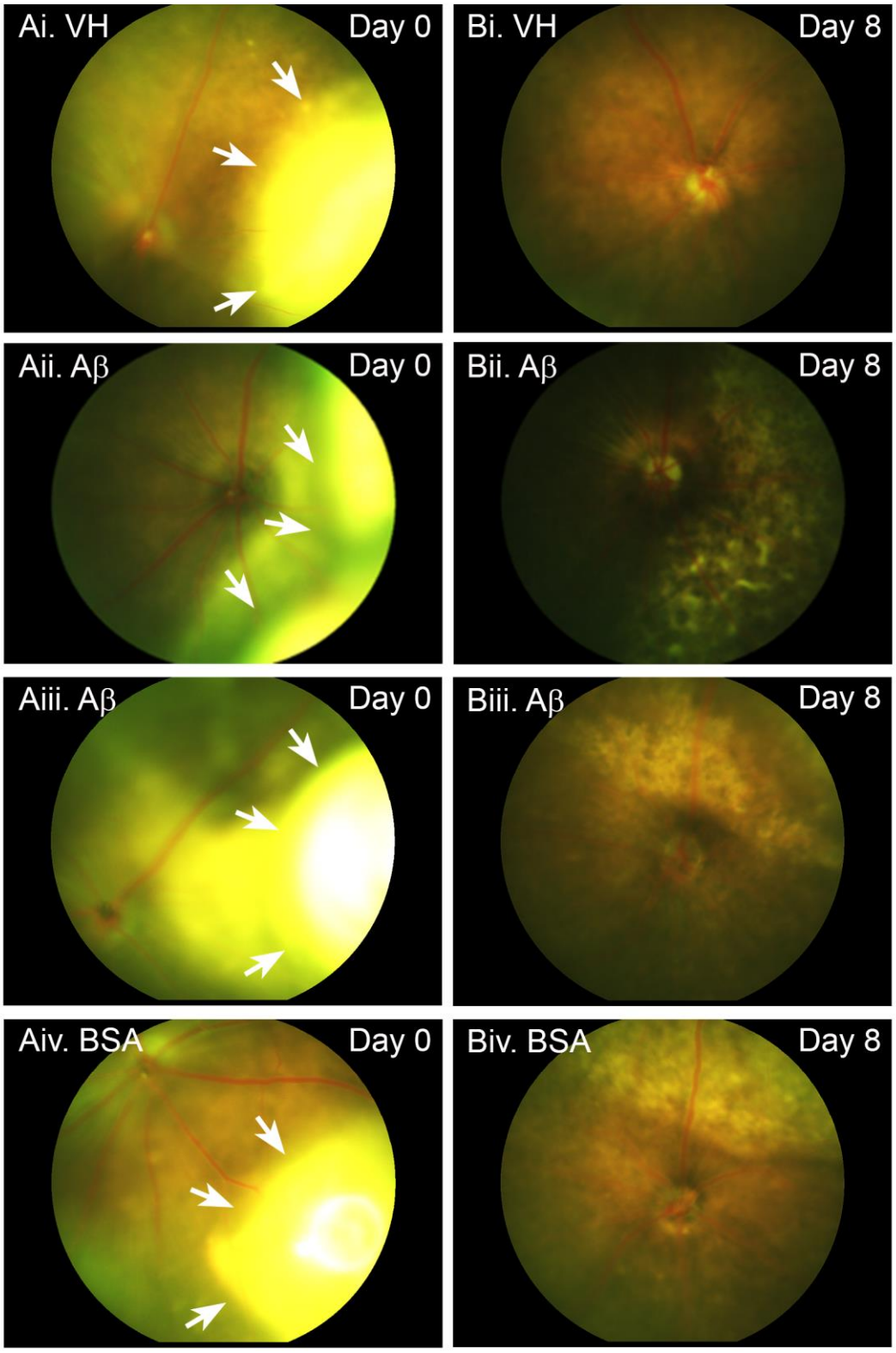

Figure 40: Fundus images showing successful subretinal injection.

Ai-iii. Example fundus images taken during the initial pilot experiment to show the retinal blebs indicative of successful transcleral subretinal injection. Retinal blebs were visualised as pale areas of retinal detachment (white arrows) with approximately 1.5μl of injected treatment filling the subretinal cavity. **Bi-iii.** Example fundus images of the eye presented in panel A, at 8 days (Week 1) post injection to confirm retinal re-attachment between surgical intervention and subsequent non-invasive retinal imaging. Details of experimental interventions are detailed on the left of each image pair. Note the extent of retinal damage in both BSA and $A\beta_{1-42}$ injected eyes at day 8 post injection. Image contrast has been altered across images here to facilitate visualisation of pathological changes to the retina.

4.3.1.3 Subretinal injection effects on animal welfare.

Mouse weights were recorded at weekly intervals following anaesthesia and surgical intervention, as a surrogate measure of animal welfare throughout the experimental time course (Figure 41).

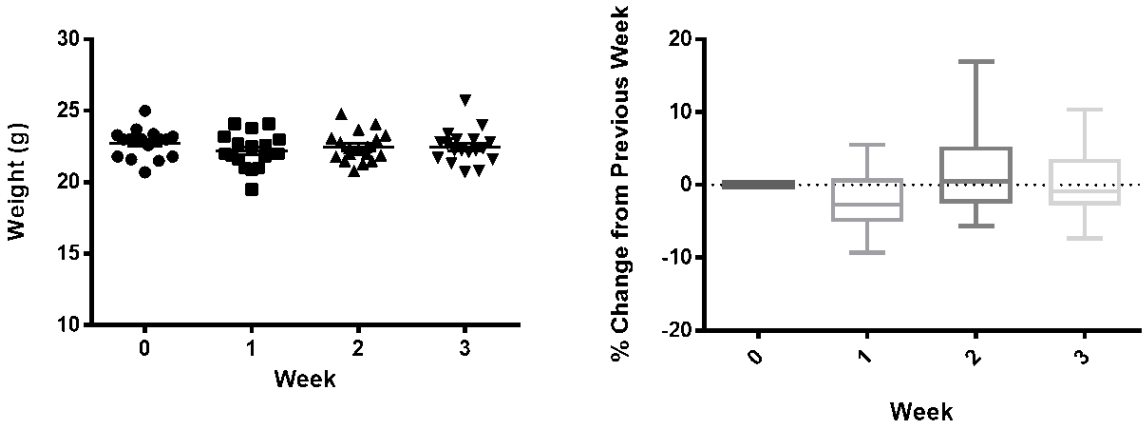

Figure 41: Effects of transcleral subretinal injection on C57BL/6 body weight

A. Average body weight measurements of experimental C57BL/6 mice. Data points are measurements of individual body weights at each experimental time point **B.** Box and whisker plots showing average % change of body weight from the previous experimental timepoint where error bars indicate minimum and maximum values. No change of greater than 9.3% was observed with respect to weight loss following sub-retinal injection over the experimental time course. Transcleral subretinal injection did not cause a significant change in weight (p= 0.5275) when assessed over the three-week period (One-way ANOVA with Tukey's multiple comparisons).

No weight loss of greater that 9.3% was observed over the entire experimental time course compared to the previous week (Figure 41). This corresponded to no significant difference between consecutive measurement when assessed by one way ANOVA (p=0.5275). Collectively, this suggests minimal effects of subretinal injection and the method of anaesthesia employed on animal welfare.

4.3.2 Pathological effects of $A\beta_{1-42}$ *in situ*

4.3.2.1 Effects of $A\beta_{1-42}$ on retinal function

Scotopic ffERGs were performed on experimental mice at one and two weeks post injection to assess the effects of $A\beta_{1-42}$ on global retinal function (Figure 42). ffERG recordings from injected eyes displayed the typical waveform expected across all experimental conditions. Specifically, no visual difference in the shape or amplitude of the wave was observed between treatment groups at both 1 and 2 weeks post subretinal injection. Slightly lower amplitudes were seen in general at 1 week post

injection. However, this is likely due to environmental influence on the day of experimentation, as all treatment groups were affected comparably.

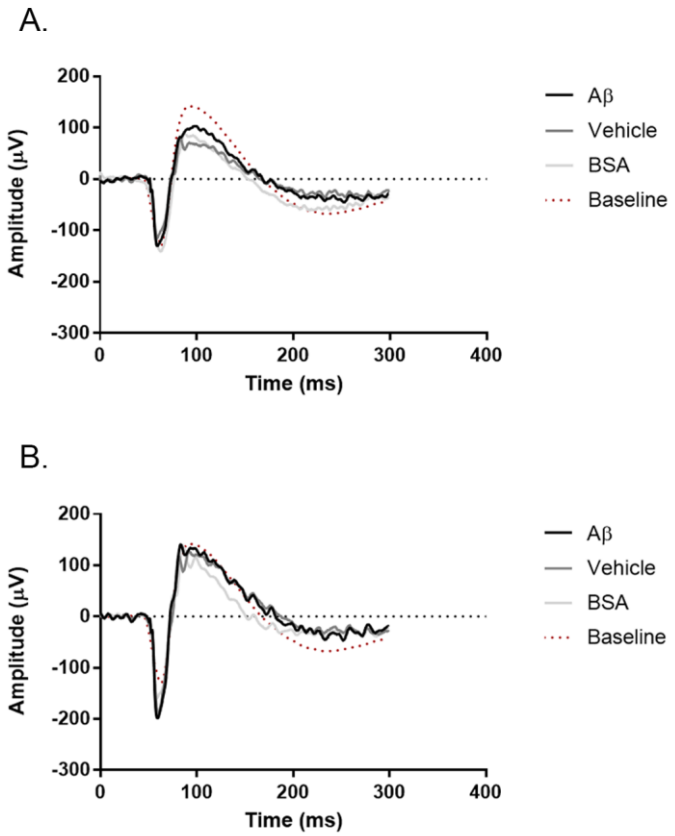

Figure 42: Scotopic ERGs of C57BL/6 mice following subretinal injection with $A\beta_{1\text{-}42}$.

Scotopic ERGs were recorded from C57BL/6 mice that had received subretinal injection with 625nM $A\beta_{1\text{-}42}$ (n=7), vehicle/sham (n=6) or 625nM BSA (n=5). ERGs were evoked with 1.5mm diameter, 6.8 cd-s/m2 white LED light for 1ms, in 2 sweeps with a 120s interval following dark adaptation for a minimum of 12 hours. Graphs represent average ERG recordings within treatment groups obtained at **A.** Week 1 and **B.** Week 2 post subretinal injection. Average baseline recordings are also shown for comparative purposes, although were not subject to the same environmental factors on the day of experimentation. No observable difference in either ERG amplitude or shape between treatment groups was noted at either 1 or 2 weeks.

Next, we conducted comparisons of A-wave and B-wave amplitudes, as well as the implicit time for each wave, to further investigate Aβ's effects on retinal function (Figure 43). No significant difference in the A-wave was seen across treatment groups at 1 or 2 weeks post subretinal injection. However, BSA exhibited a decreased trend at both experiential time points. This was mirrored by Aβ at week 1 albeit to a lesser extent. In all cases values were elevated above baseline, although this is likely due to differing environmental variables on the day of the procedure. Similarly, no significant difference was observed at 1 or 2 weeks post injection in the B-wave, where Aβ exhibited a comparable response to the vehicle/sham control. As with the A-wave, BSA exhibited a decreased trend at both time points suggesting a potential effect on inner retinal layer function. In terms

of ERG temporal properties, both Aβ and BSA demonstrated a consistently increasing trend in T(A) across the experiment. Again, this was not significant when assessed statistically but when taken collectively with Aβ and BSA effects on A-wave amplitude, may indicate a detrimental effect on photoreceptor function. In contrast, Aβ was comparable to vehicle/sham in respect of T(B) at both 1 and 2 weeks post injection, with only BSA showing a decrease in the time taken for the B-wave peak. A shorter latency was observed here relative to baseline recordings, but again was consistent across experimental conditions, suggesting it was due to external influences.

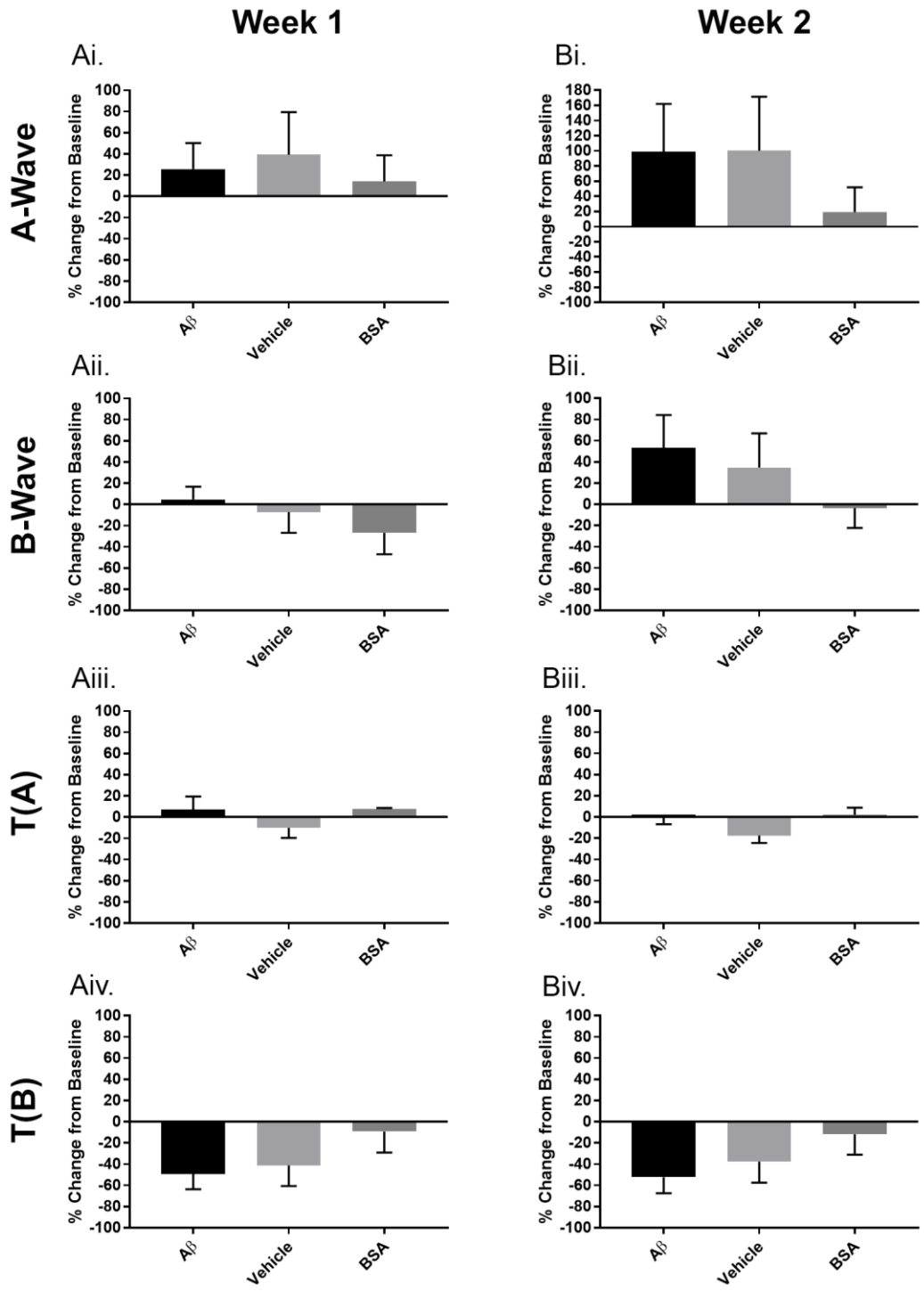

Figure 43: $A\beta_{1-42}$ effects on retinal function in C57BL/6 mice.

A-wave (Ai-Bi) and B-wave (Aii-Bii) amplitudes, along with T(A) (Aiii-Biii) and T(B) (Aiv.-Biv.), were recorded from scotopic ERGs of C57BL/6 mice that had received subretinal injection with $A\beta_{1-42}$ (n=7), vehicle/Sham (n=6), or BSA (n=5). Values were obtained at both 1 (Ai.-Aiv.) and 2 weeks (Bi.-Biv.) post injection, and calculated as a percentage change from baseline. Statistical significance was assessed between treatment groups using the Kruskal-Wallis Test with Dunn's multiple comparisons which showed no change in A-wave (p=0.9940, p=0.6659), B-wave (p=0.4486, p=4059), T(A) (p=0.3061, p=0.1259) and T(B) (p=0.2020, p=0.1133) recordings at 1 and 2 weeks post injection respectively. These results suggest that $A\beta_{1-42}$ and BSA induced retinal changes do not have a significant effect on global retinal function. Abbreviations: T(A), A-wave implicit time; T(B), B-wave implicit time.

4.3.2.2 OCT based qualitative assessment of $A\beta_{1-42}$ pathology

At week 1 (day 8) and 2 (day 14) following subretinal injection, OCT was performed to assess the association of $A\beta_{1-42}$ with disease morphology. In particular, $A\beta_{1-42}$ effects on outer retinal health and structure were of interest. Representative OCT images obtained for each of the three experimental groups are shown in Figure 44. Additionally, videos comprised of retinal cross sections from all grid locations segmented for representative mice are included in Appendix A, which demonstrate the extent of pathology observed relative to the whole retina.

Extensive retinal abnormalities were evident in $A\beta_{1-42}$ injected mice at both 8 and 15 days post injection. Specifically, the accumulation of subretinal material and fluid beneath the RPE was noted at localised regions within OCT scans. This was indicated by hyporeflective and hyperflective regions respectively (Figure 44, Ai-Cii). Interestingly, partial resolution of both subretinal fluid and Subretinal Hyperreflective Material (SHM) was observed at day 15 (Figure 44 Aii, Bii & Cii). This was associated with the emergence of small hyporeflective clefts within SHM regions. Alterations to normal retinal architecture were also observed in the BSA positive control for ocular inflammation at 8 and 15 days, which exhibited smaller areas of SHM and RPE hypertrophy (Figure 44, Di-Dii). The extent of retinal disruption within B-scans was significantly less than that observed in $A\beta_{1-42}$ injected mice, although BSA associated pathology was more widespread across the scans obtained. In contrast, the pathology observed in $A\beta_{1-42}$ injected eyes was confined to localised subretinal regions adjacent to the site of injection. Vehicle/sham injected mice displayed normal retinal architecture across OCT scans at all time points tested, suggesting a minimal effect on individual retinal layers. This is further demonstrated in the videos presented in Appendix A.

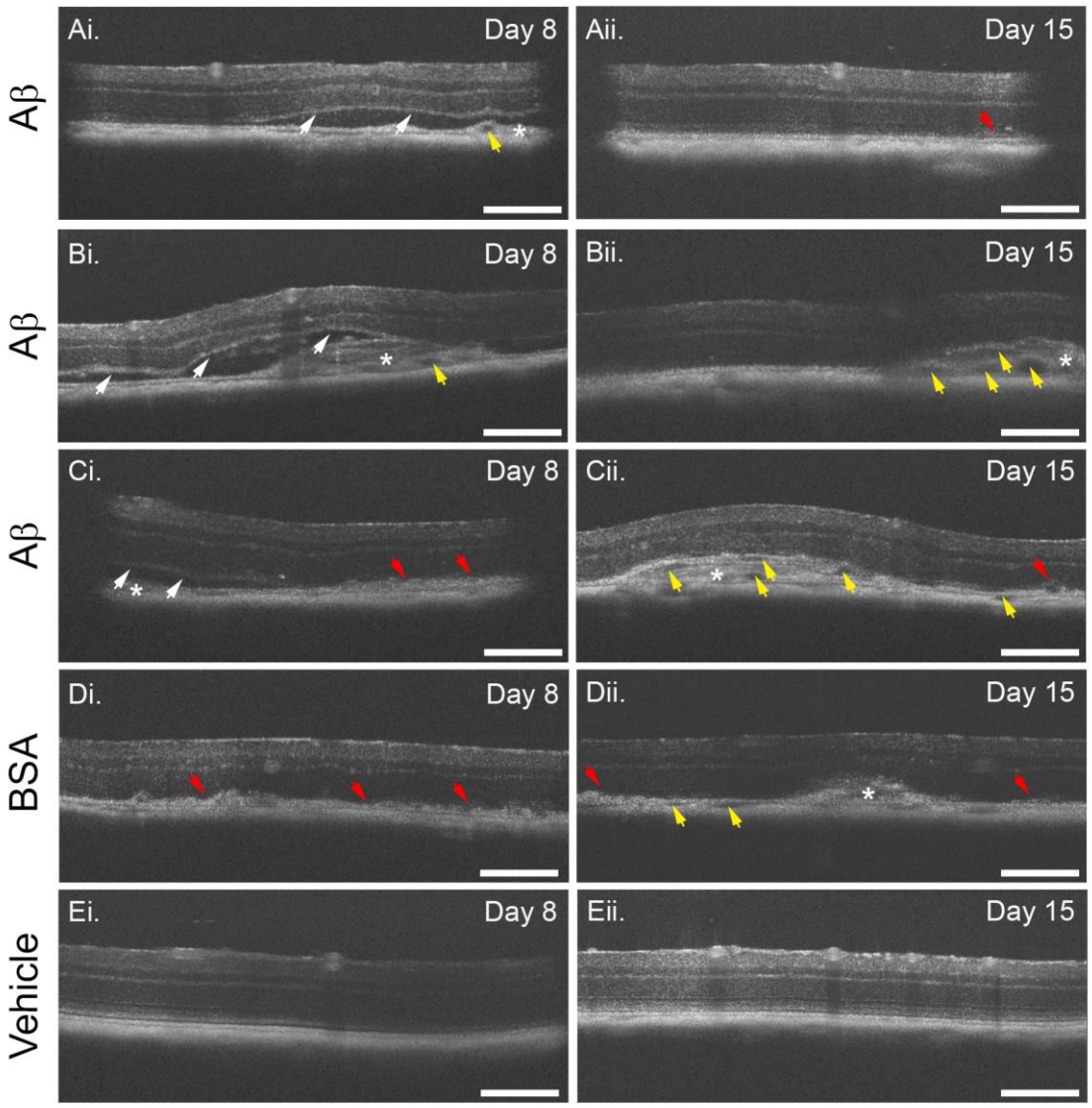

Figure 44: Representative OCT scans of C57BL/6 mice following subretinal injection.

Representative OCT B-scans of C57BL/6 mice subject to subretinal injection with 1.5μl 625nM $A\beta_{1\text{-}42}$ (A-C), 625nM BSA (D) or vehicle/sham (E) to show typical pathology observed at both 8 (Ai.-Ei.) and 15 days (Aii.-Eii.) post injection. Large areas of subretinal fluid accumulation (white arrows) were seen in $A\beta_{1\text{-}42}$ injected mice (n=7) at 8 days, along with SHM (white asterisks) and disrupted RPE (red arrows). By day 15, subretinal fluid appeared to resolve in most instances and was associated with an increase in putative cystic spaces (yellow arrows). Eyes injected with BSA (n=5) showed extensive regions of RPE disruption and presumed hypertrophy at both 8 and 15 days. In contrast, vehicle injected eyes (n=6) exhibited no pathology where normal retinal structure was observed in all but one instance. Videos spanning the entire retina of the images presented are included in Appendix A, which indicate the extent of retinal pathology observed. Scale bars represent 200μm. Abbreviations: BSA, Bovine Serum Albumin; OCT, Optical Coherence Tomography; SHM, Subretinal Hyperreflective Material.

4.3.2.3 Quantitative analysis of $A\beta_{1-42}$ effects on retinal layer thickness

OCT scans from $A\beta_{1-42}$ and BSA injected mice revealed noticeable areas of pathology, yet limited information regarding treatment effects on component retinal layer morphology could be ascertained. Segmentation was therefore performed on scans to quantify retinal cell layer thickness within experimental groups. Of particular interest was the effect of $A\beta_{1-42}$ on the outer retinal layers (Figure 45).

Segmentation analysis revealed no significant difference in the thickness of the IS, OS, photoreceptor end tips (ETPRS) or RPE following treatment with $A\beta_{1-42}$ compared to the BSA or vehicle/sham control. Similarly, no change in total retinal thickness (RT) was observed between treatment groups, despite $A\beta_{1-42}$ exhibiting a slight decrease in RT at 1 week post injection. A decreased trend in IS thickness was evident in $A\beta_{1-42}$ and BSA injected eyes at week 1, although again this was not significant and did not appear to persist at week 2. Interestingly, RPE thickness was visibly lower in $A\beta_{1-42}$ injected eyes at both experimental time points tested, supporting a potential effect of $A\beta_{1-42}$ on this cell layer.

Given Aβ's implication in glaucoma and visual manifestations of AD (Sections 1.6.3.1 and 1.6.3.2), segmentation of the inner retinal layers was also performed (Figure 46). However, no significant difference in the RNFL, GCIPL, INL, OPL or ONL was noted between treatment groups. A minimal decrease in thickness was observed in the RNFL at both 1 and 2 weeks relative to vehicle/sham and BSA, although this was not significant. Nonetheless, this may indicate a subtle biological effect of $A\beta_{1-42}$ on this cell layer. A decrease in OPL thickness at week 1 was also evident following injection with $A\beta_{1-42}$, although contradictory observations were seen at week 2.

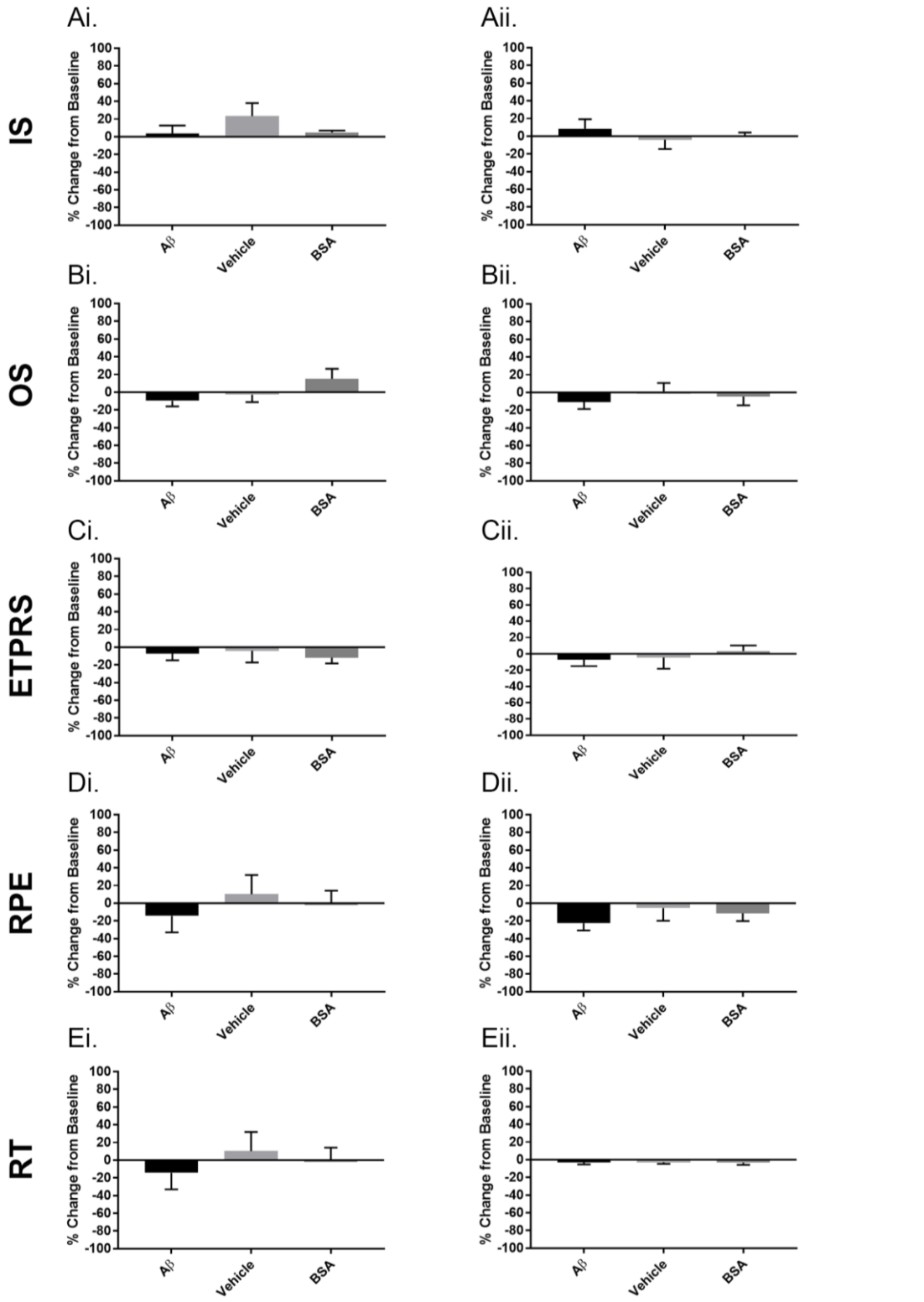

Figure 45: $A\beta_{1-42}$ effects on outer retinal layer thickness following subretinal injection.

Graphs showing the effect of subretinal injection with either $A\beta_{1-42}$ (n=7), vehicle/sham (n=6) or BSA (n=5) on the global thickness of outer retinal layers. Retinal thickness was assessed at both one (Ai.-Ei.) and two weeks (Aii.-Eii.) post injection. Data was quantified as a percentage change from baseline to account for intra-animal variability. Statistical analysis using the Kruskal-Wallis test with Dunn's multiple comparisons revealed no change in the IS (p=0.5484, p=0.8861), OS (p=0.3272, p=0.7041), ETPRS (p=0.8649, p=0.5212), RPE (p=0.4345, p=0.9245) or total RT (p=0.7351, 0.9218) at week one and two respectively. Abbreviations: IS, Inner Segments; OS, Outer Segments, ETPRS, End Tips of Photoreceptors; RPE, Retinal Pigment Epithelium; RT, total Retinal Thickness.

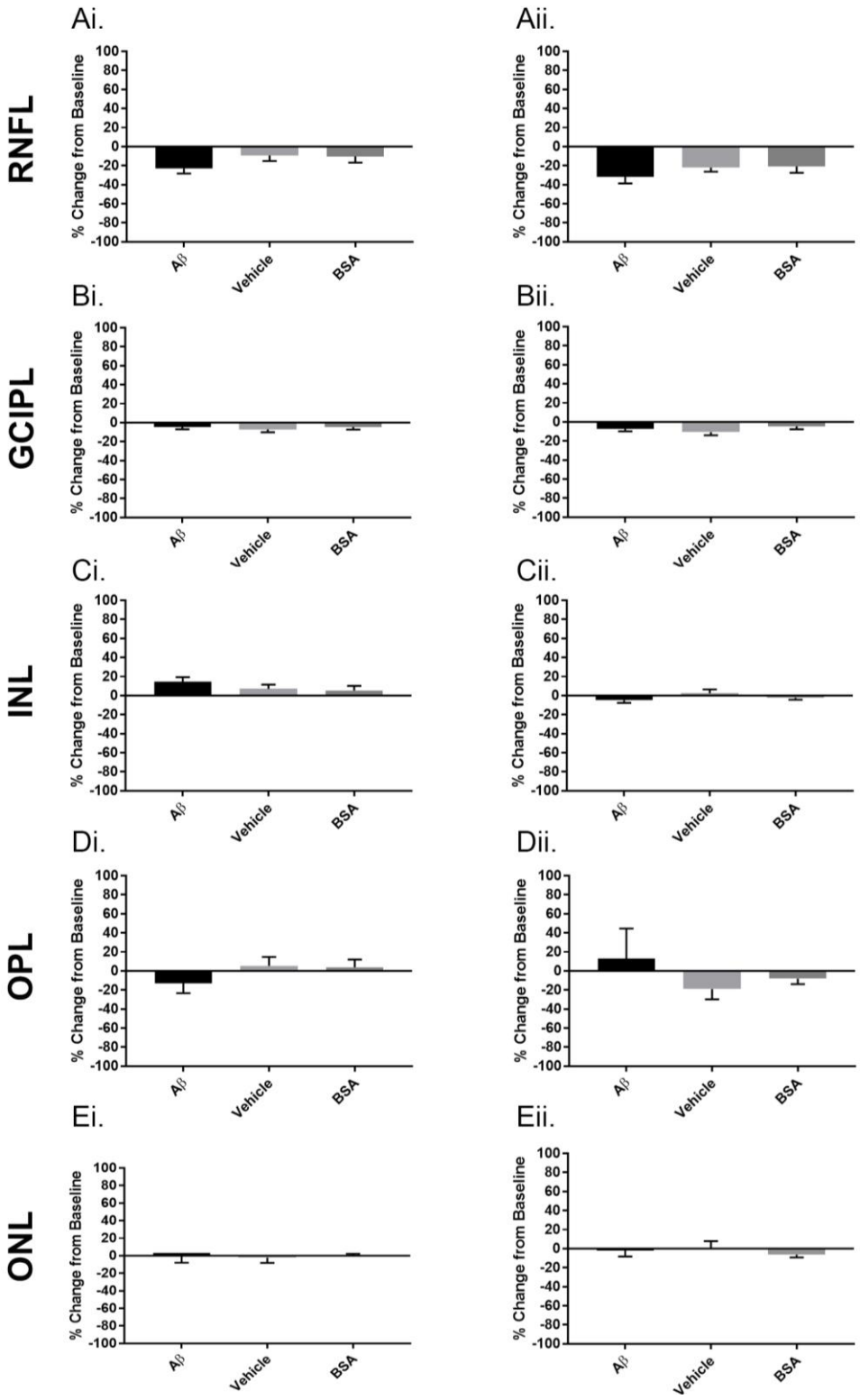

Figure 46: $A\beta_{1-42}$ effects on inner retinal layer thickness following subretinal injection.

Graphs showing the effect of subretinal injection with either $A\beta_{1-42}$ (n=7), vehicle/sham (n=6) or BSA (n=5) on the global thickness of inner retinal layers. Retinal thickness was assessed at both one (Ai.-Ei.) and two weeks (Aii.-Eii.) post injection. Data was quantified as a percentage change from baseline to account for intra-animal variability. Statistical analysis using the Kruskal-Wallis test with Dunn's multiple comparisons revealed no change in the RNFL (p=0.1789, p=0.2923), GCIPL (p=0.5313, p=0.4632), INL (p=0.4892, p=0.1758), OPL (p=0.3929, p=0.3061) or ONL (p=0.5951, p=0.4892). Abbreviations: RNFL, Retinal Nerve Fibre Layer; GCIPL, Ganglion Cell Inner Plexiform Layer; INL, Inner Nuclear Layer; OPL, Outer Plexiform Layer; ONL, Outer Nuclear Layer.

4.3.3 Histological analysis of $A\beta_{1-42}$ induced retinal pathology

Upon completion of longitudinal *in situ* studies, eyes were subject to H&E staining to further investigate $A\beta_{1-42}$ induced retinal changes. This subsection of Chapter 4 has been largely driven by undergraduate students supervised under this project. A medical student is currently pursuing histological data from eyes subject to OCT scans. Thus, no comment can be made regarding the correlation of OCT pathology with histological observations. However, previous project students have investigated $A\beta_{1-42}$ induced changes to the outer retina using eyes obtained from an initial pilot study. Here, line scan analysis was performed on histological sections to assess $A\beta_{1-42}$ effects on the PIS, POS and RPE/choroid morphology. Regions Of Interest (ROIs) were assessed blind at 200μm intervals along the length of retinal sections, and scores of either 1 or 0 were given to the PIS, POS and RPE/Choroid, corresponding to the presence or absence of pathological abnormalities respectively. The RPE and choroid were grouped under the same category here due to similarities in pigmentation. A positive score for pathology included any indication of PIS and POS atrophy or disorganisation, RPE hypertrophy, RPE hypopigmentation or hyperpigmentation and choroidal proliferation. A total of 15 sections were analysed per eye at 48μm intervals and a mean % abnormality was calculated (Figure 47). Statistical analysis of line scans using the unpaired student's t-test revealed that among the three categories scored, the only significant difference in pathology in $A\beta_{1-42}$ injected eyes was in the RPE monolayer/choroid (Figure 47 Biii.). Typically, numerous circular choroidal voids were seen here, along with disruption of the RPE monolayer (Figure 47 Aii) and the accumulation of star-like cells (Figure 47 Ai). These were absent in vehicle/sham injected controls (Figure 47 Aiii-iv). A degree of abnormality was also noted within the RPE/choroid of controls (Figure 47 Biii) but this may be explained by the natural cleavage plane that exists between the RPE and photoreceptors, which can separate upon processing causing cutting artefacts. This also explains the high abnormality observed for the control with respect to the POS, which constitutes the adjacent surface of the cleavage plane. An example of cutting artefact associated pathology is provided in Figure 47Aiii. In both instances, this limitation has been accounted for in the analysis method. An increased trend in POS pathology in $A\beta_{1-42}$ injected eyes also existed (Figure 47, Biii). However, no conclusion could be made as to whether Aβ influences or drives pathology within this layer as this difference was not deemed statistically significant. Minimal abnormalities were seen in the PIS, which appeared normal in 95% of cases (Figure 47 Bi). No comparisons with the

BSA positive control for inflammation were made here due to the limited n number (n=1) in the initial pilot study.

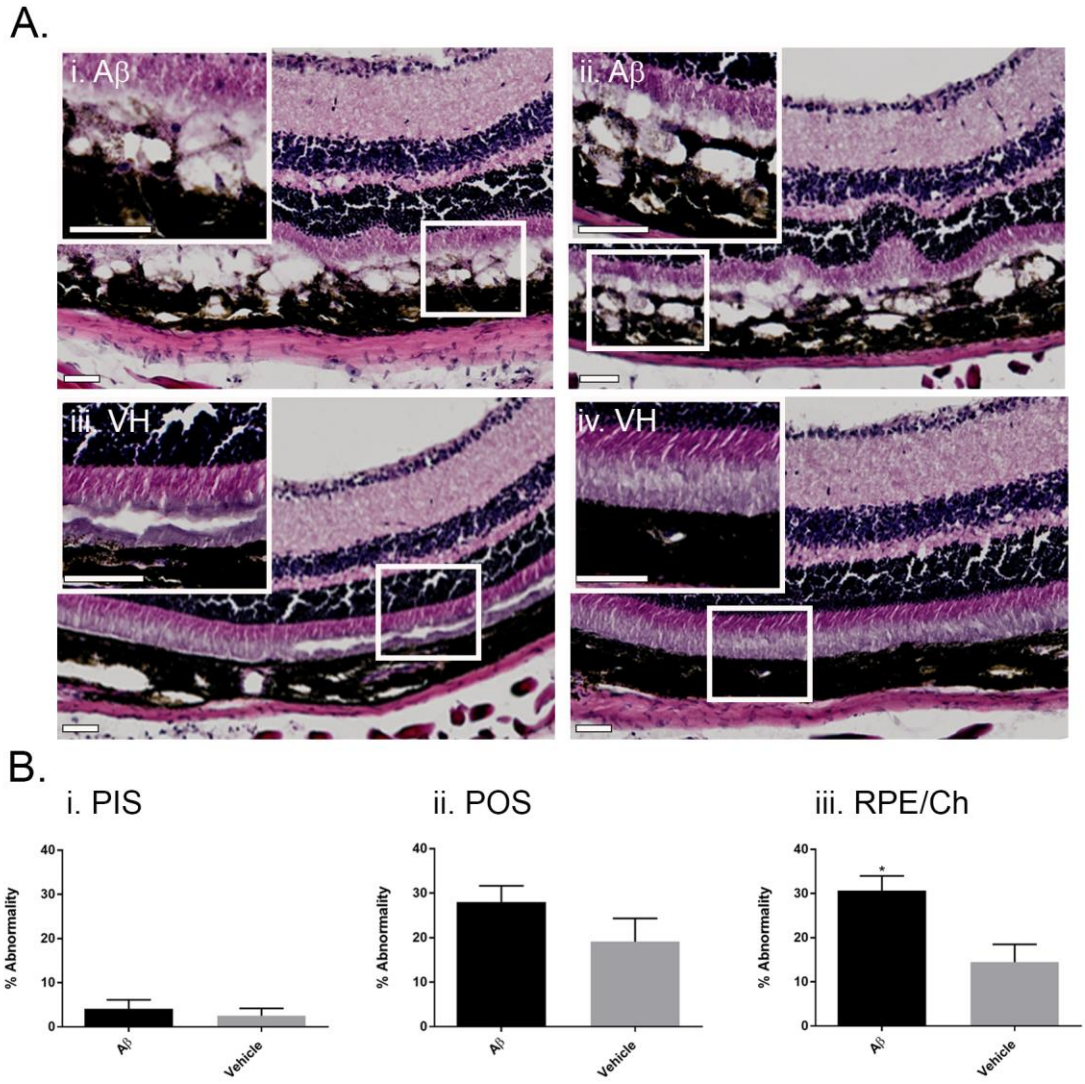

Figure 47: Histological quantification of outer retinal pathology following subretinal injection with $A\beta_{1-42}$ or vehicle/sham.

Line scan analysis was performed on H&E stained retinal sections to quantify pathology within the PIS, POS and RPE/choroid in eyes subject to subretinal injection with $A\beta_{1-42}$ (n=10) and vehicle (n=3). **Ai-Aii.** Typical pathology observed in $A\beta_{1-42}$ injected mice. Large areas of RPE disruption along with POS thinning/atrophy were noted. This was associated with an increased choroidal volume, which displayed circular voids suggestive of vessel proliferation (Aii). Star-like cells also appeared to accumulate within such regions (Ai). **Aiii.** Example of POS damage ensuing from natural cleavage of the plane between the RPE and photoreceptors. **Aiv.** Typical retinal structure observed in vehicle sham/controls where the RPE and POS remained attached. **Bi-iii.** Graphs showing the percentage abnormality recorded for outer retinal layers in response to treatments. Statistical significance was assessed using the unpaired students t-test which revealed increased RPE/Ch pathology in $A\beta_{1-42}$ injected mice ($p=0.0310$). No significant pathological difference was observed in the IS ($p=0.7137$) or OS ($p=0.2555$) between $A\beta_{1-42}$ and vehicle/sham injected eyes. Scale bars correspond to 50μm. Abbreviations: Ch, Choroid; PIS, Photoreceptor Inner Segments; POS, Photoreceptor Outer Segments; RPE, Retinal Pigment Epithelium.

4.4 Discussion

4.4.1 Overview

Clinically AMD is well defined, with distinct alterations to the retinal environment and architecture being associated with a particular disease stage or pathway of progression (Section 1.3.4). These are commonly used to inform AMD animal studies, where comparable pathological abnormalities and histopathological features to human disease cases, are often indicative of a role for a particular gene, protein or insult in disease onset/progression[331]. Aβ has been implicated in key hallmarks of AMD as well as clinical features of its progression (Section 1.6). However, as yet limited studies have been conducted *in vivo* to investigate the ability of Aβ to drive disease pathology in the absence of other retinal changes. In this chapter we investigated the ability of $A\beta_{1-42}$ to induce an AMD-like phenotype in C57BL/6 mice. In particular, we aimed to determine the association of Aβ with particular disease stage and/or phenotype.

4.4.2 Transcleral subretinal injections: a 3Rs perspective

The use of subretinal injections in rodents to deliver experimental treatments has become increasing important in the field of retinal research. This technique is widely used in both the application of viral vectors in preclinical gene therapy studies[336], as well as in the investigation of factors underpinning various retinal diseases. Here, it has been utilised in determining the effects of oligomeric $A\beta_{1-42}$ in AMD. However, no reports exist regarding the reliability of this technique and its impact on animal usage. This hinders accurate power calculations, particularly with respect to attrition rates, resulting in the unnecessary over use of animals. As such, technique success rates were recorded throughout our experiments to inform future investigations in respect of animals required (Section 4.3.1.1). The aim being to promote a reduction in numbers used per experiment.

In spite of being performed by a technical expert, we found that on average 1 in 4 to 1 in 5 subretinal injections fail, identifying a relatively high attrition rate. This lack of technical robustness presents two problems. First, result accuracy is reduced where average recordings are not possible, particularly as the experimental unit here was the individual animal. Secondly, mice with failed subretinal injection in both eyes are culled, leading to a degree of mouse wastage. Nonetheless, this technique is widely utilised and exhibits several advantages over

other techniques. For example, it allows the delivery of treatments or factors under investigation in close proximity to the photoreceptors and RPE, which constitute the fulcrum of pathogenesis in several vision threatening disorders[336]. In this respect, the presentation of this result only aims to inform this area of the literature and increase accuracy when employing this technique.

Similarly, weight measurements were conducted across the experimental time course as a surrogate measure of animal welfare. Such information will inform the refinement of subretinal injections, where if negative impacts on animal welfare are identified, interventions to minimise animal suffering may be implemented. Our results and observations suggest that subretinal injections, along with the method of anaesthesia employed within this study, have little effect on animal welfare (Figure 41). In addition to weight measurements, mice were also observed for action units of the grimace scale whilst under anaesthesia, receiving subretinal injection, or undergoing ERG or OCT. This included any detection of orbital tightening, bulging of the nose or cheeks, ear position and whisker change[337]. Whilst no quantitative assessment of this measure was performed, we noticed no such effects whilst employing the experimental techniques described. This supports the mitigation of stress as a confounding variable in the interpretation of experimental results, which has been implicated in altered metabolism and weight loss in laboratory animals previously. In summary, the results presented here support the use of the employed techniques in respect of animal welfare.

4.4.3 Global retinal function remains unimpaired following subretinal injection with $A\beta_{1-42}$ as measured by ffERG

A-wave and B-wave amplitudes are typically employed in both the clinic and laboratory to ascertain changes to retinal function in human and experimental ocular disease. In numerous retinal disorders, a reduction in the A-wave and/or B-wave amplitude is evident[27]. The implicit time for both the A-wave (T(A)) or B-wave (T(B)) is also affected across a range of retinopathies e.g. Retinitis Pigmentosa and Choroideremia, presenting as a lag in peak onset[27 338]. Thus, these parameters were investigated here to determine if the pathological changes observed (Figure 44) correlated with an impairment of retinal function. Comparisons of A-wave and B-wave amplitudes (Section 4.3.2.1) revealed no significant effect of $A\beta_{1-42}$ on photoreceptor or distal retinal cell function (Section 1.2.2). This was perhaps expected, as corresponding pathology seen in histology and OCT scans was confined to specific retinal regions. Full-field ERG (ffERG) is known to lack sufficient

sensitivity to detect early-AMD pathology and alterations to macula function in the clinic, where measurable deteriorations in function are only reported in advanced disease cases[339].As with the localised pathology seen here, this is attributable to the small size of the macula relative to the whole retina[340]. Nonetheless, this perhaps supports a role for Aβ in driving incipient macula changes in the early stages of AMD that remain undetectable by ffERG. The only noteworthy observation was a slight decreased trend in A-wave amplitude upon $A\beta_{1-42}$ injection which corresponded to a lag in T(A). We speculate that this may be indicative of minor impairments to the phototransductory properties of the photoreceptors. Focal ERG recordings would provide further insights into the effects of localised pathology on retinal function[340], but which currently remains untestable in our laboratory. In contrast the BSA positive inflammatory control induced a decreased trend in both the A-wave and B-wave amplitude at all time points tested. This is perhaps explained by the extent of retinal pathology observed in OCT scans, which overall appeared less severe than $A\beta_{1-42}$ associated pathology, but spanned a significant area of the retina. Interestingly, our results contrast previous reports of $A\beta_{1-42}$ subretinal injection effects on mouse visual function, which demonstrated a decline in A-wave, B-wave and C-wave function despite a comparable study n number and technique[341]. However, this study used the student's t-test to make comparisons between the three experimental groups, questioning the method of statistical approach and validity of this observation. In contrast, ERGs conducted on 2-3 month 5xFAD and 10 month old C57BL6 mice support our observations, which display no difference in A-wave or B-wave amplitudes despite Aβ exposures extending far beyond the timeframes employed[342].

4.4.4 Subretinal injection with $A\beta_{1-42}$ induces a localised CNV phenotype

In an attempt to investigate the deleterious effects of $A\beta_{1-42}$ on the retina, OCT scans were also scrutinised for evidence of retinal pathology. This is the only report of its kind, which facilitates the detailed analysis of $A\beta_{1-42}$ induced retinal pathology *in situ*. For the first time, the OCT scans presented here implicate $A\beta_{1-42}$ with degenerative alterations suggestive of a wet AMD phenotype. Specifically, subretinal fluid and SHM was observed along with retinal and RPE detachment, a finding commonly observed in clinical OCT scans of AMD patients[127]. In general, SHM refers collectively to the accumulation of exudate and may include haemorrhage, lipid, pigment, subretinal fibrosis and CNV[343]. The increased

prevalence of putative cystoid spaces seen at 2 weeks post-injection is also comparable to Cystoid Macula Edema (CME) seen in some wet AMD patients[127 344]. In fact, detection of CME by OCT is being increasingly encouraged as an indicator of the earliest phases of disease[344]. Previous studies investigating $A\beta_{1-42}$ effects on retinal morphology *in vivo* also support its association with an AMD-like phenotype. Accounts of RPE hypopigmentation, disorganisation, hypertrophy and extensive autophagic vacuolation have been reported previously, along with photoreceptor disruption[242 341]. In contrast to our findings, these associate $A\beta_{1-42}$ with an early dry AMD phenotype. We also noted the presence of numerous voids in histopathological studies of retinal sections here (Section 4.3.3), although these appeared to occur within the choroid and were remarkably similar to changes reported within the choroidal vasculature of aged VEGF 118/118 mice[345]. These mice display features indicative of GA, but also incur choroidal remodelling and atrophy. In fact, this observation may support the proposed involvement of $A\beta$ in altered VEGF signalling and choroidal maintenance. $A\beta_{1-42}$ associated retinal pathology observed within this study was also confined to discrete areas, reminiscent of AMD lesions. In contrast RPE disorganisation and SHM seen in the BSA positive inflammatory control spanned expansive regions of the retina but was minor in comparison. This likely translates to lack of significance observed in Section 4.3.2.1 upon comparison of ERG waveforms. Collectively, the results presented here, in addition to previous literature reports, support the ability of $A\beta_{1-42}$ to drive AMD-like pathology. However, the association of $A\beta$ with a specific disease stage remains in dispute. Indeed, its implication with both dry and wet AMD-like phenotypes may highlight divergence of the disease from a similar underlying process.

4.4.5 The global thickness profile of individual retinal layers is unaltered following subretinal injection with $A\beta_{1-42}$

In an attempt to determine the sites of primary degeneration following $A\beta_{1-42}$ exposure, OCT scans were segmented for component retinal layer thickness. In spite of obvious disturbances to the outer retina (Section 4.3.2.2), our analyses indicated no significant global reduction in any of the constituent layers (Section 4.3.2.3). This was consistent across all treatment groups and time points tested. Again, we speculate that may is due to the localised nature of the pathology observed which was minor in comparison to the expanse of the whole retina analysed. The only apparent trend was a decline in RNFL and RPE thickness

suggesting a potential effect of Aβ on these layers. This is further supported by a large body of literature. For example, thinning of the RNFL parallels AD progression[346] and is a clinical feature of glaucoma[171], both of which have been associated with increased inner retinal Aβ accumulation (Sections 1.6.3.1 and 1.6.3.2). In fact, RNFL thinning typically precedes RNFL retardance in glaucoma and is an indicator of early disease[347]. The effects of $A\beta_{1-42}$ on the RNFL are not directly applicable to AMD, in which the affected macula lacks inner retinal layers. Nonetheless, it supports the potential use of this mouse model in glaucoma and AD research with respect to Aβ's effects on visual dysfunction. Similarly, numerous studies have associated $A\beta_{1-42}$ with various aspects of RPE dysfunction (Section 1.7). The decreased trend in RPE thickness reported here further supports Aβ's involvement in the early RPE changes that precede advanced AMD pathology. In this respect, Aβ likely presents an attractive candidate for early AMD therapeutics. This was explored in a recent study that demonstrated a reduction in both $A\beta_{1-40}$ and $A\beta_{1-42}$ levels of C57BL/6 and 5xFAD mice following neprilysin treatment[342]. This enzyme degrades Aβ monomers thereby preventing aggregation in to toxic oligomeric species. In fact, neprilysin-deficient aged mice also show extensive RPE alterations[197], as well as Aβ containing drusen further supporting Aβ's involvement in disease progression. The next logical step would be to assess whether treatment with neprilysin is capable of alleviating Aβ induced pathology in such mice. In sum, concordant with our hypothesis, Aβ appears to be a key player in driving AMD pathology.

4.4.6 $A\beta_{1-42}$ primarily affects the RPE/Choroid

It is difficult to ascertain the true effects of $A\beta_{1-42}$ on component retinal layers from OCT scans alone. As such, we performed histology on experimental eyes to corroborate Aβ's apparent effects on the outer retina. Owing to the longitudinal study design, the histology of tissues presented does not correspond to mice analysed via OCT. Nonetheless, these mice underwent an identical subretinal injection procedure and are predicted to exhibit comparable pathology. In contrast to OCT scans, no regions of subretinal fluid accumulation or SHM were seen. This may be attributable to our laboratory's processing procedure, which involves removal of the anterior segment and lens prior to sectioning. Inevitably, this would provide a path of outflow for any subretinal exudate. Similarly, it is difficult to distinguish subretinal fluid from cutting artefact. Snap freezing of eyes in liquid nitrogen and post fixation of sections would enhance the possibility of detecting

fluid accumulation and is currently being trialled in the laboratory. However, $A\beta_{1-42}$ injected mice did exhibit numerous vacuoles in the choroidal vasculature/RPE, which translated to a significant difference in the degree of RPE/Choroidal abnormalities reported compared to controls. This supports the involvement of Aβ AMD, in which choroidal pathology is associated with both forms of advanced disease[348]. Such pathology is also concordant with the SHM detected in OCT scans, which usually derives from impaired or proliferating choroidal vasculature[127]. Finally, thinning of the POS layer was noted in localised regions, but as with ERG and retinal thickness plots, was not expansive enough to affect global retinal abnormality. Nonetheless, this phenotype resembles typical photoreceptor atrophy observed secondary to RPE loss in AMD. Histology of longitudinal experimental candidates will provide further insights into, as well as consolidate the OCT pathology observed (Section 4.3.2.2).

4.5 Conclusions

The data presented in this Chapter supports a key role for Aβ in driving AMD pathology. In particular, it implicates $A\beta_{1-42}$ with pathological changes typical of a wet AMD phenotype. This was not all together surprising as our research here adds to an increasing body of literature supporting a biological role for Aβ in choroidal management, as well dysregulation following an increased retinal Aβ presence in disease (Section 1.7). Our future studies aim to exploit the 5xFAD AD mouse model, which is known to accumulate retinal Aβ with age, to define the sequence of Aβ induced retinal changes that result in a AMD-like phenotype. Using this mouse model eliminates the potential flaws associated with subretinal injection. Additionally, we aim to determine the primary sight of Aβ insult. We, along with others in the field, speculate that this is almost definitely the RPE given Aβ's expansive implication in various RPE dysfunctions that occur prior to advanced pathology in AMD.

Chapter 5 Vitreous Aβ concentrations in AMD

5.1 Background

The vitreous humour resides in the posterior ocular chamber (Section 1.2.1) and is a transparent, fluid-like gel that occupies approximately 80% of the ocular volume[17]. Broadly, it can be divided into three anatomical substructures, the vitreous core, vitreous cortex and vitreous base[256]. The relative ocular locations of these are shown in Figure 48.

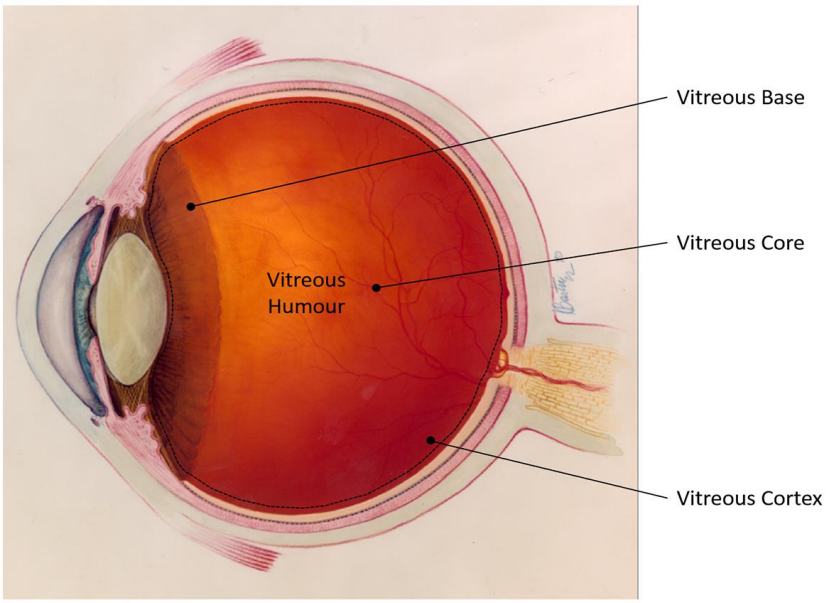

Figure 48: Diagram to illustrate the location of the generalised anatomical substructures within the vitreous humour.

The vitreous base lies posterior to the lens, comprises a high collagen content and is viscous in nature. The vitreous cortex is also collagenous, maintains adhesion to the inner limiting membrane of the retina, and surrounds the vitreous core. The latter makes up the central portion of the vitreous and is a highly hydrated extracellular matrix. The aqueous nature of the vitreous core is associated with its frequent use in the biochemical and pathological analysis of the vitreous proteome in ocular disease[256 349]. Image adapted from the National Eye Institute Photos and Images catalogue, National Institutes of Health, which may be accessed via the following link: https://nei.nih.gov/photo.

In terms of its composition, the vitreous comprises ~99% water, with collagen, hyaluronic acid, glucose, inorganic salts and hyalocytes constituting the remaining 1%[256 350]. However, this varies somewhat depending upon the specific anatomical substructure being investigated and is a factor that must be considered in study design[256 258]. Collagen and hyalocytes are mainly concentrated in the vitreous base, whereas the vitreous core is a hydrated aqueous extracellular matrix[256]. The lower viscosity associated with the vitreous core lends itself to analysis with minimal sample preparation. Hence, it is widely exploited in the proteomic analysis of the

vitreous in a variety of ocular conditions[351]. Here, the vitreous presents a valuable tool to identify causative agents and ocular biomarkers associated with disease. This is largely attributable to the close proximity of the vitreous to the retina, which results in the composition of the vitreous proteome reflecting local changes in the secretion of metabolic factors and cytokines[256]. In fact, this has led to the identification of several vitreous biomarkers for conditions including AMD[352] and DR[353 354]. Conveniently, vitreous biopsies are also by-products of routine ocular surgery, which facilitates access without the need for additional invasive procedures.

The literature discussed in Chapter 1 strongly suggests the involvement of Aβ in AMD pathology. For example, the Aβ content of drusen appears to correlate with disease susceptibility and progression[202 208 209] where it has been reported to be exclusive to the drusen of AMD patients[231]. Similarly, Aβ deposits in/around the RPE with increasing age[196 202 203] and has been associated with detrimental alterations to RPE function[242-244]. Collectively, this identifies Aβ as a prospective biomarker for disease. It is therefore of interest to the AMD field to identify whether elevated Aβ levels are consistently associated with AMD, the results of which may be used to improve the clinical phenotype and/or halt the progression of this devastating condition.

To date, previous work has reported the presence of $A\beta_{1-40}$ and $A\beta_{1-42}$ isoforms in both bovine and murine vitreous[199]. However, it was not until recently that the concentration of Aβ in human vitreous was determined. This was reported to be 537.6 ± 193.7 pg/ml and 53.7 ± 39.5 pg/ml for $A\beta_{1-40}$ and $A\beta_{1-42}$ respectively[200], highlighting a 10-fold higher content of $A\beta_{1-40}$ in the healthy human vitreous. It was also shown that $A\beta_{1-40}$ and $A\beta_{1-42}$ do not vary significantly between the ages of 55-101, when AMD prevalence increases significantly[342]. Thus, if vitreous Aβ concentration is shown to correlate with AMD pathology, elevated levels in those most at risk may be indicative of early disease. Previous studies investigating the $A\beta_{1-42}$ content of the vitreous in retinal disease, including Macular Hole (MH), DR and glaucoma, have linked both glaucoma and DR with reduced vitreous concentrations[229]. To our knowledge, only one study has been performed to date regarding the presence of Aβ peptides within the vitreous humour of AMD sufferers. This demonstrated a 6-fold increase in the presence or soluble Aβ compared to controls, and was also associated with a decrease in the soluble isoform of the Aβ receptor, RAGE[355]. However, owing to techniques employed, absolute quantification of Aβ in AMD vitreous vs. control vitreous was unachievable.

This study was also confined to a cohort of 34 control and 12 AMD patients, and therefore lacked an appropriate statistical power to draw firm conclusions. Thus, the relationship between vitreous Aβ concentration and AMD is yet to be established and remains a void in the literature regarding Aβ's involvement in AMD.

The purpose of this chapter was to initiate an analytical case-control pilot study to investigate how total vitreous Aβ concentration alters with AMD status. The aim being to test the use of Aβ as a prospective biomarker for disease susceptibility and prognosis, and to better establish the relevance of Aβ in aged and AMD retinas. Here, total Aβ concentration in vitreous biopsies from "normal" controls and AMD patients was quantified by an $A\beta_{1-x}$ ELISA, and initial statistical comparisons were made between experimental groups and disease status to determine associations. Further, the total Aβ concentration in "normal" state controls was plotted as a function of age, smoking pack-years, Mean Arterial Pressure (MAP) and primary ocular pathology to determine potential experimental confounds. This study also sought to confirm the physiological concentration of Aβ in 'normal' vitreous to better inform future *in vitro* studies in terms of biologically relevant treatment concentrations. The outcome of this final point is particularly important given the lack of clarity on accurate physiological ocular Aβ concentrations reported in the literature.

5.2 Methods

This section describes chapter specific experimental details for Chapter 5. For in depth technical protocols please refer to Chapter 2.

5.2.1 Study cohort selection

The study cohort was identified as described in Section 2.11.1. Screening of VR pre-operative lists was executed by the ophthalmology research team (Eye Unit, Southampton General Hospital), where patients were recruited onto the study subject to satisfying the inclusion criteria detailed in Table 20 for either control (normal state) or experimental (AMD) samples. In all cases, a consultant ophthalmologist performed medical assessments and determined clinical status. Further, study participation was subject to patient autonomy. Examples of information sheets, consent forms and proformas processed by the ophthalmology research team for the study described in this chapter are included in Appendix C.

5.2.2 Grading of AMD status

AMD or control status was determined from fundus and OCT examinations by at least two consultant ophthalmologists to reduce researcher bias, according to the AREDS classification system detailed in Table 20. If conflicting diagnoses were made, a third clinical assessor was recruited to confirm patient status. Diagnostic details as well as the number of assessors required per patient are detailed in Table 26, which highlights the importance of incorporating multiple clinical assessments into case-control studies. This appears to be essential for study validity. Examples of fundus and OCT images assessed by study clinicians for both control and AMD patients are presented in Figure 49.

5.2.3 Confounding factors

Information regarding patient age, gender, concomitant medical conditions and prescribed medications was also recorded to confirm a similar occurrence of potentially confounding co-variates in experimental and control groups (Table 27 and Table 28). Of particular interest was the influence of smoking history on vitreous Aβ concentration, which is a known risk factor for AMD[5]. This was quantified in pack-years, assuming 20 cigarettes per pack, according to Equation 3.

$$Pack\ Years = (CxY)/20 \qquad \text{Equation 3}$$

C = Average number of cigarettes smoked per day
Y=Total number of years spent smoking

Smoking correlates with increased blood pressure[356], another suggested risk factor for AMD development[106]. Thus, the association of MAP with vitreous Aβ concentration was also assessed and was calculated according to Equation 4.

$$Mean\ Arterial\ Pressure\ (MAP) = (2xDBP + SBP)/3 \qquad \text{Equation 4}$$

SBP = Systolic Blood Pressure (mmHg)
DBP=Diastolic Blood Pressure (mmHg)

In both instances, the normality of residuals within data sets was first confirmed using the Shapiro-Wilk test, following which the correlation of each variable with vitreous Aβ concentration was assessed with Pearson's correlation. Quantification of smoking pack-years and MAP was not possible for some participants due to lack of information provided on the proforma. However, the number of participants for which quantification of such parameters was possible is detailed in the corresponding figure legend. Correlation was confined to patients over the age of 55 akin to case-control comparisons.

Table 26: Clinical diagnosis of donor AMD status

Two consultant ophthalmologists assessed vitreous donor AMD status, where if conflicting diagnoses were made, a third assessor was recruited to confirm clinical diagnosis. Patients for which a third assessor was required are highlighted in grey. Analysis with Cohen's kappa statistic to assess inter-rater agreement showed that the strength of assessor agreement was worse than expected by chance alone (κ=-0.194). This highlights the requirement for multiple clinical assessments to ensure case-control study validity. Patient 14 was identified as having AVMD (*) and Patient 10 was identified as having myopic fundus (**) following multiple clinical assessment. These were therefore excluded from the control cohort due to the proposed genetic association of HtrA Serine peptidase 1 in both AVMD and AMD[357], and associated pathology respectively[358]. Abbreviations: AMD, Age-related Macular Degeneration; AVMD; Adult Vitelliform Macular Dystrophy.

Patient	Assessment by Consultant Ophthalmologist		
	1	2	3
1	Control	Control	-
2	Control	Control	-
3	Control	Control	-
4	Control	Control	-
5	Control	Control	-
6	Control	Control	-
7	Dry AMD	Dry AMD	-
8	Control	Control	-
9	Control	Control	-
10	Control	Control; Myopic Fundus	Control; Myopic Fundus**
11	Control	Control	-
12	Control	Control	-
13	Control	Control	-
14	Control	Dry AMD; Reticular Drusen	AVMD*
15	Control	Dry AMD; Reticular Drusen	Control
16	Control	Control	-
17	Control	Control	-
18	Control	Control	-
19	Dry AMD	Dry AMD	-
20	Control	Control	-
21	Control	Dry AMD; Reticular Drusen	Control
22	Control	Control	-
23	Control	Dry AMD; Reticular Drusen	Early Dry AMD
24	Control	Control	-
25	Control	Control	-
26	Control	Control	-
27	Control	Control	-
28	Control	Dry AMD	Dry AMD
29	Control	Control	-
30	Control	Control	-
31	Control	Dry AMD	Dry AMD

- Third opinion not required

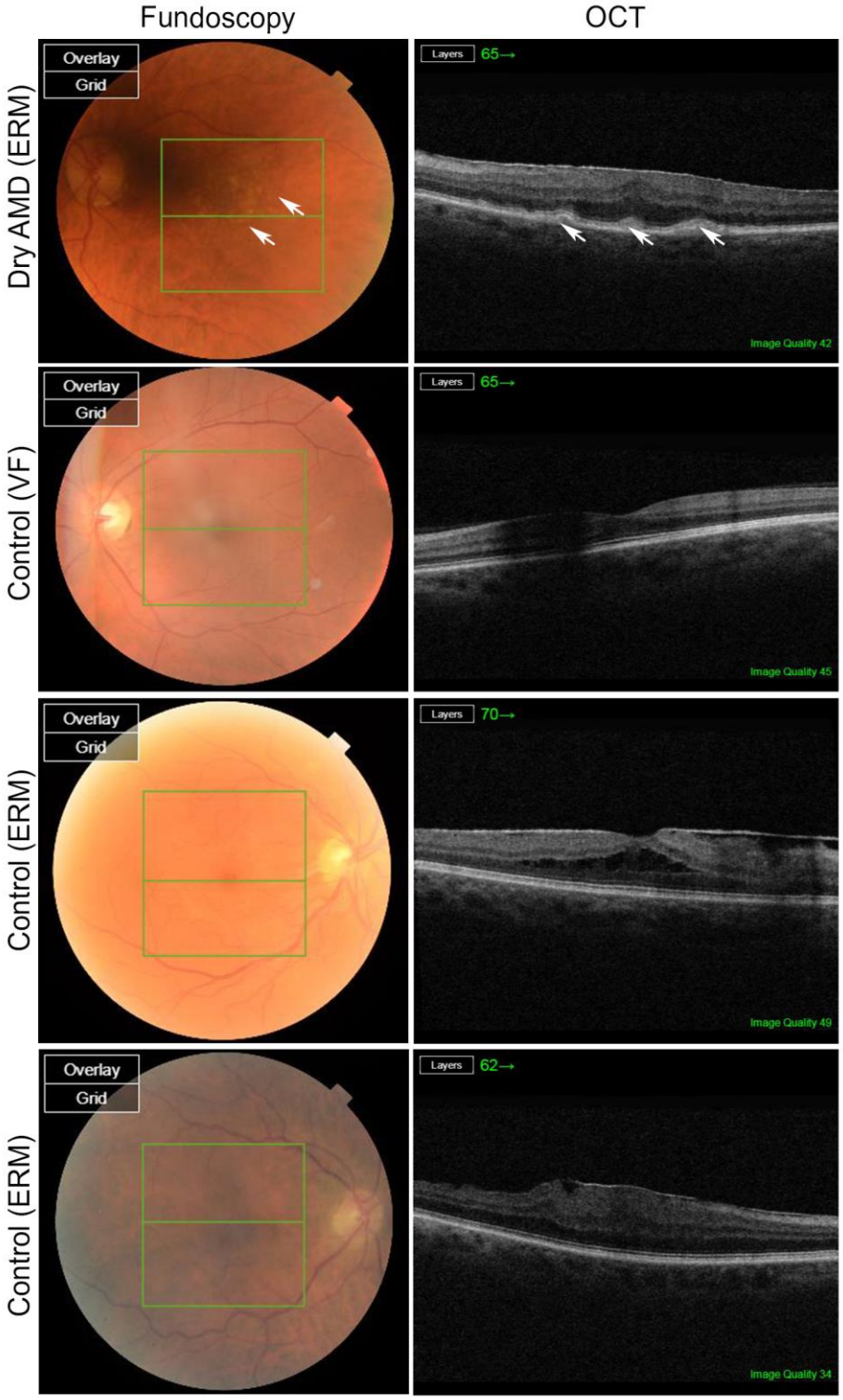

Figure 49: Example fundus and OCT images assessed by study clinicians in the determination of AMD status.

Examples of fundoscopy and optical coherence tomography images used to assess AMD status. AMD diagnosis was made according to the criteria stipulated by the AREDS classification. The example AMD status is detailed on the left of fundus/OCT pairs, where the patients underlying pathology is given in brackets. Abbreviations: AMD, Age-related Macular Degeneration; VF, Vitreous Floaters; ERM, Epiretinal Membrane. White arrows indicate the presence of multiple small drusen.

5.2.4 $A\beta_{1-x}$ ELISA quantification of total vitreous Aβ

Total Aβ ($A\beta_{1-28}$, $A\beta_{1-40}$, $A\beta_{1-42}$) in vitreous biopsies was quantified with the $A\beta_{1-x}$ ELISA kit (IBL, Japan) according to the manufacturer's instructions (Section 2.3.3). This assay is validated for the quantitative determination of human Aβ in cell culture supernatants, CSF, serum, EDTA-plasma and brain tissue extract. However, as vitreous humour had not been tested with this kit previously, LoD and SR assays were required to assess sample matrix effects and to validate assay accuracy. These were assessed as described in Section 2.3.3.1.1.

$A\beta_{1-x}$ levels in case-control samples were subsequently quantified by ELISA to determine inherent Aβ concentrations within the vitreous. Biopsies were diluted 1:4 in EIA buffer prior to use in the assay, and subsequent steps were executed as in Section 2.3.3. Triplicate technical replicates were run for each sample, from which an average sample concentration was determined. All samples tested were in the detection limits of the assay with the exception of one patient in which the Aβ concentration exceeded the threshold. For this patient, the maximum Aβ concentration detectable by the assay was plotted.

5.3 Results

5.3.1 Patient demographics

Demographic, clinical and medical information relating to vitreous sample donors was first assessed between study groups to determine whether a comparable prevalence of potential confounding variables existed (Table 27). All information contained within this table relates to donor samples collected up to March 2017, and is representative of those on which ELISA was performed to determine Aβ concentration within the vitreous.

The results of demographic analyses between study groups demonstrated a comparable average age of 71-80 years in both case and controls (p=0.1173). Similarly, a comparable percentage of males and females was also observed, although this could not be assessed statistically due to the low number of AMD patients recruited up to March 2017. However, it was noted that a 2-fold larger number of females had been recruited in the control cohort. In contrast, patient smoking history, measured as smoking pack-years, was almost 3-fold higher in the AMD group, but may be explained by the low AMD sample number for which this confounder was recorded (n=1). This limits the conclusions that can be drawn concerning the similarity of smoking pack-years between study groups, as well as its identification as a confounding variable, given that only 50% of the AMD cohort was represented. In terms of clinical factors, the number of operations performed was analogous between groups with right eye operations constituting 60% and 50% of cases in control and AMD patients respectively. The most frequent cause for surgery in controls was Epiretinal Membrane (ERM), which accounted for 73.33% of cases, followed by MH. To date, no statistical comparison of this variable with the control group could be made. However, an equal proportion of AMD patients (50%) were admitted for ERM and MH indicating that this is most likely the main cause for VR surgery in both cohorts. Conversely, MAP was 3.7-fold higher in controls, although again, the significance of this observation could not be determined due to the limited case sample size. For the same reason, it is difficult to compare the prevalence of accompanying medical conditions as well as concomitant medications taken between cohorts, despite Table 27 highlighting equivalent percentages. A greater number of statistical comparisons between potentially confounding variables will be made possible upon further sample acquisition.

Table 27: Demographic, clinical and drug associated variables within study groups collected up to March 2017.

Details of patient demographics including age, gender and smoking history, as well as clinical and drug associated variables for the study cohort collected up to March 2017. All information contained within the table relates to control and experimental (AMD) donors for which vitreous Aβ concentration was determined by ELISA. Where possible statistical significance between groups was assessed using the unpaired students t-test. No significant difference in patient age (p=0.1173) between case and control groups was noted. Abbreviations: ACE, Acetylcholine Esterase; AMD, Age-related Macular Degeneration; ERM, Epiretinal Membrane; SEM, Standard Error of the Mean; SSRI, Selective Serotonin Reuptake Inhibitors; VMT, Vitreomacular Traction syndrome.

Variable	Unit	Controls (n=15) No. (Percentage)	Cases (n=2) No. (Percentage)	P Value
DEMOGRAPHICS				
Age (years)				
18-20	No. (%)	0 (0)		
21-30	No. (%)	0 (0)		
31-40	No. (%)	0 (0)		
41-50	No. (%)	0 (0)		
51-60	No. (%)	1 (6.7)		
61-70	No. (%)	3 (20)		
71-80	No. (%)	11 (73.3)	1 (50)	
81-90	No. (%)	0 (0)	1 (50)	
	Age (Mean ± SEM)	71.6 ±1.57	79.5 ±1.06	0.1173
Gender				
Male	No. (%)	5 (33.3)	1(50)	
Female	No. (%)	10 (66.7)	1 (50)	
Smoking	Pack-Years (Mean ± SEM)	3.57 ±1.63	10	
CLINICAL FACTORS				
Surgery Eye				
Right	No. (%)	9 (60)	1 (50)	
Left	No. (%)	6 (40)	1 (50)	
Primary Cause for Vitrectomy				
ERM	No. (%)	11 (73.33)	1 (50)	
VMT	No. (%)	1 (6.67)		
Vitreous Floaters	No. (%)	1 (6.67)		
Macular Hole	No. (%)	2 (13.33)	1 (50)	
Mean Arterial Pressure	MAP (Mean ± SEM)	88.77 ± 3.61	24.04 ± 17.0	
Additional Medical Conditions				
Hypertension	No. (%)	7 (46.67)	1 (50)	
Diabetes	No. (%)	1(6.67)	1 (50)	
Arthritis	No. (%)	6 (40%)		
Stroke	No. (%)	1 (6.67)	1 (50)	
Depression/Anxiety	No. (%)	1 (6.67)		
Heart Condition (Heart murmur, atrial fibrillation, myocardial infarction, Arrhythmia)	No. (%)	4 (26.67)	1(50)	

Cancer	No. (%)	1 (6.67)	
Back/Shoulder/Spinal Problems	No. (%)	6 (40)	1 (50)
Medication			
Beta Blockers	No. (%)	5 (33.33)	1 (50)
ACE Inhibitors	No. (%)	2 (13.33)	2 (100)
Statins	No. (%)	5 (33.33)	1 (50)
Steroids	No. (%)	3 (20)	
Calcium Channel Blockers	No. (%)	4 (26.67)	
Aspirin	No. (%)	3 (20)	2 (100)
Diuretics	No. (%)	3 (20)	1 (50)
Proton Pump Inhibitors	No. (%)	2 (13.33)	
Alpha Blockers	No. (%)	3 (20)	
SSRIs	No. (%)	2 (13.33)	
P2Y12 Inhibitors	No. (%)	3 (20)	
Hypoglycemic	No. (%)		1 (50)
Ursodeoxycholic acid	No. (%)	1 (6.67)	

Table 28 details similar information regarding potentially confounding variables for all control and AMD donors collected to date. However, it must be noted that donor vitreous samples collected between March 2017 and July 2017 have not yet been analysed for Aβ concentration due to sample availability. Therefore, the information contained in Table 28 does not relate to results presented within this thesis, but rather is indicative of the ongoing nature of this study. As before, a comparable average age of between 71-80 years was recorded between groups ($p=0.0781$), whereas the percentage of males and females within cohorts was not equal. Here, a 2-fold larger number of females remained within the control group. This was not replicated in the AMD cohort in which a similar proportion of male and female donors was evident. The average number of smoking pack years was also significantly higher ($p=0.051$) in AMD donors. This highlights the need for control of the aforementioned variables in subsequent case-control analyses, if identified as confounders.

Table 28: Demographic, clinical and drug associated variables within study groups collected up to July 2017.

Details of patient demographics including age, gender and smoking history, as well as clinical and drug associated variables for the study cohort up until July 2017. Information contained within the table below relates to all control and experimental (AMD) donors from which vitreous samples have been obtained to date. Those collected after March 2017 still require ELISA analysis to determine total vitreous Aβ concentrations before further case-control comparisons can be made. Where possible statistical significance between groups was assessed using the unpaired students t-test. No significant difference in patient age (p=0.0781) or mean arterial pressure (p=0.5010) was noted between case and control groups. However, the experimental (AMD) group displayed a greater number of smoking pack-years compared to the control group (p=0.051). Abbreviations: ACE, Acetylcholine Esterase; AMD, Age-related Macular Degeneration; ERM, Epiretinal Membrane; SEM, Standard Error of the Mean; SSRI, Selective Serotonin Reuptake Inhibitors; VMT, Vitreomacular Traction syndrome.

Variable	Unit	Controls (n=22) No. (Percentage)	Cases Group (n=5) No. (Percentage)	P Value
DEMOGRAPHICS				
Age (years)				
18-20	No. (%)	0 (0)		
21-30	No. (%)	0 (0)		
31-40	No. (%)	0 (0)		
41-50	No. (%)	0 (0)		
51-60	No. (%)	1 (4.55)		
61-70	No. (%)	5 (22.73)		
71-80	No. (%)	15 (68.18)	2 (40)	
81-90	No. (%)	1 (4.55)	3 (60)	
	Age (Mean ± SEM)	72.55 ±1.45	78.4 ±1.86	0.0781
Gender				
Male	No. (%)	7 (31.82)	3(60)	
Female	No. (%)	15 (68.18)	2 (40)	
Smoking	Pack-Years (Mean ± SEM)	4.29 ±1.45	14.67±10.1	0.051
CLINICAL FACTORS				
Surgery Eye				
Right	No. (%)	12 (54.55)	3 (60)	
Left	No. (%)	10 (45.55)	2 (40)	
Primary Cause for Vitrectomy				
ERM	No. (%)	16 (72.73)	3 (60)	
VMT	No. (%)	2 (9.09)		
Vitreous Floaters	No. (%)	1 (4.55)		
Macular Hole	No. (%)	3 (13.64)	2 (40)	
Mean Arterial Pressure	MAP (Mean ± SEM)	95.75 ± 3.06	102.33 ± 7.15	0.5010
Additional Medical Conditions				
Hypertension	No. (%)	9 (40.91)	4 (80)	
Diabetes	No. (%)	3(13.64)	1 (16)	
Arthritis	No. (%)	7 (31.82)	2 (40)	
Stroke	No. (%)	1 (4.55)	1 (16)	
Depression/Anxiety	No. (%)	2 (9.09)		

Heart Condition (Heart murmur, atrial fibrillation, myocardial infarction, Arrhythmia)	No. (%)	5 (22.73)	2 (40)
Cancer	No. (%)	2 (9.09)	
Back/Shoulder/Spinal Problems	No. (%)	7 (31.82)	2 (40)
Medication			
Beta Blockers	No. (%)	7 (31.82)	4 (17.6)
ACE Inhibitors	No. (%)	3 (13.64)	2 (40)
Statins	No. (%)	8 (36.36)	1 (20)
Steroids	No. (%)	3 (13.64)	
Calcium Channel Blockers	No. (%)	6 (27.27)	1 (20)
Aspirin	No. (%)	4 (18.18)	2 (40)
Diuretics	No. (%)	5 (22.73)	2 (40)
Proton Pump Inhibitors	No. (%)	5 (22.73)	
Alpha Blockers	No. (%)	3 (13.64)	
SSRIs	No. (%)	3 (13.64)	
P2Y12 Inhibitors	No. (%)	3 (13.64)	
Hypoglycemic	No. (%)		1 (20)
Ursodeoxycholic acid	No. (%)	1 (4.55)	

As before, the results of clinical comparisons between study groups identified a similar number of left (45.55% and 40%) and right eye (54.55% and 60%) operations, with ERM followed by MH being the main cause for VR surgery. These constituted 72.23% and 13.64%, and, 60% and 40%, for control and AMD donors respectively, corroborating the results presented in Table 27. Collectively, these findings implicate ERM as the main cause for VR surgery in the present study.

In contrast to Table 27, in which MAP appeared to be 3.7-fold higher in the control cohort, Table 28 shows that MAP was comparable between case and controls upon continued acquisition of samples ($p=0.5010$). Finally, the frequency of additional common medical conditions between groups was assessed. The percentage of conditions was analogous across both cohorts relative to sample numbers, with the most common conditions being hypertension, arthritis, back/shoulder problems or an underlying heart condition. This was supported by the observation that in both groups, over 1 in 6 were taking beta blockers, almost 1 in 7 were taking ACE-inhibitors, diuretics and/or Calcium-channel blockers, and over 1 in 6 were taking aspirin. Statins were also taken by 20% of control and experimental patients highlighting the preponderance of high LDL cholesterol within the study population.

5.3.2 Spike recovery and linearity of dilution assessment of vitreous samples with the commercially available $A\beta_{1-x}$ ELISA

The human $A\beta_{1-x}$ ELISA employed to quantify the $A\beta$ concentration within vitreous samples within the present study is validated for use with cell culture medium, serum, EDTA-plasma CSF and brain tissue extract. However, to date no data exists regarding the use of this kit for the analysis of human vitreous. Therefore, it was important to validate the suitability and accuracy of the kit for this purpose.

In order to evaluate the effect of vitreous sample matrix on the measurement of vitreous $A\beta$ concentration, SR was performed. Properties such as viscosity, pH and high carbohydrate composition are all known to enhance matrix effects and thus potentially influence ELISA results. This is most commonly seen when analysing serum and plasma samples, the latter of which has a slightly lower viscosity (1.25-1.72mPa^{-s})[359] than that of human vitreous (1.78-3.56mPa^{-s}) highlighting the need to determine the effects of sample matrix here. SR was performed by adding known amounts of $A\beta_{1-40}$ to vitreous samples, corresponding to high, low and medium concentrations which were run on the $A\beta_{1-x}$ ELISA alongside similarly spiked standard diluent samples. The $A\beta$ concentration observed within vitreous samples was subsequently corrected for the respective unspiked donor control, and the corrected concentration was calculated as a percentage of the spiked concentration. This was then compared to the percentage recorded for the corresponding spiked standard diluent, where a similar percentage recovery indicated no effect of sample matrix. The results of this experiment can be seen in Table 29. In this case sample matrix refers to vitreous diluted 8-fold with standard diluent to ensure high spiked samples still fell within the range of the standard curve.

Table 29: Spike Recovery of human vitreous with the $A\beta_{1-x}$ ELISA kit (IBL, Japan).

Human vitreous samples were diluted 8-fold and spiked with known low (7.81pg/ml), medium (30pg/ml) and high (62.5pg/ml) $A\beta_{1-40}$ concentrations. Measurements were then calculated as a percentage of the spiked concentration, after correcting for the unspiked donor vitreous Aβ concentration, to give a percent recovery value. These were compared to the percent recovery of similarly spiked standard diluent, where no effect of sample matrix was associated with a percentage recovery of 100%. The higher the percentage recovery value, the lower the effect of sample matrix on the measurement determined by the $A\beta_{1-x}$ ELISA. It is evident here that human vitreous exhibits matrix effects with this ELISA kit.

	Percentage of Spike Concentration Recovered (%)		
Sample	Low Spike (7.81 pg/ml)	Medium Spike (30 pg/ml)	High Spike (62.5 pg/ml)
Standard Diluent	108%	89%	105%
Donor 1	74%	80%	144%
Donor 2	-550%	-460%	11%
Donor 3	-351%	554%	330%
Average	-276%	58%	162%

The results presented in Table 29 clearly demonstrate that human vitreous exhibits matrix effects with the $A\beta_{1-X}$ ELISA, where in low, medium and high spiked samples a 384%, 31% and 57% difference in sample concentration was recorded on average. In fact, this average is misrepresentative of the data spread observed, where in the worst instance a 658% difference was recorded between spiked sample matrix and the corresponding spiked standard diluent (Table 29; Donor 2, Low Spike). Several strategies may be employed to circumvent matrix effects, including the dilution of samples and preparation of standards in sample matrix. In both instances, this was not possible as vitreous samples had been diluted 8-fold prior to spike recovery, and no sample matrix for human vitreous exists without the protein of interest. Thus, this ELISA kit cannot be used for the absolute quantification of Aβ within human vitreous. Rather, it has been employed here to make comparisons between the relative level of Aβ within the vitreous of AMD and control patients, assuming that matrix effects are consistent across samples. From Table 29 it appears that sample matrix effects may in fact vary between donors, evidenced by the difference in the percentage of spike concentration recovered. However, these conclusions are limited to the low numbers of donors assessed. The consistency of matrix effects was therefore cross-checked as a secondary outcome measure of the LoD assay as discussed below.

The primary aim of the LoD experiment was to assess the precision of protein quantification following the dilution of samples. This is often required to ensure samples fall within the assay range of the ELISA kit. In this instance, the traditional

method of LoD was employed where a series of sample dilutions were made, and the analyte concentration calculated, taking into account the dilution factor. The results from this experiment are shown in Figure 50.

Over the range of dilutions tested, a 5-fold dilution of vitreous sample was selected for subsequent assay use, yielding 95% of the theoretical vitreous Aβ concentration achieved. Neat and 3-fold dilution of vitreous gave an enhanced percentage of the theoretical Aβ concentration but could not be employed as measured concentrations exceeded the assay limit of the ELISA. The related inaccuracy in sample Aβ concentration is highlighted here by the large error bars associated with data points. Overall, LoD of vitreous samples was acceptable over a range of dilutions indicating the flexibility of the assay for analysing Aβ content in vitreous samples, where both 5-fold, 7-fold and 51-fold dilutions all yielded concentrations within 10% of the theoretical concentration. However, caution must be exercised when performing large dilutions as there is no adjacent data to support a comparable concentration to neat vitreous, particularly as the prior 26-fold dilution performed, only yielded 56% of the theoretical concentration. The accuracy of all lower dilutions is supported by neighbouring data and thus sample dilutions within this range were deemed valid.

A.

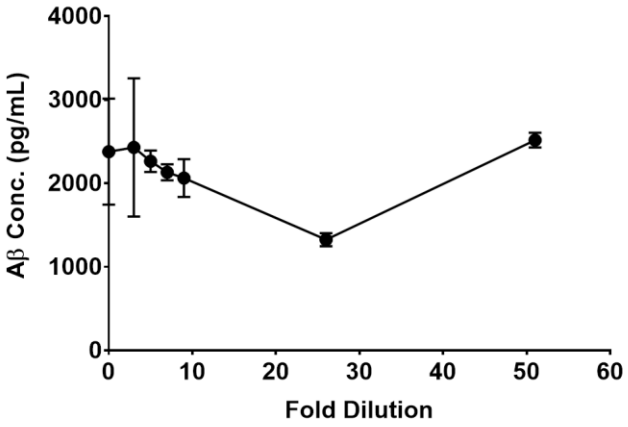

B.

Fold Dilution	Measured Value (pg/ml)	Theoretical Value (pg/ml)	Percentage (%)
1	2379.33	2379.33	100
3	810.30	793.11	102
5	453.03	475.87	95
7	304.56	339.90	90
9	229.22	264.37	87
26	51.02	91.51	56
51	49.36	46.65	106

Figure 50: Linearity of Dilution of human vitreous with the $A\beta_{1-x}$ ELISA kit (IBL, Japan).

Results of the Linearity of Dilution assay performed for human vitreous samples using the human $A\beta_{1-x}$ ELISA kit. Sample Aβ concentrations were tested at 3-fold, 5-fold, 7-fold, 9-fold, 26-fold and 51-fold dilutions. Measured sample concentrations were corrected for their corresponding dilution factor and were compared to the Aβ concentration of the undiluted sample. **A.** Graphical representation of Aβ concentrations over the range of sample dilutions. Data points represent mean corrected Aβ concentration ± SEM. Statistical comparisons were made using One-way ANOVA with Tukey's multiple comparisons which revealed no statistical difference in the calculated concentration of Aβ within vitreous samples at all dilutions tested ($p=0.4878$). **B.** Table showing the measurement value as a % of the theoretical value. Dilutions within the range of 5-fold to 7-fold were deemed appropriate for use in determining the Aβ concentration within human vitreous.

As mentioned, the results obtained from LoD were used to further to assess the consistency of matrix effects between donor samples, due to differing recoveries presented (Table 29). If matrix effects are inconsistent between samples, this influences analyte detectability, producing poor LoD results. Thus, similar to SR, information regarding the effects of sample matrix can be ascertained through LoD. Figure 50 demonstrates LoD results over the initial range of dilutions tested, in which concentrations fell within the assay range of the ELISA and exhibited tight error bars. This highlights the consistent effects of dilution on the concentration of Aβ measured and supports comparable matrix effects across vitreous samples.

A small probability exists that different Aβ concentrations within samples are balanced out by the effect of opposing differences in matrices. However, this is unlikely given that the sample group had no distinguishable factors to cause Aβ to increase. Therefore, it has been assumed that the small error observed was driven by consistency of sample matrix effects. The rest of Chapter 5 assumes that the observed matrix effects do not differ appreciably within the age-matched design employed.

5.3.3 Effects of confounders on vitreous Aβ concentration

Section 5.3.1 assessed the distribution of potential confounders within case and control groups. However, whether such variables directly influence Aβ concentration within human vitreous remains to be established. Further investigation was therefore conducted in this respect upon running of donor samples on the $A\beta_{1\text{-}x}$ ELISA. Information relating to samples in which such effects were assessed is detailed in Table 27.

5.3.3.1 Total Aβ concentration as a function of age

The effect of age on total vitreous Aβ concentration was assessed within the initial sample cohort to determine its confounder status, and consequently the need to control for age in subsequent case-control analyses (Figure 51). In this instance samples were not confined to the matching criterion of ages >55, where samples from patients between the ages of 18 to 55 were also included to obtain a data set representative of the whole population. However, patients under the age of 18 could not be included due to the ethics under which this study was performed, thereby limiting the population represented.

Total vitreous Aβ concentration in the 16 control patients assessed showed no significant correlation with age ($r=0.2246$, $p=0.4030$) when assessed with Pearson's correlation. However, no absolute conclusion can be drawn as to the effects of age on Aβ vitreous concentration due to the sample size assessed, as well as the age spread within samples, particularly as the majority of patients were within the 71-80 age category (Table 27), with only two patients below the age of 60.

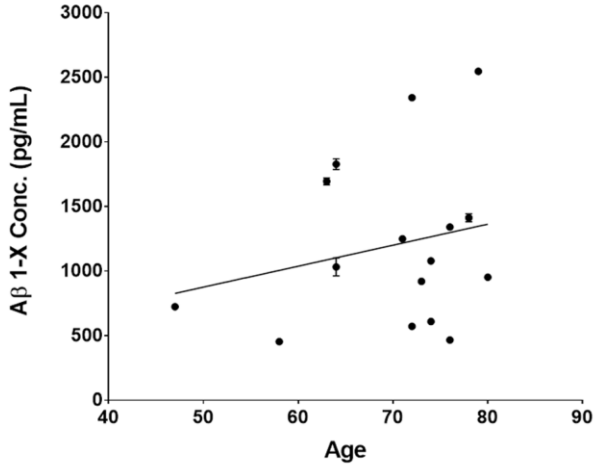

Figure 51: Total Aβ concentration in human vitreous as a function of age.

Total Aβ ($Aβ_{1-28}$, $Aβ_{1-40}$, $Aβ_{1-42}$) in human vitreous samples, quantified by ELISA, to determine the relationship between vitreous Aβ concentration and age. Data points represent mean Aβ concentration from three technical replicates performed per patient ± SEM. Correlation was assessed with Pearson's correlation which revealed no statistical correlation between vitreous Aβ concentration in control patients (n=16) and age (r=0.2246, p=0.4030).

5.3.3.2 The effect of accompanying ocular conditions on Aβ concentration

The inclusion criteria (Table 20) states that samples may be obtained from patients undergoing vitrectomy for ERM, Vitreomacular Traction Syndrome (VMT), Vitreous Floaters (VF) or MH, all of which represent 'normal' state vitreous without systemic influence. Table 27 and Table 28 demonstrate a similar frequencies of samples obtained from ERM, VMT, VF and MH, although their respective effects on vitreous Aβ concentration have not yet been determined. This was therefore plotted following $Aβ_{1-X}$ ELISA quantification to assess the effect of each ocular pathology under which patients were recruited on Aβ concentration within the vitreous (Figure 52).

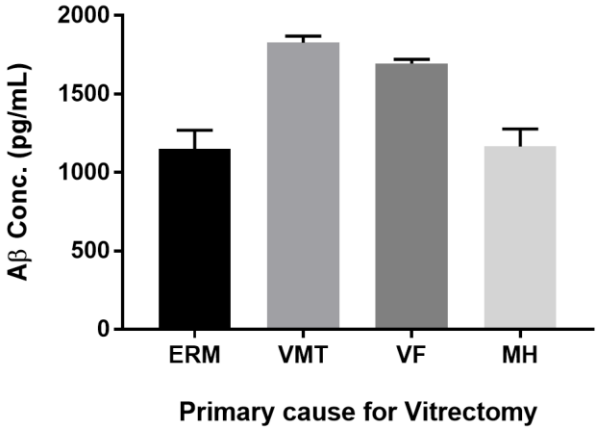

Figure 52: Effect of accompanying ocular conditions on Aβ concentration measured within the human vitreous.

The effect of the primary ocular condition for which patients (n=15) were for referred for vitreoretinal surgery, on total vitreous Aβ concentration was assessed to determine the effects of accompanying ocular diagnoses. Ocular conditions included ERM (n=11), VMT (n=1), VF (n=1) and MH (n=2). Statistical comparisons were made using the Kruskal-Wallis test with Dunn's multiple comparisons, which revealed no significant difference between Aβ concentration in differing primary concomitant ocular diagnoses (ERM vs. VMT, p= 0.1650; ERM vs. VF, p=0.4076; ERM vs. MH, p>0.9999; VMT vs. VF, p>0.9999; VMT vs. MH, p=0.6373; VF vs. MH, p> 0.9999). Due to limited vitrectomy patients referred for both VMT and VF, calculated Aβ concentrations for all three sample technical replicates were plotted to facilitate statistical comparisons. Abbreviations: AMD, Age-related Macular Degeneration; ERM, Epi-retinal membrane; VMT, Vitreomacular Traction syndrome; VF, Vitreous Floaters; MH, Macular Hole.

The results presented in Figure 52 highlight the relative consistency of Aβ concentrations across recruitment pathologies. Hence, accompanying ocular conditions associated with vitreous sample collection do not appear to influence vitreous Aβ concentration within the initial sample cohort (Table 27). This should be further assessed upon completion of sample collection to determine the requirement for additional parameters to incorporate into the final statistical model.

5.3.3.3 The effect of smoking history on Aβ concentration

Smoking represents a major AMD risk factor, as well as an important modifiable risk for disease[5]. The prevalence of this factor was notably higher in the AMD cohort analysed compared to controls (Table 27). Therefore, the effect of patient smoking history, quantified as smoking pack-years, on vitreous Aβ concentration was assessed in the initial sample cohort to determine the correlation of this variable with vitreous Aβ concentration and consequently the need to control for smoking in subsequent analyses. Here, analysis was confined to the control study population

as we hypothesised AMD patients to have higher vitreous Aβ. By excluding AMD patients this enabled the effect of smoking pack-years on Aβ concentration to be determined without the addition of extra covariates. As before, only patients over the age of 55 included in case-control comparisons were assessed.

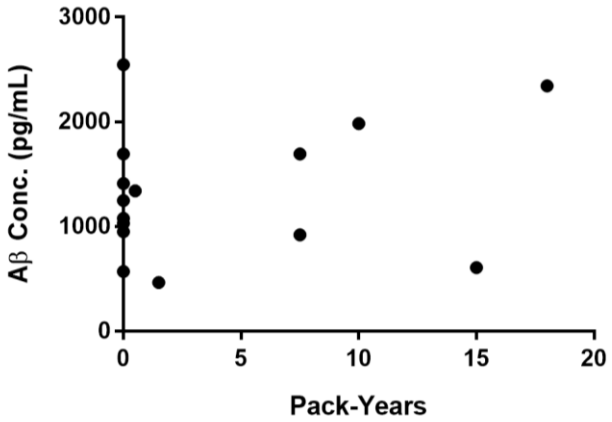

Figure 53: Effect of smoking pack-years on total vitreous Aβ concentration

The effect of patient smoking history, quantified as smoking pack-years, on total Aβ concentration within the vitreous of control study participants (n=14). Statistical significance was assessed with Pearson's correlation following confirmation of normality of residuals using the Shapiro-Wilk test. No association between smoking pack-years and total vitreous Aβ concentration was identified (r=0.168, p=0.5659). Thus, the confounding effects of patient smoking history are likely not of concern for subsequent case-control analyses. Only patients over the age of 55 were included in analyses.

Figure 53 shows that no significant correlation existed between pack-years smoked and the concentration of Aβ within the vitreous when assessed using Pearson's correlation (r= 0.168, p=0.5659). It was therefore not necessary to adjust for this factor in the results presented. Again, this variable will need to be reassessed upon completion of sample collection.

5.3.3.4 The effect of arterial pressure on Aβ concentration

Hypertension is also an AMD risk factor, in which concomitant vasoconstriction of blood vessels is thought to impair ocular blood supply[106 360]. It was noted previously that the preponderance of hypertension was comparable between study groups, (Table 27 and Table 28). However, MAP was 3.7-fold higher in control samples analysed. The direct effect of MAP on vitreous Aβ concentration was therefore determined to assess the need to control for this variable in subsequent case-control analyses (Figure 54). Again, only control patients >55 years of age collected up to March 2017 were analysed.

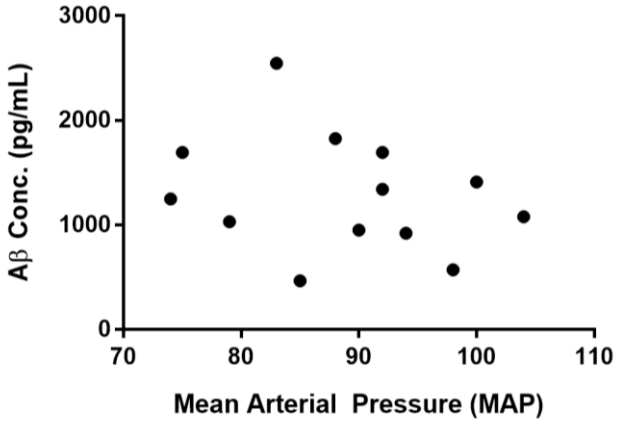

Figure 54: Effect of Mean Arterial Pressure on total vitreous Aβ concentration

The effect of Mean Arterial Pressure (MAP) on total Aβ concentration within the vitreous of control study participants (n=13). Correlation was assessed using Pearson's correlation following confirmation of normality of residuals using the Shapiro-Wilk test. No correlation was found between the concentration of Aβ within the vitreous and MAP (r=-0.2609, p=0.3893). Thus, MAP co-variance is likely not of concern for case-control analysis. Only patients over the age of 55 were included in analyses.

Figure 54 shows no relationship between MAP and the concentration of Aβ within samples analysed to date. In this respect, it was not necessary to control for this covariate in case-control analyses of samples presented herein. Similarly, no significant difference in MAP was observed in samples collected to July 2017 (Table 28; p=0.5010), although this distribution will need to be reassessed once recruitment has been completed.

5.3.4 Quantification of total Aβ in AMD patients vs. controls

Collectively, the data presented in Section 5.3.3 demonstrates that different levels of smoking and MAP do not influence the concentration of Aβ within vitreous samples analysed to date. Similarly, age and underlying ocular conditions for which patients were admitted for VR surgery, do not appear to effect Aβ concentration either. Consequently, initial comparisons of Aβ concentration between case and controls were conducted without statistical adjustment for these factors (Figure 55). Figure 55 shows that within the sample cohort up to March 2017, comparable levels of Aβ appear to reside within the vitreous of AMD and control patients. However, these results are not conclusive owing to the low AMD sample number collected and lack of statistical analyses performed.

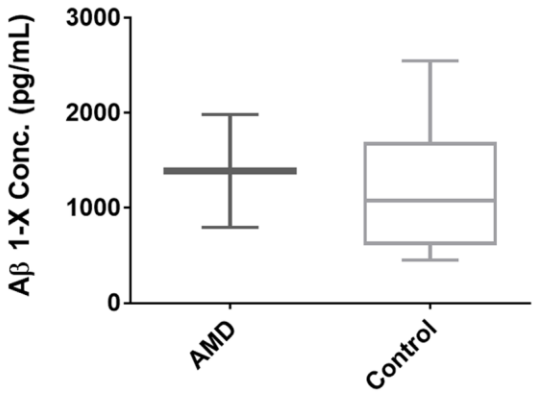

Figure 55: Total Aβ concentration in the vitreous of AMD patients vs. controls

The total Aβ ($A\beta_{1-28}$, $A\beta_{1-40}$, $A\beta_{1-42}$) concentration in both AMD (n=2) and control (n=15) vitreous samples was quantified by ELISA to determine if higher vitreous Aβ concentrations are associated with disease. Box and whisker plots show average Aβ concentration with boxes representing the interquartile range and error bars indicating the full range within each cohort.

5.4 Discussion

It is well known that the identification of novel pathological biomarkers for disease aids in the development of new therapies. This is particularly attractive for the AMD field, as identifying more generalised targets could facilitate the development of more effective and widely applicable treatments. To date, the Aβ peptide has consistently been associated with hallmarks of early AMD[202 208 209 231], as well as factors that drive CNV[197 245]. Similarly, treatment has been shown to cause RPE alterations consistent with an AMD phenotype[242] (Section 1.6 and Section 3.4.4), and several studies have implicated higher Aβ levels in the vitreous[355] and plasma[361] with AMD, the latter of which appears to correlate with disease progression[361]. This highlights the potential of Aβ as a novel therapeutic target for AMD. However, the relationship between Aβ and AMD, and in particular its use as a biomarker remains to be fully understood. This chapter forms the initial stages of a case-control project to quantify Aβ in control and AMD vitreous. The primary aim is to discern the association between vitreous Aβ concentration and AMD, as well as its implication with disease progression.

5.4.1 Suitability of the $A\beta_{1\text{-}x}$ ELISA for Aβ quantification in human vitreous

Sample matrix effects are a major consideration for accurate ELISA analyte quantification. It is not uncommon for sample matrix to confound assay measurements leading to errors in results. Factors that are most commonly associated with impaired assay performance include high sample viscosity, variable pH levels, metabolites, as well as the presence of phospholipids, carbohydrates and salt concentrations[362]. The ratio of analyte to total protein content within samples may also cause non-specific binding of antibodies, thus producing erroneous results. This is of particular importance with regard to validating assays used for human vitreous samples, which exhibit a viscosity of 300-2000cP, comprise numerous metabolites as well as a high proportion of albumin (~40%)[350]. In contrast, the pH of human vitreous is unlikely to affect assay performance, which typically has a pH within the range of 7.0-7.4[350]. Validation of the ELISA over a range of dilutions is also necessary, particularly where samples exhibit varied analyte concentrations and must be diluted differently to fall within the assay range. This was relevant here as we hypothesised Aβ to be elevated in AMD patients, and thus these samples may require greater dilution. Therefore, the suitability of the $A\beta_{1\text{-}x}$ ELISA for the quantification of vitreous Aβ concentration was first established by

examining assay precision and sample matrix effects. This was achieved by performing LoD and SR assays respectively. The results of LoD indicated that the $A\beta_{1-X}$ ELISA was suitable for use at 5, 7 and 9-fold dilutions, all of which exhibited an acceptable degree of precision compared to the theoretical sample concentration (Figure 50). Thus far, the limited number of AMD samples tested have fallen within the assay range at a 5-fold dilution suggesting that 7 and 9-fold dilutions should be more than sufficient for Aβ quantitation within control and AMD vitreous in subsequent analyses.

Next, spike recovery was performed to determine the effects of sample matrix on the accuracy of vitreous Aβ concentration measured by the $A\beta_{1-X}$ ELISA. Here, human vitreous was shown to exert considerable matrix effects, as evidenced by the significant deviation in the percentage of analyte recovery observed (Figure 50). Commonly, employed methods to circumvent matrix effects include sample dilution in standard diluent and preparation of standards in sample matrix[362]. However, this was not possible here as an 8-fold sample dilution did not appear to negate matrix effects, and human vitreous comprises inherent Aβ so cannot be used as a standard diluent. Another possible method to offset matrix effects is to reduce sample viscosity. This is achieved by high-speed centrifugation of samples at 12,000RPM for 15 minutes followed by quantification of analyte in sample supernatants[256]. However, this would prevent the detection of Aβ aggregates within vitreous samples, which pellet with the insoluble fraction. The contribution of Aβ fibrils to total Aβ concentration was also of interest to our study, and therefore this was not included in initial assay design. Further, the effects of high-speed centrifugation on protein stability have not been investigated therefore questioning its applicability here[256]. It must therefore be understood that given the matrix effects of human vitreous with the ELISA kit employed, the results presented here report comparisons between the level of Aβ within human vitreous rather than absolute Aβ concentrations. This chapter also makes the assumption that donor samples exhibit comparable matrix effects on analyte detectability, which is supported by the LoD results (Figure 50). An alternative or custom assay is required for the absolute quantification of Aβ within human vitreous, if this is indeed possible.

5.4.2 The correlation between Aβ levels and AMD remains inconclusive

The study in question has been constrained by AMD vitreous acquisition, where only two patients were recruited between August 2015 and March 2017. Unfortunately, this was beyond experimental control. The acquisition of samples relies on patient participation and referral of AMD patients to VR clinic, which occurs infrequently. However, sample collection will continue over the next few years until sufficient sample numbers (n=30/group) have been reached. An initial comparison of Aβ levels revealed no observable difference between vitreous Aβ in case and control cohorts (Figure 55), although the accuracy here is limited by the low sample number for the case group. To date, no valid conclusions can be drawn with respect to Aβ levels in the vitreous of AMD patients compared to 'normal' controls. Therefore, the data presented within this chapter pertains to the initial collection and analysis of samples, as well as ELISA assay validation of an ongoing study. Over the past 3 years, 22 controls and 5 case suitable samples have been obtained. A dedicated research technician has since been appointed to this project with the aim of targeting multiple VR clinics to reduce the time required to obtain sufficient sample numbers.

5.4.3 Future statistical considerations

An equal distribution of potential covariables between case and control cohorts is necessary to facilitate the direct estimation of exposure on the outcome, in this case vitreous Aβ concentration on the clinical manifestation of AMD. If different levels of a confounding factor exist within study populations, this must be controlled for in subsequent analyses[363]. Comparisons of vitreous donor demographic, clinical and medical information to determine the prevalence of confounding variables between study groups (Table 27 and Table 28) identified smoking pack-years and the percentage of female donors as variables that may influence subsequent analysis. If unequal distribution remains significant upon completion of sample collection, their introduction into the statistical model as covariates must be considered following advice from a clinical statistician. Further, the comparison of vitreous Aβ concentration between AMD and control patients has been confined to patients over the age of 55, as AMD prevalence increases significantly thereafter[85]. Inclusion of this analytical parameter ensures a similar age stratum within the control cohort thereby increasing the chance of statistical precision[363]. This analysis criterion constitutes 'matching' of study populations,

which may in itself confound the data and introduce bias[364]. In such circumstances the matching factor must be controlled for in statistical analyses, particularly when analysing samples over a broad age-range[364]. Table 27 and Table 28 demonstrate a similar average age between case and control cohorts indicating control over this parameter to date. However, if age is identified as a confounding factor upon completion of sample acquisition, this matching factor must be also controlled statistically. Collectively, this highlights the number of additional factors that have the potential to influence the measured outcome. A clinical statistician should be consulted upon completion of sample acquisition to decide upon and incorporate necessary parameters into the appropriate statistical model to negate the effects of covariance.

5.4.4 Future directions

Aβ concentration in human plasma is thought to be a predictor of neurological conditions such as AD. However, contradictory results have meant that the exact correlation between plasma Aβ content and AD risk remains undefined[365-367]. Nonetheless, the majority of the literature suggests a decline in plasma Aβ levels in the advanced stages of AD[368-372] analogous to observations reported in the CSF[370]. Interestingly, the converse appears to be true in AMD. Here, plasma $A\beta_{1-42}$ concentrations and the $A\beta_{1-42}/A\beta_{1-40}$ ratio is significantly higher in the plasma of AMD patients, and appears to increase with advancing disease severity[361]. This identifies elevated $A\beta_{1-42}$ as a prospective plasma biomarker of increased AMD susceptibility and/or early pathology. However, disease classification is unlikely to be aided by measurement of plasma Aβ content, as similar concentrations and $A\beta_{1-42}/A\beta_{1-40}$ ratios were seen in both GA and CNV patients[361]. If vitreous Aβ concentrations are consistent with plasma Aβ alterations, it would corroborate findings in close proximity to the RPE and further support a role for Aβ as an indicator of disease. Conversely, if plasma $A\beta_{1-42}$ alterations occur post AMD onset akin to AD, vitreous biopsies could present a method for identifying disease susceptibility in high risk individuals or for detecting early disease onset. This method of biomarker testing is highly invasive and is not practical for use in a primary care setting, although the option to test vitreous specimens as a secondary outcome of VR surgery exists. Nonetheless, it may present a viable and more reliable alternative to plasma based Aβ assays in the diagnosis and monitoring of AMD, which contains Aβ originating from several organs and is known to bind to numerous proteins within the blood[367].

Our future investigations will also analyse the levels of $A\beta_{1-40}$ and $A\beta_{1-42}$ in donor vitreous to determine if any association exists between AMD onset/progression and different Aβ isoforms or ratios.

5.4.5 Conclusions

To our knowledge, this case-control study is the first of its kind, where literature searches have revealed no robust comparative studies regarding the quantification of Aβ in AMD and control patients. The physiological concentration of $A\beta_{1-40}$ and $A\beta_{1-42}$, within the vitreous has been reported to be 537.6±193.7 pg/ml and 53.7±39.5 pg/ml[200], or approximately 50-225 pmol/g and 10-27.5 pmol/g respectively[342]. However, this information is confined to reports that fail to mention ELISA validation following the use of kits that do not specify suitability for vitreous samples. This brings the reliability of predicted ocular concentrations into question. Going forward, our work also aims to verify ocular Aβ concentrations within the posterior eye. The novelty of this work has the potential to significantly contribute to our understanding of the role of Aβ in AMD. In particular, how Aβ metabolism alters with disease status.

Chapter 6 Final Discussion

6.1 Thesis summary

The studies presented within this thesis explore the association of Aβ with AMD pathology, and investigate its effects on RPE lysosomes for the first time. We also report novel findings regarding the effects of Aβ in the living retina and our studies in human ocular fluids provide important information concerning the changing levels of this toxic protein with age and disease. In this final chapter, we summarise the key findings resulting from this research as well their potential implications for the wider AMD field.

The investigations conducted in Chapter 3 provide new insights into the physiological role of Aβ within the retina and potential pathways by which Aβ may mediate retinal disease. In mature ARPE-19 monolayers, Aβ was shown to be preferentially secreted from the basal RPE surface, where it exhibited a 1.8-fold higher concentration than the apical surface. This may help to elucidate the biological target of Aβ, which is likely in agreement with the direction of its secretion. A large proportion of this chapter also involved setting up and validating the employed culture model and method of $A\beta_{1-42}$ oligomer preparation. This will form the basis of future investigations into the effects of Aβ on RPE physiology within the Ratnayaka laboratory. Specifically, we add to a body of literature supporting the use of ARPE-19 culture models and characterising the Aβ preparation technique through the novel use of immunogold labelling.

As the RPE appears to be the fulcrum of pathogenesis in AMD, we also investigated the effects of Aβ on an important RPE function that is increasingly being implicated in disease. Specifically, the crucial role of the lysosome in RPE clearance, which represents the main point of convergence of several degradation pathways. Our data provides evidence to suggest that Aβ is, at least in part, trafficked and processed through the RPE endolysosomal system. When applied to mature ARPE-19 monolayers, Aβ was rapidly internalised and shown to colocalise with RPE late endosomes/lysosomes. In fact, functional assays incorporating the lysosomal acid hydrolase Cathepsin B supported this notion, which demonstrated an increase in activity following Aβ treatment that was independent of transcriptional augmentation. However, prolonged and increased accumulation of $A\beta_{1-42}$ within lysosomes correlated with a decline in Cathepsin B activity. Collectively, this

identifies a potential mechanism by which $A\beta_{1-42}$ can accumulate within RPE lysosomes over time and exert detrimental effects on efficient lysosome function. The enlarged/swollen morphology of $A\beta_{1-42}$ containing vesicles at 36 hours post-treatment, in addition to the apparent inability of RPE lysosomes to participate in POS phagocytosis, supports Aβ induced effects on normal lysosomal function that warrant further investigation. This revealed an altogether unexpected and novel effect of Aβ in the outer retina that could contribute to complex retinopathies in later life.

Next, we conducted a further study to investigate the effects of $A\beta_{1-42}$ *in vivo* (Chapter 4). In particular, we were interested in the role of Aβ in driving CNV-like pathology, given the basal secretion of Aβ reported in Chapter 3 along with its reported effects on the choroid and VEGF secretion in the literature (Section 1.7). Here, $A\beta_{1-42}$ was identified as a potential player in retinal degeneration. $A\beta_{1-42}$ induced retinal and choroidal changes similar to those reported in CNV patients at just 8 days after treatment, including the accumulation of subretinal fluid and SHM. Moreover, at 15 days, the extent of pathology was significantly reduced with an almost complete resolution of subretinal fluid, a reduction in SHM and the appearance of putative cystoid spaces. Thus, highlighting the evolving nature of Aβ-induced pathology. Histological analysis of tissues at end points also revealed damage to the RPE and choroid. Despite the pathology associated with $A\beta_{1-42}$, ffERG recordings revealed no statistically significant difference in global photoreceptor and inner retinal layer function. Similarly, global retinal thickness profiles were comparable between $A\beta_{1-42}$ and control treatment groups. This suggests that this model recapitulates highly localised damage, akin to that reported in AMD patients, that remains undetectable by conventional ffERG[339].

Finally, as Aβ was associated with driving hallmarks of AMD pathology *in vivo*, a preliminary study was initiated (Chapter 5) to determine the association of increased ocular Aβ concentrations with AMD. This involved quantifying Aβ levels in vitreous biopsies obtained from 'normal' control and AMD donors. Vitreous fluids showed consistent levels of Aβ with age in the initial control cohort assessed. However, several confounding factors were identified that may need to be taken in to consideration in the final statistical model. This included smoking pack-years and the number of female donors recruited. Due to the low number of AMD samples obtained during the duration of this project (n=5), we have been unable to disprove the hypothesis stated in Chapter 1. Nonetheless, this study represents a gap in the

literature, which when complete will aid in understanding if Aβ plays a key role in driving AMD pathology.

In sum, our results provide evidence to support Aβ as a novel target for AMD therapeutics and suggests several pathways by which Aβ may drive disease pathology. These, as well as the implications of our findings for the wider AMD field, will be discussed in the following section.

6.2 Implications for AMD research, pathology and treatments

The novel findings presented here add to a growing body of literature that suggests a role for the intracellular aggregation of misfolded proteins and impairment of RPE clearance mechanisms in the initial stages of AMD. We have discussed how alterations to the RPE endo-lysosomal system, UP and autophagy pathways have been implicated in AMD and how these may cumulatively give rise to this phenomenon (Section 1.4.2). The imperative role of the lysosome in RPE homeostatic function is highlighted by its presence in all of the above clearance mechanisms. This has led to the investigation of various age and disease associated compounds on efficient lysosomal function, in an attempt to identify the initiating factors of disease, as well as targets for therapeutic intervention. To date A2E, chloroquine and lipid peroxidation products have all been implicated with features of disease including lipofuscin-like autofluorescence, lysosomal acidification, impaired lytic enzyme function or impaired phagolysosomal degradation[84 322 373]. However, despite its reported effects in neurons and increased implication in AMD, no studies have investigated the effects of Aβ on RPE lysosomes.

The work presented in Chapter 3 provides the first indication of Aβ accumulation within RPE lysosomes and has shed new light on the role of this toxic peptide in AMD pathology. For the first time, it associates Aβ with early signs of RPE impairment that are only seen with advancing age, or in the initial stages of disease. Similarly, we identify Aβ as yet another compound that has the potential to accumulate within and alter lysosomal function. In this respect, attempts to restore normal lysosomal proteolysis may have the potential to yield promising therapeutic effects.

Further, our findings suggest that Aβ could play a key role in retinal angiogenesis and choroidal maintenance. The observation of pathological hallmarks reminiscent of CNV, in addition to the predominately basal secretion of Aβ reported in our work support this notion. This adds to existing literature suggesting the choroid as the biological effector of Aβ in the retina (Section 1.7). However, the association of Aβ with both and dry and wet AMD indicates that Aβ is not exclusively associated with CNV. Indeed, findings in the plasma of AMD patients appear to support this, which associate $A\beta_{1\text{-}42}$ and its ratio with $A\beta_{1\text{-}40}$ with both late AMD stages equally[361]. Thus, increased Aβ may be a useful general indicator of AMD. Given its close proximity to the retinal environment, the vitreous may reflect alterations to Aβ in the initial

stages of disease, before it becomes detectable systemically. In this respect vitreous presents an advantage over plasma. Our novel pilot study will provide the first insights into the use of vitreous humour as an AMD biomarker, and well help to elucidate the role of Aβ in AMD pathology.

In sum, the work presented within this thesis along with a vast body of literature suggests Aβ as novel target for the treatment of AMD. The work outlined in the following sections will build on our findings to further the mechanistic understanding of Aβ's involvement in AMD progression.

6.3 Future perspectives

The novel findings presented within this thesis have opened up several research avenues with regards to investigating the association of Aβ with both early and late AMD. The following section describes some of the work that will be undertaken within our laboratory to further interrogate the mechanisms of Aβ pathology alluded to in this thesis.

6.3.1 Investigating Aβ effects on lysosomal biology and function

The results presented in Section 3.3.4 suggest a mechanism by which Aβ may accumulate within RPE lysosomes over time. Western blot and densitometry analysis will help to further validate the temporal accumulation of Aβ within lysosomes, as well as its effects on Cathepsin B activity. Similarly, comparable studies of the amount of Rhodopsin present within the lysosomal fraction of treated cultures at each experimental time point ,will aid in validating the amount of POS present within lysosomes (Section 3.3.5). These experiments will offer further clarity in respect of the conclusions presented in this thesis.

As a continuation to the work described in Chapter 3, our laboratory will further investigate the effects of Aβ on normal lysosome physiology and function. This will be achieved via several experiments. The first incorporates the ratiometric probe LysoSensor Yellow/Blue DND-160 to investigate the effects of Aβ on intraluminal pH by quantifying the proportion of acidic (pH 3) to alkaline (pH 9) lysosomes. This is deemed the optimal probe for quantifying lysosomal pH changes in the RPE[374]. As mentioned in Section 1.2.3.5.1, an acidic lysosomal pH is critical for efficient acid hydrolase activity and substrate degradation. Thus, this experiment would provide an indirect indication of Aβ's lysomotropic properties within the RPE, as well as its consequences on acid hydrolase activity. Further, the ability of Aβ to induce lysosomal destabilisation could be tested through measuring Cathepsin B and β-N-acteyl-glucosaminidase (NAG) within lysosome-free cytosolic extracts. This may be achieved with the detergent digitonin, which selectively permeabilises the plasma membrane based upon cholesterol content when applied at the appropriate titration, i.e. one that leaves lysosomal membranes intact. Assays to determine cytosolic activity relative to total enzyme activity within the cell, as well as western blot analysis for acid hydrolases within this fraction would then provide an indication of the degree of lysosomal rupture. The results of these additional

studies could elucidate the mechanism connecting increased Aβ accumulation and decreased Cathepsin B activity.

The effects of Aβ on lysosome size are also of interest given the apparent swollen/enlarged physiology of lysosomes observed (Section 3.3.3.1). Quantitative morphometric analyses by immunofluorescence present several limitations including microscope resolution and human error with respect to defining organelle boundaries. As such, it is recommended that ultrastructural studies be used to investigate Aβ's effects on lysosomal morphology. In particular, serial block face scanning EM and subsequent 3D reconstruction of lysosomes would allow direct comparisons of lysosome volumes. However, given that Aβ is not present within the whole lysosomal population, appropriate power calculations would be required to determine the sample size required for statistical significance.

6.3.2 Investigating AMD-like pathology in 5xFAD mice

As a complementary approach to the acute Aβ-injection model, our future studies will employ 5xFAD (B6.Cg-Tg(APPSwFlLon,PSEN1*M146L*L286V)67799Vas/Mmjax) transgenic mice to confirm the observed effects of Aβ within the retina. The 5xFAD model develops severe amyloid pathology and cognitive deficits with age as a result of increased Aβ production within the brain[375]. This phenotype is achieved by the incorporation of five familial AD (FAD) associated mutations into human APP and PSEN1 transgenes that are inserted into exon 2 of the murine Thy1 gene located on Chromosome 3 (Chr3: 6297836). Specifically, the APP transgene incorporates the Swedish, Florida and London FAD mutations, whereas the PSEN1 transgene incorporates the M146L and L286V. These function collectively to increase Aβ production, predominantly $A\beta_{1-42}$, within the brain[375].

A large amount of research has been conducted into characterising amyloid pathology within the 5xFAD brain. However, little work has been conducted into characterising the retinal effects of increased Aβ production within this mouse model. This is surprising given that the 5xFAD model demonstrated the highest concentrations of retinal $A\beta_{1-42}$ when compared to several other widely used transgenic AD models. To our knowledge the only reports to date regarding the presence and effects of retinal Aβ in 5xFAD mice included measurable Aβ by 3 months[342 376], high levels of retinal $A\beta_{1-42}$ and low levels of CFH[377], and dry AMD-like pathology[244 378]. This included RPE hypopigmentation, loss of RPE membrane specialisation, subretinal deposits, Bruch's membrane thickening, outer BRB

impairment as well as lipofuscin and undigested POS-laden phagosome accumulation. It has also been shown recently that 5xFAD mice develop retinal and visual cortex dysfunctions with age, where mice display an impaired inner retinal response and visual acuity at just 2 months[376].

However, it should be noted that several of the aforementioned studies exploited the 5xFAD model on a hybrid B6/SJL background. Whilst this model exhibits more robust amyloid pathology than on a congenic background and is preferable for investigating Aβ's effects on the brain, it harbours mutations associated with retinal degeneration and oculocutaneous albinism, thus, potentially bringing the validity of some of the retinal pathology reported in these mice into question. As such, our studies will exploit 5xFAD mice on a C57BL6/J background, to ascertain the effects of endogenous Aβ on retinal function and morphology without interference from deleterious genes. Similar to the work conducted in Chapter 4, we will perform longitudinal ERG and OCT analyses of mouse retinas over a 15 month time course to assess the effects of an increased amyloid burden on visual function and retinal morphology respectively. Further, fluorescein angiography will be employed to investigate the involvement of Aβ in driving CNV-like pathology. Finally, an end point study design will also be incorporated to correlate pathology observed in OCT scans with histological sections, as well as to investigate the effect of Aβ on specific retinal pathways through immunofluorescence. Of specific interest are the effects of Aβ on synaptic function and the activation of an innate immune response.

6.3.3 Determining the association of vitreous Aβ concentration with AMD status

In Chapter 5, we present initial data from a pilot study to investigate the association of vitreous Aβ concentration with AMD. This study will progress over the next few years with the help of a dedicated research technician to increase the number of AMD donor samples obtained. Upon completion, the correlation of vitreous Aβ with AMD status and disease stage will be assessed. This will help to ascertain whether AMD pathology is reflected by Aβ concentrations within adjacent ocular fluids and to assess the utility of vitreous biopsies as viable biomarkers for AMD susceptibility and/or early diagnosis. However, as several factors have been identified that do not represent an equal distribution between the two study cohorts, a medical statistician will be consulted with regards to incorporating the appropriate model for analysis. As a continuation to this study, we also plan on investigating the association of specific Aβ isotypes with disease.

Appendix A

Figures presented in Appendix A are specific to those cross-referenced in Chapter 3. Please see electronic Appendix A for a representative z-scan showing Alexa Fluor® 488 tagged $A\beta_{1-42}$ colocalisation with PDMPO within the RPE. This is presented as an AVI file of both the merged green and red tiffs and using the FIJI fire look up table to aid with visualisation.

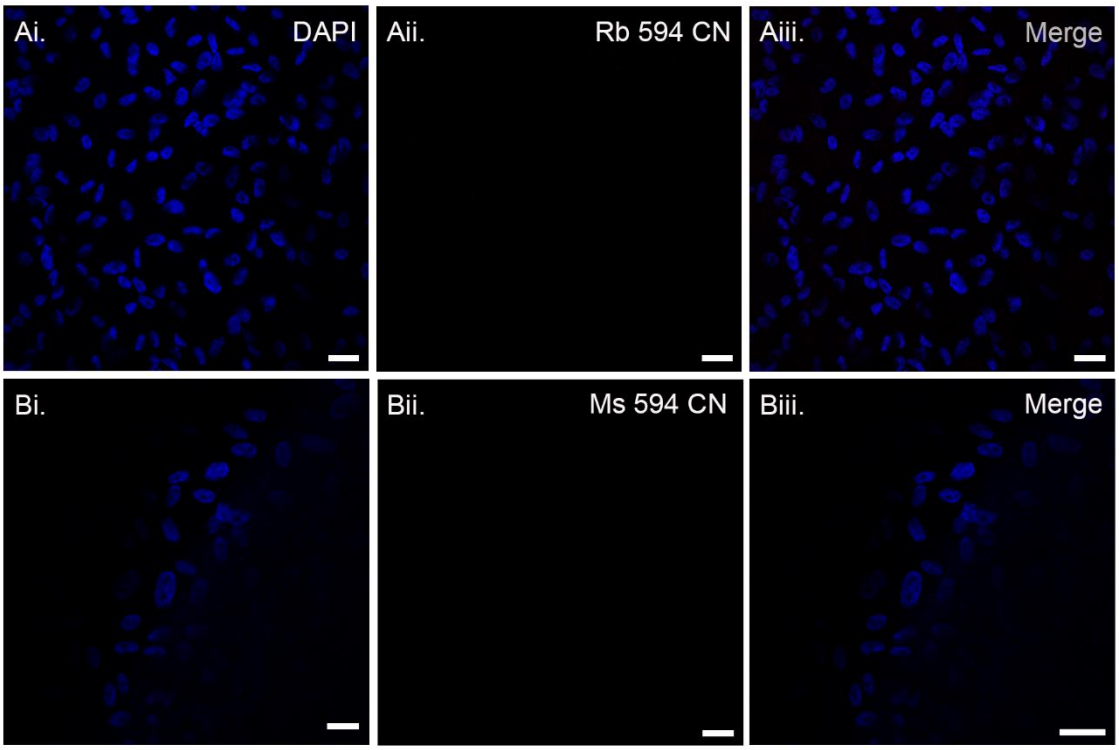

Figure 56: Secondary antibody controls employed in determining the expression of RPE specific markers within the ARPE-19 cell line.

In ARPE-19 cells incubated overnight with blocking buffer alone, no staining was observed when probed with (Ai-Aiii) Goat anti-rabbit Alexa Fluor 594 (red) or (Bi-Biii) Goat anti-mouse Alexa Fluor 594 (red). Nuclei are counterstained with DAPI (blue). Scale bars represent 20μm. Abbreviations: DAPI, 4',6-diamidino-2-phenylindole; Ms, Mouse; Rb, Rabbit. Republished from Lynn *et al.* (2018)[287] under the terms of the Creative Commons Licence.

A.

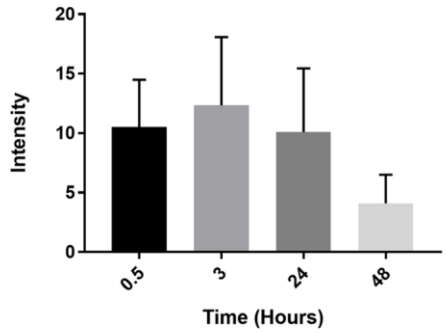

B.

Duration (Hours)	Significance (P Value)
0.5-3	>0.9999
3-24	>0.9999
24-48	>0.9999

Figure 57: Comparison of Alexa Fluor® 488 $A\beta_{1-42}$ pixel intensity variance over time.

A. Graph to show $A\beta_{1-42}$ pixel intensity as a function of time. The mean Alexa Fluor® 488 $A\beta_{1-42}$ pixel intensity was recorded across 30 fields of view per biological replicate (n=3). Data represents average pixel intensity ± SEM. Statistical comparisons between consecutive experimental time points were made using Kruskal-Wallis test with Dunn's multiple comparisons to assess variance in Alexa Fluor® 488 $A\beta_{1-42}$ intensity. B. Alexa Fluor® 488 $A\beta_{1-42}$ pixel intensity was comparable between all experimental time points and was statistically insignificant from previous time points assessed. However, a decreased trend in Alexa Fluor® 488 $A\beta_{1-42}$ pixel intensity was observed at 48 hours.

Appendix B

Figures presented in Appendix B are specific to those cross-referenced in Chapter 4. Please see electronic Appendix B for representative OCT scans of mice subject to subretinal injection with $A\beta_{1-42}$, vehicle/sham and BSA at baseline, week 1 (day 8) and week 2 (day 15) post-surgery.

Appendix C

Figures presented in Appendix A are specific to those cross-referenced in Chapter 1. Clinical paperwork presented here is purely demonstrative of the sample acquisition process. All patient information sheets, consent forms and study proformas examples shown were processed by the patient's clinical team prior to obtaining vitreous sample. Thus, no credit can be taken for this aspect of sample acquisition.

PATIENT INFORMATION SHEET

STUDY: "Pathophysiology of retinal disease" (Ref: protocol V3, 08 Dec 09)

CHIEF INVESTIGATOR: Professor Andrew Lotery, Southampton Eye Unit, Southampton General Hospital, Tremona Road, Southampton, SO16 6YD. Tel: 02381 204606

We would like to invite you to take part in a research study. Before you decide you need to understand why the research is being done and what it would involve for you. Please take time to read the following information carefully. Talk to others about the study if you wish. Ask us if there is anything that is not clear or if you would like more information. Take time to decide whether or not you wish to take part.

What is the purpose of this study?

- We would like to understand more about what occurs in patients with retinal conditions (eg. age-related macular degeneration), and compare this to those without retinal disease.
- Using the latest laboratory techniques, we would like to look for changes in fluid or tissue from the eye, in the bloodstream, and in genes from DNA
- We hope the results of this study will increase our understanding of the underlying processes occurring in retinal conditions. In future this could mean that better, more effective therapy could be developed.

Why have I been invited to take part in this study?

- You have been chosen to take part in this study because you are due to undergo routine eye surgery.
- We hope to look at 200 patients altogether. Some will have a particular retinal condition, some will not.

Do I have to take part?

- It is up to you. If you do not want to take part then you will continue to receive the normal medical care from your doctor.

What will happen to me if I take part?

- We would like to carry out the following:
  1. **Medical history**: We would like to ask about your medical history.
  2. **Blood test**: We would like to take 30ml (about 6 teaspoons) of blood, to look at your DNA and plasma / serum (the liquid part of blood). These will be analysed in the laboratory later.
  3. **Retention of sample from eye**: Normally, fluid or tissue inside your eye is removed and discarded as part of your operation. We would like to retain this for use in this research project, for laboratory analysis later. This will not affect your operation in any way.
  4. **If you are having injections:** We would like to obtain a tiny amount of fluid from inside your eye at the same time as your injection. This should not affect your injection in anyway. We would also like to repeat this one more time at your next injection, if you are agreeable.

How much of my time will the study take?

- The research will take about 20 minutes of your time, and will take place during one of your routine visits to the eye unit.

Expenses and payments

- We are unable to offer any expenses or payments for taking part in the study.

Will taking part in the study affect my daily life? Is there anything I am not allowed to do while taking part in the study?

- This study will not affect your daily life, and there are no restrictions.

What are the possible benefits of taking part?

- We cannot promise the study will help you. However information obtained from this study

may help to improve the management of people with retinal conditions in the future.

What are the possible disadvantages and risks of taking part?

Discovering changes in your genes

- There is the potential that we may find something new which was not previously known about you. If it is found that you have a changed gene in your DNA, it is possible that you and family members may be more likely to develop certain retinal conditions in the future, which may affect your vision. In some situations, certain lifestyle changes could help to reduce the risk of developing visual problems in the future.
- If you or your relatives wish to discuss any the results of your gene analysis further, then please contact Professor Lotery (details on top of page 1).
- You may also request to be informed in the eventuality that we find any significant gene change.
- We can then arrange an outpatient appointment at the eye unit to provide more information on the implications of these gene changes, and offer advice on preventative measures. We can also offer genetic counselling if required.
- Please note that any personal information about you will be kept confidentially by Professor Lotery (see below).

Provision of a blood sample

- The risks of providing a blood sample are mild bruising of the skin and mild discomfort from the needle.

Obtaining a sample of fluid from inside your eye prior to injection

- We will obtain the sample just before you have the injection, under exactly the same strict sterile conditions. The risks of obtaining this sample are additional to that of the required injection. In a recent study of more than 500 patients, around 1% developed problems after this procedure (mild transient bleeding inside the eye, inflammation, or a hole in the retina), all of which can happen after a normal injection into the eye. No patients developed infection inside the eye. (Pfahler SM et al, A prospective study of in-office diagnostic vitreous sampling in patients with vitreoretinal pathology. *Retina* 2009;**29**:1032-5).

What happens at the end of the study?

- You will continue to receive the usual medical care from your doctor.
- We may also contact you in the future regarding other research studies.

Will my taking part in this study be kept confidential?

- Yes. All information and samples which is collected about you during the course of the research will be kept strictly confidential. Our procedures for handling, processing, storage and destruction of your data match the Data Protection Act 1998.
- Your data and samples will be kept in an anonymised state, linked only to your personal information by a single record kept locked in Professor Lotery's office at Southampton General Hospital.
- Your confidential data will be accessible only to the study personnel, and to the Research Departments of Southampton University Hospital NHS Trust (the sponsors) and the local NHS trust for monitoring the quality of the study.
- Your data and samples may be shared with external scientists, but any information about you which leaves the hospital will be completely anonymous, so that you cannot be recognised
- Your data will be retained for a minimum of 5 years, and if required will be disposed of securely.
- You may have your data or samples removed at any time by contacting us.

What will happen to any samples I give?

- Your samples (including fluid or tissue retained from your eye, DNA and plasma) will be stored in a freezer in Professor Lotery's eye research laboratory at Southampton General Hospital. This laboratory has restricted access to members of the research team only.
- After this project, your samples will be kept in this same place or in a tissue bank with others like it, so that Professor Lotery can continue to study eye conditions for many years to come. Your samples will only be used for other projects if full ethical permission has been granted.

What will happen in the unlikely event that I might lose the ability to consent after the study?

- We would like to still retain the tissue and personal data collected already and use this confidentially in connection with this project. We also may use this information for further research in future, for projects which are ethically approved.

Will my GP know I am taking part in this study?

- We would like to inform your GP if you are participating in this study, unless you specifically ask us not to do so.

What if I am already taking part in another study?

- Please let us know if you are involved in another study, as you may not be able to take part in this study.

What will happen to the results of the research study?

- We aim to analyse the results of the research and publish them in leading eye research journals in three years from now – these should be accessible by contacting Professor Lotery's secretary (details on top of page 1). You will not be identified in any report/publication

Who is organising and funding the research?

- This research is being organised by a research group at the University of Southampton lead by Professor Lotery, and is being carried out as part of a PhD project. Funding will be from charities or government organisations.

Who has reviewed the study?

- All research in the NHS is looked at by independent group of people, called a Research Ethics Committee to protect your safety, rights, wellbeing and dignity. This study has been reviewed and given a favourable opinion by Southampton and South West Hampshire Research Ethics Committee.

Where can I obtain further information?

- **For specific information about this research project**: Please contact Professor Lotery's secretary (contact details on top of page 1)
- **For independent advice on this particular research study:** You may contact the Research department at Southampton University Hospitals NHS Trust: R&D Office, Duthie Building (Trust), Ground Floor, MP 138, Southampton General Hospital, Tremona Road, Southampton SO16 6YD. Tel: 02380 795078. You may also contact your hospital's Patient Advice and Liaison Service.
- **For independent advice on research in general:** Please refer to the NHS Research Ethics Service website: www.nres.npsa.nhs.uk

Who can I contact if I am unhappy?

- Any complaint about the way you have been dealt with during the study or any possible harm you might suffer will be addressed. If you have a concern about any aspect of this study, you should ask to speak to the researchers who will do their best to answer your questions (contact details on top of page 1). If you remain unhappy and wish to complain formally, you can do this through the NHS Complaints Procedure (or Private Institution). Details can be obtained from the hospital.
- We are legally bound to tell you the following: "In the event that something does go wrong and you are harmed during the research and this is due to someone's negligence then you may have grounds for a legal action for compensation against Southampton University Hospital NHS Trust (the sponsor) or your local NHS Trust but you may have to pay your legal costs. The normal National Health Service complaints mechanisms will still be available to you (if appropriate*)"*

How long do I have to decide in I want to take part in the study?

- You have as long as you wish to decide. If you are interested in taking part in this study, we would be grateful if you return the reply slip in the envelope provided before your operation date. If you change your mind later then we can always remove your data and samples.

Thank you for reading this information leaflet and for considering taking part in this study. You may keep this leaflet with you.

CONSENT FORM (staged)

Study title: "Pathophysiology of Retinal Disease"

Patient sticker

Patient Identification Number for this study: _____

Chief Investigator: Professor Andrew Lotery, Southampton Eye Unit, Tremona Road, Southampton SO16 6YD Tel: 02380 795409

PART A: Consent for the current study

(samples to be destroyed on study completion unless part B completed)

PLEASE INITIAL THE BOXES IF YOU AGREE WITH EACH SECTION:

1. I confirm that I have read and understand the information sheet dated 08 Dec 09 (version 3) for the above study and have been given a copy to keep. I have been able to ask questions about the study and I understand why the research is being done and any risks involved.

2. I agree to give a sample of blood for research in this project. I understand how the sample will be collected, that giving a sample for this research is voluntary and that I am free to withdraw my approval for use of the sample at any time without my medical treatment or legal rights being affected.

3. agree to allow collection of a residual sample of fluid or tissue from my eye during my eye operation. I understand how the sample will be collected, that giving a sample for this research is voluntary and that I am free to withdraw my approval for use of the sample at any time without my medical treatment or legal rights being affected.
4. I give permission for sections of my medical notes to be looked at by responsible individuals where it is relevant to this study. I expect that my medical notes will be treated confidentially at all times.

5. I understand that I will not benefit financially if this research leads to the development of a new treatment or test.

6. I know how to contact the research team if I need to.

7. I agree for my GP to be informed of my participation in this study

8. I agree to take part in the above study

_____	_____	_____
Name of Patient	Signature	Date

_____	_____	_____
Researcher	Signature	Date

When completed, 1 for patient; 1 for researcher site file; 1 (original) to be kept in hospital; medical notes.

PART B: Samples for storage and use in possible future studies - Linked anonymised samples

9. I give permission for my sample and the information gathered about me to be stored by Professor Andrew Lotery at the University of Southampton Eye Laboratory, Southampton General Hospital, for possible use in future projects, as described in the information sheet. I understand that some of these projects may be carried out by other researchers, including researchers working for commercial companies. I understand that **future studies will be reviewed and approved by a Research Ethics Committee prior to my sample being used, and that I can alter these decisions at any stage by letting the research team know.**

    a. I give permission for the sample to be used for research about eye disease

    b. I give permission for the sample to be used for other unrelated research studies the precise nature of which will depend upon future scientific advances.

10. I want / do not want to be told the results of any future test which may have health implications for me. **Yes No**

11. I give permission for sections of my medical notes to be looked at by responsible individuals where it is relevant to such future study. I expect that my medical notes will be treated confidentially at all times.

12. give permission for the continued storage of my samples and data in the event I lose the capacity to consent.

I agree to be contacted in future regarding other studies

_____	_____	_____
Name of Patient	Signature	Date

_____	_____	_____
Researcher	Signature	Date

When completed, 1 (copy) for patient; 1 (original) for researcher site file; 1 (copy) to be kept in hospital medical notes.

PROFORMA

STUDY ID: PR

Study title:
"PATHOPHYSIOLOGY OF RETINAL DISEASE"

REC ref: **09/H0504/67**

INITIALS:

CI: Professor Andrew Lotery,
Consultant Ophthalmologist,
Southampton General Hospital

Date	
Consent taken?	☐
Site	Southampton
Consultant	
Gender	M / F
Age	
Surgery eye	R / L
Diagnosis	Cataract / ERM / VMT / Macular hole /
AMD in surgery eye?	☐ Dry ☐ Wet ☐ Previous wet / scar AREDS grading: 1 / 2 / 3 / 4 (1: <5 small (<63), 2: multiple small / single intermediate (63-124), 3: Worse than 2 but not 4, 4: GA involving foveal centre or CNV)
Type of Surgery	☐ Phaco + IOL ☐ Vitrectomy
Samples to be obtained from eye	Aqueous / Vitreous / Epiretinal membrane Other: _____
POH:	

Appendix C

Medical history (Inc. previous systemic infection/disease)	
DH	
FH	
Smoking status	Current / Ex / Never If current / ex: No of years: ____ Average no per day: _____
BP	
Photos taken	☐ File names:
Bloods taken	☐ 3 bottles (10ml each): Whole blood, plasma, serum (2 purple, 1 red) Time Taken:
Documentation in main notes?	☐ Copy of consent form, pt information sheet, GP letter + study sticker placed in notes

Glossary of Terms

Diencephalon	Region of the brain comprising the thalamus, hypothalamus, epithalamus, subthalamus and the third ventricle. The diencephalon is located at the posterior region of the forebrain.
Hyalocytes	A macrophage-like cell type found mainly in the base of the vitreous humour.
Lateral Geniculate Nucleus	Subregion of the thalamus that is involved in the mapping and segregation of visual information from the retina.
Lymphatics	A designated supply of vessels that drain lymph fluid away from tissues back into the general circulation.
Superior Colliculus	Region of the midbrain that is implicated in eye movement
Suprachiasmatic Nucleus	Region of the thalamus located above the optic chiasm that has been implicated in controlling circadian rhythmicity.

List of References

1. Man-Kit Lam D. Evolution of Sight in the Animal Kingdom. In: Kolb H, Fernandez E, Nelson R, eds. Webvision:The Organization of the Retina and Visual System. Salt Lake City (UT): University of Utah Health Sciences Center 1995.

2. Fu Y, Yau K-W. Phototransduction in mouse rods and cones. *Pflugers Archiv : European journal of physiology* 2007;454(5):805-19. doi: 10.1007/s00424-006-0194-y

3. Ruggeri M, Major JC, McKeown C, et al. Retinal Structure of Birds of Prey Revealed by Ultra-High Resolution Spectral-Domain Optical Coherence Tomography. *Investigative ophthalmology & visual science* 2010;51(11):5789-95. doi: 10.1167/iovs.10-5633

4. Vasicek CA, Oosthuizen MK, Cooper HM, et al. Circadian rhythms of locomotor activity in the subterranean Mashona mole rat, Cryptomys darlingi. *Physiology & behavior* 2005;84(2):181-91. doi: 10.1016/j.physbeh.2004.11.005 [published Online First: 2005/02/15]

5. Fritsche LG, Fariss RN, Stambolian D, et al. Age-related macular degeneration: genetics and biology coming together. *Annual review of genomics and human genetics* 2014;15:151-71. doi: 10.1146/annurev-genom-090413-025610

6. Owen CG, Jarrar Z, Wormald R, et al. The estimated prevalence and incidence of late stage age related macular degeneration in the UK. *The British journal of ophthalmology* 2012;96(5):752-6. doi: 10.1136/bjophthalmol-2011-301109 [published Online First: 2012/02/15]

7. Casten R, Rovner B. Depression in Age-Related Macular Degeneration. *Journal of visual impairment & blindness* 2008;102(10):591-99.

8. Ohno-Matsui K. Parallel findings in age-related macular degeneration and Alzheimer's disease. *Progress in retinal and eye research* 2011;30(4):217-38. doi: 10.1016/j.preteyeres.2011.02.004

9. Ratnayaka JA, Serpell LC, Lotery AJ. Dementia of the eye: the role of amyloid beta in retinal degeneration. *Eye (London, England)* 2015 doi: 10.1038/eye.2015.100 [published Online First: 2015/06/20]

10. Shang F, Taylor A. Roles for the ubiquitin-proteasome pathway in protein quality control and signaling in the retina: implications in the pathogenesis of age-related macular degeneration. *Molecular aspects of medicine* 2012;33(4):446-66. doi: 10.1016/j.mam.2012.04.001 [published Online First: 2012/04/24]

11. Kaarniranta K, Tokarz P, Koskela A, et al. Autophagy regulates death of retinal pigment epithelium cells in age-related macular degeneration. *Cell Biology and Toxicology* 2017;33(2):113-28. doi: 10.1007/s10565-016-9371-8

12. Keeling E, Lotery AJ, Tumbarello DA, et al. Impaired Cargo Clearance in the Retinal Pigment Epithelium (RPE) Underlies Irreversible Blinding Diseases.

Cells 2018;7(2) doi: 10.3390/cells7020016 [published Online First: 2018/02/24]

13. Liu RQ, Zhou QH, Ji SR, et al. Membrane localization of beta-amyloid 1-42 in lysosomes: a possible mechanism for lysosome labilization. *The Journal of biological chemistry* 2010;285(26):19986-96. doi: 10.1074/jbc.M109.036798 [published Online First: 2010/05/01]

14. Nixon RA, Cataldo AM, Mathews PM. The endosomal-lysosomal system of neurons in Alzheimer's disease pathogenesis: a review. *Neurochemical research* 2000;25(9-10):1161-72. [published Online First: 2000/11/04]

15. Zheng L, Cedazo-Minguez A, Hallbeck M, et al. Intracellular distribution of amyloid beta peptide and its relationship to the lysosomal system. *Translational neurodegeneration* 2012;1(1):19. doi: 10.1186/2047-9158-1-19 [published Online First: 2012/12/06]

16. Nixon RA, Yang D-S. Autophagy Failure in Alzheimer's Disease – Locating the Primary Defect. *Neurobiology of disease* 2011;43(1):38-45. doi: 10.1016/j.nbd.2011.01.021

17. Purves DA, G. J; Fitzpatrick, D; Hall, W.C; LaMantia, AS; McNamara, J. O; White, L.E. Vision: The Eye. Neuroscience. 4 ed. Sunderland, MA, USA: Sinauer Associates, Inc. 2008:253-88.

18. Sakamoto T, Ishibashi T. Hyalocytes: essential cells of the vitreous cavity in vitreoretinal pathophysiology? *Retina (Philadelphia, Pa)* 2011;31(2):222-8. doi: 10.1097/IAE.0b013e3181facfa9 [published Online First: 2011/01/18]

19. Hiscott P. Vitreous biopsy pathology: new kid on the block. *Current Diagnostic Pathology* 2001;7(1):45-55. doi: https://doi.org/10.1054/cdip.2000.0049

20. Khandhadia S, Cherry J, Lotery AJ. Age-related macular degeneration. *Advances in experimental medicine and biology* 2012;724:15-36. doi: 10.1007/978-1-4614-0653-2_2 [published Online First: 2012/03/14]

21. Kolb H. Simple Anatomy of the Retina In: Kolb H, Fernandez E, Nelson R, eds. Webvision:The Organization of the Retina and Visual System. Salt Lake City (UT): University of Utah Health Sciences Center 1995.

22. Strauss O. The Retinal Pigment Epithelium. In: Kolb H, Fernandez E, Nelson R, eds. Webvision: The Organization of the Retina and Visual System. Salt Lake City (UT): University of Utah Health Sciences Center 1995.

23. Saade CJA-DF, J.M. Rod photoreceptors protect from cone degeneration-induced retinal remodeling and restore visual responses in zebrafish. *Journal of Neuroscience* 2013;33(5):1804-14.

24. Ratnayaka A, Lynn SA. Alzheimer's-Related Amyloid Beta Peptide Aggregates in the Ageing Retina: Implications for Sight Loss and Dementia. In: Moretti D, ed. Update on Dementia. Rijeka: InTech 2016.

25. Kolb H. Roles of Amacrine Cells. In: Kolb H, Fernandez E, Nelson R, eds. Webvision: The Organization of the Retina and Visual System. Salt Lake City (UT): University of Utah Health Sciences Center 1995.

26. Sanes JRZ, S.L. Design Principles of Insect and Vertebrate Visual Systems. *Neuron* 2010;66(1):15-36.

27. Creel DJ. The Electroretinogram and Electro-oculogram: Clinical Applications. In: Kolb H, Fernandez E, Nelson R, eds. Webvision: The Organization of the Retina and Visual System. Salt Lake City (UT): University of Utah Health Sciences Center 1995.

28. Perlman I. The Electroretinogram: ERG In: Kolb H, Fernandez E, Nelson R, eds. Webvision: The Organization of the Retina and Visual System. Salt Lake City (UT): University of Utah Health Sciences Center 1995.

29. Bonilha VL. Age and disease-related structural changes in the retinal pigment epithelium. *Clinical ophthalmology (Auckland, NZ)* 2008;2(2):413-24. [published Online First: 2008/06/01]

30. Strauss O. The retinal pigment epithelium in visual function. *Physiological reviews* 2005;85(3):845-81. doi: 10.1152/physrev.00021.2004 [published Online First: 2005/07/01]

31. Holtkamp GM, Kijlstra A, Peek R, et al. Retinal pigment epithelium-immune system interactions: cytokine production and cytokine-induced changes. *Progress in retinal and eye research* 2001;20(1):29-48. [published Online First: 2000/11/09]

32. Cavallotti C, Cerulli L. Age-Related Changes of the Human Eye. In: Cavallotti C, Cerulli L, eds. Age-Related Changes of the Human Eye: Humuna Press 2008.

33. Boulton M, Dayhaw-Barker P. The role of the retinal pigment epithelium: topographical variation and ageing changes. *Eye (London, England)* 2001;15(Pt 3):384-9. doi: 10.1038/eye.2001.141 [published Online First: 2001/07/14]

34. Bhutto I, Lutty G. Understanding age-related macular degeneration (AMD): Relationships between the photoreceptor/retinal pigment epithelium/Bruch's membrane/choriocapillaris complex. *Molecular aspects of medicine* 2012;33(4):295-317. doi: 10.1016/j.mam.2012.04.005

35. Boulton ME. Studying melanin and lipofuscin in RPE cell culture models. *Experimental eye research* 2014;126:61-7. doi: 10.1016/j.exer.2014.01.016 [published Online First: 2014/08/26]

36. Rizzolo LJ. Barrier properties of cultured retinal pigment epithelium. *Experimental eye research* 2014;126:16-26. doi: 10.1016/j.exer.2013.12.018

37. Rizzolo LJ, Peng S, Luo Y, et al. Integration of tight junctions and claudins with the barrier functions of the retinal pigment epithelium. *Progress in retinal and eye research* 2011;30(5):296-323. doi: 10.1016/j.preteyeres.2011.06.002 [published Online First: 2011/06/28]

38. Rizzolo LJ. Development and role of tight junctions in the retinal pigment epithelium. *Int Rev Cytol* 2007;258:195-234. doi: 10.1016/s0074-7696(07)58004-6 [published Online First: 2007/03/07]

39. Young B, Heath JW, Stevens A, et al. Wheater's functional histology: a text and colour atlas. 6 ed. Edinburgh: Churchill Livingstone 2000.

40. Peng S, Rao VS, Adelman RA, et al. Claudin-19 and the Barrier Properties of the Human Retinal Pigment Epithelium. *Investigative ophthalmology & visual science* 2011;52(3):1392-403. doi: 10.1167/iovs.10-5984

List of References

41. Konrad M, Schaller A, Seelow D, et al. Mutations in the Tight-Junction Gene Claudin 19 (CLDN19) Are Associated with Renal Magnesium Wasting, Renal Failure, and Severe Ocular Involvement. *American Journal of Human Genetics* 2006;79(5):949-57.

42. Chiba H, Osanai M, Murata M, et al. Transmembrane proteins of tight junctions. *Biochimica et biophysica acta* 2008;1778(3):588-600. doi: 10.1016/j.bbamem.2007.08.017 [published Online First: 2007/10/06]

43. Marneros AG, Fan J, Yokoyama Y, et al. Vascular endothelial growth factor expression in the retinal pigment epithelium is essential for choriocapillaris development and visual function. *The American journal of pathology* 2005;167(5):1451-9. doi: 10.1016/s0002-9440(10)61231-x [published Online First: 2005/10/28]

44. Bhutto IA, McLeod DS, Hasegawa T, et al. Pigment epithelium-derived factor (PEDF) and vascular endothelial growth factor (VEGF) in aged human choroid and eyes with age-related macular degeneration. *Experimental eye research* 2006;82(1):99-110. doi: 10.1016/j.exer.2005.05.007 [published Online First: 2005/07/16]

45. Nickla DL, Wallman J. THE MULTIFUNCTIONAL CHOROID. *Progress in retinal and eye research* 2010;29(2):144-68. doi: 10.1016/j.preteyeres.2009.12.002

46. Organisciak DT, Vaughan DK. Retinal Light Damage: Mechanisms and Protection. *Progress in retinal and eye research* 2010;29(2):113-34. doi: 10.1016/j.preteyeres.2009.11.004

47. Kevany BM, Palczewski K. Phagocytosis of Retinal Rod and Cone Photoreceptors. *Physiology (Bethesda, Md)* 2010;25(1):8-15. doi: 10.1152/physiol.00038.2009

48. Mazzoni F, Safa H, Finnemann SC. Understanding photoreceptor outer segment phagocytosis: Use and utility of RPE cells in culture. *Experimental eye research* 2014;0:51-60. doi: 10.1016/j.exer.2014.01.010

49. D'Cruz PM, Yasumura D, Weir J, et al. Mutation of the receptor tyrosine kinase gene Mertk in the retinal dystrophic RCS rat. *Human molecular genetics* 2000;9(4):645-51. [published Online First: 2000/03/04]

50. Feng W, Yasumura D, Matthes MT, et al. Mertk triggers uptake of photoreceptor outer segments during phagocytosis by cultured retinal pigment epithelial cells. *The Journal of biological chemistry* 2002;277(19):17016-22. doi: 10.1074/jbc.M107876200 [published Online First: 2002/02/28]

51. Finnemann SC, Bonilha VL, Marmorstein AD, et al. Phagocytosis of rod outer segments by retinal pigment epithelial cells requires alpha(v)beta5 integrin for binding but not for internalization. *Proceedings of the National Academy of Sciences of the United States of America* 1997;94(24):12932-7. [published Online First: 1997/11/25]

52. Law A-L, Parinot C, Chatagnon J, et al. Cleavage of Mer Tyrosine Kinase (MerTK) from the Cell Surface Contributes to the Regulation of Retinal Phagocytosis. *The Journal of biological chemistry* 2015;290(8):4941-52. doi: 10.1074/jbc.M114.628297

53. Parinot C, Chatagnon J, Nandrot EF. Opposite roles of MerTK ligands Gas6 and Protein S for RPE phagocytosis regulation. *Investigative ophthalmology & visual science* 2014;55(13):361-61.

54. Nandrot EF, Anand M, Almeida D, et al. Essential role for MFG-E8 as ligand for αvβ5 integrin in diurnal retinal phagocytosis. *Proceedings of the National Academy of Sciences* 2007;104(29):12005-10. doi: 10.1073/pnas.0704756104

55. Young RW. The renewal of rod and cone outer segments in the rhesus monkey. *The Journal of cell biology* 1971;49(2):303-18. [published Online First: 1971/05/01]

56. Kinnunen K, Petrovski G, Moe MC, et al. Molecular mechanisms of retinal pigment epithelium damage and development of age-related macular degeneration. *Acta ophthalmologica* 2012;90(4):299-309. doi: 10.1111/j.1755-3768.2011.02179.x [published Online First: 2011/11/25]

57. Ji CH, Kwon YT. Crosstalk and Interplay between the Ubiquitin-Proteasome System and Autophagy. *Molecules and Cells* 2017;40(7):441-49. doi: 10.14348/molcells.2017.0115

58. Ryhanen T, Hyttinen JM, Kopitz J, et al. Crosstalk between Hsp70 molecular chaperone, lysosomes and proteasomes in autophagy-mediated proteolysis in human retinal pigment epithelial cells. *Journal of cellular and molecular medicine* 2009;13(9b):3616-31. doi: 10.1111/j.1582-4934.2008.00577.x [published Online First: 2008/11/20]

59. Doherty GJ, McMahon HT. Mechanisms of endocytosis. *Annual review of biochemistry* 2009;78:857-902. doi: 10.1146/annurev.biochem.78.081307.110540 [published Online First: 2009/03/26]

60. Wandinger-Ness A, Zerial M. Rab Proteins and the Compartmentalization of the Endosomal System. *Cold Spring Harbor Perspectives in Biology* 2014;6(11):a022616. doi: 10.1101/cshperspect.a022616

61. Grant BD, Donaldson JG. Pathways and mechanisms of endocytic recycling. *Nature reviews Molecular cell biology* 2009;10(9):597-608. doi: 10.1038/nrm2755

62. Poteryaev D, Datta S, Ackema K, et al. Identification of the switch in early-to-late endosome transition. *Cell* 2010;141(3):497-508. doi: 10.1016/j.cell.2010.03.011 [published Online First: 2010/05/04]

63. Hu Y-B, Dammer EB, Ren R-J, et al. The endosomal-lysosomal system: from acidification and cargo sorting to neurodegeneration. *Translational neurodegeneration* 2015;4(1):18. doi: 10.1186/s40035-015-0041-1

64. Klettner A, Kauppinen A, Blasiak J, et al. Cellular and molecular mechanisms of age-related macular degeneration: from impaired autophagy to neovascularization. *The international journal of biochemistry & cell biology* 2013;45(7):1457-67. doi: 10.1016/j.biocel.2013.04.013 [published Online First: 2013/04/23]

65. Green DR, Oguin TH, Martinez J. The clearance of dying cells: table for two. *Cell Death And Differentiation* 2016;23:915. doi: 10.1038/cdd.2015.172

List of References

66. Mao Y, Finnemann SC, Parent C. Essential diurnal Rac1 activation during retinal phagocytosis requires αvβ5 integrin but not tyrosine kinases focal adhesion kinase or Mer tyrosine kinase. *Molecular Biology of the Cell* 2012;23(6):1104-14. doi: 10.1091/mbc.e11-10-0840

67. Mao Y, Finnemann SC. Regulation of phagocytosis by Rho GTPases. *Small GTPases* 2015;6(2):89-99. doi: 10.4161/21541248.2014.989785

68. Roni L, Sergio G, Johnathan C. The life cycle of phagosomes: formation, maturation, and resolution. *Immunological Reviews* 2016;273(1):156-79. doi: doi:10.1111/imr.12439

69. Liu J, Lu W, Reigada D, et al. Restoration of Lysosomal pH in RPE Cells from Cultured Human and ABCA4(−/−) Mice: Pharmacologic Approaches and Functional Recovery. *Investigative ophthalmology & visual science* 2008;49(2):772-80. doi: 10.1167/iovs.07-0675

70. Ash JD, Grimm C, Hollyfield JG, et al. Retinal Degenerative Diseases: Mechanisms and Experimental Therapy. New York: Springer 2014.

71. Authier F, Posner BI, Bergeron JJM. Endosomal proteolysis of internalized proteins *FEBS letters* 1996;389:55-60.

72. Xu H, Ren D. Lysosomal physiology. *Annual review of physiology* 2015;77:57-80. doi: 10.1146/annurev-physiol-021014-071649 [published Online First: 2015/02/11]

73. Feher J. 2.1 - Cell Structure. In: Feher J, ed. Quantitative Human Physiology (Second Edition). Boston: Academic Press 2017:101-19.

74. Kennedy CJ, Rakoczy PE, Constable IJ. Lipofuscin of the retinal pigment epithelium: a review. *Eye (London, England)* 1995;9 (Pt 6):763-71. doi: 10.1038/eye.1995.192 [published Online First: 1995/01/01]

75. Alizadeh P, Smit-McBride Z, Oltjen SL, et al. Regulation of cysteine cathepsin expression by oxidative stress in the retinal pigment epithelium/choroid of the mouse. *Experimental eye research* 2006;83(3):679-87. doi: 10.1016/j.exer.2006.03.009 [published Online First: 2006/05/11]

76. Klionsky DJ. Autophagy revisited: a conversation with Christian de Duve. *Autophagy* 2008;4(6):740-3. [published Online First: 2008/06/24]

77. Kroemer G, Mariño G, Levine B. Autophagy and the integrated stress response. *Molecular cell* 2010;40(2):280-93. doi: 10.1016/j.molcel.2010.09.023

78. Galluzzi L, Baehrecke EH, Ballabio A, et al. Molecular definitions of autophagy and related processes. *The EMBO journal* 2017;36(13):1811-36. doi: 10.15252/embj.201796697

79. Cuervo AM, Wong E. Chaperone-mediated autophagy: roles in disease and aging. *Cell Research* 2014;24(1):92-104. doi: 10.1038/cr.2013.153

80. Saez I, Vilchez D. The Mechanistic Links Between Proteasome Activity, Aging and Age-related Diseases. *Current Genomics* 2014;15(1):38-51. doi: 10.2174/138920291501140306113344

81. Viiri J, Hyttinen JM, Ryhanen T, et al. p62/sequestosome 1 as a regulator of proteasome inhibitor-induced autophagy in human retinal pigment

epithelial cells. *Mol Vis* 2010;16:1399-414. [published Online First: 2010/08/04]

82. Guha S, Baltazar GC, Coffey EE, et al. Lysosomal alkalinization, lipid oxidation, and reduced phagosome clearance triggered by activation of the P2X7 receptor. *FASEB journal : official publication of the Federation of American Societies for Experimental Biology* 2013;27(11):4500-9. doi: 10.1096/fj.13-236166 [published Online First: 2013/08/22]

83. Sparrow JR. Lipofuscin of the Retinal Pigment Epithelium. In: Holz F, Spaide R, Bird AC, et al., eds. Atlas of Fundus Autofluorscence Imaging. Berlin, Heidelberg: Springer Berlin Heidelberg 2007:3-16.

84. Guha S, Liu J, Baltazar G, et al. Rescue of compromised lysosomes enhances degradation of photoreceptor outer segments and reduce lipofuscin-like autofluorescence. *Advances in experimental medicine and biology* 2014;801:105-11. doi: 10.1007/978-1-4614-3209-8_14

85. Gehrs KM, Anderson DH, Johnson LV, et al. Age-related macular degeneration--emerging pathogenetic and therapeutic concepts. *Annals of medicine* 2006;38(7):450-71. doi: 10.1080/07853890600946724 [published Online First: 2006/11/15]

86. Resnikoff S, Pascolini D, Etya'ale D, et al. Global data on visual impairment in the year 2002. *Bulletin of the World Health Organization* 2004;82(11):844-51. doi: /S0042-96862004001100009 [published Online First: 2005/01/11]

87. Pennington KL, DeAngelis MM. Epidemiology of age-related macular degeneration (AMD): associations with cardiovascular disease phenotypes and lipid factors. *Eye and Vision* 2016;3:34. doi: 10.1186/s40662-016-0063-5

88. Gordois A, Cutler H, Pezzullo L, et al. An estimation of the worldwide economic and health burden of visual impairment. *Global public health* 2012;7(5):465-81. doi: 10.1080/17441692.2011.634815 [published Online First: 2011/12/06]

89. Minassian D, Reidy A. Future sight loss in the decade 2010 to 2020: an epidemiological and economic model., 2009:1-386.

90. Wong WL, Su X, Li X, et al. Global prevalence of age-related macular degeneration and disease burden projection for 2020 and 2040: a systematic review and meta-analysis. *The Lancet Global Health*;2(2):e106-e16. doi: 10.1016/S2214-109X(13)70145-1

91. Amoaku W, Bishop PN, Foss AJ, et al. Age-related macular degeneration: collaborating to find a cure, 2016:1-64.

92. Lotery A, Trump D. Progress in defining the molecular biology of age related macular degeneration. *Human genetics* 2007;122(3-4):219-36. doi: 10.1007/s00439-007-0406-3

93. Lim J. Age-Related Macular Degeneration. 3rd ed. UK: CRC Press 2013.

94. Davis MD, Gangnon RE, Lee LY, et al. The Age-Related Eye Disease Study severity scale for age-related macular degeneration: AREDS Report No. 17. *Archives of ophthalmology (Chicago, Ill : 1960)* 2005;123(11):1484-98. doi: 10.1001/archopht.123.11.1484 [published Online First: 2005/11/16]

95. Friedman DS, O'Colmain BJ, Munoz B, et al. Prevalence of age-related macular degeneration in the United States. *Archives of ophthalmology (Chicago, Ill : 1960)* 2004;122(4):564-72. doi: 10.1001/archopht.122.4.564 [published Online First: 2004/04/14]

96. Smith W, Mitchell P, Wang JJ. Gender, oestrogen, hormone replacement and age-related macular degeneration: results from the Blue Mountains Eye Study. *Australian and New Zealand journal of ophthalmology* 1997;25 Suppl 1:S13-5. [published Online First: 1997/05/01]

97. Espinosa-Heidmann DG, Marin-Castano ME, Pereira-Simon S, et al. Gender and estrogen supplementation increases severity of experimental choroidal neovascularization. *Experimental eye research* 2005;80(3):413-23. doi: 10.1016/j.exer.2004.10.008 [published Online First: 2005/02/22]

98. Bressler SB, Muñoz B, Solomon SD, et al. Racial differences in the prevalence of age-related macular degeneration: The salisbury eye evaluation (see) project. *Archives of Ophthalmology* 2008;126(2):241-45. doi: 10.1001/archophthalmol.2007.53

99. VanderBeek BL, Zacks DN, Talwar N, et al. Racial Differences in Age-Related Macular Degeneration Rates in the United States: A Longitudinal Analysis of a Managed Care Network. *American journal of ophthalmology* 2011;152(2):273-82.e3. doi: 10.1016/j.ajo.2011.02.004

100. Kawasaki R, Yasuda M, Song SJ, et al. The prevalence of age-related macular degeneration in Asians: a systematic review and meta-analysis. *Ophthalmology* 2010;117(5):921-7. doi: 10.1016/j.ophtha.2009.10.007 [published Online First: 2010/01/30]

101. Colijn JM, Buitendijk GHS, Prokofyeva E, et al. Prevalence of Age-Related Macular Degeneration in Europe: The Past and the Future. *Ophthalmology* 2017 doi: 10.1016/j.ophtha.2017.05.035 [published Online First: 2017/07/18]

102. U.S. Department of Health and Human Services, Centres for Disease Control and Prevention, National Center for Chronic Disease Prevention and Health Promotion, et al. The Health Consequences of Smoking: 50 Years of Progress: A Report of the Surgeon General. Atlanta, GA: U.S, 2014:1-1081.

103. Tan JS, Mitchell P, Kifley A, et al. Smoking and the long-term incidence of age-related macular degeneration: the Blue Mountains Eye Study. *Archives of ophthalmology (Chicago, Ill : 1960)* 2007;125(8):1089-95. doi: 10.1001/archopht.125.8.1089 [published Online First: 2007/08/19]

104. Evans JR, Fletcher AE, Wormald RPL. 28 000 Cases of age related macular degeneration causing visual loss in people aged 75 years and above in the United Kingdom may be attributable to smoking. *British Journal of Ophthalmology* 2005;89(5):550-53. doi: 10.1136/bjo.2004.049726

105. Seddon JM, Willett WC, Speizer FE, et al. A prospective study of cigarette smoking and age-related macular degeneration in women. *Jama* 1996;276(14):1141-6. [published Online First: 1996/10/09]

106. Katsi VK, Marketou ME, Vrachatis DA, et al. Essential hypertension in the pathogenesis of age-related macular degeneration: a review of the current evidence. *Journal of hypertension* 2015;33(12):2382-8. doi: 10.1097/hjh.0000000000000766 [published Online First: 2015/11/05]

107. Hyman L, Schachat AP, He Q, et al. Hypertension, cardiovascular disease, and age-related macular degeneration. *Archives of Ophthalmology* 2000;118(3):351-58. doi: 10.1001/archopht.118.3.351

108. Montgomery MP, Kamel F, Pericak-Vance MA, et al. Overall diet quality and age-related macular degeneration. *Ophthalmic epidemiology* 2010;17(1):58-65. doi: 10.3109/09286580903450353

109. Seddon JM, Cote J, Rosner B. Progression of age-related macular degeneration: association with dietary fat, transunsaturated fat, nuts, and fish intake. *Archives of ophthalmology (Chicago, Ill : 1960)* 2003;121(12):1728-37. doi: 10.1001/archopht.121.12.1728 [published Online First: 2003/12/10]

110. Coleman AL, Seitzman RL, Cummings SR, et al. The Association of Smoking and Alcohol Use with Age-Related Macular Degeneration in the Oldest Old: the Study of Osteoporotic Fractures. *American journal of ophthalmology* 2010;149(1):160-69. doi: 10.1016/j.ajo.2009.07.025

111. Krishnadev N, Meleth AD, Chew EY. Nutritional supplements for age-related macular degeneration. *Current opinion in ophthalmology* 2010;21(3):184-89. doi: 10.1097/ICU.0b013e32833866ee

112. Klein R, Cruickshanks KJ, Nash SD, et al. The prevalence of age-related macular degeneration and associated risk factors. *Archives of ophthalmology (Chicago, Ill : 1960)* 2010;128(6):750-8. doi: 10.1001/archophthalmol.2010.92 [published Online First: 2010/06/16]

113. Klein RJ, Zeiss C, Chew EY, et al. Complement factor H polymorphism in age-related macular degeneration. *Science (New York, NY)* 2005;308(5720):385-9. doi: 10.1126/science.1109557 [published Online First: 2005/03/12]

114. Haines JL, Hauser MA, Schmidt S, et al. Complement factor H variant increases the risk of age-related macular degeneration. *Science (New York, NY)* 2005;308(5720):419-21. doi: 10.1126/science.1110359 [published Online First: 2005/03/12]

115. Fagerness JA, Maller JB, Neale BM, et al. Variation near complement factor I is associated with risk of advanced AMD. *European journal of human genetics : EJHG* 2009;17(1):100-4. doi: 10.1038/ejhg.2008.140 [published Online First: 2008/08/08]

116. Gold B, Merriam JE, Zernant J, et al. Variation in factor B (BF) and complement component 2 (C2) genes is associated with age-related macular degeneration. *Nature genetics* 2006;38(4):458-62. doi: 10.1038/ng1750 [published Online First: 2006/03/07]

117. Yu Y, Bhangale TR, Fagerness J, et al. Common variants near FRK/COL10A1 and VEGFA are associated with advanced age-related macular degeneration. *Human molecular genetics* 2011;20(18):3699-709. doi: 10.1093/hmg/ddr270 [published Online First: 2011/06/15]

118. Holz FGP, D; Spaide, R.F; Bird, A.C. Age-related Macular Degeneration. 2 ed: Springer 2013.

119. Klein R, Peto T, Bird A, et al. The epidemiology of age-related macular degeneration. *Am J Ophthalmol* 2004;137(3):486-95. doi: 10.1016/j.ajo.2003.11.069 [published Online First: 2004/03/12]

120. Frank RN, Puklin JE, Stock C, et al. Race, iris color, and age-related macular degeneration. *Transactions of the American Ophthalmological Society* 2000;98:109-15; discussion 15-7. [published Online First: 2001/02/24]

121. Anderson DH, Mullins RF, Hageman GS, et al. A role for local inflammation in the formation of drusen in the aging eye. *Am J Ophthalmol* 2002;134(3):411-31. [published Online First: 2002/09/05]

122. Umeda S, Suzuki MT, Okamoto H, et al. Molecular composition of drusen and possible involvement of anti-retinal autoimmunity in two different forms of macular degeneration in cynomolgus monkey (Macaca fascicularis). *FASEB journal : official publication of the Federation of American Societies for Experimental Biology* 2005;19(12):1683-5. doi: 10.1096/fj.04-3525fje [published Online First: 2005/08/16]

123. Joachim N, Mitchell P, Burlutsky G, et al. The Incidence and Progression of Age-Related Macular Degeneration over 15 Years: The Blue Mountains Eye Study. *Ophthalmology* 2015;122(12):2482-9. doi: 10.1016/j.ophtha.2015.08.002 [published Online First: 2015/09/19]

124. Wang L, Clark ME, Crossman DK, et al. Abundant Lipid and Protein Components of Drusen. *PloS one* 2010;5(4):e10329. doi: 10.1371/journal.pone.0010329

125. Haugsdal J, Sohn E. Age-related macular degeneration: from one medical student to another.: EyeRounds.org.; 2013 [Available from: http://eyerounds.org/tutorials/AMD-medical-student/ accessed 21.02.18.

126. de Jong PT. Age-related macular degeneration. *The New England journal of medicine* 2006;355(14):1474-85. doi: 10.1056/NEJMra062326 [published Online First: 2006/10/06]

127. Schmidt-Erfurth U, Waldstein SM. A paradigm shift in imaging biomarkers in neovascular age-related macular degeneration. *Progress in retinal and eye research* 2016;50:1-24. doi: 10.1016/j.preteyeres.2015.07.007 [published Online First: 2015/08/27]

128. Fernández M, Gil M, Gonzalez F, et al. Diagnostic usefulness of indocyanine green angiography (ICGA) in age-related macular degeneration (AMD) AMD Book. Portugal: GER Group, 2017.

129. The Age-Related Eye Disease Study (AREDS): design implications. AREDS report no. 1. *Controlled clinical trials* 1999;20(6):573-600. [published Online First: 1999/12/10]

130. Chew E, Clemons T, SanGiovanni J, et al. Lutein + zeaxanthin and omega-3 fatty acids for age-related macular degeneration: the Age-Related Eye Disease Study 2 (AREDS2) randomized clinical trial. *Jama* 2013;309(19):2005-15. doi: 10.1001/jama.2013.4997 [published Online First: 2013/05/07]

131. Amadio M, Govoni S, Pascale A. Targeting VEGF in eye neovascularization: What's new?: A comprehensive review on current therapies and oligonucleotide-based interventions under development. *Pharmacological*

research 2016;103:253-69. doi: 10.1016/j.phrs.2015.11.027 [published Online First: 2015/12/19]

132. Moorfields Eye Hospital NHS Foundation Trust. Patient Information: Anti-VEGF intravitreal injection treatment.

133. Ford KM, Saint-Geniez M, Walshe T, et al. Expression and role of VEGF in the adult retinal pigment epithelium. *Investigative ophthalmology & visual science* 2011;52(13):9478-87. doi: 10.1167/iovs.11-8353 [published Online First: 2011/11/08]

134. Lotery A. Progress in understanding and treating age-related macular degeneration. *Eye (London, England)* 2008;22(6):739-41. doi: 10.1038/sj.eye.6703035 [published Online First: 2008/06/13]

135. Nowak JZ. Age-related macular degeneration (AMD): pathogenesis and therapy. *Pharmacological reports : PR* 2006;58(3):353-63. [published Online First: 2006/07/18]

136. Ambati J, Fowler Benjamin J. Mechanisms of Age-Related Macular Degeneration. *Neuron* 2012;75(1):26-39. doi: https://doi.org/10.1016/j.neuron.2012.06.018

137. Sarna T, Burke JM, Korytowski W, et al. Loss of melanin from human RPE with aging: possible role of melanin photooxidation. *Experimental eye research* 2003;76(1):89-98. [published Online First: 2003/02/19]

138. Ugarte M, Hussain AA, Marshall J. An experimental study of the elastic properties of the human Bruch's membrane-choroid complex: relevance to ageing. *The British journal of ophthalmology* 2006;90(5):621-26. doi: 10.1136/bjo.2005.086579

139. Louie JL, Kapphahn RJ, Ferrington DA. Proteasome function and protein oxidation in the aged retina. *Experimental eye research* 2002;75(3):271-84. [published Online First: 2002/10/18]

140. Kapphahn RJ, Bigelow EJ, Ferrington DA. Age-dependent inhibition of proteasome chymotrypsin-like activity in the retina. *Experimental eye research* 2007;84(4):646-54. doi: 10.1016/j.exer.2006.12.002 [published Online First: 2007/01/30]

141. Calderwood SK, Murshid A, Prince T. The shock of aging: molecular chaperones and the heat shock response in longevity and aging--a mini-review. *Gerontology* 2009;55(5):550-8. doi: 10.1159/000225957 [published Online First: 2009/06/24]

142. Lopez-Otin C, Blasco MA, Partridge L, et al. The hallmarks of aging. *Cell* 2013;153(6):1194-217. doi: 10.1016/j.cell.2013.05.039 [published Online First: 2013/06/12]

143. Grune T, Jung T, Merker K, et al. Decreased proteolysis caused by protein aggregates, inclusion bodies, plaques, lipofuscin, ceroid, and 'aggresomes' during oxidative stress, aging, and disease. *The international journal of biochemistry & cell biology* 2004;36(12):2519-30. doi: 10.1016/j.biocel.2004.04.020 [published Online First: 2004/08/25]

144. Loeffler KU, Mangini NJ. Immunolocalization of ubiquitin and related enzymes in human retina and retinal pigment epithelium. *Graefe's Archive*

for Clinical and Experimental Ophthalmology 1997;235(4):248-54. doi: 10.1007/BF00941767

145. Fernandes AF, Guo W, Zhang X, et al. Proteasome-dependent regulation of signal transduction in retinal pigment epithelial cells. *Experimental eye research* 2006;83(6):1472-81. doi: 10.1016/j.exer.2006.07.024 [published Online First: 2006/10/10]

146. Ambati J, Anand A, Fernandez S, et al. An animal model of age-related macular degeneration in senescent Ccl-2- or Ccr-2-deficient mice. *Nat Med* 2003;9(11):1390-7. doi: 10.1038/nm950 [published Online First: 2003/10/21]

147. Fernandes AF, Bian Q, Jiang J-K, et al. Proteasome Inactivation Promotes p38 Mitogen-activated Protein Kinase-dependent Phosphatidylinositol 3-kinase Activation and Increases Interleukin-8 Production in Retinal Pigment Epithelial Cells. *Molecular Biology of the Cell* 2009;20(16):3690-99. doi: 10.1091/mbc.E08-10-1068

148. Korolchuk VI, Menzies FM, Rubinsztein DC. A novel link between autophagy and the ubiquitin-proteasome system. *Autophagy* 2009;5(6):862-3. [published Online First: 2009/05/22]

149. Zhan J, He J, Zhou Y, et al. Crosstalk Between the Autophagy-Lysosome Pathway and the Ubiquitin-Proteasome Pathway in Retinal Pigment Epithelial Cells. *Current molecular medicine* 2016;16(5):487-95. [published Online First: 2016/05/03]

150. Tang B, Cai J, Sun L, et al. Proteasome inhibitors activate autophagy involving inhibition of PI3K-Akt-mTOR pathway as an anti-oxidation defense in human RPE cells. *PloS one* 2014;9(7):e103364. doi: 10.1371/journal.pone.0103364 [published Online First: 2014/07/26]

151. Korolchuk VI, Menzies FM, Rubinsztein DC. Mechanisms of cross-talk between the ubiquitin-proteasome and autophagy-lysosome systems. *FEBS letters* 2010;584(7):1393-8. doi: 10.1016/j.febslet.2009.12.047 [published Online First: 2009/12/31]

152. Mitter SK, Rao HV, Qi X, et al. Autophagy in the Retina: A Potential Role in Age-Related Macular Degeneration. *Advances in experimental medicine and biology* 2012;723:83-90. doi: 10.1007/978-1-4614-0631-0_12

153. Golestaneh N, Chu Y, Xiao Y-Y, et al. Dysfunctional autophagy in RPE, a contributing factor in age-related macular degeneration. *Cell Death & Disease* 2017;8(1):e2537. doi: 10.1038/cddis.2016.453

154. Mitter SK, Song C, Qi X, et al. Dysregulated autophagy in the RPE is associated with increased susceptibility to oxidative stress and AMD. *Autophagy* 2014;10(11):1989-2005. doi: 10.4161/auto.36184

155. Wang AL, Lukas TJ, Yuan M, et al. Autophagy and exosomes in the aged retinal pigment epithelium: possible relevance to drusen formation and age-related macular degeneration. *PloS one* 2009;4(1):e4160. doi: 10.1371/journal.pone.0004160 [published Online First: 2009/01/09]

156. Sparrow JR, Fishkin N, Zhou J, et al. A2E, a byproduct of the visual cycle. *Vision research* 2003;43(28):2983-90. [published Online First: 2003/11/13]

157. Shamsi FA, Boulton M. Inhibition of RPE lysosomal and antioxidant activity by the age pigment lipofuscin. *Investigative ophthalmology & visual science* 2001;42(12):3041-6. [published Online First: 2001/11/01]

158. Sinha D, Valapala M, Shang P, et al. Lysosomes: regulators of autophagy in the retinal pigmented epithelium. *Experimental eye research* 2016;144:46-53. doi: 10.1016/j.exer.2015.08.018

159. Brandstetter C, Mohr LKM, Latz E, et al. Light induces NLRP3 inflammasome activation in retinal pigment epithelial cells via lipofuscin-mediated photooxidative damage. *Journal of Molecular Medicine* 2015;93(8):905-16. doi: 10.1007/s00109-015-1275-1

160. Radu RA, Hu J, Yuan Q, et al. Complement System Dysregulation and Inflammation in the Retinal Pigment Epithelium of a Mouse Model for Stargardt Macular Degeneration. *The Journal of biological chemistry* 2011;286(21):18593-601. doi: 10.1074/jbc.M110.191866

161. Benilova I, Karran E, De Strooper B. The toxic Abeta oligomer and Alzheimer's disease: an emperor in need of clothes. *Nature neuroscience* 2012;15(3):349-57. doi: 10.1038/nn.3028 [published Online First: 2012/01/31]

162. Walsh DM, Selkoe DJ. A beta oligomers - a decade of discovery. *Journal of neurochemistry* 2007;101(5):1172-84. doi: 10.1111/j.1471-4159.2006.04426.x [published Online First: 2007/02/09]

163. Cam JA, Bu G. Modulation of beta-amyloid precursor protein trafficking and processing by the low density lipoprotein receptor family. *Molecular neurodegeneration* 2006;1:8. doi: 10.1186/1750-1326-1-8 [published Online First: 2006/08/26]

164. O'Brien RJ, Wong PC. Amyloid precursor protein processing and Alzheimer's disease. *Annual review of neuroscience* 2011;34:185-204. doi: 10.1146/annurev-neuro-061010-113613 [published Online First: 2011/04/05]

165. Johnson LV, Leitner WP, Rivest AJ, et al. The Alzheimer's A beta -peptide is deposited at sites of complement activation in pathologic deposits associated with aging and age-related macular degeneration. *Proceedings of the National Academy of Sciences of the United States of America* 2002;99(18):11830-5. doi: 10.1073/pnas.192203399

166. De Strooper B. Proteases and proteolysis in Alzheimer disease: a multifactorial view on the disease process. *Physiological reviews* 2010;90(2):465-94. doi: 10.1152/physrev.00023.2009

167. LaFerla FM, Green KN, Oddo S. Intracellular amyloid-beta in Alzheimer's disease. *Nature reviews Neuroscience* 2007;8(7):499-509. doi: 10.1038/nrn2168 [published Online First: 2007/06/07]

168. Zhang X, Song W. The role of APP and BACE1 trafficking in APP processing and amyloid-beta generation. *Alzheimer's research & therapy* 2013;5(5):46. doi: 10.1186/alzrt211 [published Online First: 2013/10/10]

169. Selkoe DJ. Physiological production of the beta-amyloid protein and the mechanism of Alzheimer's disease. *Trends in neurosciences* 1993;16(10):403-9. [published Online First: 1993/10/01]

List of References

170. Haass C, Selkoe DJ. Soluble protein oligomers in neurodegeneration: lessons from the Alzheimer's amyloid beta-peptide. *Nature reviews Molecular cell biology* 2007;8(2):101-12. doi: 10.1038/nrm2101

171. Guo L, Salt TE, Luong V, et al. Targeting amyloid-beta in glaucoma treatment. *Proceedings of the National Academy of Sciences of the United States of America* 2007;104(33):13444-9. doi: 10.1073/pnas.0703707104 [published Online First: 2007/08/09]

172. Chow VW, Mattson MP, Wong PC, et al. An overview of APP processing enzymes and products. *Neuromolecular medicine* 2010;12(1):1-12. doi: 10.1007/s12017-009-8104-z [published Online First: 2010/03/17]

173. Kumar S, Rezaei-Ghaleh N, Terwel D, et al. Extracellular phosphorylation of the amyloid beta-peptide promotes formation of toxic aggregates during the pathogenesis of Alzheimer's disease. *The EMBO journal* 2011;30(11):2255-65. doi: 10.1038/emboj.2011.138 [published Online First: 2011/04/30]

174. Shankar GM, Bloodgood BL, Townsend M, et al. Natural oligomers of the Alzheimer amyloid-beta protein induce reversible synapse loss by modulating an NMDA-type glutamate receptor-dependent signaling pathway. *The Journal of neuroscience : the official journal of the Society for Neuroscience* 2007;27(11):2866-75. doi: 10.1523/jneurosci.4970-06.2007 [published Online First: 2007/03/16]

175. Lesne S, Koh MT, Kotilinek L, et al. A specific amyloid-beta protein assembly in the brain impairs memory. *Nature* 2006;440(7082):352-7. doi: 10.1038/nature04533 [published Online First: 2006/03/17]

176. Broersen K, Jonckheere W, Rozenski J, et al. A standardized and biocompatible preparation of aggregate-free amyloid beta peptide for biophysical and biological studies of Alzheimer's disease. *Protein engineering, design & selection : PEDS* 2011;24(9):743-50. doi: 10.1093/protein/gzr020 [published Online First: 2011/05/14]

177. Serpell L. Alzheimer's amyloid fibrils: structure and assembly. *Biochemet Biophysica Acta* 1999;1502(2000):16-30.

178. Rambaran RS, L.C. Amyloid fibrils:Abnormal protein assembly. *Prion* 2008;2(3):112-17.

179. Iannuzzi C, Irace G, Sirangelo I. The effect of glycosaminoglycans (GAGs) on amyloid aggregation and toxicity. *Molecules (Basel, Switzerland)* 2015;20(2):2510-28. doi: 10.3390/molecules20022510 [published Online First: 2015/02/05]

180. Ratnayaka JA, Lynn SA, Griffiths H, et al. An ex-vivo platform for manipulation and study of Retinal Pigment Epithelial (RPE) cells in long-term culture. *Investigative ophthalmology & visual science* 2015;56(7):2332-32.

181. Lee J, Culyba EK, Powers ET, et al. Amyloid-beta forms fibrils by nucleated conformational conversion of oligomers. *Nature chemical biology* 2011;7(9):602-9. doi: 10.1038/nchembio.624 [published Online First: 2011/08/02]

182. Broersen K, Rousseau F, Schymkowitz J. The culprit behind amyloid beta peptide related neurotoxicity in Alzheimer's disease: oligomer size or conformation? *Alzheimer's research & therapy* 2010;2(4):12. doi: 10.1186/alzrt36

183. Bezprozvanny I. Amyloid goes global. *Science signaling* 2009;2(63):pe16. doi: 10.1126/scisignal.263pe16 [published Online First: 2009/03/26]

184. Kim W, Hecht MH. Sequence determinants of enhanced amyloidogenicity of Alzheimer A{beta}42 peptide relative to A{beta}40. *The Journal of biological chemistry* 2005;280(41):35069-76. doi: 10.1074/jbc.M505763200 [published Online First: 2005/08/05]

185. Di Carlo M. Beta amyloid peptide: from different aggregation forms to the activation of different biochemical pathways. *European biophysics journal : EBJ* 2010;39(6):877-88. doi: 10.1007/s00249-009-0439-8 [published Online First: 2009/03/24]

186. Hardy J, Selkoe DJ. The amyloid hypothesis of Alzheimer's disease: progress and problems on the road to therapeutics. *Science (New York, NY)* 2002;297(5580):353-6. doi: 10.1126/science.1072994

187. Ashe KH. Mechanisms of memory loss in Abeta and tau mouse models. *Biochemical Society transactions* 2005;33(Pt 4):591-4. doi: 10.1042/bst0330591 [published Online First: 2005/07/27]

188. Kowalska A, Pruchnik-Wolinska D, Florczak J, et al. Genetic study of familial cases of Alzheimer's disease. *Acta biochimica Polonica* 2004;51(1):245-52. doi: 045101245 [published Online First: 2004/04/20]

189. Weller RO, Subash M, Preston SD, et al. Perivascular drainage of amyloid-beta peptides from the brain and its failure in cerebral amyloid angiopathy and Alzheimer's disease. *Brain pathology (Zurich, Switzerland)* 2008;18(2):253-66. doi: 10.1111/j.1750-3639.2008.00133.x [published Online First: 2008/03/28]

190. Hawkes CA, Jayakody N, Johnston DA, et al. Failure of perivascular drainage of beta-amyloid in cerebral amyloid angiopathy. *Brain pathology (Zurich, Switzerland)* 2014;24(4):396-403. doi: 10.1111/bpa.12159 [published Online First: 2014/06/20]

191. Yoon S-S, Jo SA. Mechanisms of Amyloid-β Peptide Clearance: Potential Therapeutic Targets for Alzheimer's Disease. *Biomolecules & Therapeutics* 2012;20(3):245-55. doi: 10.4062/biomolther.2012.20.3.245

192. Ferreira ST, Vieira MN, De Felice FG. Soluble protein oligomers as emerging toxins in Alzheimer's and other amyloid diseases. *IUBMB life* 2007;59(4-5):332-45. doi: 10.1080/15216540701283882 [published Online First: 2007/05/17]

193. Wisniewski T, Goñi F. Immunotherapeutic Approaches for Alzheimer's Disease. *Neuron* 2015;85(6):1162-76. doi: 10.1016/j.neuron.2014.12.064

194. Dutescu RM, Li QX, Crowston J, et al. Amyloid precursor protein processing and retinal pathology in mouse models of Alzheimer's disease. *Graefe's archive for clinical and experimental ophthalmology = Albrecht von Graefes Archiv fur klinische und experimentelle Ophthalmologie* 2009;247(9):1213-21. doi: 10.1007/s00417-009-1060-3

195. Wang J, Zhu C, Xu Y, et al. Development and expression of amyloid-beta peptide 42 in retinal ganglion cells in rats. *Anatomical record (Hoboken, NJ : 2007)* 2011;294(8):1401-5. doi: 10.1002/ar.21438 [published Online First: 2011/07/01]

196. Wang J, Ohno-Matsui K, Morita I. Elevated amyloid beta production in senescent retinal pigment epithelium, a possible mechanism of subretinal deposition of amyloid beta in age-related macular degeneration. *Biochemical and biophysical research communications* 2012;423(1):73-8. doi: 10.1016/j.bbrc.2012.05.085

197. Yoshida T, Ohno-Matsui K, Ichinose S, et al. The potential role of amyloid beta in the pathogenesis of age-related macular degeneration. *The Journal of clinical investigation* 2005;115(10):2793-800. doi: 10.1172/JCI24635

198. Boulton ME, Cai J, Grant MB. gamma-Secretase: a multifaceted regulator of angiogenesis. *Journal of cellular and molecular medicine* 2008;12(3):781-95. doi: 10.1111/j.1582-4934.2008.00274.x [published Online First: 2008/02/13]

199. Prakasam A, Muthuswamy A, Ablonczy Z, et al. Differential accumulation of secreted AbetaPP metabolites in ocular fluids. *Journal of Alzheimer's disease : JAD* 2010;20(4):1243-53. doi: 10.3233/JAD-2010-100210

200. Parthasarathy R, Fautsch MP, Pepperberg DR. Quantification of amyloid-beta in mouse and human eye tissues. *Investigative ophthalmology & visual science* 2014;55(13):1317-17.

201. Ho T, Vessey KA, Cappai R, et al. Amyloid precursor protein is required for normal function of the rod and cone pathways in the mouse retina. *PloS one* 2012;7(1):e29892. doi: 10.1371/journal.pone.0029892 [published Online First: 2012/01/27]

202. Anderson DH, Talaga KC, Rivest AJ, et al. Characterization of β amyloid assemblies in drusen: the deposits associated with aging and age-related macular degeneration. *Experimental eye research* 2004;78(2):243-56. doi: 10.1016/j.exer.2003.10.011

203. Hoh Kam J, Lenassi E, Jeffery G. Viewing ageing eyes: diverse sites of amyloid Beta accumulation in the ageing mouse retina and the up-regulation of macrophages. *PloS one* 2010;5(10) doi: 10.1371/journal.pone.0013127

204. Hickman SE, Allison EK, El Khoury J. Microglial dysfunction and defective beta-amyloid clearance pathways in aging Alzheimer's disease mice. *The Journal of neuroscience : the official journal of the Society for Neuroscience* 2008;28(33):8354-60. doi: 10.1523/jneurosci.0616-08.2008 [published Online First: 2008/08/15]

205. Wildsmith KR, Holley M, Savage JC, et al. Evidence for impaired amyloid beta clearance in Alzheimer's disease. *Alzheimer's research & therapy* 2013;5(4):33. doi: 10.1186/alzrt187 [published Online First: 2013/07/16]

206. Ning A, Cui J, To E, et al. Amyloid-beta deposits lead to retinal degeneration in a mouse model of Alzheimer disease. *Investigative ophthalmology & visual science* 2008;49(11):5136-43. doi: 10.1167/iovs.08-1849 [published Online First: 2008/06/21]

207. Wang J, Ohno-Matsui K, Morita I. Cholesterol enhances amyloid beta deposition in mouse retina by modulating the activities of Abeta-regulating enzymes in retinal pigment epithelial cells. *Biochemical and biophysical research communications* 2012;424(4):704-9. doi: 10.1016/j.bbrc.2012.07.014

208. Isas JM, Luibl V, Johnson LV, et al. Soluble and mature amyloid fibrils in drusen deposits. *Investigative ophthalmology & visual science* 2010;51(3):1304-10. doi: 10.1167/iovs.09-4207

209. Luibl V, Isas JM, Kayed R, et al. Drusen deposits associated with aging and age-related macular degeneration contain nonfibrillar amyloid oligomers. *The Journal of clinical investigation* 2006;116(2):378-85. doi: 10.1172/JCI25843

210. Kirby E, Bandelow S, Hogervorst E. Visual impairment in Alzheimer's disease: a critical review. *Journal of Alzheimer's disease : JAD* 2010;21(1):15-34. doi: 10.3233/jad-2010-080785 [published Online First: 2010/02/26]

211. Tzekov R, Mullan M. Vision function abnormalities in Alzheimer disease. *Survey of ophthalmology* 2014;59(4):414-33. doi: 10.1016/j.survophthal.2013.10.002 [published Online First: 2013/12/07]

212. Valenti DA. Alzheimer's disease: visual system review. *Optometry (St Louis, Mo)* 2010;81(1):12-21. doi: 10.1016/j.optm.2009.04.101 [published Online First: 2009/12/17]

213. Liu RT, Gao J, Cao S, et al. Inflammatory mediators induced by amyloid-beta in the retina and RPE in vivo: implications for inflammasome activation in age-related macular degeneration. *Investigative ophthalmology & visual science* 2013;54(3):2225-37. doi: 10.1167/iovs.12-10849

214. Javaid FZ, Brenton J, Guo L, et al. Visual and Ocular Manifestations of Alzheimer's Disease and Their Use as Biomarkers for Diagnosis and Progression. *Frontiers in neurology* 2016;7:55. doi: 10.3389/fneur.2016.00055 [published Online First: 2016/05/06]

215. Armstrong RA. Alzheimer's Disease and the Eye. *Journal of Optometry* 2009;2(3):103-11.

216. Syed AB, Armstrong RA, Smith CU. A quantitative analysis of optic nerve axons in elderly control subjects and patients with Alzheimer's disease. *Folia neuropathologica / Association of Polish Neuropathologists and Medical Research Centre, Polish Academy of Sciences* 2005;43(1):1-6. [published Online First: 2005/04/14]

217. Blanks JC, Torigoe Y, Hinton DR, et al. Retinal pathology in Alzheimer's disease. I. Ganglion cell loss in foveal/parafoveal retina. *Neurobiology of aging* 1996;17(3):377-84. [published Online First: 1996/05/01]

218. Sadun AA, Bassi CJ. Optic nerve damage in Alzheimer's disease. *Ophthalmology* 1990;97(1):9-17. [published Online First: 1990/01/01]

219. Liu B, Rasool S, Yang Z, et al. Amyloid-peptide vaccinations reduce {beta}-amyloid plaques but exacerbate vascular deposition and inflammation in the retina of Alzheimer's transgenic mice. *The American journal of pathology* 2009;175(5):2099-110. doi: 10.2353/ajpath.2009.090159 [published Online First: 2009/10/17]

220. Assessing Peripheral Retinal Drusen Progression in Alzheimer's Dementia: A Pilot Study Using Ultra-Wide Field Imaging. The Association for Research in Vision in Opthalmology; 2014; Orlando, FA, USA. IOVS.

221. Koronyo-Hamaoui M, Koronyo Y, Ljubimov AV, et al. Identification of amyloid plaques in retinas from Alzheimer's patients and noninvasive in vivo optical imaging of retinal plaques in a mouse model. *NeuroImage* 2011;54 Suppl 1:S204-17. doi: 10.1016/j.neuroimage.2010.06.020 [published Online First: 2010/06/17]

222. Sivak JM. The aging eye: common degenerative mechanisms between the Alzheimer's brain and retinal disease. *Investigative ophthalmology & visual science* 2013;54(1):871-80. doi: 10.1167/iovs.12-10827 [published Online First: 2013/02/01]

223. Davis BM, Crawley L, Pahlitzsch M, et al. Glaucoma: the retina and beyond. *Acta neuropathologica* 2016;132(6):807-26. doi: 10.1007/s00401-016-1609-2

224. Bayer TA, Wirths O. Intracellular accumulation of amyloid-Beta - a predictor for synaptic dysfunction and neuron loss in Alzheimer's disease. *Frontiers in aging neuroscience* 2010;2:8. doi: 10.3389/fnagi.2010.00008 [published Online First: 2010/06/17]

225. Tamura H, Kawakami H, Kanamoto T, et al. High frequency of open-angle glaucoma in Japanese patients with Alzheimer's disease. *Journal of the neurological sciences* 2006;246(1-2):79-83. doi: 10.1016/j.jns.2006.02.009 [published Online First: 2006/03/28]

226. Blanks JC, Hinton DR, Sadun AA, et al. Retinal ganglion cell degeneration in Alzheimer's disease. *Brain research* 1989;501(2):364-72. [published Online First: 1989/11/06]

227. McKinnon SJ, Lehman DM, Kerrigan-Baumrind LA, et al. Caspase activation and amyloid precursor protein cleavage in rat ocular hypertension. *Investigative ophthalmology & visual science* 2002;43(4):1077-87. [published Online First: 2002/03/30]

228. McKinnon SJ. Glaucoma: ocular Alzheimer's disease? *Frontiers in bioscience : a journal and virtual library* 2003;8:s1140-56. [published Online First: 2003/09/06]

229. Yoneda S, Hara H, Hirata A, et al. Vitreous fluid levels of beta-amyloid((1-42)) and tau in patients with retinal diseases. *Japanese journal of ophthalmology* 2005;49(2):106-8. doi: 10.1007/s10384-004-0156-x [published Online First: 2005/04/20]

230. Mehta PD, Pirttilä T, Mehta SP, et al. Plasma and cerebrospinal fluid levels of amyloid β proteins 1-40 and 1-42 in alzheimer disease. *Archives of neurology* 2000;57(1):100-05. doi: 10.1001/archneur.57.1.100

231. Dentchev T, Milam AH, Lee VMY, et al. Amyloid-β is found in drusen from some age-related macular degeneration retinas, but not in drusen from normal retinas. *Molecular Vision* 2003;9:184-90.

232. Zipfel PF, Lauer N, Skerka C. The role of complement in AMD. *Advances in experimental medicine and biology* 2010;703:9-24. doi: 10.1007/978-1-4419-5635-4_2 [published Online First: 2010/08/17]

233. Wang J, Ohno-Matsui K, Yoshida T, et al. Altered Function of Factor I Caused by Amyloid : Implication for Pathogenesis of Age-Related Macular Degeneration from Drusen. *The Journal of Immunology* 2008;181(1):712-20. doi: 10.4049/jimmunol.181.1.712

234. Hageman GS, Anderson DH, Johnson LV, et al. A common haplotype in the complement regulatory gene factor H (HF1/CFH) predisposes individuals to age-related macular degeneration. *Proceedings of the National Academy of Sciences of the United States of America* 2005;102(20):7227-32. doi: 10.1073/pnas.0501536102

235. Howlett DR, Bate ST, Collier S, et al. Characterisation of amyloid-induced inflammatory responses in the rat retina. *Experimental brain research* 2011;214(2):185-97. doi: 10.1007/s00221-011-2819-4 [published Online First: 2011/08/19]

236. Gao J, Liu RT, Cao S, et al. NLRP3 inflammasome: activation and regulation in age-related macular degeneration. *Mediators of inflammation* 2015;2015:690243. doi: 10.1155/2015/690243 [published Online First: 2015/02/24]

237. Celkova L, Doyle SL, Campbell M. NLRP3 Inflammasome and Pathobiology in AMD. *Journal of clinical medicine* 2015;4(1):172-92. doi: 10.3390/jcm4010172 [published Online First: 2015/08/04]

238. Doyle SL, Campbell M, Ozaki E, et al. NLRP3 has a protective role in age-related macular degeneration through the induction of IL-18 by drusen components. *Nat Med* 2012;18(5):791-8. doi: 10.1038/nm.2717 [published Online First: 2012/04/10]

239. Tseng WA, Thein T, Kinnunen K, et al. NLRP3 inflammasome activation in retinal pigment epithelial cells by lysosomal destabilization: implications for age-related macular degeneration. *Investigative ophthalmology & visual science* 2013;54(1):110-20. doi: 10.1167/iovs.12-10655 [published Online First: 2012/12/12]

240. Halle A, Hornung V, Petzold GC, et al. The NALP3 inflammasome is involved in the innate immune response to amyloid-β. *Nature immunology* 2008;9(8):857-65. doi: 10.1038/ni.1636

241. Jo E-K, Kim JK, Shin D-M, et al. Molecular mechanisms regulating NLRP3 inflammasome activation. *Cellular and Molecular Immunology* 2016;13(2):148-59. doi: 10.1038/cmi.2015.95

242. Bruban J, Glotin AL, Dinet V, et al. Amyloid-β (1-42) alters structure and function of retinal pigmented epithelial cells. *Aging Cell* 2009;8:162-77.

243. Cao L, Wang H, Wang F, et al. Aβ-Induced Senescent Retinal Pigment Epithelial Cells Create a Proinflammatory Microenvironment in AMD. *Investigative ophthalmology & visual science* 2013;54(5):3738-50. doi: 10.1167/

244. Park SW, Kim JH, Mook-Jung I, et al. Intracellular amyloid beta alters the tight junction of retinal pigment epithelium in 5XFAD mice. *Neurobiology of aging* 2014;35(9):2013-20. doi: 10.1016/j.neurobiolaging.2014.03.008 [published Online First: 2014/04/09]

245. Cunvong K, Huffmire D, Ethell DW, et al. Amyloid-beta increases capillary bed density in the adult zebrafish retina. *Investigative ophthalmology & visual science* 2013;54(2):1516-21. doi: 10.1167/iovs.12-10821

246. Dunn KC, Aotaki-Keen AE, Putkey FR, et al. ARPE-19, a human retinal pigment epithelial cell line with differentiated properties. *Experimental eye research* 1996;62(2):155-69. doi: 10.1006/exer.1996.0020 [published Online First: 1996/02/01]

247. Soura V, Stewart-Parker M, Williams TL, et al. Visualization of co-localization in Abeta42-administered neuroblastoma cells reveals lysosome damage and autophagosome accumulation related to cell death. *The Biochemical journal* 2012;441(2):579-90. doi: 10.1042/bj20110749 [published Online First: 2011/10/01]

248. The Molecular Probes Handbook: A Guide to Fluorescent Probes and Labeling Technologies. 11th ed. USA: Life Technologies Corporation 2010.

249. Technologies I. Magic Red®Cathepsin Assay Manual [Product Manual]. Bloomington, MN, USA: ImmunoChemistry Technologies, LLC; 2017 [updated 14/06/201707/01/2018]. Available from: https://www.bio-rad-antibodies.com/static/uploads/ifu/ict937.pdf accessed 07/01/2018.

250. Krohne TU, Holz FG, Kopitz J. Apical-to-basolateral transcytosis of photoreceptor outer segments induced by lipid peroxidation products in human retinal pigment epithelial cells. *Investigative ophthalmology & visual science* 2010;51(1):553-60. doi: 10.1167/iovs.09-3755 [published Online First: 2009/08/22]

251. Schraermeyer U, Enzmann V, Kohen L, et al. Porcine iris pigment epithelial cells can take up retinal outer segments. *Experimental eye research* 1997;65(2):277-87. doi: 10.1006/exer.1997.0339 [published Online First: 1997/08/01]

252. Mao Y, Finnemann SC. Analysis of photoreceptor outer segment phagocytosis by RPE cells in culture. *Methods in molecular biology (Clifton, NJ)* 2013;935:285-95. doi: 10.1007/978-1-62703-080-9_20

253. Kilkenny C, Browne WJ, Cuthill IC, et al. Improving Bioscience Research Reporting: The ARRIVE Guidelines for Reporting Animal Research. *PLoS Biology* 2010;8(6) doi: 10.1371/journal.pbio.1000412

254. Uusitalo H. An acute ocular inflammatory reaction induced by intravitreal bovine serum albumin in presensitized rabbits: the effect of phentolamine. *Acta Ophthalmol (Copenh)* 1984;62(4):636-42. [published Online First: 1984/08/01]

255. Xiao J, Wu S, Wang Y, et al. Inhibitory effects of tetrandrine on bovine serum albumin-induced uveitis in rabbits. *Journal of ocular pharmacology* 1993;9(2):151-6. [published Online First: 1993/01/01]

256. Angi M, Kalirai H, Coupland SE, et al. Proteomic analyses of the vitreous humour. *Mediators of inflammation* 2012;2012:148039. doi: 10.1155/2012/148039 [published Online First: 2012/09/14]

257. Thevi T. All that Glitters is not Gold: A Misdiagnosed Case of Retinopathy. *Int J Sci Stud* 2015;3(5):202-04. doi: DOI:10.17354/ijss/2015/377

258. Skeie JM, Mahajan VB. Dissection of Human Vitreous Body Elements for Proteomic Analysis. *Journal of visualized experiments : JoVE* 2011(47):2455. doi: 10.3791/2455

259. Zinchuk V, Zinchuk O, Okada T. Quantitative Colocalization Analysis of Multicolor Confocal Immunofluorescence Microscopy Images: Pushing Pixels to Explore Biological Phenomena. *Acta Histochemica et Cytochemica* 2007;40(4):101-11. doi: 10.1267/ahc.07002

260. Costes SV, Daelemans D, Cho EH, et al. Automatic and Quantitative Measurement of Protein-Protein Colocalization in Live Cells. *Biophysical Journal* 2004;86(6):3993-4003. doi: 10.1529/biophysj.103.038422

261. Dunn KW, Kamocka MM, McDonald JH. A practical guide to evaluating colocalization in biological microscopy. *American Journal of Physiology - Cell Physiology* 2011;300(4):C723-C42. doi: 10.1152/ajpcell.00462.2010

262. Kuehnel W. Color Atlas of Cytology, Histology, & Microscopic Anatomy. 4th ed. Stuttgart: Thieme 2003.

263. Nixon RA. Endosome function and dysfunction in Alzheimer's disease and other neurodegenerative diseases. *Neurobiology of aging* 2005;26(3):373-82. doi: 10.1016/j.neurobiolaging.2004.09.018 [published Online First: 2005/01/11]

264. Cataldo AM, Barnett JL, Pieroni C, et al. Increased neuronal endocytosis and protease delivery to early endosomes in sporadic Alzheimer's disease: neuropathologic evidence for a mechanism of increased beta-amyloidogenesis. *The Journal of neuroscience : the official journal of the Society for Neuroscience* 1997;17(16):6142-51. [published Online First: 1997/08/15]

265. Layfield R, Cavey JR, Lowe J. Role of ubiquitin-mediated proteolysis in the pathogenesis of neurodegenerative disorders. *Ageing Res Rev* 2003;2(4):343-56. [published Online First: 2003/10/03]

266. Cole GM, Timiras PS. Ubiquitin-protein conjugates in Alzheimer's lesions. *Neuroscience Letters* 1987;79(1):207-12. doi: https://doi.org/10.1016/0304-3940(87)90698-7

267. Nixon RA, Wegiel J, Kumar A, et al. Extensive involvement of autophagy in Alzheimer disease: an immuno-electron microscopy study. *J Neuropathol Exp Neurol* 2005;64(2):113-22. [published Online First: 2005/03/09]

268. Selkoe DJ. Amyloid protein and Alzheimer's disease. *Scientific American* 1991;265(5):68-71, 74-6, 78. [published Online First: 1991/11/01]

269. Boland B, Kumar A, Lee S, et al. Autophagy Induction and Autophagosome Clearance in Neurons: Relationship to Autophagic Pathology in Alzheimer's Disease. *The Journal of neuroscience : the official journal of the Society for Neuroscience* 2008;28(27):6926-37. doi: 10.1523/JNEUROSCI.0800-08.2008

270. Nixon RA. Autophagy in neurodegenerative disease: friend, foe or turncoat? *Trends in neurosciences* 2006;29(9):528-35. doi: 10.1016/j.tins.2006.07.003 [published Online First: 2006/07/25]

271. Cataldo AM, Barnett JL, Berman SA, et al. Gene expression and cellular content of cathepsin D in Alzheimer's disease brain: evidence for early up-

regulation of the endosomal-lysosomal system. *Neuron* 1995;14(3):671-80. [published Online First: 1995/03/01]

272. Cataldo AM, Paskevich PA, Kominami E, et al. Lysosomal hydrolases of different classes are abnormally distributed in brains of patients with Alzheimer disease. *Proceedings of the National Academy of Sciences of the United States of America* 1991;88(24):10998-1002.

273. Haque A, Banik NL, Ray SK. New insights into the roles of endolysosomal cathepsins in the pathogenesis of Alzheimer's disease: cathepsin inhibitors as potential therapeutics. *CNS & neurological disorders drug targets* 2008;7(3):270-7. [published Online First: 2008/08/05]

274. Serrano-Puebla A, Boya P. Lysosomal membrane permeabilization in cell death: new evidence and implications for health and disease. *Annals of the New York Academy of Sciences* 2016;1371(1):30-44. doi: 10.1111/nyas.12966 [published Online First: 2015/11/26]

275. Johansson A-C, Appelqvist H, Nilsson C, et al. Regulation of apoptosis-associated lysosomal membrane permeabilization. *Apoptosis* 2010;15(5):527-40. doi: 10.1007/s10495-009-0452-5

276. Boya P, Kroemer G. Lysosomal membrane permeabilization in cell death. *Oncogene* 2008;27(50):6434-51. doi: 10.1038/onc.2008.310 [published Online First: 2008/10/29]

277. Yang AJ, Chandswangbhuvana D, Margol L, et al. Loss of endosomal/lysosomal membrane impermeability is an early event in amyloid Abeta1-42 pathogenesis. *Journal of neuroscience research* 1998;52(6):691-8. [published Online First: 1998/07/21]

278. Gouras GK, Tsai J, Naslund J, et al. Intraneuronal Abeta42 accumulation in human brain. *The American journal of pathology* 2000;156(1):15-20. [published Online First: 2000/01/07]

279. Langui D, Girardot N, Hamid El Hachimi K, et al. Subcellular Topography of Neuronal Aβ Peptide in APPxPS1 Transgenic Mice. *The American journal of pathology* 2004;165(5):1465-77.

280. Kaarniranta K, Sinha D, Blasiak J, et al. Autophagy and heterophagy dysregulation leads to retinal pigment epithelium dysfunction and development of age-related macular degeneration. *Autophagy* 2013;9(7):973-84. doi: 10.4161/auto.24546

281. Kaarniranta K, Hyttinen J, Ryhanen T, et al. Mechanisms of protein aggregation in the retinal pigment epithelial cells. *Frontiers in bioscience (Elite edition)* 2010;2:1374-84. [published Online First: 2010/06/03]

282. Toops KA, Tan LX, Lakkaraju A. A detailed three-step protocol for live imaging of intracellular traffic in polarized primary porcine RPE monolayers. *Experimental eye research* 2014;124:74-85. doi: 10.1016/j.exer.2014.05.003

283. Finnemann SC. Role of avb5 integrin in regulating phagocytosis by the retinal pigment epithelium. In: M.M.; L, J.G.; H, R.E. A, eds. Retinal Degenerations Advances in Experimental Medicine and Biology. Boston, MA: Springer 2003.

284. Westenskow PD, Moreno SK, Krohne TU, et al. Using Flow Cytometry to Compare the Dynamics of Photoreceptor Outer Segment Phagocytosis in iPS-Derived RPE Cells. *Investigative ophthalmology & visual science* 2012;53(10):6282-90. doi: 10.1167/iovs.12-9721

285. Finnemann SC, Silverstein RL. Differential Roles of CD36 and αvβ5 Integrin in Photoreceptor Phagocytosis by the Retinal Pigment Epithelium. *The Journal of Experimental Medicine* 2001;194(9):1289-98.

286. Madara JL. Regulation of the movement of solutes across tight junctions. *Annual review of physiology* 1998;60:143-59. doi: 10.1146/annurev.physiol.60.1.143 [published Online First: 1998/04/29]

287. Lynn S, Keeling E, Dewing J, et al. A convenient protocol for establishing a human cell culture model of the outer retina. [version 1; referees: 1 approved]. *F1000Research* 2018;7(1107) doi: 10.12688/f1000research.15409.1

288. Rajasekaran SA, Huynh TP, Wolle DG, et al. Na, K-ATPase subunits as markers for epithelial-mesenchymal transition in cancer and fibrosis. *Molecular cancer therapeutics* 2010;9(6):1515-24. doi: 10.1158/1535-7163.MCT-09-0832

289. Ablonczy Z, Dahrouj M, Tang PH, et al. Human retinal pigment epithelium cells as functional models for the RPE in vivo. *Investigative ophthalmology & visual science* 2011;52(12):8614-20. doi: 10.1167/iovs.11-8021 [published Online First: 2011/10/01]

290. Kamao H, Mandai M, Okamoto S, et al. Characterization of Human Induced Pluripotent Stem Cell-Derived Retinal Pigment Epithelium Cell Sheets Aiming for Clinical Application. *Stem Cell Reports* 2014;2(2):205-18. doi: 10.1016/j.stemcr.2013.12.007

291. Sonoda S, Spee C, Barron E, et al. A protocol for the culture and differentiation of highly polarized human retinal pigment epithelial cells. *Nature protocols* 2009;4(5):662-73. doi: 10.1038/nprot.2009.33

292. Serpell L. Amyloid structure. *Essays in biochemistry* 2014;56:1-10. doi: 10.1042/bse0560001 [published Online First: 2014/08/19]

293. Williams TL, Day IJ, Serpell LC. The effect of Alzheimer's Abeta aggregation state on the permeation of biomimetic lipid vesicles. *Langmuir : the ACS journal of surfaces and colloids* 2010;26(22):17260-8. doi: 10.1021/la101581g [published Online First: 2010/10/07]

294. Ryan J. Endotoxins and Cell Culture, 2008:1-7.

295. Kozera B, Rapacz M. Reference genes in real-time PCR. *Journal of Applied Genetics* 2013;54(4):391-406. doi: 10.1007/s13353-013-0173-x

296. Silver N, Best S, Jiang J, et al. Selection of housekeeping genes for gene expression studies in human reticulocytes using real-time PCR. *BMC Molecular Biology* 2006;7:33-33. doi: 10.1186/1471-2199-7-33

297. Penna I, Vella S, Gigoni A, et al. Selection of Candidate Housekeeping Genes for Normalization in Human Postmortem Brain Samples. *International Journal of Molecular Sciences* 2011;12(9):5461-70. doi: 10.3390/ijms12095461

298. Fernandez-Godino R, Garland DL, Pierce EA. Isolation, culture and characterization of primary mouse RPE cells. *Nature protocols* 2016;11:1206. doi: 10.1038/nprot.2016.065

299. Hu J, Bok D. A cell culture medium that supports the differentiation of human retinal pigment epithelium into functionally polarized monolayers. *Molecular Vision* 2000;7:14-19.

300. Maminishkis A, Chen S, Jalickee S, et al. Confluent Monolayers of Cultured Human Fetal Retinal Pigment Epithelium Exhibit Morphology and Physiology of Native Tissue. *Investigative ophthalmology & visual science* 2006;47(8):3612-24. doi: 10.1167/iovs.051622

301. Blenkinsop TA, Salero E, Stern JH, et al. The culture and maintenance of functional retinal pigment epithelial monolayers from adult human eye. *Methods in molecular biology (Clifton, NJ)* 2013;945:45-65. doi: 10.1007/978-1-62703-125-7_4 [published Online First: 2012/10/26]

302. Ahmado A, Carr AJ, Vugler AA, et al. Induction of differentiation by pyruvate and DMEM in the human retinal pigment epithelium cell line ARPE-19. *Investigative ophthalmology & visual science* 2011;52(10):7148-59. doi: 10.1167/iovs.10-6374 [published Online First: 2011/07/12]

303. Lynn SA, Ward G, Keeling E, et al. Ex-vivo models of the Retinal Pigment Epithelium (RPE) in long-term culture faithfully recapitulate key structural and physiological features of native RPE. *Tissue and Cell* 2017;49(4):447-60. doi: https://doi.org/10.1016/j.tice.2017.06.003

304. Johnson LV, Forest DL, Banna CD, et al. Cell culture model that mimics drusen formation and triggers complement activation associated with age-related macular degeneration. *Proceedings of the National Academy of Sciences of the United States of America* 2011;108(45):18277-82. doi: 10.1073/pnas.1109703108

305. Ren H, Birch NP, Suresh V. An Optimised Human Cell Culture Model for Alveolar Epithelial Transport. *PloS one* 2016;11(10):e0165225. doi: 10.1371/journal.pone.0165225 [published Online First: 2016/10/26]

306. Cao L, McCaig CD, Scott RH, et al. Polarizing intestinal epithelial cells electrically through Ror2. *Journal of Cell Science* 2014;127(15):3233-39. doi: 10.1242/jcs.146357

307. Jansen J, Schophuizen CM, Wilmer MJ, et al. A morphological and functional comparison of proximal tubule cell lines established from human urine and kidney tissue. *Experimental cell research* 2014;323(1):87-99. doi: 10.1016/j.yexcr.2014.02.011 [published Online First: 2014/02/25]

308. Christensen DRG, Brown FE, Cree AJ, et al. Sorsby fundus dystrophy – A review of pathology and disease mechanisms. *Experimental eye research* 2017;165:35-46. doi: https://doi.org/10.1016/j.exer.2017.08.014

309. Kuznetsova AV, Kurinov AM, Aleksandrova MA. Cell Models to Study Regulation of Cell Transformation in Pathologies of Retinal Pigment Epithelium. *Journal of Ophthalmology* 2014;2014:18. doi: 10.1155/2014/801787

310. Rawes V, Kipling D, Kill IR, et al. The kinetics of senescence in retinal pigmented epithelial cells: A test for the telomere hypothesis of ageing? *Biochemistry (Moscow)* 1997;62(11):1291-95.

311. Samuel W, Jaworski C, Postnikova OA, et al. Appropriately differentiated ARPE-19 cells regain phenotype and gene expression profiles similar to those of native RPE cells. *Molecular Vision* 2017;23:60-89.

312. Bauer H, Zweimueller-Mayer J, Steinbacher P, et al. The Dual Role of Zonula Occludens (ZO) Proteins. *Journal of Biomedicine and Biotechnology* 2010;2010 doi: 10.1155/2010/402593

313. Gottardi CJ, Arpin M, Fanning AS, et al. The junction-associated protein, zonula occludens-1, localizes to the nucleus before the maturation and during the remodeling of cell-cell contacts. *Proceedings of the National Academy of Sciences of the United States of America* 1996;93(20):10779-84. [published Online First: 1996/10/01]

314. Lehmann GL, Benedicto I, Philp NJ, et al. Plasma membrane protein polarity and trafficking in RPE cells: Past, present and future. *Experimental eye research* 2014;126:5-15. doi: https://doi.org/10.1016/j.exer.2014.04.021

315. Glotin AL, Debacq-Chainiaux F, Brossas JY, et al. Prematurely senescent ARPE-19 cells display features of age-related macular degeneration. *Free radical biology & medicine* 2008;44(7):1348-61. doi: 10.1016/j.freeradbiomed.2007.12.023

316. Okamoto N, Tobe T, Hackett S, et al. Transgenic mice with increased expression of vascular endothelial growth factor in the retina: a new model of intraretinal and subretinal neovascularization. . *Am J Pathol* 1997;151:281-91.

317. Schwesinger C, Yee C, Rohan R, et al. Intrachoroidal neovascularization in transgenic mice overexpressing vascular endothelial growth factor in the retinal pigment epithelium. *Am J Pathol* 2001;158:1161–72.

318. Park SW, Kim J, Park S, et al. RAGE mediated intracellular Ab uptake contributes to the breakdown of tight junction in retinal pigment epithelium. *Oncotarget* 2015;6(34):35263-73.

319. Song MS, Baker GB, Todd KG, et al. Inhibition of beta-amyloid1-42 internalization attenuates neuronal death by stabilizing the endosomal-lysosomal system in rat cortical cultured neurons. *Neuroscience* 2011;178:181-8. doi: 10.1016/j.neuroscience.2010.12.055 [published Online First: 2011/01/26]

320. Cha MY, Han SH, Son SM, et al. Mitochondria-specific accumulation of amyloid beta induces mitochondrial dysfunction leading to apoptotic cell death. *PloS one* 2012;7(4):e34929. doi: 10.1371/journal.pone.0034929

321. Ferrington DA, Sinha D, Kaarniranta K. Defects in Retinal Pigment Epithelial Cell Proteolysis and the Pathology Associated with Age-related Macular Degeneration. *Progress in retinal and eye research* 2016;51:69-89. doi: 10.1016/j.preteyeres.2015.09.002

322. Krohne TU, Kaemmerer E, Holz FG, et al. Lipid peroxidation products reduce lysosomal protease activities in human retinal pigment epithelial cells via two different mechanisms of action. *Experimental eye research*

2010;90(2):261-6. doi: 10.1016/j.exer.2009.10.014 [published Online First: 2009/11/10]

323. Cataldo AM, Hamilton DJ, Nixon RA. Lysosomal abnormalities in degenerating neurons link neuronal compromise to senile plaque development in Alzheimer disease. *Brain research* 1994;640(1-2):68-80. [published Online First: 1994/03/21]

324. Karp G. Cell and Molecular Biology: Concepts and Experiments. 6 ed. Hoboken, New Jersey: John Wiley & Sons, Inc 2010.

325. Peters S, Reinthal E, Blitgen-Heinecke P, et al. Inhibition of lysosomal degradation in retinal pigment epithelium cells induces exocytosis of phagocytic residual material at the basolateral plasma membrane. *Ophthalmic research* 2006;38(2):83-8. doi: 10.1159/000090268 [published Online First: 2005/12/15]

326. Stoka V, Turk V, Turk B. Lysosomal cathepsins and their regulation in aging and neurodegeneration. *Ageing Research Reviews* 2016;32:22-37. doi: https://doi.org/10.1016/j.arr.2016.04.010

327. Zheng L, Kagedal K, Dehvari N, et al. Oxidative stress induces macroautophagy of amyloid beta-protein and ensuing apoptosis. *Free radical biology & medicine* 2009;46(3):422-9. doi: 10.1016/j.freeradbiomed.2008.10.043 [published Online First: 2008/11/29]

328. He Y, Hara H, Núñez G. Mechanism and Regulation of NLRP3 Inflammasome Activation. *Trends in Biochemical Sciences* 2016;41(12):1012-21. doi: 10.1016/j.tibs.2016.09.002

329. Katunuma N. Posttranslational Processing and Modification of Cathepsins and Cystatins. *Journal of Signal Transduction* 2010;2010 doi: 10.1155/2010/375345

330. Elizabeth Rakoczy P, Yu MJT, Nusinowitz S, et al. Mouse models of age-related macular degeneration. *Experimental eye research* 2006;82(5):741-52. doi: https://doi.org/10.1016/j.exer.2005.10.012

331. Pennesi ME, Neuringer M, Courtney RJ. Animal models of age related macular degeneration. *Molecular aspects of medicine* 2012;33(4):487-509. doi: 10.1016/j.mam.2012.06.003

332. Volland S, Esteve-Rudd J, Hoo J, et al. A Comparison of Some Organizational Characteristics of the Mouse Central Retina and the Human Macula. *PloS one* 2015;10(4):e0125631. doi: 10.1371/journal.pone.0125631

333. Coffey PJ, Gias C, McDermott CJ, et al. Complement factor H deficiency in aged mice causes retinal abnormalities and visual dysfunction. *Proceedings of the National Academy of Sciences of the United States of America* 2007;104(42):16651-56. doi: 10.1073/pnas.0705079104

334. Ufret-Vincenty RL, Aredo B, Liu X, et al. Transgenic mice expressing variants of complement factor H develop AMD-like retinal findings. *Investigative ophthalmology & visual science* 2010;51(11):5878-87. doi: 10.1167/iovs.09-4457 [published Online First: 2010/06/12]

335. Hahn P, Qian Y, Dentchev T, et al. Disruption of ceruloplasmin and hephaestin in mice causes retinal iron overload and retinal degeneration

with features of age-related macular degeneration. *Proceedings of the National Academy of Sciences of the United States of America* 2004;101(38):13850-5. doi: 10.1073/pnas.0405146101 [published Online First: 2004/09/15]

336. Muhlfriedel R, Michalakis S, Garcia Garrido M, et al. Optimized technique for subretinal injections in mice. *Methods in molecular biology (Clifton, NJ)* 2013;935:343-9. doi: 10.1007/978-1-62703-080-9_24 [published Online First: 2012/11/15]

337. Langford DJ, Bailey AL, Chanda ML, et al. Coding of facial expressions of pain in the laboratory mouse. *Nature methods* 2010;7(6):447-9. doi: 10.1038/nmeth.1455 [published Online First: 2010/05/11]

338. McBain VA. Electrophysiology Testing in Patients with Inherited Retinal Disease. In: Azuara-Blanco A, Hossain P, Lois N, eds. Diagnostic Technologies in Ophthalmology: Bentham Science Publishers 2012.

339. Wood A, Margrain T, Binns AM. Detection of Early Age-Related Macular Degeneration Using Novel Functional Parameters of the Focal Cone Electroretinogram. *PloS one* 2014;9(5):e96742. doi: 10.1371/journal.pone.0096742

340. Berrow EJ, Bartlett HE, Eperjesi F, et al. The electroretinogram: a useful tool for evaluating age-related macular disease? *Documenta ophthalmologica Advances in ophthalmology* 2010;121(1):51-62. doi: 10.1007/s10633-010-9226-1 [published Online First: 2010/03/17]

341. Liu C, Cao L, Yang S, et al. Subretinal injection of amyloid-beta peptide accelerates RPE cell senescence and retinal degeneration. *International journal of molecular medicine* 2015;35(1):169-76. doi: 10.3892/ijmm.2014.1993 [published Online First: 2014/11/12]

342. Parthasarathy R, Chow KM, Derafshi Z, et al. Reduction of amyloid-beta levels in mouse eye tissues by intra-vitreally delivered neprilysin. *Experimental Eye Research* 2015;138:134-44. doi: https://doi.org/10.1016/j.exer.2015.06.027

343. Shah VP, Shah SA, Mrejen S, et al. Subretinal hyperreflective exudation associated with neovascular age-related macular degeneration. *Retina (Philadelphia, Pa)* 2014;34(7):1281-8. doi: 10.1097/iae.0000000000000166 [published Online First: 2014/04/04]

344. Coscas G, Jose C-V, Soubrane G. Macular Edema: Definition and Basic Concepts. In: Coscas G, Loewenstein A, Cunha-Vaz J, et al., eds. Macular Edema. 2nd ed: Karger Medical and Scientific Publishers 2017.

345. Saint-Geniez M, Kurihara T, Sekiyama E, et al. An essential role for RPE-derived soluble VEGF in the maintenance of the choriocapillaris. *Proceedings of the National Academy of Sciences* 2009;106(44):18751-56. doi: 10.1073/pnas.0905010106

346. Liu D, Zhang L, Li Z, et al. Thinner changes of the retinal nerve fiber layer in patients with mild cognitive impairment and Alzheimer's disease. *BMC Neurology* 2015;15:14. doi: 10.1186/s12883-015-0268-6

347. Xu G, Weinreb RN, Leung CKS. Retinal nerve fiber layer progression in glaucoma: a comparison between retinal nerve fiber layer thickness and

retardance. *Ophthalmology* 2013;120(12):2493-500. doi: 10.1016/j.ophtha.2013.07.027 [published Online First: 2013/09/24]

348. Querques G, Costanzo E, Miere A, et al. Choroidal Caverns: A Novel Optical Coherence Tomography Finding in Geographic Atrophy. *Investigative ophthalmology & visual science* 2016;57(6):2578-82. doi: 10.1167/iovs.16-19083

349. Bishop PN. Structural macromolecules and supramolecular organisation of the vitreous gel. *Progress in retinal and eye research* 2000;19(3):323-44. doi: https://doi.org/10.1016/S1350-9462(99)00016-6

350. Donati S, Caprani SM, Airaghi G, et al. Vitreous Substitutes: The Present and the Future. *BioMed Research International* 2014;2014:12. doi: 10.1155/2014/351804

351. Alovisi C, Panico C, de Sanctis U, et al. Vitreous Substitutes: Old and New Materials in Vitreoretinal Surgery. *Journal of Ophthalmology* 2017;2017:3172138. doi: 10.1155/2017/3172138

352. Kersten E, Paun CC, Schellevis RL, et al. Systemic and ocular fluid compounds as potential biomarkers in age-related macular degeneration. *Survey of ophthalmology* 2018;63(1):9-39. doi: https://doi.org/10.1016/j.survophthal.2017.05.003

353. McAuley AK, Sanfilippo PG, Hewitt AW, et al. Vitreous biomarkers in diabetic retinopathy: A systematic review and meta-analysis. *Journal of Diabetes and its Complications* 2014;28(3):419-25. doi: https://doi.org/10.1016/j.jdiacomp.2013.09.010

354. Zorena K, Raczy, #x144, et al. Biomarkers in Diabetic Retinopathy and the Therapeutic Implications. *Mediators of inflammation* 2013;2013:11. doi: 10.1155/2013/193604

355. Fan F, Montemari AL, Rossi S, et al. Up-regulation Of Soluble Amyloid Beta And Down-regulation Of Soluble RAGE In The Vitreous Of Age-related Macular Degeneration Patients. *Investigative ophthalmology & visual science* 2012;53(14):6423-23.

356. Virdis A, Giannarelli C, Neves MF, et al. Cigarette smoking and hypertension. *Current pharmaceutical design* 2010;16(23):2518-25. [published Online First: 2010/06/17]

357. Jaouni T, Averbukh E, Burstyn-Cohen T, et al. Association of pattern dystrophy with an HTRA1 single-nucleotide polymorphism. *Archives of ophthalmology (Chicago, Ill : 1960)* 2012;130(8):987-91. doi: 10.1001/archophthalmol.2012.1483 [published Online First: 2012/08/16]

358. Wong TY, Ohno-Matsui K, Leveziel N, et al. Myopic choroidal neovascularisation: current concepts and update on clinical management. *The British journal of ophthalmology* 2015;99(3):289-96. doi: 10.1136/bjophthalmol-2014-305131 [published Online First: 2014/07/06]

359. McGhee M. A Guide to Laboratory Investigations. 5th ed. Oxford: Radcliffe Publishing Ltd 2008.

360. Hogg RE, Woodside JV, Gilchrist SE, et al. Cardiovascular disease and hypertension are strong risk factors for choroidal neovascularization.

Ophthalmology 2008;115(6):1046-52.e2. doi: 10.1016/j.ophtha.2007.07.031 [published Online First: 2007/10/24]

361. Guymer R, Cipriani T, Rittenhouse KD, et al. Plasma levels of amyloid beta and other proinflammatory mediators in patients with age-related macular degeneration. *Graefe's archive for clinical and experimental ophthalmology = Albrecht von Graefes Archiv fur klinische und experimentelle Ophthalmologie* 2015;253(8):1347-54. doi: 10.1007/s00417-015-2970-x [published Online First: 2015/03/07]

362. Souw D. ARP Blog – Matrix effects 2017 [Available from: http://blog.arp1.com/arp-blog-matrix-effects/.

363. Sedgwick P. Analysing case-control studies: adjusting for confounding. *BMJ : British Medical Journal* 2013;346 doi: 10.1136/bmj.f25

364. Pearce N. Analysis of matched case-control studies. *BMJ* 2016;352 doi: 10.1136/bmj.i969

365. Snyder HM, Carrillo MC, Grodstein F, et al. Developing Novel Blood-Based Biomarkers for Alzheimer's Disease. *Alzheimer's & dementia : the journal of the Alzheimer's Association* 2014;10(1):109-14. doi: 10.1016/j.jalz.2013.10.007

366. Poljak A, Sachdev PS. Plasma amyloid beta peptides: an Alzheimer's conundrum or a more accessible Alzheimer's biomarker? *Expert Review of Neurotherapeutics* 2017;17(1):3-5. doi: 10.1080/14737175.2016.1217156

367. Toledo JB, Shaw LM, Trojanowski JQ. Plasma amyloid beta measurements - a desired but elusive Alzheimer's disease biomarker. *Alzheimer's research & therapy* 2013;5(2):8. doi: 10.1186/alzrt162 [published Online First: 2013/03/09]

368. Janelidze S, Stomrud E, Palmqvist S, et al. Plasma β-amyloid in Alzheimer's disease and vascular disease. *Scientific Reports* 2016;6:26801. doi: 10.1038/srep26801

369. Honig LS, Kang M-S, Tang M-X, et al. PLASMA AB40 AND AB42 DECLINE WITH PROGRESSION OF DEMENTIA. *Alzheimer's & Dementia: The Journal of the Alzheimer's Association* 2014;10(4):P271. doi: 10.1016/j.jalz.2014.04.440

370. Seppälä TT, Herukka SK, Hänninen T, et al. Plasma Aβ42 and Aβ40 as markers of cognitive change in follow-up: a prospective, longitudinal, population-based cohort study. *Journal of Neurology, Neurosurgery, and Psychiatry* 2010;81(10):1123-27. doi: 10.1136/jnnp.2010.205757

371. Kawarabayashi T, Younkin LH, Saido TC, et al. Age-dependent changes in brain, CSF, and plasma amyloid (beta) protein in the Tg2576 transgenic mouse model of Alzheimer's disease. *The Journal of neuroscience : the official journal of the Society for Neuroscience* 2001;21(2):372-81. [published Online First: 2001/02/13]

372. Graff-Radford NR, Crook JE, Lucas J, et al. Association of low plasma Abeta42/Abeta40 ratios with increased imminent risk for mild cognitive impairment and Alzheimer disease. *Archives of neurology* 2007;64(3):354-62. doi: 10.1001/archneur.64.3.354 [published Online First: 2007/03/14]

373. Finnemann SC, Leung LW, Rodriguez-Boulan E. The lipofuscin component A2E selectively inhibits phagolysosomal degradation of photoreceptor

phospholipid by the retinal pigment epithelium. *Proceedings of the National Academy of Sciences of the United States of America* 2002;99(6):3842-47. doi: 10.1073/pnas.052025899

374. Guha S, Coffey EE, Lu W, et al. Approaches for detecting lysosomal alkalinization and impaired degradation in fresh and cultured RPE cells: evidence for a role in retinal degenerations. *Experimental eye research* 2014;126:68-76. doi: 10.1016/j.exer.2014.05.013

375. Oakley H, Cole SL, Logan S, et al. Intraneuronal beta-amyloid aggregates, neurodegeneration, and neuron loss in transgenic mice with five familial Alzheimer's disease mutations: potential factors in amyloid plaque formation. *The Journal of neuroscience : the official journal of the Society for Neuroscience* 2006;26(40):10129-40. doi: 10.1523/jneurosci.1202-06.2006 [published Online First: 2006/10/06]

376. Criscuolo C, Cerri E, Fabiani C, et al. The retina as a window to early dysfunctions of Alzheimer's disease following studies with a 5xFAD mouse model. *Neurobiology of aging* 2018;67:181-88. doi: 10.1016/j.neurobiolaging.2018.03.017 [published Online First: 2018/05/08]

377. Alexandrov PN, Pogue A, Bhattacharjee S, et al. Retinal amyloid peptides and complement factor H in transgenic models of Alzheimer's disease. *Neuroreport* 2011;22(12):623-7. doi: 10.1097/WNR.0b013e3283497334 [published Online First: 2011/07/08]

378. Park SW, Im S, Jun HO, et al. Dry age-related macular degeneration like pathology in aged 5XFAD mice: Ultrastructure and microarray analysis. *Oncotarget* 2017;8(25):40006-18. doi: 10.18632/oncotarget.16967 [published Online First: 2017/05/04]